STUDY OF ORGANIC SEMICONDUCTOR BASED PHOTOVOLTAIC DEVICES: LIGHT SENSORS AND SOLAR CELLS

KARWAN WASMAN QADIR

UNIVERSITY OF MALAYA
KUALA LUMPUR

2016

STUDY OF ORGANIC SEMICONDUCTOR BASED PHOTOVOLTAIC DEVICES: LIGHT SENSORS AND SOLAR CELLS

KARWAN WASMAN QADIR

THESIS SUBMITTED IN FULFILMENT OF THE REQUIREMENTS FOR THE DEGREE OF DOCTOR OF PHILOSOPHY

FACULTY OF SCIENCE
UNIVERSITY OF MALAYA
KUALA LUMPUR

2016

UNIVERSITY OF MALAYA
ORIGINAL LITERARY WORK DECLARATION

Name of Candidate: **Karwan Wasman Qadir**
Registration/Matric No: **SHC120049**
Name of Degree: **Doctor of Philosophy**
Title of Thesis ("this Work"):
STUDY OF ORGANIC SEMICONDUCTOR BASED PHOTOVOLTAIC DEVICES: LIGHT SENSORS AND SOLAR CELLS

Field of Study: **Experimental Physics (Physics)-Organic Electronics**

I do solemnly and sincerely declare that:

(1) I am the sole author/writer of this Work;
(2) This Work is original;
(3) Any use of any work in which copyright exists was done by way of fair dealing and for permitted purposes and any excerpt or extract from, or reference to or reproduction of any copyright work has been disclosed expressly and sufficiently and the title of the Work and its authorship have been acknowledged in this Work;
(4) I do not have any actual knowledge nor do I ought reasonably to know that the making of this work constitutes an infringement of any copyright work;
(5) I hereby assign all and every rights in the copyright to this Work to the University of Malaya ("UM"), who henceforth shall be owner of the copyright in this Work and that any reproduction or use in any form or by any means whatsoever is prohibited without the written consent of UM having been first had and obtained;
(6) I am fully aware that if in the course of making this Work I have infringed any copyright whether intentionally or otherwise, I may be subject to legal action or any other action as may be determined by UM.

Candidate's Signature Date:

Subscribed and solemnly declared before,

Witness's Signature Date:

Name: **Dr. Khaulah Sulaiman**
Designation: **Associate Professor**

ABSTRACT

Recently, organic photovoltaic devices (OPVDs) have been extensively studied and demonstrated as promising candidates for light sensing applications. The novel materials are used in optoelectronic applications, utilizing their intrinsic physical, chemical and electrical characteristics. Organic semiconductors offer many physical and chemical properties that can be easily tailored by incorporating functional groups or manipulating physical conditions to meet specific requirements. The best feature of organic semiconductors is their solution processability at room temperature using simple and low cost deposition techniques. Aiming at the interesting properties of organic semiconductors, in this thesis, we have extensively explored organic semiconductors based solar cells and light sensors for optoelectronic applications. Dye sensitized photo sensors using water soluble organic photo sensitizer, Nickel (II) phthalocyanine-tetrasulfonic acid tetrasodium salt (NiTsPc) have been fabricated and investigated. Two different types of TiO_2 films (untreated and NaOH-treated) are prepared to serve as anodes for the sensors. Both films are subsequently sensitized by NiTsPc using aqueous solution. Commercially available Iodolyte Z100 and platinum coated indium doped tin oxide (ITO) are used as electrolyte and cathode, respectively. The NaOH-treated sensor demonstrates 2.81 times increase in sensitivity in terms of photo-conductivity as compared to the untreated sensor. The NaOH-treated sensor, however, surpasses the other sensor in terms of response/recovery times and stability in plateau values of the photocurrent. The proposed photosensor is eco-friendly and economical for commercial applications. A binary blend of two polymers, poly[2,6-(4,4-bis-(2-ethylhexyl)-4H-cyclopenta [2,1-b;3,4-b']dithiophene)-alt-4,7(2,1,3-benzothiadiazole)] (PCPDTBT) and poly[2-methoxy-5-(2-ethylhexyloxy)-1,4-phenylenevinylene] (MEH-PPV) as a sensitizer has been employed for a visible light dye sensitized photo sensor (DSPS). The proposed combination of the polymers covers almost the entire visible light spectrum.

The dependence of the current generation in the dye sensitized photo sensor is investigated as a function of varied incident light intensities. The output shows a linear relation as a function of incident light in the range of 0-30000 lx. The photo-conductivity sensitivity of the dye sensitized photo sensor is about 2.02×10^{-5} Sm/W. The average response time of the sensor is found ∼382 ms. In addition to consistency and repeatability, the fabrication of this sensor is economical and environmentally friendly. The effect of thermal annealing on the optical, morphological and photovoltaic properties of bulk heterojunction solar cell based on the poly[2,5-bis(3-dodecylthiophen-2-yl)thieno[3,2-*b*]thiophene] (PBTTT-C_{12}) and[6,6]-phenyl C_{71}-butyric acid methyl ester ($PC_{71}BM$) has been investigated. The ITO/PEDOT:PSS/PBTTT-C_{12}:$PC_{71}BM$/Al devices are fabricated on glass substrates from the PBTTT-C_{12}:$PC_{71}BM$ (1:4) solution in dichlorobenzene. Atomic Force Microscopy (AFM) is used to investigate the surface morphology of the PBTTT-C_{12}:$PC_{71}BM$ thin films. The AFM results show that the surface roughness of the thin film decreases with increasing annealing temperature, making the annealed film smoother as compared to the non-annealed sample. The efficiency of the ITO/PEDOT:PSS/PBTTT-C_{12}:$PC_{71}BM$/Al photovoltaic devices increases from 1.85 to 2.48% with an increment in the temperature ranging from 0 ℃ to 150 ℃.

ABSTRAK

Kebelakangan ini, peranti foto-voltan organik dikaji dengan giatnya apabila ia menunjukkan potensi besar dalam aplikasi mengesan cahaya. Bahan baru dengan mempunyai kelainan sifat fizikal, kimia, dan elekrikal, telah banyak digunakan dalam aplikasi opto-elektronik. Bahan seperti semikonduktor organik ini membenarkan sifat fizikal dan kimianya diubah dengan pengubahsuaian kumpulan berfungsinya bagi memenuhi kehendak tertentu. Ciri terbaik semikonduktor organik ini adalah kebolehannya dalam pemprosesan berbentuk larutan pada suhu bilik yang disifatkan sebagai ringkas dan jimat. Dalam tesis ini, aplikasi bagi semikonduktor organik dalam pembuatan sel solar dan pengesan cahya, telah dikaji. Sejenis pewarna yang larut dalam air, iaitu garam *Nikel (II) ftalosianina-asid tetrasulfonik tetranatrium* (NiTsPc) telah digunakan dalam fabrikasi dan ujikaji sel solar berasaskan pewarna. Dua variasi filem TiO_2 (tulen dan dirawat NaOH) telah disediakan sebagai anod untuk peranti pengesan cahaya. Bahan seperti Iodolyte Z100 dan ITO bersadur platinum, masing-masing digunakan sebagai elektrolit dan katod. Pengesan cahaya dengan TiO_2 yang dirawat NaOH menunjukkan peningkatan kepekaan sebanyak 2.81 kali ganda pada foto-konduktivitinya jika dibandingkan dengan peranti yang tak dirawat NaOH. Disamping itu, pengesan cahaya yang dirawat NaOH ini telah melepasi prestasi pengesan cahaya yang lain pada masa respon an kestabilannya. Pengesan cahaya yang dicadangkan ini adalah mesra alam dan ekonomikal untuk tujuan komersial. Campuran dua bahan polimer *Poli[2,6-(4,4-bis-(2-etilheksil)-4H-siklopenta [2,1-b;3,4-b']ditiofena)-alt-4,7(2,1,3-benzotiadiazola)]* (PCPDTBT) dan *Poli[2-metoksi-5-(2-etilheksiloksi)-1,4-fenilenavinilena]* (MEH-PPV) telah digunakan dalam pengesan cahaya nampak berasaskan pewarna. Gabungan bahan-bahan polimer yang dicadangkan ini mampu menyerap hampir kesemua spekrum cahaya nampak. Penghasilan arus peranti ini diuji dengan keamatan cahaya yang berbeza. Ia menunjukkan hubungan linear antara penghasilan arus dan keamatan cahaya dalam julat 0-30000 lx. Kepekaan foto-konduktiviti untuk pengesan cahaya berasaskan pewarna ini adalah 2.02×10^{-5} Sm/W. Manakala purata masa respon adalah $\sim$382 ms. Selain dari sifat peranti ini yang konsisten dan mampu diulang-ulang, ia boleh dihasilkan dengan kos yang rendah dan mesra alam. Kesan pemanasan terhadap sifat optikal, bentuk, dan foto-voltan bagi sel solar berasaskan *poly[2,5-bis(3-dodecylthiophen-2-yl)thieno[3,2-b]thiophene]* (PBTTT-C_{12}) dan *[6,6]-phenyl C_{71}-butyric acid methyl ester* ($PC_{71}BM$) turut dikaji. Peranti ITO/PEDOT:PSS/PBTTT-C_{12}:$PC_{71}BM$/Al dibina dengan campuran bahan aktif PBTTT-C_{12}:$PC_{71}BM$ dalam nisbah 1:4 yang dilarutkan di dalam dichlorobenzene. Sifat bentuk bagi permukaan filem PBTTT-C_{12}:$PC_{71}BM$ disiasat menggunakan Mikroskopi Daya Atom (AFM). Keputusan AFM menunjukkan permukaan filemnya menjadi kurang kasar dengan peningkatan suhu pemanasan, lalu menjadikan sampel yang dipanaskan ini lebih rata berbanding yang tak dirawat. Keberkesanan bagi sel solar ITO/PEDOT:PSS/PBTTT-C_{12}:$PC_{71}BM$/Al ini meningkat dari 1.85 kepada 2.48% dengan peningkatan suhu dari 0 ℃ ke 150 ℃.

ACKNOWLEDGEMENTS

All praises and glory to almighty (Allah ﷲ) (جل جلاله) for bestowing countless blessings, including physical robustness in me, on account of which I was able to complete this thesis. I humbly offer salutations upon all Prophets, the source of guidance and knowledge to all mankind.

I am grateful and highly indebted to my research advisor, Associate Prof. Dr. Khaulah Sulaiman. I extend my heartfelt respect for her unflagging encouragement and diligent supervision. Her co-operative and amiable nature is indeed exemplary. In point of fact, I was doubly blest as I also worked under guidance of Dr. Zubair Ahmad (former Post Doc, Physics Department, Faculty of Science). He was always willing to guide me for being more productive and efficient in every single task that needed to be done in time. His useful comments and counseling has led to significant achievements in this work. They should receive most of my gratitude for what I have achieved today.

I would also like to extend my sincerest gratitude to Prof. Dato' Dr. Mohd Amin Jalaludin (Vice-Chancellor, University of Malaya), Prof. Dr. Zanariah Abdullah (Dean, Faculty of Science), Prof. Dr. Hasan Abu Kassim (Head, Department of Physics) and Prof. Datin Dr. Saadah Abd Rahman (Head, Low Dimensional Material Research Centre (LDMRC)) for providing excellent research-oriented environment and high-tech equipment at University of Malaya. Also, it has been a great pleasure to interact and learn from the faculty members of LDMRC. Many thanks to Miss. Norlela and Mr. Mohd Arof for administrating the labs and equipment.

Special thanks to my fellow lab mates Dr. Shahino, Dr. Qayyum, Miss. Rupak, Dr. Fakhra Aziz, Mr. Izzat, Mr. Muhamad Doris, Mr. Lim Lih Wei, and Dr. Mansoor Ani Najeeb who made my postgraduate study a wonderful and enriching experience.

I am enormously indebted to Mr. Mqdad Wasman and Eng. Farhad Wasman who never left my side and enthusiastically supported all of my studies, helped and guided me through difficult times till got to my final destination.

I lost my uncle Mr. Abdullah Qadir during course of my PhD study. May his soul rest in eternal peace, Ameen. I owe tremendous gratitude to my lovely mother Zulaikha Mawlood and my father Wasman Qadir (late) who devoted the best years of their lives into my education. They always wanted me to acquire higher education and whose prayers and unconditional love made this uphill task possible. Special thanks for the eminent support from Attorney Sherzad, Eng. Arsalan, Attorney Sawda, Associate Prof. Dr. Suhaila, Mrs. Mahabad, Miss. Rupak (best buddy) and Eng. Sazgar. Huge thanks to my beloved wife Shaima, who supports me with love and tender heart, and for understanding, endless patience and encouragement when it was most required. I am deeply grateful to almighty Allah for the cutest addition to our family; Layan and Rasan, who always give me sweetest smiles. Thanks to my parents in law for their support, love and trust.

Thanks to the Ministry of Higher Education & Scientific Research, Kurdistan Region-Iraq for its financial support to me through awarding Scholarship for PhD studies.

Thank you very much Malaysia for being such a wonderful host for three years. Friendly people, rich culture, ecological beauty; everything about Malaysia has been truly remarkable. Special thanks to Malaysian government for financially supporting my study.

Karwan Wasman

Jan. 16th, 2016

TABLE OF CONTENTS

Abstract iii

Abstrak v

Acknowledgements vii

Table of Contents ix

List of Figures xiii

List of Tables..xix

List of Abbreviations..xx

CHAPTER 1: INTRODUCTION..1

1.1 Introduction to Organic Semiconductors..1

1.2 Motivation..5

1.3 Thesis Objective 10

1.4 Thesis Framework 11

CHAPTER 2: BACKGROUND AND LITERATURE REVIEW..13

2.1 Part One: Dye Sensitized Photo Sensor (DSPS)..13

  2.1.1 Photo Sensitizer (Dyes) 15

    2.1.1.1 Phthalocyanines (Pcs) 19

    2.1.1.2 MEH-PPV 22

    2.1.1.3 PCPDTBT 23

  2.1.2 Photo Anode: TiO_2 Electrode or Working Electrode 25

  2.1.3 Redox Mediator (Electrolyte)..29

  2.1.4 Photo Cathode (Counter Electrode or Back Contact)..33

  2.1.5 Conductive Glass Substrate Materials (ITO Glass)..35

  2.1.6 Packing (Sealing) of Device..37

2.2 Dye Sensitized Photo Sensor Interfaces 37
2.2.1 The Process of Electron Transfer in DSPS 39
2.3 Excitons 49
2.4 Photo Sensor 50
2.5 Importance Sensing Parameters 51
2.5.1 Responsivity 51
2.5.2 Response-Recovery Time 52
2.6 Part Two: Bulk Heterojunction Solar Cell 52
2.6.1 Relationships between Morphology and Device Performance 57
2.6.1.1 Solvent Choice, Solvent Additives and Solvent Annealing (Slow Growth) 58
2.6.1.2 Thermal Annealing (Pre-Annealing) and Post-Annealing 60
2.6.1.3 Ratio of Donor-acceptor 64
2.6.2 Characterization Techniques 65
2.6.3 Open Circuit Voltage Evolution 66
2.6.4 Short Circuit Current Evolution 68
2.6.5 Fill Factor and Power Conversion Efficiency Evolution 69

CHAPTER 3: MATERIALS AND METHODS 72
3.1 Materials and Chemical 72
3.1.1 Organic Dye and Polymer Materials 73
3.1.2 TiO_2 Anatase 75
3.1.3 Solvents 77
3.1.4 Electrodes and Substrates 80
3.1.5 Electrolytes 81
3.2 Cleaning Substrates and Plasma Treatments 82
3.3 Preparation Methods 84

3.3.1 Vacuum Thermal Evaporation 84

3.3.2 Sputter Coating 89

3.3.3 Spin Coating 91

3.3.4 Doctor Blade Technique and Working Electrode Preparation 94

3.4 Thickness Determination of Thin Films 96

3.5 Characterization Technique 98

3.5.1 Electrical Characterization 99

3.5.1.1 Current-Voltage Characterization 99

3.5.1.2 Incident Photon-to-Current Conversion Efficiency (IPCE) 105

3.5.2 Optical Characterization (Surface Spectroscopy) 108

3.5.2.1 Ultra-Violet-Visible-Near Infra-Red Spectrometer (UV-VIS-NIR) 108

3.5.2.2 Photoluminescence Measurement 112

3.5.3 Surface Topography 115

3.5.3.1 Atomic Force Microscopy (AFM) 115

3.5.3.2 Field Emission Scanning Electron Microscope (FESEM) 118

CHAPTER 4: PERFORMANCE ENHANCEMENT OF NITSPC BASED PHOTO SENSOR USING TREATED TIO$_2$ NPS FILM 123

4.1 Chapter Overview 123

4.2 Introduction 123

4.3 Fabrication of Dye Sensitized Photo Sensor 124

4.4 Results and Discussion 126

4.5 Conclusion 135

CHAPTER 5: BINARY BLEND BASED DYE SENSITIZED PHOTO SENSOR USING PCPDTBT AND MEH-PPV COMPOSITE AS A LIGHT SENSITIZER 137

5.1 Introduction 137

5.2 Fabrication Method of Dye Sensitized Photo Sensor (DSPS) 138

5.3 Result and Discussion: 141

5.4 Conclusion 153

CHAPTER 6: THERMAL ANNEALING EFFECT ON THE OPTICAL, ELECTRICAL AND MORPHOLOGICAL PROPERTIES OF THE PBTTT-C_{12}:$PC_{71}BM$ BLEND FILMS 157

6.1 Chapter Overview 157

6.2 Introduction 157

6.3 Fabrication of Bulk Heterojunction Cells 158

6.4 Results and Discussion 159

6.5 Conclusion 167

CHAPTER 7: SUMMARIES AND FUTURE DIRECTIONS 170

7.1 Summary 170

7.2 Future Outlook 172

References 175

List of Publications and Papers Presented 210

LIST OF FIGURES

Figure 1.1: Commercially available examples of organic semiconductor applications; (a) Alan J. Heeger with foil of flexible organic solar cell, (b) Process of xerography by canon photocopier employing organic semiconductors, (c) A high performance luminescent window with white organic light emitting diodes (OLED) developed by OSRAM. When the window is exposed to AC power, it functions as panel lighting with brightness of 1000 cd/m^2, yet when powered off, its transparency reached 75% with a large-scale area around 90 cm^2.(d) Featuring an OLED display by Samsung Galaxy smartphone, (e) Lighting tiles with essentially glare-free made by OSRAM..3

Figure 1.2: Examples of different classe organic semiconductor structures. Nickel phthalocyanine (small molecule) and poly(para-phenylene) (polymer), respectively. 3

Figure 1.3: Record efficiencies development for all types of organic solar cells (except perovskite cells) compared with inorganic cells from 1991 until 2015. This is a part of the last updated graph (Dec 18 2015) for record cell efficiencies assembled by and courtesy of the National Renewable Energy Laboratory (National Renewable Energy Laboratory, 2015). 5

Figure 1.4: Number of published articles from 2005 to 2015 from Web Of Science-Core Collection with the topic keywords “solar cell OR photovoltaic cell” AND “organic OR polymer OR small molecular”. 5

Figure 2.1: 3D schematic depiction of structure and function of typical TiO_2 based DSSC (not to scale). The primary particle TiO_2 anatase diameter is 8-20 nm and void space is ca. 50%. A sheet resistivity at room temperature and light transmittance of ITO generally is 10-15 Ω/sq. and $\sim 90\%$ respectively. Diameter of platinum nanoparticles typically ~ 5 nm (Murphy, 2015). 14

Figure 2.2: Chemical structure of the co-adsorbent Chenodeoxycholic acid (cheno) (Daeneke et al., 2011). 18

Figure 2.3: Molecular structure of metal-free phthalocyanine (H_2Pc) with carbon assignments. 20

Figure 2.4: Chemical structure of TiO_2 surface with the possible binding modes of representative complexes. The CB of the TiO_2 is formed by the empty 3d orbitals of the Ti^{4+} ions, while the VB is mainly constituted by the occupied 2p orbitals of the O^{2-} ions (Zhang, Kim, & Choi, 2014). 27

Figure 2.5: Schematic diagram of the electrolyte (the pathway for the reduction of the oxidized dye ($D +$) by iodide ($I -$)). The light harvesting in DSPS is accomplished by dye molecules located at the interface of an electrolyte and a mesoporous wide

band gap TiO_2 electrode. At that time, the redox mediator is employed to regenerate the oxidized dye, following a photo-induced charge injection from the dye into the CB of TiO_2 electrode. The difference between the Fermi level (EF) of the TiO_2 and the redox potential of the mediator is represented by the Voc of the cell. The below figure is the details of seven redox reactions of the $(I -/I3-)$ system and their relative electrochemical potentials. Some of these reactions are important for the DSPS. The indicated differences in formal potentials are $a = (RTF)\ln K3; b = (RT2F)\ln K2; c = b - a; d = RT2F\ln K1;$ and $e = c + d$ (Boschloo & Hagfeldt, 2009)... 32

Figure 2.6: Different interface indications in the DSPS (Kaufmann Eriksson, 2014)....38

Figure 2.7: (Above) Energy level schematic illustration of the interfacial electron transfer reactions and the electronic processes occurs in DSPS. The favorable reactions (electron transfer processes) contributing to the energy conversion are indicated by the indigo arrows (1), the unlike reactions (recombination) loss channels which limit the photovoltaic performance by dashed red and the hole transfer processes marked by purple arrows (2). The energy levels are approximately given with respect to normal hydrogen electrode (NHE) in V and vacuum in eV. Below the schematic are shown the dynamics of the electron transfer processes. In detail Fig (below), the free energy stored in the charge separated states are corresponded to the vertical scale. The determination of the free energy of injected electrons is considered by the TiO_2 Fermi level which is assuming the chemical potential of the redox electrolyte below a Fermi level 0.6 V of TiO_2. Blue arrows are indicated forward processes of light absorption, electron injection, dye regeneration, and charge transport. Black arrows show the competing loss pathways of electron recombination and excited state decay to ground with dye cations and oxidized redox couple (Dualeh, 2014; Listorti et al., 2011)...41

Figure 2.8: The electron transport schematic diagram by diffusion with concentration gradient in the mesoporous TiO_2 electrode as driving force. The electron transport is described by the trapping-detrapping mechanism where the injected free electrons might be trapped in the band gap states of the semiconductor and the electron transport continues when the trapped electrons are thermally detrapped back into the conduction band of the semiconductor electrode (Yang, 2014). ...46

Figure 2.9: The difference of exciton radii due to the different dielectric permittivity of the material. (a) Frenkel exciton bound electron-hole pair where the hole is localized at a position in the crystal. (b) Wannier exciton bound electron-hole pair is not localized at a crystal position, but across the lattice (Schwoerer & Wolf, 2008) (c) Visualization of an exciton as excited state with exciton binding energy Eb in a potential diagram for one electron (Tress, 2014)...................................50

Figure 2.10: General schematic device architecture of four types of organic solar cells. The red and blue domains appear as a phase of electron donor and electron acceptor respectively. (a) A single layer semiconductor which has greatly low

efficiency because the electrodes arise too weak of electric field from the different work functions which cannot overcome the strong tendency for recombination between electrons and holes (b) bilayer is the first bulk heterojunction in which the transformation of photo-induced electron occurs in planar interfaces between two semiconductors from a donor to acceptor, so there should be a thin active layer in order to utilize all excitons. Thus, the bilayer has limited performance due to the occurance of dissociation excitons prior to recombination only near interface. The transformation of photo-induced electron have more opportunities to occur due to the extended interface and interpenetrate network semiconductors through the film, i.e. each interface is within an exciton diffusion length distance (~ 10 nm) from the site of absorbing, thus all excitons can separate. This is achieved in a (c) bulk heterojunction or (d) ordered bulk heterojunction (He, Qiu, & Lin, 2011; Liu, Gu, Jung, Jo, & Russell, 2012). 55

Figure 2.11: Architecture of the energy levels of the HOMO and LUMO of donor and acceptor molecules, where E_g and E_d represent the donor molecule band gap and the energy level offset of LUMO between donor and acceptor molecules, V_b shows the potential field interface arising between the LUMO of acceptor molecules and HOMO of donor molecules from the energy offset (He et al., 2011) 55

Figure 2.12: Simplified schematic mechanism from light absorption to extraction of charges (photocurrent), charge transfer and then transport in a structure of bulk heterojunction solar cell. (a) In the donor material, exciton generate by photon absorption. (b) Diffusion of exciton to the donor-acceptor interface. (c) Generation free charge carrier from exciton dissociation, by transferring generates current (an electron) to the acceptor due to material disorder of donor with acceptor and electric field. (d) The charge carriers transport to the electrodes (electrons to cathode and holes to anode) to provide photocurrent. The loss mechanisms are shown in each step as; 1/ step (a), when photons are non-absorbed. 2/ Decay excitons in step (b). 3/ In step (c), the bound pair geminate recombination. 4/ In step (d), bimolecular recombination (Gaudiana & Brabec, 2008; Yeh & Yeh, 2013). 56

Figure 3.1: The molecular structure of polymers and dyes materials. 75

Figure 3.2: (a) Molecular and crystal structure of TiO_2 Anatase material, (b) XRD result of TiO_2 Anatase (Aldrich, 2015)... 77

Figure 3.3: Photograph of the used ETCHER machine. 83

Figure 3.4: (a) Photograph of Thermal Evaporation System inside Low Dimensional Material Research Centre (LDMRC) Clean Room and (b) inside Glove Box. ... 86

Figure 3.5: Schematic diagram of the thermal evaporation equipment inside Glove Box. 87

Figure 3.6: Schematic of a device BHJ solar cell with PBTTT-C_{12}:$PC_{71}BM$ blend....... 88

Figure 3.7 a: Reference sputter coating rate of Platinum thin film by JFC-1600 Auto Fine Coater. 91

Figure 3.8: (a) The spin coating machine. (b) Schematic processes of the spin coating technique. 93

Figure 3.9: Schematic showing Doctor Blade Coating Technique. 96

Figure 3.10: KLA Tencor P.6 surface profilometer equipment. 98

Figure 3.11: Standard schematic of an optical profilometer (AZoNetwork, 2015). 98

Figure 3.12: IV curve (black point) showing the MPP, Jsc and Voc values. The grey curve represent the power-voltage curve (Gabrielsson, 2014). 100

Figure 3.13: Photograph of the Oriel Solar Simulator. 101

Figure 3.14: Comparison between the output spectrum of the xenon arc lamp and spectrum of the standard AM 1.5. As clear that the xenon light source was very close to that of sunlight which is a large portion of arc lamp spectra lie in the visible region (390-780 nm). 102

Figure 3.15: (a) Photograph of the Keithley 236 SMU Programmable IV Source equipment. (b) An SMU instrument configured as a constant current source and a voltmeter (analog-eetimes, 2015). 103

Figure 3.16: Architecture scheme of the rectangular step Neutral Density filters (NDL-25S-4) with dimension details (Thorlabs, 2016). 105

Figure 3.17: Characteristics of IPCE for a solar cell based on D35 and a cobalt electrolyte (Kaufmann Eriksson, 2014). 106

Figure 3.18: The QEPVSI-b Quantum Efficiency Measurement System..................... 108

Figure 3.19: The photograph of Lambda 750 spectrometer and the energy diagram of electronic transitions in molecules. When the incoming photon energy matches the transition energy an electron can be excited and the excited state is empty. 110

Figure 3.20: Operation principle of a two beam UV-VIS-NIR spectrometer in transmission and diffuse reflection geometry. 112

Figure 3.21: The layout of RENISHAW *inVia* Raman Microscope, with all the key components highlighted. 113

Figure 3.22: Energy diagram of absorption of light in organic materials (Renishaw, 2015). 114

Figure 3.23: Schematic of working principle of the PL spectrometer. 115

Figure 3.24: The working principle of the D3000 AFM (Pekkola, 2014). 116

Figure 3.25: The different imaging mode of the AFM indicated in the Lennart-Jones potential. 117

Figure 3.26: FESEM (JEOL JSM-7600F). 118

Figure 3.27: Areas of interaction of the electrons with the matter and the information depth of the detected radiation and electrons, respectively (Pekkola, 2014)..... 119

Figure 3.28: Schematic basic parts of a Scanning Electron Microscope. 122

Figure 4.1: Molecular structure of NiTsPc, device design and working mechanism of the photo sensors... 126

Figure 4.2: FESEM micrographs: (a) untreated TiO_2 film and (b) TiO_2 film obtained after treating with NaOH.. 127

Figure 4.3: The characteristic behavior of current vs. illumination intensity and voltage vs. illumination intensity of the photo sensors. (a) Photo sensors fabricated using untreated TiO_2. (b) Photo sensors fabricated using treated TiO_2...................... 130

Figure 4.4: The characteristic behavior of dependences logarithmic current and voltage on logarithmic light intensity of the photo sensors for (a) photo sensors fabricated using untreated TiO_2, (b) photo sensors fabricated using treated TiO_2. 132

Figure 4.5: Dynamic photocurrent vs. time of the DS photo sensors at +0.2 V with periodic on/off 150 mW/cm^2 illumination light. 134

Figure 5.1: A schematic approximate energy level diagram of modelled DSPS with a $I -$ $/I3 -$redox electrolyte (Iodolyte). Which is illustrated the LUMO (or electron affinity (EA)) and the HOMO (or ionization potential (IP)) of PCPDTBT and MEH-PPV binary blend polymer donors as well as the electrodes work function used in this device. A band gap of an organic polymer is the difference between the energy of its LUMO and HOMO. 140

Figure 5.2: Design and schematic working mechanism of the DSPS. 140

Figure 5.3: Ultra-violet/visible/infra-red (UV-VIS-IR) optical spectra of PCPDTBT: MEH-PPV blend films at different volumetric ratio. Which are the optimum ratios in term of flat absorption profile with more uniform and even absorption height as compare to other ratios. 142

Figure 5.4: The UV-VIS-NIR spectra of organic polymer MEH-PPV and PCPDTBT independent thin films. 142

Figure 5.5: PL spectra of PCPDTBT:MEH-PPV blends at different volumetric ratio. 144

Figure 5.6: The PL spectra of MEH-PPV and PCPDTBT independently. 144

Figure 5.7: Illuminance vs. Isc measurements for PCPDTBT:MEH-PPV DSPS with different ratios at (0) bias voltage at room temperature.................................... 146

Figure 5.8: Illuminance vs. Isc measurements of PCPDTBT and MEH-PPV independently at (0) bias voltage at room temperature..................................... 146

Figure 5.9: (CONTINUED) The response time of the DSPS devices: PCPDTBT (a), MEH-PPV (b), PCPDTBT:MEH-PPV (1:0.4) (c), PCPDTBT:MEH-PPV (1:0.6) (d) and PCPDTBT:MEH-PPV (1:0.8) (e), under pulsed optical illumination intensity 100 mW/cm2 at 0V biasing voltage and delay time 0.01 sec. 151

Figure 5.10: External quantum efficiency (EQE) spectrum of the PCPDTBT and MEH-PPV and blend films based DSPS... 153

Figure 6.1: Absorption spectra of the PBTTT-C_{12} and PBTTT-C_{12}:$PC_{71}BM$ blend as a function of annealing temperature in the visible light spectrum regions.......... 160

Figure 6.2: (a) Shows the PL spectrum of the PBTTT-C_{12} pristine thin film on glass. (b) PL spectra of the blend films a function of annealing temperature. 161

Figure 6.3: AFM images of the PBTTT-C_{12}:$PC_{71}BM$ (1:4) thin films on ITO coated glass substrates, (a) non-annealed, (b) annealed at 50 ℃, (c) annealed at 100 ℃, and (d) annealed at 150 ℃.. 163

Figure 6.4: J-V characteristics of ITO/PEDOT:PSS/PBTTT-C_{12}:$PC_{71}BM$/Al BHJ solar cells annealed at different temperatures... 165

Figure 7.1: A PEDOT:PSS film as a CE in schematic of the DSSC (Chou, Chou, Kuo, & Wang, 2013)... 173

LIST OF TABLES

Table 3.1: Specifications of TiO_2 anatase nanoparticles (Aldrich, 2015). 76

Table 3.2: The organic materials, their respective solvents(s), and concentration of the solutions prepared for various studies. 79

Table 3.3: Specifications of JEOL JFC-1600 Auto Fine Coater (JEOL, 2009). 90

Table 5.1: Comparison of the key sensing parameters of the DSPS. 152

Table 6.1 Comparison result between the present work and a previous work 166

LIST OF ABBREVIATIONS

ABL	:	Anode Buffer Layer
AC	:	Alternating Current
AFM	:	Atomic Force Microscopy
AM	:	Air Mass
ATO	:	Antimony doped Tin Oxide
AZO	:	Aluminium doped Zinc Oxide
BHJ	:	Bulk Heterojunction
BHJC	:	Bulk Heterojunction Cell
BSE	:	Backscattered Electrons
CB	:	Conduction band
CE	:	Counter electrode
CNT	:	Carbon Nanotubes
CuPc	:	Copper Phthalocyanine
DI	:	De-Ionized
DIO	:	1,8-diiodooctane
DS	:	Dye Sensitized
DSC	:	Dye Sensitized Cell
DSSCs	:	Dye Sensitized Solar Cells
DSPS	:	Dye sensitized Photo Sensor
DSSC	:	Dye sensitized solar cell
EA	:	Electron affinity
EDOT	:	3,4-Ethylenedoxythiophene
EF	:	Fermy level Energy
EQE	:	External Quantum Efficiency

ET : Electron Transfer

FePc : Iron Phthalocyanine

FESEM : Field Emission Scanning Electron Microscope

FET : Field Effect Transistor

FF : Fill Factor

FTO : Fluorine doped Tin Oxide

HJ : Heterojunction

HOMO : Highest Occupied Molecular Orbital

HTM : Hole Transport Materials

IP : Ionization Potential

IPCE : Incident Photon-to-Current Conversion Efficiency

IR : Infra-Red

ITO : Indium doped Tin Oxide

J-V : Cureent Density-Voltage

LDMRC : Low Dimensional Material Research Centre

LED : Light Emitting Diodes

LHE : Light Harvesting Efficiency

LM : Light Microscopy

LMCT : Ligand-to-Metal Charge Transfer

LUMO : Lowest Unoccupied Molecular Orbital

MLCT : Metal-to-Ligand Charge Transfer

MO : Molecular Orbital

MPP : Maximum Power Point

M_W : Molecular Weight

NaOH : Sodium Hydroxide

N3 : Ru (2,2’-bipyrdine-4,4’-dicarboxylate acid)$_2$(μ-CN)Ru(CN)(2,2’-bipyrdine)$_2$)$_2$

N719 : Di-tetrabutylammonium cis-bis(isothiocyanato)bis(2,2′-bipyridyl-4,4′-dicarboxylato)ruthenium(II)

NC : Nanocrystalline

ND : Neutral Density

NFE : Nearly-Free Electron

NHE : Normal Hydrogen Electrode

NIR : Near Infra-Red

NP : Nano Particle

NR : Nano-Roads

NREL : National Renewable Energy Laboratory

OD : Optical density

ODT : Octanedithiol

OEs : Organic Electronics

OLED : Organic Light Emitting Diodes

OP : Organic Photovoltaic

OPD : Organic Photovoltaic Detector

OPS : Organic Photo Sensor

OPV : Organic Photovoltaic

OPVDs : Organic Photovoltaic Devices

OS : Organic Semiconductor

OSC : Organic Solar Cell

OSRAM : Oil Spill Risk Analysis Model

PBT : Poly(butylene terephthalate)

PBTTT-C_{12}	:	poly[2,5-bis(3-dodecylthiophen-2-yl)thieno[3,2-*b*]thiophene]
PCBM	:	methanofullerene
$PC_{71}BM$	:	[6,6]-phenyl C_{71} butyric acid methyl ester
PCDTBT	:	Poly[[9-(1-octylnonyl)-9H-carbazole-2,7-diyl]-2,5-thiophenediyl-2,1,3-benzothiadiazole-4,7-diyl-2,5-thiophenediyl]
PCE	:	Photon-to-Current Conversion Efficiency
PCPDTBT	:	Poly[2,6-(4,4-bis-(2-ethylhexyl)-4H-cyclopenta[2,1-b;3,4-b']dithiophene)-alt-4,7(2,1,3-benzothiadiazole)]
PEDOT	:	Poly(3,4-ethylenedioxythiophene)
PEG	:	Poly(ethylene glycol)
PEI	:	Poly(ethyleneimine)
PEIE	:	Ethoxylated-polyethyleneimine
PET	:	Polyethylene terephthalate
PH	:	Potential Hydrogen
PHT	:	Poly(ethylene terephthalate)
PL	:	Photoluminescence
PPV	:	Poly(phenylenevinylene)
PSC	:	Polymer Solar Cell
PTFE	:	Polytetrafluoroethylene (Teflon)
PV	:	Photovoltaic
P-V	:	Power-Voltage
QE	:	Quantum Efficiency
RF	:	Radio Frequency
RPL	:	Radio Photoluminescent

SC : Solar Cell

SE : Secondary Electron

SEM : Scanning Electron Microscope

SMU : Source Measure Unit

SQ : Squaraine

TCO : Transparent conducting oxide

THF : Tetrahydrofuran

Ti^{IV} : Titanium(IV)

TiO : Titanium(II) Oxide

TiO_2 : Titanium(IV) Oxide, anatase

UCSB : University of California, Santa Barbara

UKM : National University of Malaysia

UM : University of Malaya

UNSW : University of New South Wales

UV : Ultra-violet

VB : Valence band

Vis : Visible

VPP : Vapor phase polymerization

XRD : X-ray Powder Diffraction

ZnO : Zinc Oxide

CHAPTER 1: INTRODUCTION

1.1 Introduction to Organic Semiconductors

Organic semiconductors (OSs) as a new material class hold tremendous potential which has been intensively incorporated and investigated in wide applications of organic electronic devices especially in photo sensors and solar cells. This is because the devices using OSs are lighter, 1000 times thinner than a human hair, cheaper, easier to manufacture, disposable, more flexible and more eco-benign compared to the corresponding ones based on inorganic semiconductors. Thus their use has led to the introduction of a new generation of products and new applications of consumer electronic devices. Moreover, the dependence on renewable energies without using fossil fuels is one of the greatest current and future challenges. Fortunately, the possibility of this alteration is high since the emergence of OSs and organic electronics (OEs). OSs are organic compounds which are mostly carbon and hydrogen atoms based, with the typical properties of semiconductor. Other elements such as heteroatoms are usually also included such as sulfur, nitrogen or oxygen. The combination of the benefits of mechanical and chemical organic compounds with the electronic advantages of semiconducting materials makes OSs one of the most interesting class of materials. OSs and conductors also "offer a unique combination of properties not available from any other known materials" as stated by Nobel prize winner A. J. Heeger (Heeger, 2001). This is due to adequate conductivity with absorption and emission of visible light to operate many devices instead of classical semiconductors such as solar cells, light emitting diodes, lighting panels, photo sensors, displays and field effect transistors (see Figure 1.1).

OSs are classified mainly into small molecules and conjugated polymers (Figure 1.2), and are basically classified by the distinguishing molecular structure and charge carrier transport type (n-type and p-type), which are mainly related to each other. This is because the structure of molecular orbitals and the chemical bonds configuration both effect the charge transport. The simplest type of organic is small molecules which are chemical (conjugated polycyclic) compounds with specific molecular weight (less than 1000). However, polymers are composed of covalently coupled molecules or the repeating small structural entities or units along the chain without well-defined M_W, with the ability of electrical charge transport. In general, small molecules can be utilized to form thin films using a vacuum thermal evaporator, which is also known as dry method. On the other hand, thin film formation from a semiconducting polymer normally need to use a wet method such as spin coating or ink-printing. However, polymers are easy and useful material to form thin films with large surface area. Moreover, small molecules are surpassing polymers in potential advantages such as relative simplicity, ease of purification, reproducible synthesis and the monodispersity of the resulting material (Rand & Richter, 2014). Furthermore, small molecules are more soluble in organic solvents, while the functionalization to enhance polymer's solubility leads to loss of its mobility. Furthermore, various molecular parameters of small molecules can be modified which leads to easier control of charge transport. Small molecules are generally classified into three types which are linear, 2D fused ring compounds, and heterocyclic oligomers (Madhavan, 2002).

The need to understand the photophysical properties of organic semiconductors and for researchers who aim to improve and develop design semiconductor devices, the following three OS varieties are useful to distinguish organic from inorganic semiconductors (Köhler & Bässler, 2015).

Despite that all types of OSs having a similar semiconducting properties, a slight difference in their properties of associated photophysical and excited states depend on the coupling and order in the solid.

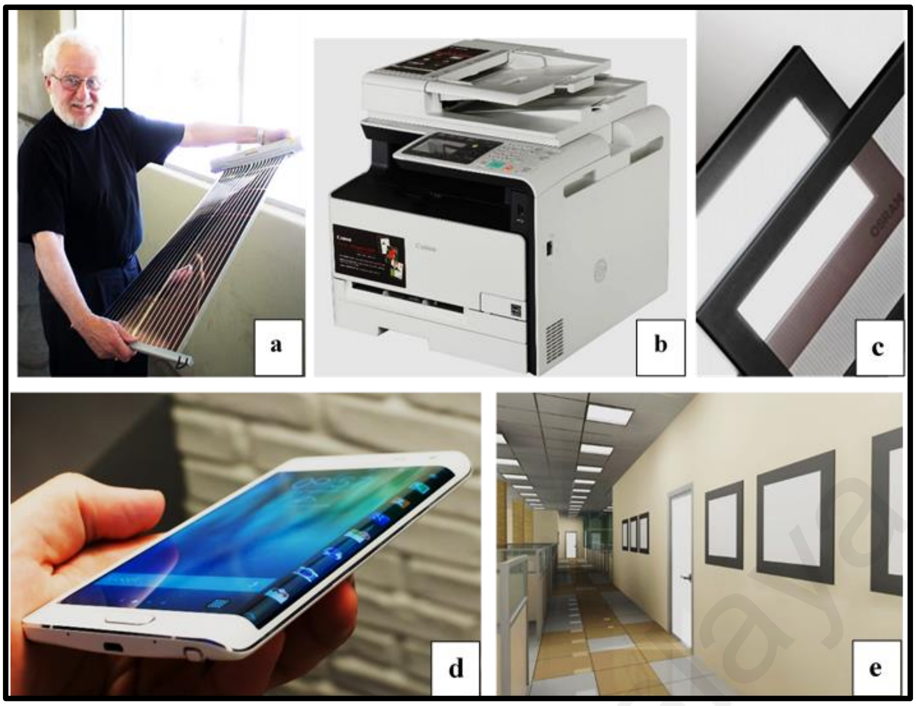

Figure 1.1: Commercially available examples of organic semiconductor applications; (a) Alan J. Heeger with foil of flexible organic solar cell, (b) Process of xerography by canon photocopier employing organic semiconductors, (c) A high performance luminescent window with white organic light emitting diodes (OLED) developed by OSRAM. When the window is exposed to AC power, it functions as panel lighting with brightness of 1000 cd/m^2, yet when powered off, its transparency reached 75% with a large-scale area around 90 cm^2.(d) Featuring an OLED display by Samsung Galaxy smartphone, (e) Lighting tiles with essentially glare-free made by OSRAM.

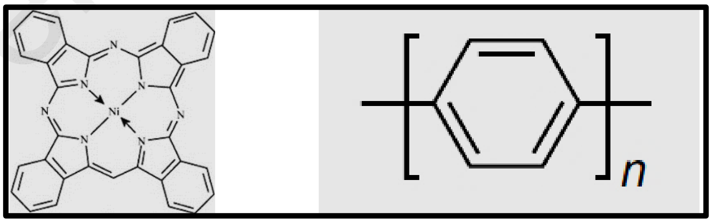

Figure 1.2: Examples of different classe organic semiconductor structures. Nickel phthalocyanine (small molecule) and poly(para-phenylene) (polymer), respectively.

Molecular crystals; the molecules (instead of atoms in inorganic crystals) are formed and characterized like any crystal, having a point lattice and a basis held together by weak Van-der-Waals interactions and electrically neutral (instead of covalent and ionic bonding). As polyacenes, anthracene, pentacene, naphthalene, tetracene pyrene and perylene are some examples of crystal forming molecules which are flat, large and aromatic. *Amorphous molecular films*; thin films of organic amorphous molecules are highly disordered OSs which are used for several device applications through spin coat or thermal evaporation deposition. *Polymer films*; polymer blends are less vulnerable to crystallization and more stable thermodynamically, motivating researchers to use them in blending which are processed from solution more than molecules. Thus polymers can be deposited in several techniques like spin coating, ink-jet deposition, and industrial R2R coating.

On the application of OSs, certain aspects on organic solar cells and many good effieciencies have been recorded which still lag behind the standards for inorganic solar cells. However, it is a promising alternative for renewable energy in the near future. Figure 1.3 shows the development of the certified efficiency records from 1991 to 2015 for all types of organic solar cells (except perovskite cells) compared with inorganic cells. Furthermore, due to interest the researchers, the number of publications with topics covering “organic semiconductors” has dramatically increased over the last ten years. From the period 2005 to 2015, the number of publications using the keywords “solar cell OR photovoltaic cell” AND “organic OR polymer OR small molecular” from Web Of Science-Core Collection incredibly increased yearly from around 600 to 5500 times (look at Figure 1.4).

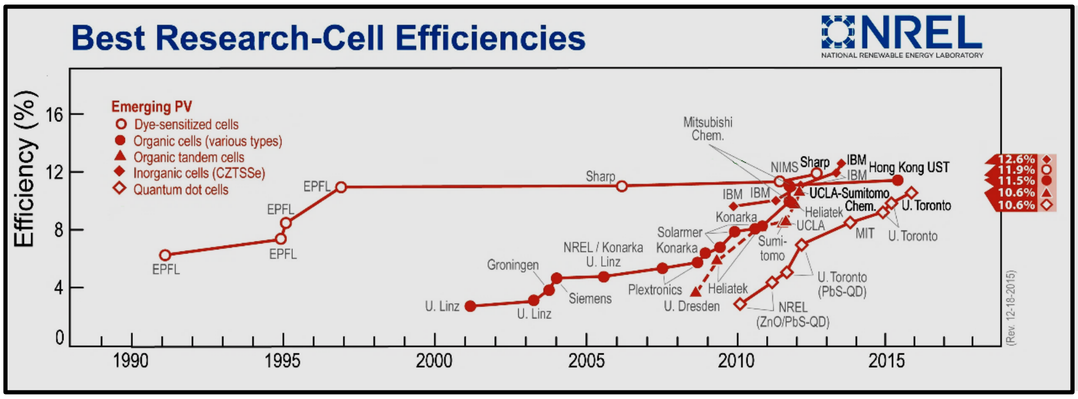

Figure 1.3: Record efficiencies development for all types of organic solar cells (except perovskite cells) compared with inorganic cells from 1991 until 2015. This is a part of the last updated graph (Dec 18 2015) for record cell efficiencies assembled by and courtesy of the National Renewable Energy Laboratory (National Renewable Energy Laboratory, 2015).

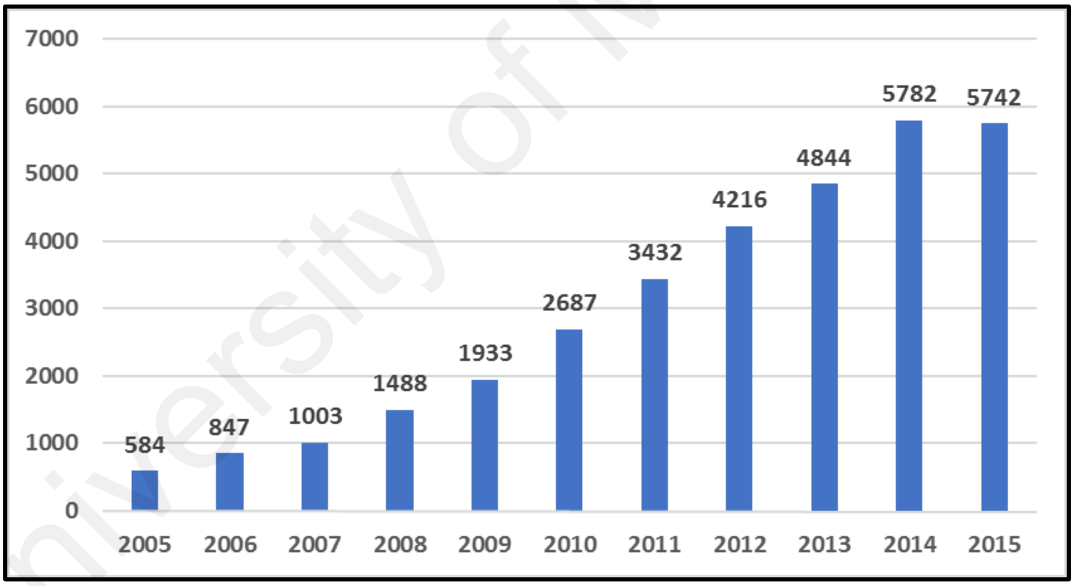

Figure 1.4: Number of published articles from 2005 to 2015 from Web Of Science-Core Collection with the topic keywords "solar cell OR photovoltaic cell" AND "organic OR polymer OR small molecular".

1.2 Motivation

A- Dye Sensitized Photo Sensor

Organic semiconductors are currently attracting immense interest for organic electronic devices such as solar cells, data storage memories, sensors, organic transistors, and organic light emitting displays (Handa, Wietasch, Thelakkat, Durrant, & Haque, 2007). Among these devices, sensors for environmental parameters such as light, temperature, and humidity play a pivotal role in meteorology, agriculture, industrial processing, and environmental control (Jung, Ji, & Varadan, 2007; Karimov et al., 2012; Morooka, Suzuki, & Yoneya, 2008). Light sensors in particular have a wide range of applications, both in civilian and military areas, which include flame sensing, digital imaging, biological research, optical communication, and missile plume detection (Peumans, Yakimov, & Forrest, 2003; Skorka & Joseph, 2011; Takada, Hayashi, Mitsui, Maehara, & Ihama, 2007; Wang et al., 2010; Zhang et al., 2009). Also, photo sensors have found wide-ranging applications in military, civilian, chemical and biological analysis as well as in clinical diagnostics due to their selectivity.

Most of the sensor devices have been fabricated by utilizing classical semiconductors, graphene, and metal oxides and are embedded ubiquitously in our surroundings (Lin, Lee, & Wang, 2010; Tsai et al., 2011; Wang & Lee, 2011; Zhang et al., 2014; Zribi & Fortin, 2009). These photodetectors are ultra-fast and are envisaged to be proven technology. However, researchers are now continuously directing their efforts to address the issues of their troublesome, time-consuming and expensive fabrication techniques.

Organic photo sensors have been studied more thoroughly in recent years due to reduced production cost and their suitability for flexible, low cost devices, eco-friendly and disposable electronic devices (Maiellaro et al., 2014). Unlike inorganic materials, organic materials have physical and chemical properties that can be easily tailored by the incorporation of functional groups or the manipulation of physical conditions to meet the specific requirements (Liao & Yan, 2013). Due to significantly reduced material consumption (1 g/m^2 because organic dyes have high absorption coefficients in the range 10^5 cm^{-1} which almost covers the incoming absorbable light within a layer of few tens nano-meters and leads to devices with thickness < 200 nm) and the lower manufacturing costs, organic material based sensors are rapidly becoming the most important part of an instrumentation. The development of new materials and tuning of specific material functionality can be provided during the synthesis process. Hence, optimization of the electrical properties of the organic materials can be done in order to achieve better efficiencies for their potential applications in electronic devices. However, their efficiencies are still significantly lower than their inorganic counterparts, which are generally attributed to poor electrical properties such as low charge carrier mobility and low dielectric constant (Koster, Shaheen, & Hummelen, 2012). Although the mobility of organic semiconductors cannot be compared with inorganic semiconductors, their electrical parameters are supposed to be enough for the sensor applications (Ahmad, Abdullah, & Sulaiman, 2013). Electrical properties of most organic materials are reliant on ambient environment, and this characteristic has made them very favorable for the development of various types of sensors (Ahmad, Abdullah, & Sulaiman, 2012; Ahmad et al., 2011). Organic materials are solution processable and have an adjustable viscosity to suit various film solution deposition techniques as well.

Organic photo sensing platforms have been proposed in various configurations, i.e., tandem geometry (Zhang et al., 2010), bulk heterojunction, (Zafar, Ahmad, Sulaiman, Hamzah, & Rahman, 2014) and organic-inorganic hybrid blend (Rauch et al., 2009). Operation mechanism of all these aforementioned sensors is based on increase in photo-conductivity. With the increase in optical power density impinging on the OPD, the photocurrent increased. Another type of photo sensor known as dye sensitized photo sensor (DSPS) has also been introduced in our studies (Karwan, Ahmad, & Sulaiman, 2014). Organic dye-based light sensor is also an eco-friendly and low cost approach. Among the dyes, porphyrins, naphthalocyanines, squarines, perylines, phthalocyanines, and cyanines are widely used and envisaged to be potential sensitizers (Imahori et al., 2010; Imahori, Umeyama, & Ito, 2009). An aqueous solution of organic compound, Nickel (II) phthalocyanine-tetrasulfonic acid tetrasodium salt (NiTsPc), was used as photo sensitizer. The DSPS provides a technically and economically credible alternative concept to the other geometries of the photo sensors. The concept of the DSPS is similar to sensitized solar cell that was first reported by Grätzel et al. (O'regan & Gratzel, 1991). In contrast to the conventional systems where the semiconductor assumes both the task of light absorption and charge carrier transport, the two functions are separated in DSPS. Light is absorbed by a sensitizer which is anchored to the surface of a wide band semiconductor. Charge separation takes place at the interface via photo-induced electron injection from the dye into the conduction band of the solid. Carriers are transported in the conduction band of the semiconductor to the charge collector. The use of sensitizers having a broad absorption band in conjunction with oxide films of non-crystalline morphology permit to sense a broad range of light spectrum. Nearly quantitative conversion of incident photon into electric current could be achieved over a large spectral range extending from the ultra-violet (UV) to the near infra-red (NIR) region. There is a good prospect to produce highly sensitive DSPSs at lower cost than the conventional devices.

The aim of the present work in this thesis is to explore the possibilities to help improve the sensing parameters of the photo sensors via TiO_2 photo anode treated by NaOH and employing binary blend of organic semiconductor polymers as sensitizer.

B- Bulk Heterojunction Solar Cell

According to current forecasts, an inevitable drop in the world oil production rate is predicted to start within next one to two decades. Overall, oil prices will then increase, forcing the introduction of renewable energy sources. Among the range of renewable sources, low cost and environmental friendly alternative PVs are the most promising source because of the abundant supply of solar energy. As reported by the University of New South Wales (UNSW) with their PERL cell technology, silicon is still considered the leading technology in the world market of solar cells, with maximum power conversion efficiencies reaching 25% of the incoming solar energy (Green, Emery, Hishikawa, Warta, & Dunlop, 2014), which is close to the theoretical predicted upper limit of 33% (Green, 2002) for single-crystalline devices. Recently inorganic solar cells consisting of optimal combination of bandgaps for multi-junction structures have been reported with the efficiency ~ 40% (Ameri, Li, & Brabec, 2013; Green et al., 2014). However, the cost driving factor for the production of inorganic solar cells is the expensive investment into costly semiconductor processing technologies (Brabec, Christoph J., 2004). As a result, the idea of solar cells based on thin plastic substrates fabricated by coating and printing techniques is not only exciting but highly attractive from a cost standpoint.

It is well known that organic semiconductors have many advantages over inorganic. These can be processed from solution at room temperature onto flexible substrates using simple and low cost deposition techniques (e.g. spin coating, ink-jet/screen printing and vacuum deposition techniques). Organic photovoltaic cells have attracted great attention because they are considered as renewable and really clean energy sources (Brabec, C.J., 2004; Brabec, Sariciftci, & Hummelen, 2001; Coakley & McGehee, 2004; Padinger, Rittberger, & Sariciftci, 2003; Shaheen et al., 2001). Polymer tandem solar cell with 10.6% power conversion efficiency has been reported at laboratory level (You et al., 2013). Currently, numerous types of organic photovoltaic device structures are under examination. Specifically, donor (D)/acceptor(A) based BHJ PV devices have been the subject of great consideration and P3HT:PCBM composite based D/A blend system is one of the most widely investigated organic active layers (Li, Shrotriya, Huang, et al., 2005). However, P3HT hinders the option to efficiently yield the longer wavelength region of the visible spectrum. PV scientists are now focusing attention on exploring new donor organic semiconductors with improved light absorption over most of the visible spectrum as reported in the Refs. (Chen et al., 2009a; Liang et al., 2008). These are the only few examples, and there are many other materials that show their potential as promising candidates for OPVs such as PCDTBT (Li, Zhu, & Yang, 2012) and PBTTT (Parmer et al., 2008a).

This part of aim in this present work is to enhance the surface morphology and overall efficiency of the BHJ cell by thermal annealing active layer.

1.3 Thesis Objective

Although significant R&D efforts have been directed in order to improve the sensing performance of the organic photo sensors and the efficiency of organic solar cells, there is still room for further improvement. The main objective of this thesis is to introduce the organic semiconductors (small molecules and organic polymers) and to fabricate dye sensitized photo sensor as a new type of photo sensor and bulk heterojunction solar cells. The target is to improve the sensitivity of photo sensor through photo anode treatment (small molecules used as sensitizer NiTsPc) and mixing two polymers (PCPDTBT and MEH-PPV) in order to broaden the absorption of sensor device and to improve the efficiency of BH cell (PBTTT-C_{12} and $PC_{71}BM$ as polymers) through thermal annealing process. Moreover, a deeper understanding of the fundamental knowledge of sensing parameters and the related findings could be a platform to improve existing photo sensor device for suitable commercial applications. The objectives of this research thesis work can be summarized as follows:

I. **To characterize the physical properties of the selected organic semiconductor (small molecules and organic polymers) materials**

including the optical, morphological, and electrical properties prior to the fabrication of DSPS and BH solar cells.

II. **To fabricate the solution processable Thin Film Solar Cell and dye sensitized photo sensors using an aqueous solution of organic small molecule compound, Nickel (II) phthalocyanine-tetrasulfonic acid tetrasodium salt (NiTsPc) and using a binary blend PCPDTBT:MEH-PPV as photo sensitizer for visible light in order to provide a broad light absorption in visible region.**

III. **To study and improve the responsivity (response time) of dye sensitized photo sensor.**

IV. **To enhance the performance (PV properties) of Thin Film Solar Cell by thermal annealing effect and to improve the thin film features of surface morphology.**

1.4 Thesis Framework

Chapter one provides a brief introduction of organic semiconductors and its important application with an analysis of the increased number of publications for last ten years, followed by several key motivations that inspired and assisted the thesis studies to be performed. This chapter has also included the aim and objectives of this thesis.

Chapter two presents the background and working principles of solar cells and sensors by way of literature review to provide an overview of the recent developments. The overview is divided into two main parts. In part one the underlying physical fundamental and working principle of DSPS are explained and the details of the main components with the process of electron transfer, interfaces between each component, excitons and photo sensor are presented. Then important sensing parameters are presented concentrating on responsivity and response-recovery time. Part two focused on the BH solar cells, explaining the relationships between morphology and cell performance in detail with the all characterization techniques available at present. Finally, evolution of the open circuit voltage, short circuit current, fill factor and power conversion efficiency are presented in detail.

Chapter three gives the selection materials overview which included organic dyes and polymers, TiO_2, solvents and electrolytes. Substrate cleaning and treatments, the sample preparation and the brief explanation of the setup of material characterization employed for the experiments are presented here. In chapter four, performance enhancement of NiTsPc based novel photo sensor using treated TiO_2 nano particles (NPs) film is reported. The explanation of TiO_2 treatment and fabrication of photo sensor are presented in detail. The result on binary blend based DSPS using PCPDTBT and MEH-PPV composite as a light sensitizer is shown in chapter five. Chapter six provides thermal annealing effect on the optical, electrical and morphological properties of the PBTTT-C_{12}:PC_{71}BM blend films. The fabrication and measurement results on BHJ solar cells are described in detail.

Finally, chapter seven summarizes the research work reported in this thesis and gives an outlook on future new research directions and still remains open questions in the second section of this chapter.

CHAPTER 2: BACKGROUND AND LITERATURE REVIEW

This chapter is divided into two main parts. In the first part, the background of overall study of dye sensitized photo sensor (DSPS) is presented starting with the main components of DSPS in section 2.1. In section 2.2 various interactions between the interfaces of different components are explained in detail, in which all electron transfer reactions occur at the interfaces in DSPS. The generation of excitons as well as their types are discussed in section 2.3, and the new types of photo sensors with the important sensing parameters are presented in section 2.4 and 2.5. The second part in this chapter provides the background and literature review related to the bulk heterojunction solar cells. Section 2.6.1 presents the relationship between morphology and performance of BHJ solar cells, while the list of characterization tools for study of structural morphology is provided in section 2.6.2. Finally, special emphasis is put on the evolution of open circuit voltage, short circuit current, fill factor and power conversion efficiency which are explained in section 2.6.3 until 2.6.5 in detail.

2.1 Part One: Dye Sensitized Photo Sensor (DSPS)

In order to understand the dye sensitized photo sensor (DSPS), dye sensitized solar cell (DSSC) is initially discussed because all the working mechanisms and concepts of the DSPS are similar to sensitized solar cell. Gerischer et al. laid the basis for DSSC in 1960s with the discovery that a dye adsorbed by ZnO could generate a photocurrent (Gerischer, Michel-Beyerle, Rebentrost, & Tributsch, 1968). However, it wasn’t until 1991 that O’Regan and Grätzel launched a DSSC (see Figure 2.1). That DSSC had an efficiency of 7.1-7.9% in simulated solar light and 12% in diffuse daylight based on a nanocrystalline TiO_2 substrate (nc-TiO_2) and the ruthenium dye Ru (2,2’-bipyrdine-4,4’-dicarboxylate acid)$_2$(μ-CN)Ru(CN)(2,2’-bipyrdine)$_2$)$_2$, also known as N3, using an iodide/triiodide electrolyte system (Oregan & Gratzel, 1991). Since then it has been reported that liquid DSSCs have increased in performance (Mathew et al., 2014; Yella et al., 2011). Perovskite materials is similar system using luminance absorber have been very successful in recent years with efficiency of 18% (Burschka Julian, 2013; Jeon et al., 2015; Nie et al., 2015). In this thesis the conventional liquid based DSPS have been employed.

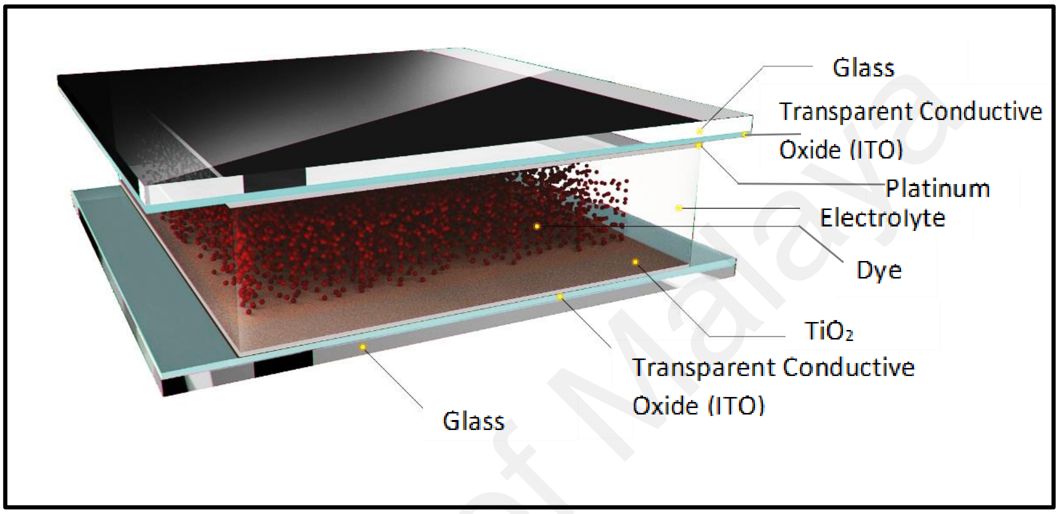

Figure 2.1: 3D schematic depiction of structure and function of typical TiO_2 based DSSC (not to scale). The primary particle TiO_2 anatase diameter is 8-20 nm and void space is ca. 50%. A sheet resistivity at room temperature and light transmittance of ITO generally is 10-15 Ω/sq. and ~ 90% respectively. Diameter of platinum nanoparticles typically ~ 5 nm (Murphy, 2015).

Grätzel's cell success was mainly due to the following two important factors; the use of a TiO_2 nanostructure which is responsible for achieving high surface area thus allowing better absorption of dye molecules onto it and second, the strong chemisorption between the dye molecules and the TiO_2 film through the carboxylic groups of the ruthenium complex (Shahroozi, 2015). This was a breakthrough for this kind of solar cell. With the highly increased surface area, it was possible to absorb much more dye than on a flat surface of the same substrate size and thus to increase the light harvesting drastically. The principle of sensitization goes back to J. Moser in 1887, who sensitized a solid silver halide electrode with erythrosine (Moser, 1887).

Dye sensitized photo sensor (DSPS) are typically fabricated with affordable and abundant materials which are usually cost effective and eco-benign. In standard DSPS, there are six main components as depicted in Figure 2.1 (above). **Two conductive glass substrate materials** (it is possible to use a flexible plastic substrate) are usually coated with indium doped tin oxide (ITO). These external conductive substrates provide a sturdy construction and complete the electronic loop of the device. **A photo anode** (working electrode) is one of the electrodes consisting of a thin layer of mesoporous metal oxide semiconductor (often TiO_2 particle size ca. 20-25 nm) deposited onto an ITO glass substrate. The mesoporous TiO_2 film is sensitized (colored) with a **dye (sensitizer)**. The dye secured in a porous nanocrystalline absorbs the photons and acts as light harvesting material. Starting with the absorption of a photon by dye molecules, the dye injects electrons into the mesoporous TiO_2, causing it to enter an exited state. The other electrode is **the photo cathode**; the counter electrode consists in a thin catalyst layer (often platinum or carbon) grown on another ITO glass substrate. **The electrolyte (redox mediator)** is located in between the two electrodes reduced at the platinized counter electrode after the sensitizer is decayed to their ground state by incoming electrons from the electrolyte. All these components, exciton generation, and charge transportation at the interfaces will be discussed in the following sections.

2.1.1 Photo Sensitizer (Dyes)

Sensitizing dye molecules as light harvesting component are anchored onto the surface of the working electrode since the most semiconductor materials exhibit no absorption in the visible spectral region and are used for working electrode due to their large band gaps. Studies of photo sensitizers (dye molecules) had significant influence and play an important role for the performance development of DSPS. A best sensitizer for DSPS ought to initially absorb light across the entire visible spectrum but preferably extending into the red/NIR range due to the high photon flux of the sun in these wavelength regions in order to harvest the maximum possible light. Second, the dye ought to bind strongly to the semiconductor surface in order to achieve high stable devices and efficient electron injection. Therefore most dyes used in DSPS ought to necessarily have at least one anchoring group linked to the TiO_2 surface through Carboxyl groups (-COOH), found in organic acids (Chang et al., 2011; Chen et al., 2011; Xu et al., 2011; Zhang, Liu, Wang, Zhou, & Wang, 2011), Phosphate (-PO_3H_2), found in ADP, ATP and phospholipids (Chen et al., 2007; Wenger et al., 2006), Sulfo group (-SO_3H) in Sulfonic acid chemical class (Wang, Li, & Huang, 2000; Yao, Shan, Li, Yin, & Huang, 2003), Pyridyl groups (-Py) in Pyridine derivative chemical class (Ooyama et al., 2013), or other Nitro groups (-NO_2,), Propionic acid and Thieno-thiophene or Thiophene (coded as D-ST and D-SS respectively) (Cong et al., 2012; Hao et al., 2009; Li, Jiang, Shao, & Yang, 2006). Introducing long alkyl chains into the donor or linker group of the dye molecules was found to be a crucial modification of organic dyes since the long side chains tend to prevent dye aggregations by serving as spacers to separate the dye molecules bound on the TiO_2 surface and to prohibit the charge recombination by protecting the TiO_2 surface from the hole transport materials and the sites of the dye molecules with high hole concentrations and also good electronic communication between the two parts (Yang, 2014). Anchoring to TiO_2 through a number of other functional groups has also achieved, such as Salicylate, Phosphonic acid and acetyl acetonate derivatives (Pellejà i Puxeu, 2014). Third, have a suitably high redox potential for regeneration following excitation and be stable over many years of exposure to sunlight.

The energy levels of the sensitizer need to be appropriately positioned relative to the conduction band (CB) of the metal oxide semiconductor and the redox potential of the redox couple in the electrolyte (or highest occupied molecular orbital (HOMO) of the hole transport materials (HTM)) to ensure efficient charge separation. This means that the LUMO ought to necessarily be more negative than the CB edge of the semiconductor (i.e. the level of the excited state LUMO should lie above the CB of the metal oxide semiconductor to ensure electron injection from the sensitizer), and the HOMO level of the dye ought to be more positive than potential of the redox couple (i.e. the redox potential level of the ground state HOMO should be lower than redox level of the electrolyte for efficient regeneration of the dye and to ensure hole injection into the HTM). The mismatch of these two energy levels with either the TiO_2 CB or the redox energy levels leads to unwanted device efficiency losses. Also, for the longer wavelength photons which have lower energy, it is more difficult to make efficient devices as the HOMO-LUMO gap is narrower (Dualeh, 2014; Pellejà i Puxeu, 2014; Robertson, 2006).

Furthermore, the electron recombination between the photo-injected electrons at the TiO_2 and the oxidized dye is influenced by the spatial orientation of the HOMO and LUMO in addition to the electron injection of the dye into the semiconductor CB and the photo sensitizer regeneration (Clifford et al., 2004). In particular, the LUMO should be in close contact with the semiconductor surface and the dye cation should be separated from the electrode surface.

Preventing dye aggregation is also important. Aggregation decreases photocurrent and reduces the device efficiency. Preventing dye aggregation on Titanium oxide surface can be solved through optimization of the dye molecular structure or by addition of co-adsorbents. It consists in adding to the dye solution an appropriate amphiphilic organic acid which competes with the carboxylic groups of the dye and is able to prevent their aggregation. Chenodeoxycholic acid (cheno) is one of the most common co-adsorbents for several dyes such as N3 and N719 due to its bulky size and normally inserted between the photo sensitizers on the TiO_2 surface. It can also reduce the back electrons in the TiO_2 nanoparticles and decrease this recombination process, which is known to improve photocurrent I_{sc} and photovoltaic V_{oc} of the final device as shown in Figure 2.2 (Ren, Feng, Zhou, Huang, & Wang, 2010). Moreover, co-grafting of the dye and the co-adsorbent results in the formation of a mixed monolayer which should be more tightly packed than when the sensitizer is adsorbed alone, providing a more effective insulated barrier for the back electron transfer from the TiO_2 CB to the triiodide electrolyte (Palma, 2014; Pellejà i Puxeu, 2014; Wang, P. et al., 2003).

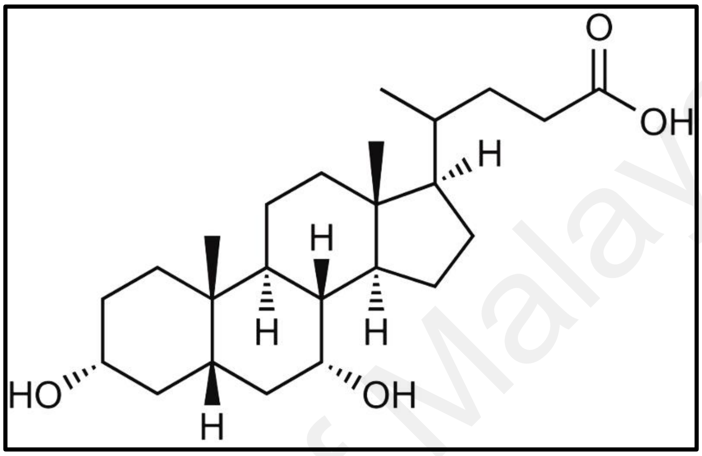

Figure 2.2: Chemical structure of the co-adsorbent Chenodeoxycholic acid (cheno) (Daeneke et al., 2011).

The last property that ought to be taken into account during exposure to solar radiation and in the electrolyte media is the thermal, chemical and electrochemical stability of the dye. The sensitizer under illumination and in terms of electrochemistry (the dye can undergo illumination corresponding to the number of catalytic redox turnovers[1]) should remain serviceable without significant loss of device performance. Furthermore, to prevent desorption from semiconductor surface the attachment of the sensitizer (dye) to

---

[1] The dye should be stable enough to sustain about 10^8 turnover cycles corresponding to approximately 20 years of exposure to natural light (Gratzel, 2003).

the semiconductor should be sufficiently strong. The best example is pure solid N3 dye which is stable up to 280 ℃ even in ambient air where decarboxylation sets in (Gratzel, 2003).

Based on these requirements, many different dyes as metal complexes, phthalocyanines, porphyrins and metal-free organic dyes have been designed and applied to DSCs in the past decades. For instance, the electrochemical properties of the photo sensitizers (dyes) employed for DSPSs in this research are specified and explained below.

2.1.1.1 Phthalocyanines (Pcs)

Phthalocyanines (Pcs) are a family of symmetrical aromatic molecules based on an extensive delocalized two-dimensional 18 π-electron system which exhibit a large number of unique properties and are often used as dyes and pigments. Tcherniac and Braun discovered metal-free phthalocyanine (H_2Pc) from the synthesis of o-cyanobenzamide from acetic acid and phthalimide as a dark by-product as shown in Figure 2.3 (Braun & Tcherniac, 1907). They are very thermally stable, have low solubility and versatile compounds, capable of including more than 70 different metallic and non-metallic ions in the ring cavity. Moreover, it is possible to incorporate a variety of peripheral substituents around the phthalocyanine core, as well as replacing some of the four isoindole units by other heterocyclic moieties, giving rise to different phthalocyanine analogues. Phthalocyanine complex compounds with metals in the center were discovered and have been extensively studied during the last 30 years, with considerable interest in their physical properties. A researcher from Switzerland synthesized copper phthalocyanine (CuPc) just one year after iron phthalocyanine (FePc) was discovered at Scottish Dyes, Ltd (McKeown, 1998). Un-substituted Pcs, which usually present p-channel mobility’s, are sublime instead of melting at high temperatures under vacuum. The solubility of Pcs increases by addition of peripheral substitutes which can change their charge carrier’s type by adding electron, and has led to organic dye aggregation studies (Snow, 2003). Strong electron-withdrawing groups are often added to the molecular structure in order to shrink the gap between the Fermi level and the LUMO band (Conduction Band) through synthetic design: those groups increase the electron affinity, stabilize the molecule anionic form thus making the charge efficiently inject and transport (Chua et al., 2005).

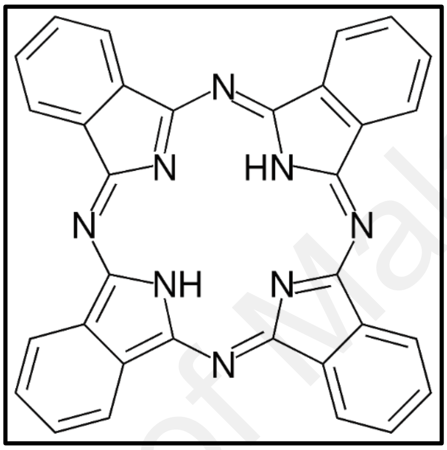

Figure 2.3: Molecular structure of metal-free phthalocyanine (H_2Pc) with carbon assignments.

Initially, phthalocyanines were widely used as dyes and pigments. Their use in molecular physics came about in 1935 when Robertson reported a direct X-ray analysis of crystalline H_2Pc (Wiggins, 2013). These compounds possess an intense absorption in the Soret-band (B band) at around 340 nm and Q band (around 650-700 nm), as well as promising photochemical, electrochemical and thermal properties, and are thus of interest to use as near infra-red (NIR) photosensitizers for dye sensitized photo sensor (DSPS). To date, many researchers have also investigated the several properties of phthalocyanine derivatives and use in organic devices. The solubility of these dyes is normally very poor and needs to be improved by structural optimization in order to facilitate the dye sensitization process. Another major problem with Pcs is their strong tendency to aggregate on the semiconductor surface, which requires a co-adsorbent to suppress dye aggregation (Pellejà i Puxeu, 2014).

The alternative sensitizers to Ru(II) polypyridyl complexes based on electronic, thermal and redox properties are found to be phthalocyanines for DSPS. Pcs are tetra pyrrolic cycle organic molecules which can find applications in several fields (Giribabu, Sudhakar, & Velkannan, 2012). To develop new efficient metal complex photo sensitizers, an increase in the absorption coefficient of the metal complex as well as an increase in the red shift of the absorption region is needed because the absorption coefficient decreases as the red shift increases (Luque & Hegedus, 2011).

2.1.1.1.1 Nickel Phthalocyanine

J.R. Silva (Silva, Brito, Tanimoto, & de Souza, 2011) reported that insoluble nickel phthalocyanine can be made water soluble by sulfonation of the phthalocyanine ring. Nickel (II) phthalocyanine-tetrasulfonic acid tetrasodium salt (NiTsPc) thus formed is a potential candidate for device applications in the area of electronics and optoelectronics (Fakir, Ahmad, & Sulaiman, 2012; Fernandes, Vieira, de Queiroz, Guimaraes, & Zucolotto, 2010; Vieira, Figueiredo, de Queiroz, Zucolotto, & Guimarães, 2011; Wiziack et al., 2009). NiTsPc exhibits a p-type semi-conductivity and shows an ohmic and space-charged limited conduction at low and higher applied voltages, respectively, when suitable metal electrodes are employed (Anthopoulos & Shafai, 2002). Hole mobility of NiTsPc is reported as 10^{-5} m^2/Vs. As for the photophysical property, J.B. Brito previously reported that absorption spectrum of NiTsPc aqueous solution exhibits two absorption peaks in B and Q band, respectively (Brito et al., 2012). The intense peak in Q band (centered at 620 nm) is associated with dimers and a shoulder peak in same band within 650-660 nm which is attributed to NiTsPc monomers. The B band in the UV region (at around 340 nm) also dominates the absorption spectrum of NiTsPc. The choice of

NiTsPc as sensitizer in this study is by virtue of its significant visible wavelength absorption, water solubility feature, and eco-friendly nature. Semiconductor TiO_2 (band gap, Eg ~ 3.2 eV), has been used to facilitate light-induced redox processes because of its conductive electronic structure (Niehues, Scarminio, & takashima, 2010).

In this research, Nickel (II) phthalocyanine-tetrasulfonic acid tetrasodium salt (NiTsPc) among the Pcs complexes is chosen. The molecular structure of NiTsPc is shown in (Figure 3.1). NiTsPc is employed as a dye sensitizer for DSPS (Karwan et al., 2014) (see CHAPTER 4:) due to the following motives (Shah, 2010):

- **It has relatively higher mobility value as compared with mobility values reported for several other Pcs (Ahmad, Z. et al., 2012; Karwan et al., 2014; Yang, Zhang, Qiu, & Lin, 2012). This particular property makes it a very promising organic material for the development of future electronic devices.**
- **Its photo-conductivity and electrical conductivity are also relatively higher compared to other Metallophthalocyanine (Anthopoulos & Shafai, 2003; Qiu et al., 2009).**
- **The studies on NiTsPc show that it is also a suitable active material for the fabrication of highly sensitive gas sensors (Sayyad et al., 2008; Schoch & Temofonte, 1988).**

2.1.1.2 MEH-PPV

Poly(phenylenevinylene) (PPV) is a conjugated polymer of the rigid-rod polymer family which has attracted significant attention due to electrically conducting upon doping and is the only polymer of this type that can be processed into a highly ordered crystalline thin film (Hasobe, Fukuzumi, Kamat, & Murata, 2008; Skotheim & Reynolds, 2007). Several optoelectronic devices has been introduced by using conducting polymer materials as an active medium, such as field effect transistors, light emitting diodes (LED), and photo-diode (bulk heterojunction) (Zhang, Johansson, Andersson, Hummelen, & Inganas, 2003). One of these important polymer classes which is the first soluble PPV in common organic solvents is poly[2-methoxy-5-(2-ethylhexyloxy)-1,4-phenylenevinylene] (MEH-PPV) that has been used as a highly efficient light emitting material in electroluminescence devices and extensive work has been devoted to this special polymer (Hasobe et al., 2008; Wu, Shi, Chen, Han, & Peng, 2004). The molecular structure of the poly[2-methoxy-5-(2-ethylhexyloxy)-1,4-phenylenevinylene] (MEH-PPV) is shown in (Figure 3.1). MEH-PPV with average M_n 70,000-100,000, molecular weight, M_w of 100×10^3 GPC and small energy band gap ~2.1 eV is one of the earliest polymer exhibits fairly good hole mobility and environmental stable in the polymer solar cell history which is developed by Wudl et al. (Semendy, Meissner, & Wijewarnasuriya, 2011; Wudl, 1993; Yu, Pakbaz, Zwang, & Heeger, 1994). The observation of photovoltaic effect on the other hand in the devices fabricated from conjugated polymers such as MEH-PPV mean that it able to harvest light efficiently in this visible wavelength range. The details of the optical peak absorption are illustrated at (Figure 5.3 and Figure 5.4). One of the most interesting applications is that DSPS can made from MEH-PPV as the dye sensitizer, which can cover most parts of the visible range when it mixes with PCPDTBT in 1:4 volumetric ratios (Karwan, Ahmad, Sulaiman, Yap, & Touati, 2015).

2.1.1.3 PCPDTBT

Poly[2,6-(4,4-bis-(2-ethylhexyl)-4H-cyclopenta [2,1-b;3,4-b’] dithiophene)-alt-4,7 (2,1,3-benzothiadiazole)] (PCPDTBT) is the first conjugated polymer that has low (narrow) bandgap and high efficient photovoltaic response in the near IR region of sun spectrum. The HOMO and LUMO energy level of the PCPDTBT lies between -4.9 to -5.3 eV and -3.5 to -3.8 eV respectively. It processes an electrochemical bandgap (E_g^{echem}) of 1.7 eV and optical bandgap (E_g^{opt}) of 1.4 eV which is absorbed deeply in spectrum

(Qiao, 2015; Soci et al., 2007). PCPDTBT has been synthesized and designed by Mühlbacker et al. in 2006, which has a broad absorption band at the wavelengths λ=350-850 nm with an average M_w 7,000-20,000 and it is a donor and acceptor alternating conjugated polymer (Gong et al., 2010; Qiao, 2015; Yam, 2010). The molecular structure and the absorption spectra of the PCPDTBT are depicted in Figure 3.1 and Figure 5.4, respectively. In the case of DSPS, PCPDTBT exhibits as a donor material with high hole mobility (Morana et al., 2008) because it is contributes with MEH-PPV in blend form as a dye sensitizer to facilitate light-induced redox processes (see CHAPTER 5:) (Karwan et al., 2015).

In this study, the binary blend of poly[2-methoxy-5-(2-ethylhexyloxy)-1,4-phenylenevinylene] (MEH-PPV) and poly[2,6-(4,4-bis-(2-ethylhexyl)-4H-cyclopenta [2,1-b;3,4-b’]dithiophene)-alt-4,7(2,1,3-benzothiadiazole)] (PCPDTBT) were used as a sensitizer for the reported DSPS. These polymers are known as electron donor polymers (Liang et al., 2014). MEH-PPV and PCPDTBT have been investigated individually in numerous work (Agostinelli et al., 2008; Ahmad, Suhail, et al., 2013; Chu et al., 2011; Liu, X. et al., 2012; Mühlbacher et al., 2006; Peet et al., 2007; Zafar, Ahmad, & Sulaiman, 2015; Zafar et al., 2014). The absorption range of MEH-PPV is 400 to 550 nm, however the absorption of PCPDTBT lies in the range of 550-850 nm. The combination of these both materials would significantly broaden the absorption spectrum. In continuation of efforts to make cheap, reliable, environmentally friendly photo detectors for the whole visible solar spectrum, the present work aimed to demonstrate an organic visible photo sensor in order to enhance the photo-sensitivity range and facilitate light-induced redox processes.

2.1.2 Photo Anode: TiO_2 Electrode or Working Electrode

The photo anode consists of a mesoporous semiconductor film that has been attached (sintered) onto the transparent conducting oxide (TCO) such as ITO glass substrate (see 3.1.4 Electrodes and Substrates) either by blading technique or screen printing (see 3.3.4). Light harvesting, electron injection and collection, and unfavorable electron recombination are all correlated with the photo anode which plays a significant role in converting photons into electrical energy in DSSC and DSPS. It is important to mention that semiconductor Titanium oxide (TiO_2) is by far the most common and gives the highest efficiency, but there are many other alternative metal oxide systems such as ZnO, SnO2, Nb2O5 and WO3 exist (Park & Kim, 2008). Besides these simple oxides, core-shell structures such as ZnO coated SnO2 have been tested, as well as ternary oxides like SrTiO3 and Zn2SnO4. In part of this work thesis, the focus is only on n-type DSPSs based on TiO_2.

Since mesoporous TiO_2 structure composite of nanoparticles was used in the breakthrough paper by Grätzel's cell then there has been a tremendous development of different kinds of nanostructures such as nanotubes, nanowires, nanorods, nanosheets, nanobowls and microbeats. For all different kinds of TiO_2 structures look at reference (Hagfeldt, Boschloo, Sun, Kloo, & Pettersson, 2010). Besides using TiO_2 as a semiconductor in photochemical applications, it is a versatile compound that is used widely as a highly efficient catalyst, microorganism photolysis, gratings, antifogging, toothpaste, self-cleaning materials, white pigment in paint, sunscreen and food (E171) etc. TiO_2 was also used by Fujishima and Honda in the famous paper "Electrotechnical Photolysis of water at a Semiconductor Electrode" (Fujishima & Honda, 1972). In another application, TiO_2 is suitable for hydrogen production from water because of the band positions where CB more negative than the redox potential of H_2/H_2O and the valence band (VB) is more positive than the redox potential for H_2O/O_2 (Ellis, 2014).

TiO_2 has several crystal forms occurring naturally, which are Rutile, Anatase and Brookite, which is stable, nontoxic, cheap, and has a high refractive index (n $= 2.4 - 2.5$). The most stable phase thermodynamically among them is Rutile form for the macroscopic crystals. However, anatase is more chemically active than Rutile for nanocrystals smaller 20 nm (Kalyanasundaram, 2010), thus anatase is the one preferred in DSPSs and DSSCs. Moreover, the band gap of anatase is 3.2 eV while 3.0 eV is for Rutile which leads to higher V_{oc} and higher Fermi level in DSPS application due to the higher CB edge of anatase. On the other hand, the commercial TiO_2 nanoparticle currently is DeGussa P25 with particle size 25 nm which is composed of 80% anatase and 20% Rutile because anatase is metastable and is prone to convert to Rutile upon heating. A comparison of the results of solar cell performances between anatase and Rutile TiO_2 based DSSC showed that anatase based cell is 30% higher in terms of (I_{sc}) short circuit current than Rutile based cell while both have the same (V_{oc}) open circuit voltage. This is because Rutile attributed smaller dye absorption amount on the Rutile photoanode and slower rate of electron transfer due to lower coordination number (Kelzenberg et al., 2010; Mawhinney et al., 2000; Yu, 2014).

At a temperature of 25 ℃, experimentally the conduction band potential of colloidal TiO_2 (anatase), which depends on pH, is obtained as Equation 2-1. The CB will move towards more positive value when the pH increase. Thus it affects the kinetics of the DSPS. This value of Equation 2-2 is commonly used for position of the CB in TiO_2.

$$E_{CB}(TiO_2) = -(0.12 \pm 0.02) - 0.059(pH)\ V\ (vs. NHE)$$ **Equation 2-1**

$$E_{CB}(pH\ 7) = -0.5\ V\ (vs. NHE)$$ **Equation 2-2**

$$E_{CB}(pH\ 0) = -0.14\ V\ (vs. NHE)$$ **Equation 2-3**

Surface Ti^{IV} sites are Lewis acids, which enable the absorption of dyes, thus offering a convenient way to attach dye molecules with electron-rich anchoring groups such as Figure 2.4. This chemical species i.e. Lewis acids is favored over other materials for the photoelectrode in DSPS.

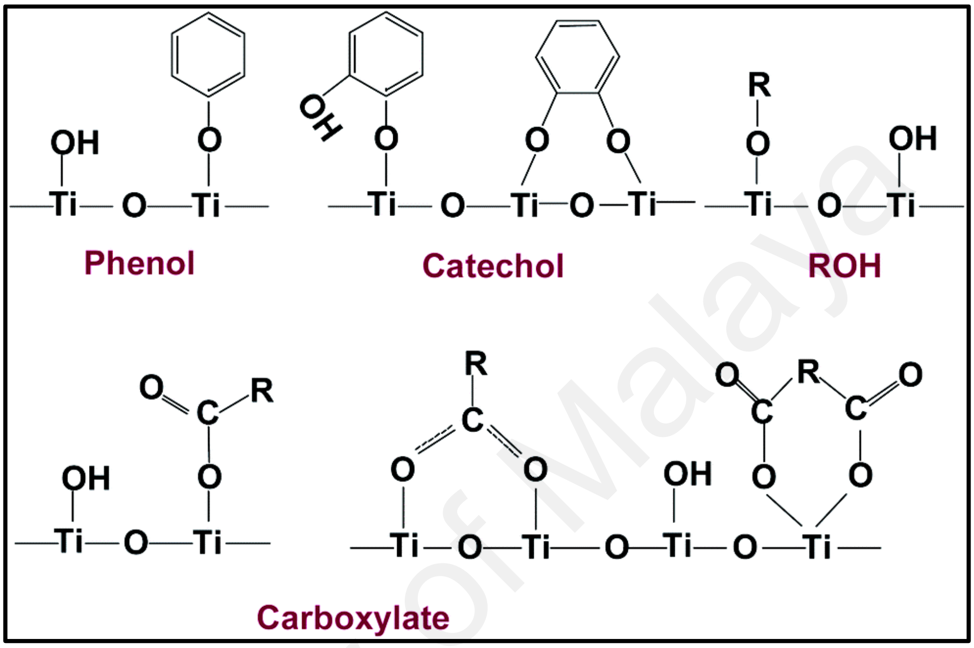

Figure 2.4: Chemical structure of TiO_2 surface with the possible binding modes of representative complexes. The CB of the TiO_2 is formed by the empty 3d orbitals of the Ti^{4+} ions, while the VB is mainly constituted by the occupied 2p orbitals of the O^{2-} ions (Zhang, Kim, & Choi, 2014).

When it comes to dye sensitized photo sensor, mesoporous TiO_2 is used as the photoelectrode which act as electron acceptors, and dyes work as electron donors. For this purpose, TiO_2 deposited as mentioned above follow sintering to around 450℃ (Barbe et al., 1997). Consequently more dye can be adsorbed due to increase in the surface area more than 1000 times that of dense flat TiO_2 electrode, which leads to higher light absorption (Barbe et al., 1997; Pekkola, 2014; Snaith & Grätzel, 2007). Barbe et al. investigate that the metal oxide TiO_2 electrode (from Degussa AS), has a porosity about 60% with surface area 51 m^2/g (Barbe et al., 1997) and average size of TiO_2 is around 15 nm (Gratzel, 2003) while the diameter of the standard dye N719 used in DSPS and DSSC is 1-2 nm (Lin et al., 2009). Thus, the dye is able to penetrate the structure of mesoporous because the TiO_2 pores are big enough.

On the other hand, the open circuit voltage in DSPS generated under illumination corresponds to the difference between the Fermi energy level of the electron in solid (Titania) and the redox potential (I_3^-/I^-) of the electrolyte or the HOMO of the solid-state HTM. However, the Fermi energy level of the semiconducting nanoparticle layer is determined by the position of the TiO_2 CB and the charge generation and recombination (Han, Pringle, & Cheng, 2014), which initially depends on the type of materials, but is additionally shifted by the trap density, inclusion of mobile charges (electrons) from dyes, and changes in the surface environment of the metal oxide layer caused by additives. Therefore, open circuit voltage (V_{oc}) varies with the properties of the electrolyte or HTM material and the dyes sensitizer (Kim, 2014).

In this section, the most desirable semiconductor characteristics in DSPS are summarized below (Harlow, 2014):

- **The semiconductor must not absorb much light, if any, in the visible region of the solar spectrum. A semiconductor that absorbs light created holes in its VB forming an unfavorable pathway where holes can oxidize the reduced dye.**
- **Should be nanocrystalline. The high surface area increases the number of sites for dye adsorption and magnifies the absorption cross section substantially within a given area as compared to a monolayer of dye (Liu, Zeng, Zhou, & Zou, 2011).**
- **Should have very few vacancy or trap sites. The more efficiently electrons can be collected only with more homogeneous semiconductor thin film on a pure substrate.**

- **Should be chemically stable in the reaction conditions when the cell exposed to light. Also, the CB edge should remain at a reasonable negative energy to allow metal-to-ligand charge transfer (MLCT) excited state injection. MLCT is most commonly observed in complexes with ligands having low-lying $\boldsymbol{\pi}^*$ orbitals, especially aromatic ligands. This means that the LUMO of the ligand dye ought to be more negative than the CB edge of the metal oxide semiconductor.**

2.1.3 Redox Mediator (Electrolyte)

In DSPS, the electrolyte is generally formed by an organic solvent consisting of redox couple, called redox mediator. Iodide/triiodide $(\boldsymbol{I^-/I_3^-})$ typically as a redox couple is dissolved in an organic solvent such as acetonitrile, which is used in the breakthrough paper of (Oregan & Gratzel, 1991). The electrolyte redox couple is of crucial importance for stable operation of a DSPS and DSSC, and is responsible for transporting the charges between the working electrode (photo anode) and counter electrode (photo cathode) during the regeneration step of the oxidized dye species. The electrolyte redox mediator must restore the ground state of the oxidized species and the dye is formed then which is in turn reduced to the counter electrode during migrating by diffusion between the two electrodes. The regeneration rate of the oxidized dye to its ground state at achievable concentrations must occur as fast as possible because of its inclination to physical degradation (covalent bonds can start to break apart and/or crosslink) (Palma, 2014).

The redox couple such as $(\boldsymbol{I^-/I_3^-})$ is a two electron redox mediator. This kind of electrolyte shows a slow rate of electron recombination at the TiO_2 interface, absorbs slightly and offers fast diffusion. Thus it differs substantially from the transition metal based redox mediators which are one electron redox mediators. Another drawback with the iodide/triiodide $(\boldsymbol{I^-/I_3^-})$ is a large driving force is required for regeneration of the dye, which leads to loss of large internal potential and limits the output voltage and overall performance of the device (Boschloo & Hagfeldt, 2009). The reason for the large expenditure required for efficient dye regeneration is due to the kinetics of complex regeneration involving formation of intermediates such as the $\boldsymbol{I_2^-}$ radical (Boschloo & Hagfeldt, 2009; Pelet, Moser, & Grätzel, 2000). Therefore, kinetically fast one electron redox mediators have been used with some interesting results in which they do not suffer from this limitation and enable the reduction of the driving force for dye regeneration. One electron redox mediators include ferrocene/ferrocenium (Fc/Fc^+), copper complexes (Cu(I)/(II)), cobalt complexes (Co(II/III)) and mediator mixtures. However, the high rate of recombination with electrons between the TiO_2 and the oxidized dyes is the main drawback of these one electron redox mediators compared to the system of $(\boldsymbol{I^-/I_3^-})$ (Listorti, O'Regan, & Durrant, 2011). Electron transfer reactions based on the redox mediator $(\boldsymbol{I^-/I_3^-})$ are summarized in Equation 2-6 to Equation 2-8 (below) in a DSPS and DSSC involved in photocurrent generation (Daeneke et al., 2011). Equation 2-6 is most likely a one electron transfer reaction between $\boldsymbol{D^+}$ and $\boldsymbol{I^-}$. However, it is unlikely for the oxidation of iodide to free iodine radical $(\boldsymbol{I^\bullet})$ due to energy reasons (Hagfeldt et al., 2010). The driving force for regeneration of the dye is determined by the difference between the formal reduction potential of $\boldsymbol{I_2^{-\bullet}/I^-}$ and $\boldsymbol{D^+/D}$ as Hagfeldt et al. have argued, and they determined that the value of $\boldsymbol{E^0}(\boldsymbol{I_2^{-\bullet}/I^-})$ in acetonitrile is +1.23 V vs NHE (Hagfeldt et al., 2010). Figure 2.5 illustrates the schematic diagram of the redox couple $(\boldsymbol{I^-/I_3^-})$ in the DSPS with typical time constants.

$$D + h\nu \rightarrow D^*$$ **Equation 2-4**

$$D^* \rightarrow e^-(\mathrm{TiO_2}) + D^+$$ **Equation 2-5**

$$D^+ + I^- \rightarrow (D - I)$$ **Equation 2-6**

$$(D - I) + I^- \rightarrow D + I_2^{-\bullet}$$ **Equation 2-7**

$$2I_2^{-\bullet} \rightarrow I_3^- + I^-$$ **Equation 2-8**

Diiodide radicals ($\boldsymbol{I_2^{-\bullet}}$) is formed from the reaction between oxidized dye and iodide (Boschloo & Hagfeldt, 2009). The complex ($\boldsymbol{D - I}$) in Equation 2-6 is formed when the oxidized dye ($\boldsymbol{D^+}$) is reduced by iodide ($\boldsymbol{I^-}$), after electron injection from the excited dye ($\boldsymbol{D^*}$) (Equation 2-5). When a second iodide ion comes in, the complex ($\boldsymbol{D - I}$) dissociates to dye in the ground state $\boldsymbol{D}$ and $\boldsymbol{I_2^{-\bullet}}$ form. And finally, triiodide and iodide are formed from the two diiodide radicals reaction as shown in Equation 2-8 (Boschloo & Hagfeldt, 2009).

Several different alternative redox mediators have been used such as Br_2/Br^-, quinone/hydroquinone, halogens, interhalogens, pseudohalogen, nitroxide radicals, sulphides, nickel (III/IV), $(\mathrm{SCN})_2/\mathrm{SCN}^-$, and $(\mathrm{SeCN})_2/\mathrm{SeCN}^-$. All these alternative redox mediators can be found in (Listorti et al., 2011). Even though redox potentials of these alternative mediators are more positive and observed some improve on the V_{oc}, however, with these systems, low power conversion efficiencies obtained which leads to slow regeneration reaction of the dyes (Listorti et al., 2011).

It is important to mention that so far, many redox couples and electrolytes have been explored in different types, including $\boldsymbol{I^-/I_3^-}$ in solid inorganic materials (Meng et al., 2003), ionic liquid (Wang, Zakeeruddin, Moser, Humphry-Baker, & Gratzel, 2004), gel (Wang, Peng et al., 2003), solid polymer (Kang et al., 2005), plastic crystal system (Wang, Peng et al., 2004), small organic molecules (Krüger et al., 2001) and hole conducting organic polymers (Saito et al., 2004). At the moment of writing, the best performances have been obtained with (Co(II/III)) (Nusbaumer, Zakeeruddin, Moser, & Gratzel, 2003) or $\boldsymbol{I^-/I_3^-}$ redox couple in conjunction with ruthenium (Ru) based dyes.

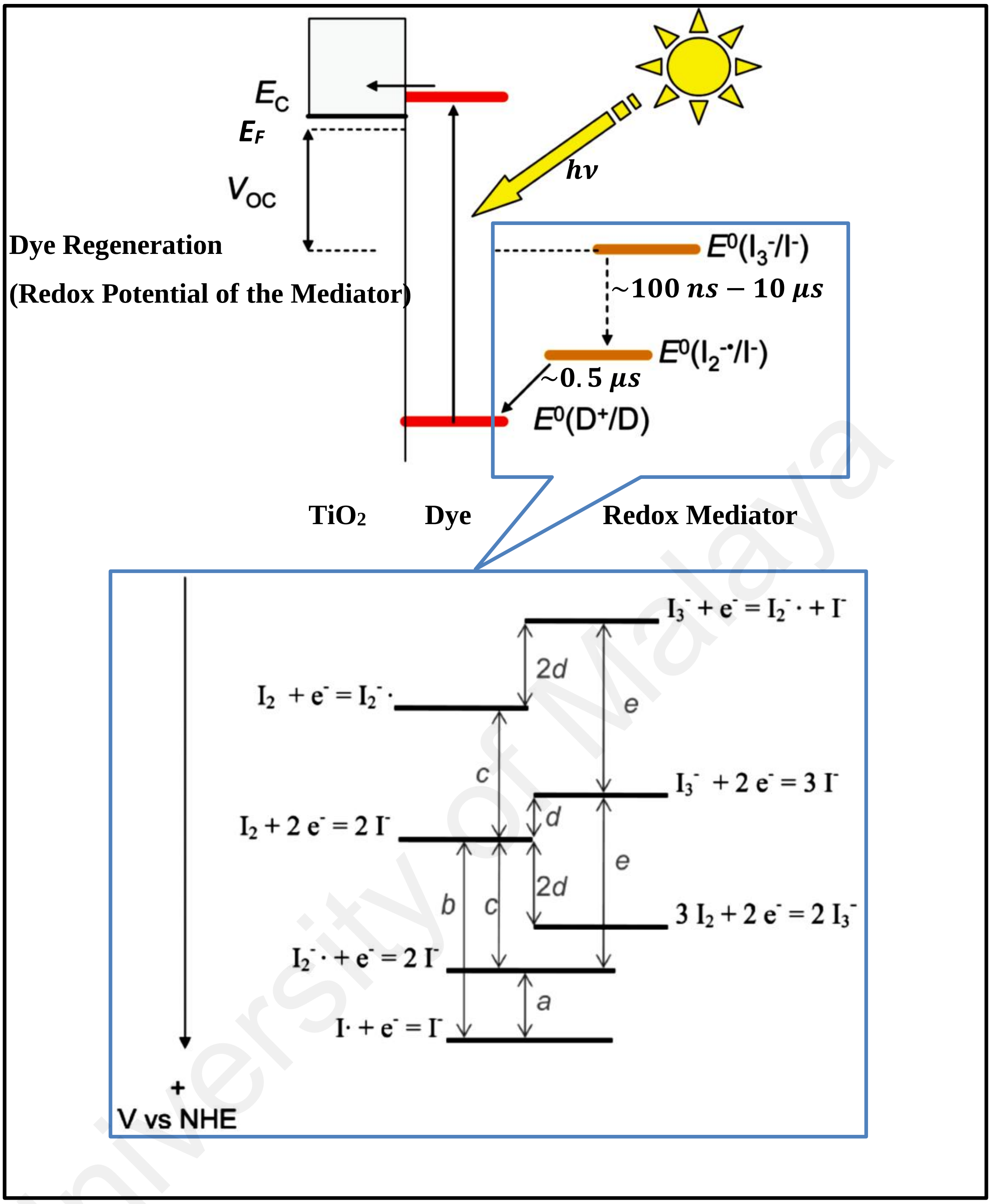

Figure 2.5: Schematic diagram of the electrolyte (the pathway for the reduction of the oxidized dye (D^+) by iodide (I^-)). The light harvesting in DSPS is accomplished by dye molecules located at the interface of an electrolyte and a mesoporous wide band gap TiO₂ electrode. At that time, the redox mediator is employed to regenerate the oxidized dye, following a photo-induced charge injection from the dye into the CB of TiO₂ electrode. The difference between the Fermi level (EF) of the TiO₂ and the redox potential of the mediator is represented by the V_{oc} of the cell. The below figure is the details of seven redox reactions of the (I^-/I_3^-) system and their relative electrochemical potentials. Some of these reactions are important for the DSPS. The indicated differences in formal potentials are $a = \left(\frac{RT}{F}\right)\ln(K_3)$; $b = \left(\frac{RT}{2F}\right)\ln(K_2)$; $c = b - a$; $d = \left(\frac{RT}{2F}\right)\ln(K_1)$; and $e = c + d$ (Boschloo & Hagfeldt, 2009).

The choice of a good electrolyte involves some different requirements, as summarized below:

i. **Electrolyte must have a good contact between the dye and the counter electrode. The dyes are regenerated through oxidizing I^- to form I_3^- and then, in order to regenerate I^- and continue the redox cycle, I_3^- must be transported from the working anode to the counter electrode to receive electrons there (Ku & Lu, 2011; Pellejà i Puxeu, 2014).**
ii. **The redox couple should be fully reversible where each form of the species is stable and efficiently converted between them. That is, it must have a completely reversible redox cycle in the working conditions (i.e., in presence of the used dye, at the considered temperature and with the used electrolyte, etc.) (Harlow, 2014; Palma, 2014).**
iii. **The redox couple potential in electrolyte should be sufficiently negative to provide the driving force necessary, and negative enough to re-reduce the oxidized dye. At the same time, in order not to waste attainable energy and keep a high V_{oc}, the redox potential should not be too negative. This is because a too negative V_{oc} effects the performance of devices (Harlow, 2014).**
iv. **The electrolyte should neither desorb nor degrade the dye from the metal oxide surface, and should be stable optically, thermally, chemically and electrochemically (Pellejà i Puxeu, 2014).**

2.1.4 Photo Cathode (Counter Electrode or Back Contact)

The mean functions of the counter electrode for DSPS are to return electrons to redox mediator (electrolyte) by reducing the oxidized redox species and present as low resistance as possible to attain an efficient device. Counter electrode is a TCO substrate coated with a thin layer of catalyst such as (platinum, various forms of carbon as graphite or black carbon and conductive polymers like cobalt sulphide or PEDOT). The choice of suitable catalyst for the regeneration of the redox couple depends on which electrolyte will be used. At the moment the common counter electrode material for the $\boldsymbol{I^-/I_3^-}$ redox system is platinum due to the relatively high charge transfer resistance of ITO (above $10^3\ \Omega\ \mathrm{cm}^2$ (Katusic et al., 2006)) and Fluorine doped Tin Oxide (FTO) (>$10^6\ \Omega\ \mathrm{cm}^2$). Platinum is very easy to prepare by several methods such as spray pyrolysis, electro-deposition, sputtering and thermal deposition. The platinum thin films were found not suitable for counter electrode improvements when prepared by thermal deposition and electro-deposition due to dissolution in $\boldsymbol{I^-/I_3^-}$ electrolyte.

The nanoscale platinum clusters have achieved long term stability and best performance is achieved by thermal decomposition of platinum chloride compounds. The low Pt loading (5 $\mu\mathrm{g\ cm}^{-2}$ corresponding to a one monolayer Pt) is needed on these electrodes (Papageorgiou, Maier, & Grätzel, 1997). Thus the counter electrode is optically transparent with very low charge transfer resistance (< 1 $\Omega\ \mathrm{cm}^2$).

However, platinum does not show the most efficient in the cobalt redox system after the introduction of cobalt complexes (Co(II/III)) as redox mediator. Conductive polymer (PEDOT) has been substituted Pt and has been shown to be efficient for cobalt, as well as for sulfur based redox couples (Ahmad, S. et al., 2012; Ellis, 2014; Tian et al., 2012).

On the other hand, for counter electrode of DSSC (solid) and BHJ devices, evaporated metal layer by thermal deposition is the best such as Ag and Au. The favorable counter electrode in most cases is Ag due to high conductivity the reflectance of Ag, which leads to an enhanced photon capture by reflecting the transmitted photons back into the dye sensitized light harvesting layer (Yang, 2014). However, various conductive carbon based materials are often employed, such as highly conductive carbon nanotubes (CNTs) developed as counter electrode which is solution processable and low cost.

Finally, the best counter electrode can be summarized as below (Harlow, 2014):

- **The counter electrode ought to have high exchange current density, thus a low sheet and charge transfer resistance making it kinetically easy for passage of electrons to reduce the oxidized dyes.**
- **Overall no chemical reactions (dissolution in I^{-}/I_3^{-} electrolyte) should occur at the electrode surface.**
- **In order to create the driving force to reduce the redox couple in solution, the Fermi level of the counter electrode ought to be negative enough (Papageorgiou, 2004).**
- **The reflective counter electrode is benefited when the device is illuminated through the photo anode side.**

2.1.5 Conductive Glass Substrate Materials (ITO Glass)

In the fabrication of DSPS, the photo cathode and the photo anode ought to be laid onto a conductive material where electrons and holes can easily be collected and moved along without any losses. The conductive materials coated on glass substrate must be, according to the DSPS design in this study, heat stable, rigid, not absorb visible light nor reflect or scatter much incident light. The most common conductive materials (transparent conducting oxide) widely employed for DSPS and DSSC is ITO and FTO due to excellent transmittance ($\sim 80-90\%$), high sheet resistivity (10-15 Ω/sq.), durable conductor, high work function and thermal stability. In this work thesis, only ITO have been used as it offers higher electrical conductive ($\sim 10^{-4}\,\Omega\,\mathrm{cm}$ (Palma, 2014)), lower surface roughness and more transparency ($\sim 90\%$) than FTO. In principle applications, because the ITO work function of around (4.5-4.7 eV) which lies between the HOMO and LUMO of most organic semiconducting materials, it is highly capable of injecting or collecting charge carriers across the photo anode (Zhong, Liu, Huang, Wu, & Cao, 2011). The efficient collection means that the Fermi level of ITO is below that of the semiconductor materials (TiO_2). However, because of low thermal stability of ITO films (during sintering procedure up to 550 ℃), FTO-glass is the most eligible for DSSC applications (Palma, 2014). The main drawback of the FTO-glass is the roughness and geometry of FTO grain which effects the uniformity and adhesion of the TiO_2 compact layer when it is spread onto the FTO-glass (Yuan, 2013).

It is important to note that when a single layer of ITO or FTO-glass is sintered at high temperature (above 300 ℃), the electrical conductivity decreases and the sheet resistance increases, leading to loss energy and low device performance. The increase in sheet resistance is possibly due to reduction of the carrier density. When ITO films are annealed above 300 ℃, oxygen in the air starts to fill the oxygen vacancies which function as an electron supplier (Gong, Liang, & Sumathy, 2012). In order to improve the properties of substrate and prevent the loss of charge carriers in high temperature, double layered conducting glass structures has been fabricated to achieve thermal stability, better electron transport and to prevent oxidation. The double layer structure such as thin layer of ATO (antimony doped tin oxide), FTO, SnO_2 and AZO (aluminium doped zinc oxide) are deposited onto ITO surface. The double layer has proved much better structure than single layer of ITO, as the resistivity of FTO/ITO film increased by less than 10%, even though it was exposed to high temperature of 300-600 ℃ for 1 h in air (Gong et al., 2012; Ngamsinlapasathian, Sreethawong, Suzuki, & Yoshikawa, 2006).

On the other hand, the conductive polymers are expected to be replace the ITO conductive electrode due to the ability to generate complete flexible conductive polymer film and conductive polymers are inexpensive compared to ITO. The largest shortcoming of conductive polymers is the conductivity degradation and the conductivity is about ten times lower than that of ITO. The conductivity of ITO is about 6000 S/cm while the conductivity of the PEDOT:TsO films is about 1500 S/cm which is produced by exposing solid thin film of the iron(III) tosylate to EDOT vapor through vapor phase polymerization (VPP). After modifying the VPP method Evans et al. observed the conductivity of PEG-PPG-PEG is about 2500 S/cm (Brabec, Scherf, & Dyakonov, 2011; Qiao, 2015). This means that much research needs to be done to replace ITO by conductive polymers due to drawbacks regarding degradation and relative low conductivity.

2.1.6 Packing (Sealing) of Device

Sealing of DSPS or DSSC is one of the main crucial challenges of device technology, which is directly related to the long term performance and stability of the device. Sealing material prevents loss or leakage and electrolyte solution evaporates in between the two electrodes of the device. In addition, the intrusion of ambient oxygen and water may lead to the phenomena of photo oxidation. On one hand sealing material ought to be chemically and photo-chemically stable against the solvent and the electrolyte components. On the other hand, it ought to stick well with the TCO-glass. For DSPS and DSSC several sealing materials have been employed such as silicon and epoxy. Another common type sealing material that is used in this work is meltonix (DuPont surlyn) thermoplastic film purchased from Solaronix. Additionally, for outer sealing material, to achieve long term stable device, oxygen-tight glues such as epoxy resin are usually employed.

2.2 Dye Sensitized Photo Sensor Interfaces

The complexity of the DSPS partly stems from the large variety of interactions between the different components, in which all electron transfer reactions occur at the interfaces in DSPS. Common interaction regions as interfaces between solid, molecular or liquid which give them different nature characters are mentioned below. The essential function for the DSPS is the geometrical and energetic matching of these interfaces. Figure 2.6 shows the different schematic drawn interfaces in the DSPS.

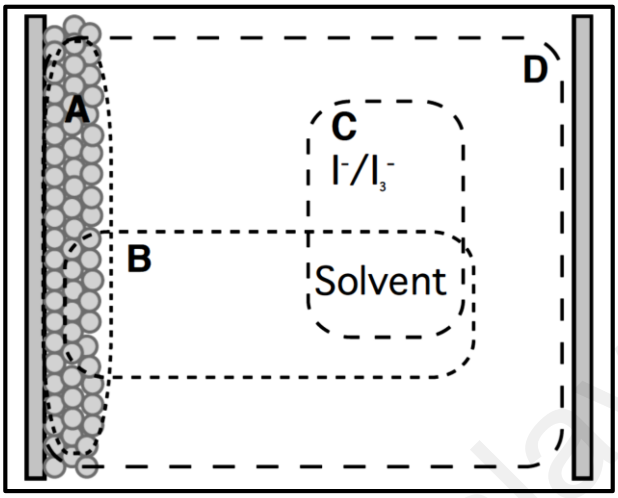

Figure 2.6: Different interface indications in the DSPS (Kaufmann Eriksson, 2014).

The first interface from the working electrode is between the conductive glass (ITO) and the semiconductor (TiO_2) where a good electronic connection is important. In Figure 2.6, (A) is the interface between the semiconductor electrode and the sensitizer (dye) molecules i.e. molecular-electrode interface with interesting parameters such as geometrical configuration, matching of energy and surface coverage. The limit of the performance of the DSPS is set by the energy matching between the photo sensitizer molecules and the semiconductor. No injection of electrons will occur if the difference between the energy levels of the semiconductor conduction band and the excited dye is too small. On the other hand, there will be unnecessary energy losses if the difference is very large. (B) is the most complex interface between the electrode, photo sensitizer (dye) and solvent components, i.e. the interface is between the solvent/electrolyte and the working electrode. Of great importance here is energy matching due to different nature and geometrical changes. The solvation of the dye molecules and perhaps also of the semiconductor interface can affect the energy level alignment of the DSPS system and understanding the structure and size of this solvation can help in the development of new materials. The solute and the solvent interface in the electrolyte (C) is the solute-solvent interface, in which the electrolyte contains at least two different salts and a solvent. Inside the electrolyte several ions are present in a solvent. The traditionally used redox couple is as mentioned iodide/triiodide or more recently a cobalt complex based system. The kinetics of these redox couples are quite well studied in an electrochemical manner (Boschloo & Hagfeldt, 2009; Feldt et al., 2013; Feldt, Wang, Boschloo, & Hagfeldt, 2011; Feldt et al., 2010; Listorti et al., 2011). In this thesis the iodide/triiodide system has been used. (D) is the indication of the entire system (not including counter electrode). Finally, the interface is between the electrolyte and the counter electrode. The necessity for a good charge transport to the oxidized sensitizer molecules is a good catalyst and electronic connection between the counter electrode and the electrolyte in order to improve regeneration.

2.2.1 The Process of Electron Transfer in DSPS

Disparate silicon solar cells are where charge separation is driven by the built-in electric field in nanostructured bulk heterojunction such as DSPSs. The DSPS operating mechanism by several interfacial electron transfer reactions in cooperation can be described. This process is based on the kinetic competition between energy, electron transfer and processes of charge transport, which means each reaction can be kinetically described by its reaction rate constant. As such the key for good photovoltaic performance lies in the relative time-scales between the beneficial and unfavorable electronic processes. Thus, these reactions can be divided into two groups: the desirable forward reactions including photo-excitation, electron injection, sensitizer (dye) regeneration, electron transport in TiO_2 and hole conduction through the redox potential of the electrolyte or hole transport materials (HTM); the unwanted backward reactions, such as the relaxation of photo-excited state of the dye, the recombination between redox potential and free electrons in TiO_2 and the recombination between free electrons and oxidized dye molecules. Figure 2.7 depicts schematic of the relevant photophysical and electron transfer processes involved in the operation of a DSPS. The corresponding time-scales are also included for the individual processes. Among these interfacial electron transfer (ET) reactions, the forward reactions benefit from the charge separation and therefore contribute to the energy conversion while the backward reactions represent the charge recombination reactions and therefore become the limitations of photovoltaic performance in DSPS devices (Yang, 2014).

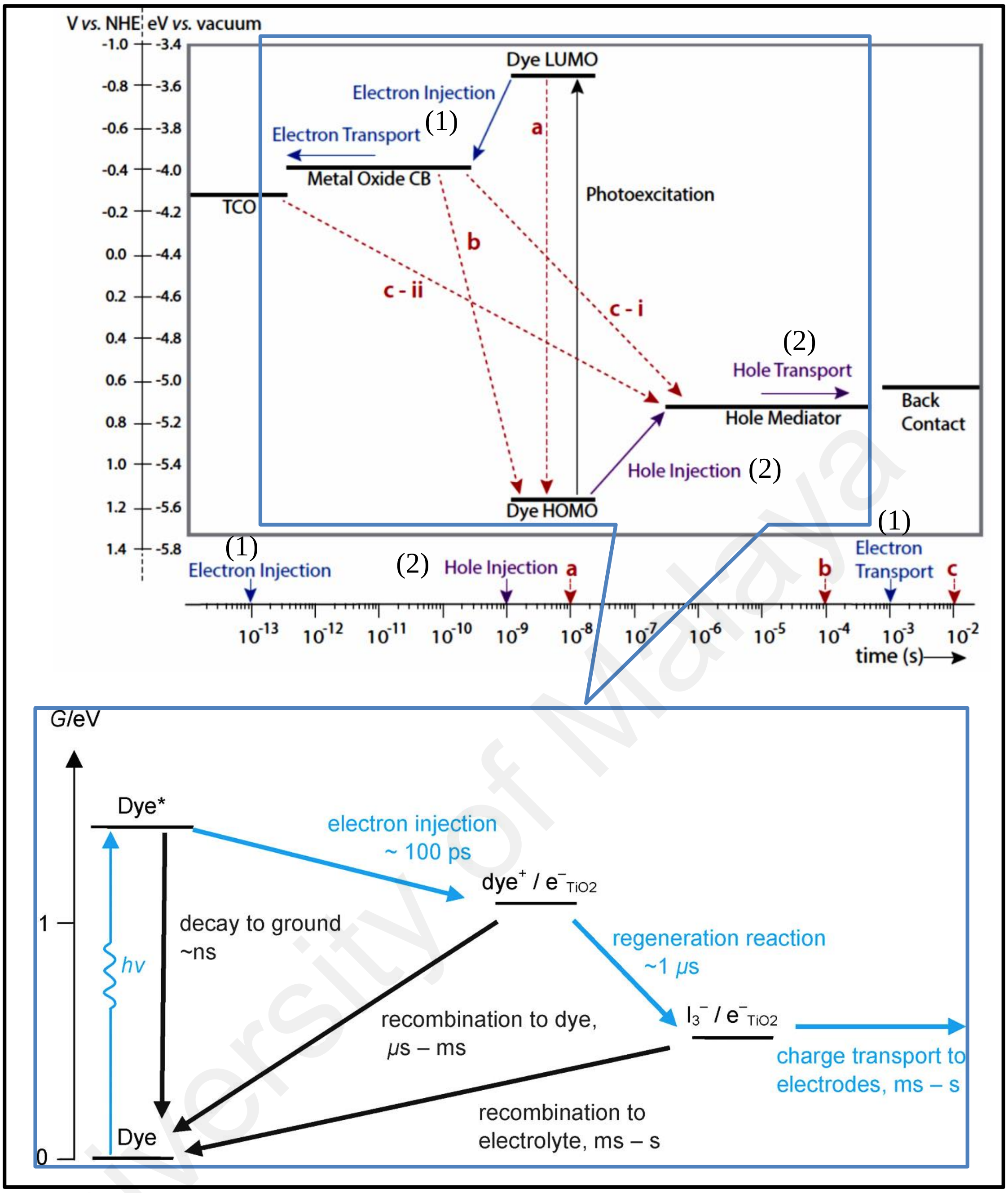

Figure 2.7: (Above) Energy level schematic illustration of the interfacial electron transfer reactions and the electronic processes occurs in DSPS. The favorable reactions (electron transfer processes) contributing to the energy conversion are indicated by the indigo arrows (1), the unlike reactions (recombination) loss channels which limit the photovoltaic performance by dashed red and the hole transfer processes marked by purple arrows (2). The energy levels are approximately given with respect to normal hydrogen electrode (NHE) in V and vacuum in eV. Below the schematic are shown the dynamics of the electron transfer processes. In detail Fig (below), the free energy stored in the charge separated states are corresponded to the vertical scale. The determination of the free energy of injected electrons is considered by the TiO_2 Fermi level which is assuming the chemical potential of the redox electrolyte below a Fermi level 0.6 V of TiO_2. Blue arrows are indicated forward processes of light absorption, electron injection, dye regeneration, and charge transport. Black arrows show the competing loss pathways of electron recombination and excited state decay to ground with dye cations and oxidized redox couple (Dualeh, 2014; Listorti et al., 2011).

Photo-excitation: the dye molecule absorbs a photon leading to the excitation of an electron from its HOMO which is highest energy level compared to the TiO_2 conduction band to its LUMO as shown in Equation 2-9. The incident photon energy of this photo-excitation should be greater than or equal to the HOMO-LUMO gap of the sensitizer. Thus charge separation occurs due to this process. The excited dye molecule within the lifetime either injects an electron through the anchor group into the CB of TiO_2, Equation 2-10, or relaxes back by irradiative or non-irradiative decays to the ground state as shown in Equation 2-11.

Electron Injection: the reaction kinetics suggest that the process of electron transfer from the photo-excited state of dye into the TiO_2 CB takes place within range of femtosecond (fs) to picosecond (ps) on the timescale, while the lifetime of the photo-excited state before relaxation lasts in nanosecond (ns) range (Dualeh, 2014; Listorti et al., 2011; Yang, 2014). Thus excited state of the dye can be quenched by the redox couple species present in the electrolyte. The iodine based redox couple can quench the excited dye by generating either oxidative ($\boldsymbol{D}^{+}$) or reductive ($\boldsymbol{D}^{-}$) quenching according to Equation 2-10 (Listorti et al., 2011). The efficiency of charge separation will reduce with presence of oxidative quenching, while if the dye anion is capable of efficiently injecting an electron into the semiconductor, reductive quenching may result in efficient charge photo-generation (Listorti et al., 2011).

Therefore, the electron transfer (ET) reaction rate constant of electron injection (κ_{inj}) is orders of magnitude greater than that of sensitizer relaxation (κ_{rel}). To clarify, this process quantified by the favorable electron injection efficiency (η_{inj}) which is a measure of electron fractions that are injected into the CB of TiO_2 (e_{CB}^{-}) after photo-excitation as shown in Equation 2-12.

$$D \overset{h\nu}{\rightarrow} D^{*}$$ **Equation 2-9**

$$D^{*} \rightarrow D^{+} + e_{CB}^{-}$$

$$D^{*} + I_2 \rightarrow D^{+} + I_2^{-}\ (Oxidative)$$ **Equation 2-10**

$$D^{*} + I^{-} \rightarrow D^{-} + \frac{1}{2} I_2\ (Reductive)$$

$$D^{*} \rightarrow D\ (+h\nu)$$ **Equation 2-11**

$$\eta_{inj} = \frac{\kappa_{inj}}{\kappa_{inj} + \kappa_{rel}}$$ **Equation 2-12**

Regeneration of Sensitizer (dye): furthers the oxidized dye regenerated by the electron transfer from the redox potential of the electrolyte or hole transport mediator (HTM) after charge separation and electron injection, and then hole towards the counter electrode as shown in Equation 2-13. On the other hand, the charge carrier recombines the free electrons in the TiO$_2$ (mainly the CB) to oxidized sensitizer molecules as shown in Equation 2-14 or to the holes located on HTM competes with sensitizer reduction in Equation 2-15. In general, a high regeneration efficiency (η_{reg}) occurs when the rate constant of dye regeneration (κ_{reg}) is greater than recombination to hole carrier species (κ_{rec}), which is determined by the following Equation 2-16 in similar manner to (η_{inj}).

$$HTM + D^{+} \rightarrow HTM^{+} + D\ (Solid\ State)$$

Equation 2-13

$$2D^{+} + 3I^{-} \rightarrow 2D + \frac{I_3^{-}}{I_3^{-}} + 2e^{-} \rightarrow 3I^{-}$$

$$D^{+} + e_{CB}^{-} \rightarrow D$$ **Equation 2-14**

$$HTM^{+} + e_{CB}^{-} \rightarrow HTM$$ **Equation 2-15**

$$\eta_{reg} = \frac{\kappa_{reg}}{\kappa_{reg} + \kappa_{rec}}$$ **Equation 2-16**

Charge Transport: unlike in the conventional p-n junctions, the injected electrons in the TiO_2 CB (e^-_{CB}), are transported through the mesoporous TiO_2 electrode (current collecting photo anode) by diffusion controlled process rather than drift current. However, in a DSPS (which is liquid electrolyte) the two pathways of recombination free electrons to either the oxidized sensitizer molecules which means the oxidized redox active species formed following sensitizer regeneration diffuse to the counter electrode (photo cathode) where it is reduced, or the hole carrier of HTMs competes with the electron transport. The kinetic rate constant of the electron recombination (κ_{rec}) must be smaller than that of the diffusion through TiO_2 (κ_{trans}) which otherwise leads to loss of photo-generated charge in order to successfully collect the separated charge carriers with a favorable charge collection efficiency (η_{cc}), (Equation 2-17) to provide the electrical power in external circuit (Hagfeldt et al., 2010; Yang, 2014). Thus, the kinetic competition between the initial photo-induced charge separation processes and the loss mechanisms govern the photon-to-current conversion efficiency of the photo sensitizer device.

$$\eta_{cc} = \frac{\kappa_{trans}}{\kappa_{trans} + \kappa_{rec}}$$ **Equation 2-17**

The red dashed arrows in Figure 2.7 (above) represent the following loss channels (Dualeh, 2014):

- **Excited State Deactivation (a), the radiative or non-radiative relaxation of the photo-excited dye back to its initial ground state is a possible loss mechanism instead of the electron injection into the TiO_2 CB. However, this process is typically considerably slower than the electron injection, ensuring quantitative charge separation.**
- **Back Electron Transfer (b), the recombination pathway of this loss channel is in indirect competition with the hole injection into the**

electrolyte (or HTM) which involves the recombination of electrons in the TiO_2 CB with oxidized dye, and its magnitude is ten order times slower than electron injection (Marchioro, 2014).

- **Hole-Electron Recombination (c), charge (electrons) can recombine from TiO_2 CB (c-i) and/or ITO (c-ii) with holes of accepters in the electrolyte (or HTM) which is normally referred to as the electron lifetime. In addition to process (b) these loss mechanisms typically occur on a similar time scale as the electron transport in the TiO_2 in which the lifetimes observed with the I^-/I_3^- are very long (1-20 ms) (Hagfeldt et al., 2010). Thus to achieve high sensitive device this recombination process needs to be slower than the charge transport. Commonly, surface treatment of the TiO_2 surface in particular and molecular engineering of the dye sensitizer are used to modify the kinetic of the charge transfer reactions (Dualeh, 2014).**

A number of interconnected nanoparticles are comprised of mesoporous TiO_2 electrode with relatively small diameters, usually the range within 20-25 nm and n-doped, with a low density of doping about $10^{17}\ \text{cm}^{-3}$ (Boschloo, Goossens, & Schoonman, 1997). Unlike the p-n junctions, with the absence of internal electric field in such a network composed by nanoparticles surrounded by ions in the liquid electrolyte, it is observed that the band bending is neglected (O'Regan, Moser, Anderson, & Graetzel, 1990). Instead, for the electron transport, a concentration gradient of the injected electrons in the photo anode (TiO_2 electrode) appears to be the major driving force by diffusion towards the ITO substrate through the mesoporous network (Södergren, Hagfeldt, Olsson, & Lindquist, 1994; Solbrand et al., 1997; Yang, 2014). In the band gap of TiO_2 electrode of the DSPS, the variation in the electron diffusion coefficient with the photon irradiation intensity controlled by a trapping-detrapping mechanism due to the electronic transport depends on the density of the trap states (Bisquert & Zaban, 2003).

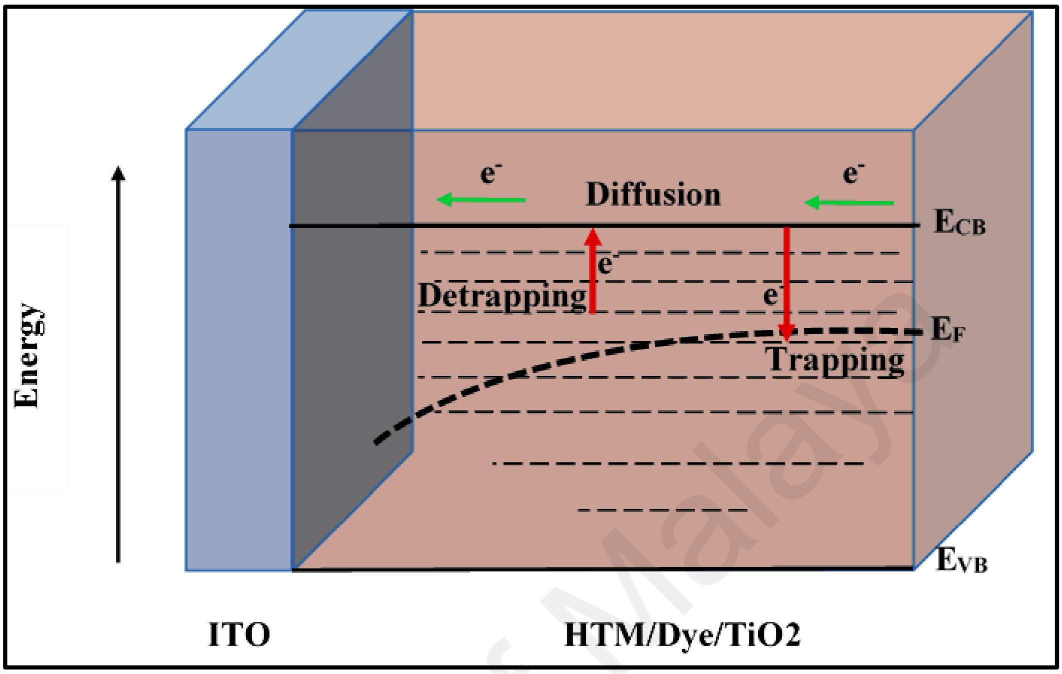

Figure 2.8: The electron transport schematic diagram by diffusion with concentration gradient in the mesoporous TiO_2 electrode as driving force. The electron transport is described by the trapping-detrapping mechanism where the injected free electrons might be trapped in the band gap states of the semiconductor and the electron transport continues when the trapped electrons are thermally detrapped back into the conduction band of the semiconductor electrode (Yang, 2014).

Between the valence band (VB) and the CB certain localized energies are states of the TiO_2 semiconductor, which are termed as states of band gap as shown in Figure 2.8 (above). The electron transport process begins when photon induces the free electrons from VB into CB of TiO_2. The gradient distribution of electron concentration declines along the mesoporous TiO_2 to its lowest value in the ITO due to the extraction of electrons from ITO substrate side at working conditions. A relatively small driving force leads the free electrons before they are trapped in the band gap states to travel along certain distance by the absence of internal electric field. By thermal effect the trapped electrons can be detrapped back into the diffusion transport towards the ITO substrate. Once the free electrons are collected after they encounter a series of trapping-detrapping processes at the conducting electrode, the photocurrent in the external circuit is detected (Nelson, 1999; Yang, 2014).

In Equation 2-18, (D_n) is defined as the chemical diffusion coefficient which is approximately independent of position (homogenous Fermi level) and commonly used to characterize the electron diffusion process, where the D_0 and n_c designate the diffusion coefficient and the concentration of the free electrons in the TiO_2 conduction band respectively while the n_L denotes the concentration of trapped electrons (Bisquert & Vikhrenko, 2004).

$$D_n = \frac{D_0}{\left(1 + \frac{\partial n_L}{\partial n_c}\right)}$$ **Equation 2-18**

The D_n can be regarded as an effective electron diffusion coefficient, which is illumination light intensity dependent due to the contribution from the dynamic equilibrium between the free electrons in TiO_2 CB and the trapped electrons in band gap states (Yang, 2014).

According to Equation 2-18, since D_n approaches its maximum in the vicinity of D_0, higher concentration of free electrons in TiO_2 CB advances the diffusion of electron transport while the probability of electron recombination to hole carrying species becomes unfavorably higher as well. Consequently, a compromise needs to be considered between the longer electron life time τ_n and the faster electron diffusion. Equation 2-19 represents the time constant for the decay which describes how fast the recombination process occurs. Due to the equilibrium between trapped and free electrons, the dependence of τ_n on intensity of light applies as well as the D_n (Bisquert & Vikhrenko, 2004; Yang, 2014).

$$\tau_n = \left(1 + \frac{\partial n_L}{\partial n_c}\right).\tau_0$$ **Equation 2-19**

The case of $\frac{\partial n_L}{\partial n_c}$ >> 1 results in a higher probability of recombination with greater κ_{rec}, in which trapping and detrapping governs the response time, where the lifetime effective electron becomes shorter and shorter to its minimum in the vicinity of the constant free electron lifetime τ_0. On the other hand, the electron diffusion length (L_D) defined in Equation 2-20 to characterize the equilibrium between electron lifetime and diffusion coefficient by kinetic measurements provide τ_n and D_n which is commonly used to describe how far an electron can diffuse before recombination occurs on average through the TiO_2 mesoporous electrode (Bisquert & Vikhrenko, 2004; Yang, 2014).

$$L_D = \sqrt{D_n \tau_n}$$ **Equation 2-20**

In general, the charge carrier transporting materials can be done in three different ways to be perform charge transport such as the hole transport (positive charge carrier), electron transport (negative charge carrier) and ambipolar charge (transport of both charge carriers simultaneously. Equation 2-21 represents the conductivity of the ambipolar charge transporting materials which is used to characterize how fast the electric current can be conducted through the conducting materials.

$$\sigma = e\mu_p c_p + e\mu_n c_n$$ **Equation 2-21**

where *e* is elementary charge, μ and *c* are the mobility (how fast the charge carrier can be transported) and concentrations of two charge carriers in these materials respectively. The *p* designates holes while the *n* denotes electrons (Bisquert & Vikhrenko, 2004; Yang, 2014).

2.3 Excitons

An exciton is a bound state of an electron and hole which are attracted to each other by the electrostatic Coulomb force generated by absorption of photons. Compared to organic materials, inorganic materials have different excited state characteristics due to their larger dielectric constant. The type of exciton affects the photo-physics of the systems. Exciton can be transferred to a neighboring molecule providing an energy transport by migration. In inorganic materials, an exciton can be delocalized in case of strong intermolecular interactions in which a large dielectric constant ($\varepsilon \approx 12$) causes effective screening of the Columbic interaction between electron and hole, called Wannier excitons as present in highly crystalline semiconductors. These generated excitons are weakly bound with a binding energy of about 0.015 eV, and larger exciton radius (≤ 100 Å) than lattice distance. Their binding energy is comparable to k_bT thus free charge can be generated from these excitons as shown in Figure 2.9 (Tress, 2014; Wannier, 1937).

In organic materials, the exciton called Frenkel exciton is mainly located on one (small) molecule or chromophore (conjugated segment of a polymer) having a relatively small radius of less than 10 Å and a smaller dielectric permittivity ($\varepsilon \approx 4$) due to the stronger Columbic interaction. It can also be treated as an electrically neutral quasi-particle with polaronic nature. Such a Frenkel exciton can be regarded as a tightly bound electron-hole pair with the exciton binding energy of 0.2-1.4 eV as difference between its energy and the internal energy of a completely separated electron-hole pair as shown in Figure 2.9.

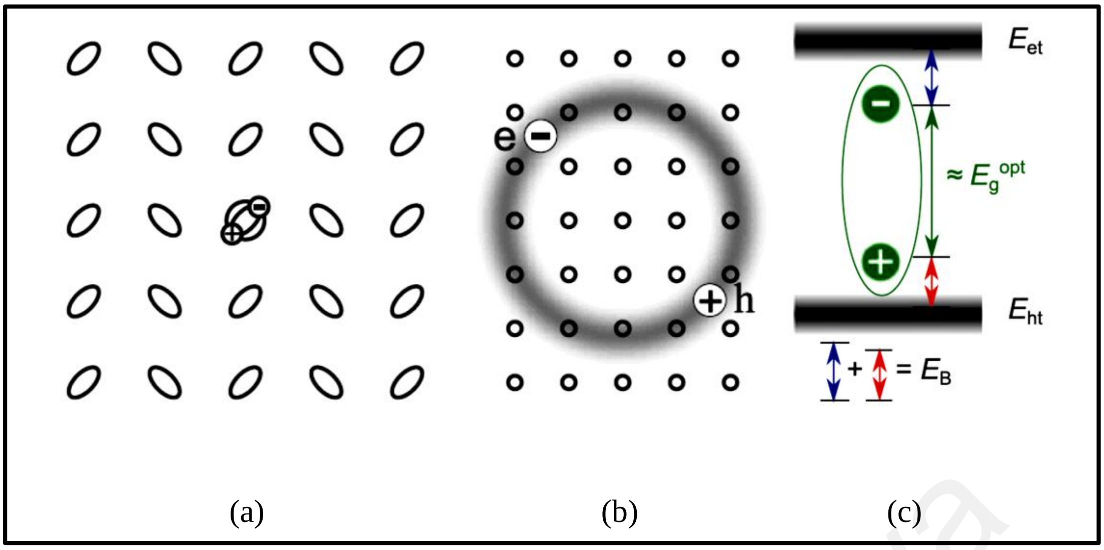

Figure 2.9: The difference of exciton radii due to the different dielectric permittivity of the material. (a) Frenkel exciton bound electron-hole pair where the hole is localized at a position in the crystal. (b) Wannier exciton bound electron-hole pair is not localized at a crystal position, but across the lattice (Schwoerer & Wolf, 2008) (c) Visualization of an exciton as excited state with exciton binding energy E_b in a potential diagram for one electron (Tress, 2014).

Charge separation takes place at the interface via photo-induced electron injection from the dye into the conduction band of the TiO_2, which can provide energy steps between electronic states.

2.4 Photo Sensor

The term sensor originates from the word sense, which means to observe the properties or presence of things. Thus, any device that responds or detects chemical or physical stimulus is called a sensor, i.e. a device with an electrical signal output converted via a chemical or physical quantity (Addington & Schodek, 2005; Shah, 2010). Therefore, photo sensor may be defined as an electronic component that detects the presence of visible light, transmission of infra-red (IR), and/or energy of ultra-violet (UV) (Rouse, 2005). In the fabrication of sensors organic semiconductor materials are employed while most photo sensors consist of inorganic semiconductor which have a photo-conductivity property in which the radiation intensity when striking these materials is able to vary their electrical conductance (Rouse, 2005; Shah, 2010). The properties of organic materials in organic photo sensors (OPSs) change with the interaction of temperature, pressure, gasses, humidity, visible light, electromagnetic waves, chemical, biological, mechanical displacement, radioactive radiation, etc. (Shah, 2010). There are several advantages that organic semiconductor sensors have over others such as higher absorption coefficient, simple technology, lower cost on large-scale production, higher degree of sensitivity with external agents, higher selectivity, greater electronic tenability, flexibility and chemically functionalized (Saleem, Sayyad, Karimov, Yaseen, & Ali, 2009; Sayyad et al., 2008; Shah, 2010; Zubair, 2011).

Photo-diode, bipolar photo-transistor and photo sensitive field effect transistor (photo FET) are the most common types of photo sensors. The transparent windows of these device packages (electrodes) is distinguished with normal diode, bipolar transistor and field effect transistor, in which light radiant energy easily penetrates and reaches the junction layers between the semiconductor materials inside (Rouse, 2005). Another type of photo sensor is dye sensitized photo sensor (DSPS) (Karwan et al., 2015; Karwan et al., 2014) which is essentially the same as the DSSC (have already mentioned and discussed before in detail), except that is used to detect visible light only. This advantage opened the gate that many organic semiconductor materials can be applicable and used as dye sensitizer without high efficiency requirement.

2.5 Importance Sensing Parameters

Few noteworthy sensing parameters of the photo sensor are as follows:

2.5.1 Responsivity

The responsivity (*R*) is a meritorious figure for photo sensor and it is defined as the ratio of output photocurrent density (with expression of mA/cm^2) to the incident optical (light) power (with expression of W/cm^2). It is expressed as in Equation 2-22 (Webster & Eren, 2014; Xie, 2013):

$$R = \frac{J_{ph}}{P_{in}}$$ **Equation 2-22**

where, J_{ph} is the photocurrent density of the photo sensor by the absorption of incident light, and P_{in} is the measured incident light power. Responsivity of a photo sensor gives an inkling how effectively a photo sensor can convert incident light into current output. Typically, the responsivity of the photo sensor varies with the wavelength of the incident light, magnitude of the applied bias and the temperature of the surrounding (Zafar, 2015).

2.5.2 Response-Recovery Time

Dynamic response of the photo sensor is the time taken by the photo sensor's output signal to reach from 10% to 90% of its amplitude (response time) and to drop from 90% to 10% (recovery time) in response to a stepped light input signal. An ideal photo sensor should be fast enough to follow the input optical signal. The recovery times of the photo sensor in particular are strongly dependent on the applied bias voltage. The charge carriers are swept out of the device at increasing speed with an increasing electric field (Valouch et al., 2007; Zafar, 2015).

2.6 Part Two: Bulk Heterojunction Solar Cell

The major motivation of using organic solar cells is based on bulk heterojunction (BHJ). The sun is the largest energy source which provides more than sufficient clean energy and with the high efficient inorganic solar cells technology running into cost bottlenecks. Solution processable bulk heterojunction solar cell is one of the third generation of organic photovoltaics technologies that includes polymer or small molecular organic solar cell. The low cost production, light weight, high throughput manufacture processes, portable and wide selection of functional materials gained serious attraction in recent decades. Another advantage of the packaging of organic solar cells by lamination technologies makes organic solar cells a viable contender in the commercialization. However, from the first report of a new design solution bulk heterojunction solar cell in 1995 by Cambridge and UCSB until 2000 the best efficiency reported barely reached greater than 1%, and today efficiencies are achieved beyond 10%. However, the state-of-the-art efficiency of inorganic solar concentrator cell is beyond 45% which means the organic solar cell still a long way go to compete (Green, Emery, Hishikawa, Warta, & Dunlop, 2015; Halls et al., 1995; Kim et al., 2006; Liang et al., 2010; Scharber et al., 2006; Yu, Gao, Hummelen, Wudl, & Heeger, 1995).

The general structure of the first approach BHJ cells is similar to the organic light emitting diodes (OLED). Figure 2.10 illustrates a single layer semiconductor solar cell and three types of bulk heterojunction cells. The heart of BHJ cells is the photoactive layer which contained at least two organic compounds. One of the materials is called electron donor which had strong affinity for holes and the other an electron acceptor for electrons. These donor and acceptor materials (layer of photoactive blend) in all types of solar cells are confined in between a pair of different conducting electrodes (cathode and anode). Typically, a metal with low work function such as Al, Mg or Ca is used as cathode and glass or any flexible transparent substrate (as polyethylene terephthalate (PET)) coated Indium Tin Oxide (ITO) is used as anode. Moreover, buffer layers are mostly in between both interfaces of anode and cathode of typical BHJ device structures. These additional layers (buffer layers) are considered as obligatory and have an important role in achieving highly efficient solar cell because it serves as charge collection and transport layer. The thickness of buffer layers and electrodes are typically 50-100 nm while photoactive blend layer is 100-200 nm (Nelson, 2011). With the concept of bulk heterojunction, the efficiency of solar cell improved because the interfacial area heavily increases at almost 10 nm scale length between phase of donor and acceptor. Thus, the highly efficient dissociation of the photo-generated electron-hole pairs (excitons) to free charge carriers between the acceptor and donor material are the essential and fundamental electronic interactions of the BHJ architecture.

Light absorption and generating electron-hole pairs (excitons) are the major role of donor materials which are localized on a single segment within a (few nm^3) volume, as it is distinguished from inorganic cells (Nelson, 2011). On the other hand, organic semiconductor phases in solar cell have low dielectric permittivity constant (typically $\varepsilon = 3 - 4$) and the electronic interactions are weak and non-covalent between organic molecules. Photo-generated excitons have strong coulombic force bound ($0.2 - 1.4$ eV) (Dang, Hirsch, Wantz, & Wuest, 2013). Thus, the energy band gap (E_g) is insufficient between the HOMO and LUMO of the electron donor molecule to break up the coulombic force of excitons as shown in Figure 2.11. For this issue, exciton dissociating into free carrier charges and electron pathways creation is the responsibility by an acceptor material by the deference of free energy. Because of the potential field (V_b) of interface arising from the offset energy level between the LUMO of electron acceptor molecule and the HOMO of electron donor molecule, split excitons after the excitons diffuse to the donor/acceptor interface. Subsequently, to complete the circuit, free electrons and holes by hopping process transport to the respective electrodes governed by the electric field between electrodes. The four steps to complete process of photocurrent generation are illustrated in detail in Figure 2.12.

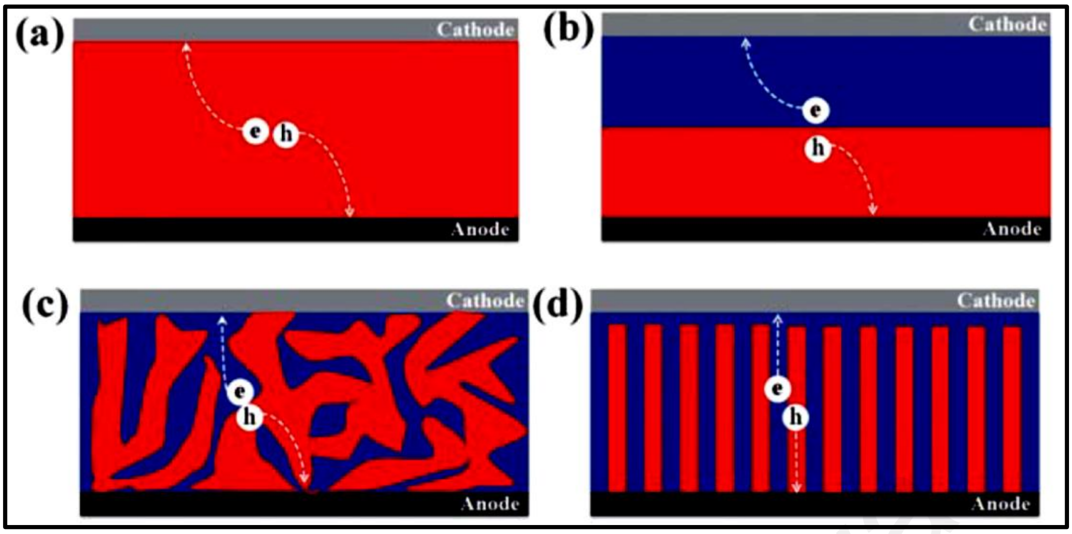

Figure 2.10: General schematic device architecture of four types of organic solar cells. The red and blue domains appear as a phase of electron donor and electron acceptor respectively. (a) A single layer semiconductor which has greatly low efficiency because the electrodes arise too weak of electric field from the different work functions which cannot overcome the strong tendency for recombination between electrons and holes (b) bilayer is the first bulk heterojunction in which the transformation of photo-induced electron occurs in planar interfaces between two semiconductors from a donor to acceptor, so there should be a thin active layer in order to utilize all excitons. Thus, the bilayer has limited performance due to the occurance of dissociation excitons prior to recombination only near interface. The transformation of photo-induced electron have more opportunities to occur due to the extended interface and interpenetrate network semiconductors through the film, i.e. each interface is within an exciton diffusion length distance (~ 10 nm) from the site of absorbing, thus all excitons can separate. This is achieved in a (c) bulk heterojunction or (d) ordered bulk heterojunction (He, Qiu, & Lin, 2011; Liu, Gu, Jung, Jo, & Russell, 2012).

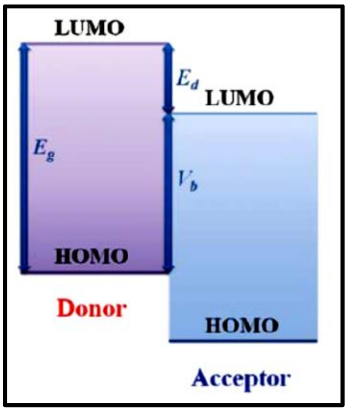

Figure 2.11: Architecture of the energy levels of the HOMO and LUMO of donor and acceptor molecules, where E_g and E_d represent the donor molecule band gap and the energy level offset of LUMO between donor and acceptor molecules, V_b shows the potential field interface arising between the LUMO of acceptor molecules and HOMO of donor molecules from the energy offset (He et al., 2011).

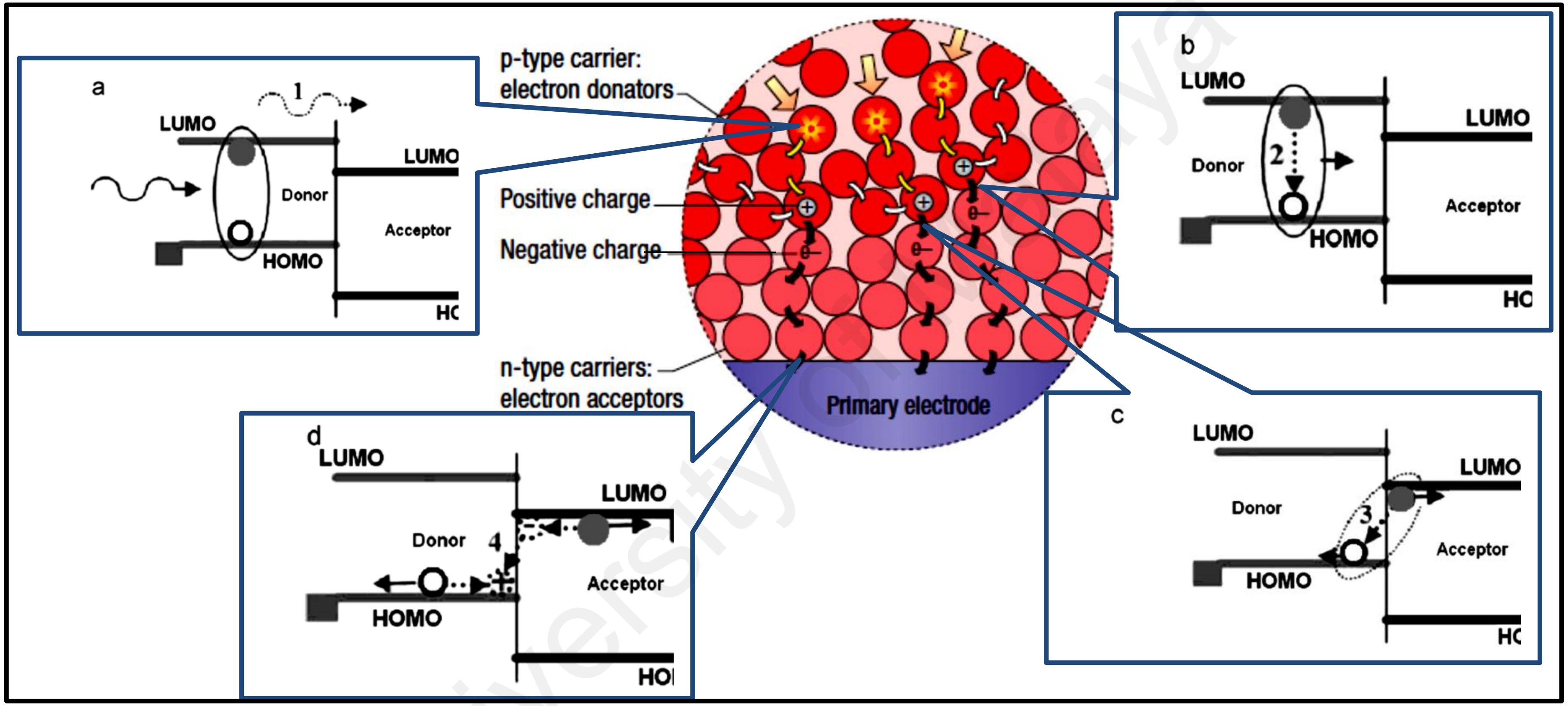

Figure 2.12: Simplified schematic mechanism from light absorption to extraction of charges (photocurrent), charge transfer and then transport in a structure of bulk heterojunction solar cell. (a) In the donor material, exciton generate by photon absorption. (b) Diffusion of exciton to the donor-acceptor interface. (c) Generation free charge carrier from exciton dissociation, by transferring generates current (an electron) to the acceptor due to material disorder of donor with acceptor and electric field. (d) The charge carriers transport to the electrodes (electrons to cathode and holes to anode) to provide photocurrent. The loss mechanisms are shown in each step as; 1/ step (a), when photons are non-absorbed. 2/ Decay excitons in step (b). 3/ In step (c), the bound pair geminate recombination. 4/ In step (d), bimolecular recombination (Gaudiana & Brabec, 2008; Yeh & Yeh, 2013).

2.6.1 Relationships between Morphology and Device Performance

To enhance power conversion efficiency, a large number of published studies have been conducted on optoelectronic properties through effective designing and adjusting of molecular structures to optimize broad absorption of the visible light spectrum, HOMO and LUMO levels. For rational performance improvement a prerequisite and more common study is on the blend structure morphologies with photovoltaic performance relationship (Chen et al., 2009b; Henson, Müllen, & Bazan, 2012; Huang, Kramer, Heeger, & Bazan, 2014; Huang, Zhang, et al., 2012; Mishra & Bäuerle, 2012).

As mentioned in previous section, the thoroughly blended BHJ concept has been developed because when the light is absorbed in molecular semiconductors free electrons and holes cannot be created directly due to strong binding energy of excitons which is simply mixing donor and acceptor materials under appropriate conditions to yield high photocurrent due to efficient exciton dissociation between the interface of the domains. Exciton dissociation is enhanced when the donor and acceptor are finely intermixed, but due to a low density in percolation system of conduction pathways, the charge transport will be strongly inhibited. Exciton recombination also increased with the finely intermixed HJs, which decreases the overall device efficiency (Dang et al., 2013). On the other hand, the charge collection at the electrodes will enhance with the complete separation of the D and A as in structure of a bilayer, while exciton dissociation decrease. So the difficult challenge is the control of active layer morphology in order to maximize efficiency of organic solar cells, which is essential to govern the physics of the photovoltaic processes. It is also required to understand phase separation of active layer materials with access to architecture of new polymers (Brabec et al., 2011; Dang et al., 2013).

There are two main methods to control and modify the morphology of active layers depending on the architecture and application, which are physical and chemical methods in order to enhance the device performance. Physical methods are classified into five methods which are solvent additives or changing solvents, solvent annealing, thermal annealing and post-annealing, polar solvent effect, and ratio of donor:acceptor. Whereas, there are three main types of chemical modifications of polymer functional groups which are main chain, side chain and molecular weight (Huang et al., 2014). Moreover, the morphology of organic thin films can be modified by the conditions during processing which are spin coating, thermal evaporation, and other treatments of post-deposition as treatment of polar solvent, a conjugated insertion polyelectrolyte between the electrode and active layer as an interlayer (Huang et al., 2014; Krebs, 2008).

2.6.1.1 Solvent Choice, Solvent Additives and Solvent Annealing (Slow Growth)

In various ways, the morphology of the active layer is strongly dependent on the choice of solvent which can be significant because each solvent has a specific evaporation rate which depends on the nature of the solvent during the method of thin film deposition. The first study performed on morphology has been done by (Yang & Heeger, 1996) in OPV which they used poly(1,4-phenylene vinylene) based polymers. For conjugated polymer of poly(2-methoxy-5-(3’,7’-dimethyloctyloxy)-p-phenylene vinylene) (MDMO-PPV) with methanofullerene (PCBM), Shaheen et al. obtained high efficiency at the early research stages of OPV due to modification of the molecular morphology. The active layer composite allowed for a thorough mixture increasing the interaction degree between chains with the only change from Toluene to Chlorobenzene solvent which result in increased current density and efficiency from approximately 2.33 mA/cm^2, 0.9% to 5.25 mA/cm^2, 2.5% respectively (Brabec et al., 2010; Liu, F. et al., 2012; Wienk et al., 2003). During the process of solution deposition, the efficiency of the device significantly increases by solvent additives. Peet J. et al. investigated an improvement of the morphology of thin film by a small addition of octanedithiol (ODT) into the solution of polymer [2,6-(4,4-bis(2-ethylhexyl)-4H-cyclopenta[2,1-b;3,4-b']dithiophene)-alt-4,7-(2,1,3-benzothiadiazole)] (PCPDTBT) which significantly increases the efficiency of the device from (2.8 to 5.5)% (Huang et al., 2014; Peet et al., 2007; Peet et al., 2006). In inverted structure bulk heterojunction solar cell using two different fullerene ($PC_{70}BM$ and $PC_{60}BM$) in poly[2-octyldodecyloxy-benzo[1,2-b;3,4-b]dithiophene-alt-5,6-bis(dodecyloxy)-4,7-di(thieno[3,2-b]thiophene-2-yl)-benzo[c][1,2,5]thiadiazole] (PBDT-TBT-alkoBT), Khatiwada et al. investigated that after addition of additive 1,8-diiodooctane (DIO), the charge transport has been improved which leads to increase efficiency of device overall. This is due to change in the intermixed granular to fibrous morphology because the solubility of fullerene increased ($PC_{70}BM$ higher than $PC_{60}BM$) and polymer solubility reduced in chloroform as the solvent. The finer phase separation between fullerenes and polymer are related to the fibrous morphology which have been controlled to improve the performance of devices (Khatiwada et al., 2015).

In solvent annealing, the prepared active layer films (after spin coating) are left for relatively long periods in a partially closed volume (glass petri dish) with solvent drops or their vapors. In this slow approach of the structural evolution process, the solvent is slowly evaporated which is another effective method to crystalize the blend components and modify the phase separation and alter the morphology of the active layer's OSC device (Dang et al., 2013; Huang et al., 2014; Yam, 2010). Solvent annealing study generally focusing on the type of solvent, time of solvent drying, crystallinity and phase evolution (Bull, T. A., L. S. Pingree, S. A. Jenekhe, D. S. Ginger, & C. K. Luscombe, 2009; Hegde et al., 2012; Huang et al., 2014; Li et al., 2007; Liu et al., 2009; Lu, Li, & Yang, 2007). With combining the processing of the addition of DIO as chemical additive and solvent annealing treatment with THF vapors at room temperature, Kumar et al. reported the improvement of morphological features of ($VC89:PC_{71}BM$) BHJ OSC which leads to increase the efficiency from 4.63% to 6.66% which is the best value for small molecule. This enhancement is because the increase in crystallite size of donor and crystalline volume of the active layer which is linked with better charge transport. Moreover, the improvement of the phase segregation of the active layer is also linked with larger light absorption which leads to more charge generation and efficient charge collection (Kumar et al., 2015).

2.6.1.2 Thermal Annealing (Pre-Annealing) and Post-Annealing

Controlled surface morphology and thermal and solvent treatments are important techniques in order to optimize the major photovoltaic parameters such as open circuit voltage, short circuit current and fill factor. Thermal annealing is one of the simplest ways to improve the active layer morphology and can significantly improve the properties and structure of materials (Wang et al., 2005) thus improving the performance of BHJ OSC. The first successful application of thermal annealing treatment was reported by Dittmer et al. in the P3HT blended with the molecular perylene tetracarboxyl diimide (EP-PTC:P3HT) system. After performed annealing at 80 ℃ for 1 hour under nitrogen condition, the EQE of the device enhanced the entire wavelength due to increased hole mobility which is linked to increase crystallinity of electron donor component, since it is known the process of slow crystallization of P3HT occurs above 32 ℃ (Dittmer, Marseglia, & Friend, 2000; Zhao, Yuan, Roche, & Leclerc, 1995). Then, Padinger et al., successfully increased the efficiency of P3HT:$PC_{61}BM$ OSC up to 3.5% by thermal annealing active layer. Thermal treatment assisted to embed some of the molecules of $PC_{61}BM$ into region of P3HT due to recrystallization of the P3HT to bigger fibrillar crystals which forms greater aggregation of fullerene and more diffusion (Brabec et al., 2010; Erb et al., 2005; Huang et al., 2014; Padinger et al., 2003; Yang et al., 2005). Kim et al. also reported that the annealing effect on the morphology of the P3HT:PCBM film and electronic properties. Their investigation exhibits that the annealing step not only leads to more efficient charge transport and charge collection at the electrodes but it can also contribute a slight increment in the absorption intensity (Kim, So, & Moon, 2007). In the P3HT:PCBM blend, the most effective strategy toward constructing the nanoscale donor-acceptor percolated networks with well-optimized morphology is the application of annealing treatment at high temperature. However, in contrast, devices based on the new generation donor materials such as PCDTBT, are better performed without the post thermal annealing step. For instance, Zhao et al. (Zhao et al., 2013) reported that the topography of the PCDTBT:$PC_{71}BM$ blended films become rougher with increased root mean square roughness as the annealing temperature is above 60 ℃ and the more efficient PCDTBT:$PC_{71}BM$ solar cell can be realized without any thermal annealing treatment.

All above mentioned processes have applied thermal annealing before cathode deposition (electrode evaporation) known as (pre-annealing), while post-annealing is applied after the devices are completed (cathode deposition) (Li, Shrotriya, Yao, & Yang, 2005; Ma, Yang, Gong, Lee, & Heeger, 2005). Ma et al. demonstrated that the current density and fill factor (FF) of the P3HT:PCBM blends system increase by post-annealing treatment (Ma et al., 2005). Strong enhancement of the efficiency (a tenfold increase) by the important single factor of increment in the hole mobility was investigated by Mihailetchi et al. They have analyzed the photocurrent generation and charge transport by the effect of post-annealing in BHJ of P3HT:PCMB blends. The hole mobility in the P3HT phase increases dramatically more than three times compared with the non-annealed cells due to improvement of the films crystallinity for four min at optimum 110 ℃ (Mihailetchi, Xie, de Boer, Koster, & Blom, 2006). Loos et al. infer that the key to obtaining high performance cells are the thin and long fibrillar crystals of P3HT in PCBM layer which is a homogeneous nanocrystalline obtained by studying morphology of spin coated and post-annealed photoactive layer. This is linked to controlling de-mixing degree and charge transport observed in their devices (Yang et al., 2005).

In this work, focus is given on the effect of pre-thermal annealing of the morphology of donor-acceptor (active layer) materials. It is demonstrated that the features of surface morphology and photovoltaic properties of the PBTTT-C_{12}:$PC_{71}BM$ films significantly improved due to reduced surface unevenness which leads to increase the efficiency (see CHAPTER 6:) (Qadir, Ahmad, & Sulaiman, 2015). Section (2.6.1.2.1) explains the relationship between surface roughness and thermal annealing in detail.

2.6.1.2.1 Thermal effect and Surface Roughness

The study and knowledge of the various surface morphology and textures which includes roughness, waviness, flaws and lay at the atomic and nano-metric resolution are important for electronic, engineering and application of devices, which make it possible to probe the surface of thin films and mechanical manufacturing (Kumar & Rao, 2012; Seah, 2014). To determine the surface roughness, the best instrument that provides a profile closer to the true values is atomic force microscope (AFM). This is because in many cases both the lateral and height resolution of surface roughness are in nano and atomic scale. Thus AFM showing the observation and evaluations of the films morphology and texture precisely. However, for more required measurement it is still not clear how close the results are to real surface (Kumar & Rao, 2012; Seah, 2014). The magnetic, electrical, mechanical, optical and surface properties of thin films are depending on the porosity, average size, roughness and distribution of particle size which dramatically influence the performance of OSC devices (Kumar & Rao, 2012). There is a relative relationship between surface roughness and condition of annealing treatment. This means that the roughness is increased or decreased with annealing treatment depending on the properties of the materials that have been used for the donor and acceptor layer.

Stephen and co-workers (Wei et al., 2010) converted amorphous squaraine (SQ) donor thin film to polycrystalline by post-annealing treatment. They showed the influence of crystallinity and morphology improve the performance of SQ/C_{60} device controlled by thermal annealing. The thermal treatment increases the surface roughness of SQ (2 factor) which leads to increase the diffusion length of exciton, exciton dissociation efficiency, better pathways of hole transport, increased FF and efficiency at 110 ℃. The correlation between electric properties, nanoscale structural of BHJ solar cells with the annealing process was reported by Wang and co-authors (Li et al., 2014). Thermal annealing effects the phase separation, increases the surface roughness slowly and then abruptly leads to dramatic improvement of device performance (PCE) from 1.3% to 4.6% due to stacking the aggregation of PCBM and crystalline P3HT for interpenetrated network.

Park et al. investigated the ZnO:Al surface roughness film and crystal structural changes with the effect of post-annealing samples for 60 min at 300 ℃. Post-annealing effectively decreased the value of roughness (0.924 nm) of ZnO:Al films. Smoother surfaces lead to improvement of the interfacial properties between the donor-acceptor materials and TCO films which is linked to the performance increment in organic electronic devices (Choi, Kang, & Park, 2013). In this thesis, it has been demonstrated that the annealing treatment effects the surface morphology of the PBTTT-C_{12}:PC_{71}BM thin films. The AFM map shows that the surface roughness of thin films decreases with increasing annealing temperature, smoother annealed films improve the devices efficiency from 1.85% to 2.48%.

On the other hand, thermal treatment of devices are not applicable and show poorer performance especially in flexible substrates such as poly(ethylene terephthalate) because PET has a low glass transition temperature (Al-Ibrahim, Roth, Zhokhavets, Gobsch, & Sensfuss, 2005; Dennler et al., 2006; Padinger et al., 2003; Spanggaard & Krebs, 2004).

Then, the technique of thermal annealing free for that reason has been proposed by Berson et al. They used the blend of P3HT nanofiber and PCBM active layer to optimize device performance and demonstrated 3.6% efficiency. At high to room temperature slowly cooling P3HT nanofiber has been formatted by dissolving completely in p-xylene in solution with high concentration and the stability of P3HT:PCBM nanostructure remained for several weeks (Berson, De Bettignies, Bailly, & Guillerez, 2007; Perepichka & Perepichka, 2009).

2.6.1.3 Ratio of Donor-acceptor

The morphology of active layer and device performance strongly depend on the donor-acceptor ratio, and in addition to being more efficient, a careful choice ratio of donor and acceptor results in more durable BHJ OSC (Cardinaletti et al., 2014; Huang et al., 2014). Performance and morphology in BHJ blends can be affected by the donor-acceptor ratio which influences the crystalline order, the size and phase distribution, phase separation, leading to changes in transport of charge carrier and the number of interfaces for dissociation of exciton. (Hau et al., 2010; Huang et al., 2014). Moreover, the lower performance of devices and lower organic material mobility's are due to higher probability of charge carrier recombination and low probability of exciton dissociation which is linked to reduce interfaces of donor and acceptor (Hau et al., 2010).

To better understand the effect of D:A ratios, Bazan and co-authors (Huang et al., 2014) list many reports that have been done in the range of 7:3 to 1:4 according to the choice of materials employed. This ranges is required in order to form optimal ratio of donor and acceptor, maximum interfacial area with bicontinuous percolation pathways (Chen et al., 2012; Huang, Guo, et al., 2012; Huang et al., 2011; Huang, Zhang, et al., 2012; Li, Shrotriya, Huang, et al., 2005; Peet et al., 2007; Shaheen et al., 2001; Sun et al., 2012; Wang, E. et al., 2010; Zhang, Y. et al., 2011). Serdar and co-authors (Shaheen et al., 2001) reported the optimum ratio (1:4) of the MDMO-PPV:$PC_{61}BM$ (D:A) system to mix well fullerene with amorphous polymers.

In nanostructures the attempt to find understanding of the molecular order studying PBTTT is very useful which has attracted the attention of many researchers for BHJ OSC due to its high mobility of charge carrier. Researchers have used PBTTT in blend system with 1:4 with efficiency 2.35%, while in 1:1 blends efficiency 0.16% has been achieved (Chabinyc, Toney, Kline, McCulloch, & Heeney, 2007; Kline et al., 2007; McCulloch et al., 2006; Parmer et al., 2008b). Very good intercalation of fullerenes into the amorphous and semi-crystalline polymer has been achieved near 1:4 of PBTTT:$PC_{71}BM$ by (Mayer et al., 2009). In this work, a ratio of 1:4 was used which was an optimum ratio of PBTTT-C_{12}:$PC_{71}BM$ system as an active layer of BHJ OSC, thus the device demonstrated the superior performance from 1.85% to 2.48% by means of thermal annealing treatment (Qadir et al., 2015).

2.6.2 Characterization Techniques

The ability to monitor the morphology in organic devices is a vital and important part of controlling morphology. There are various extensive structural characterization techniques employed for monitoring morphology in which the application determines the choice and have been developed and carried out on organic solar cells. Key tools for morphology study include X-ray scattering and various forms of electron microscopies and scanning probe microscopies, which can be listed as follows: (Huang et al., 2014; Krebs, 2008)

- **Grazing Incidence Wide-Angle X-ray Scattering (GIWAXS)**
- **Grazing Incidence Small-Angle X-ray Scattering (GISAXS)**
- **Resonant Soft X-ray Scattering (R-SoXS)**

- **Small-Angle Neutron Scattering (SANS)**
  - **Grazing Incidence Small-Angle Neutron Scattering (GISANS)**
- **Transmission Electron Microscopy (TEM)**
  a. **Energy-Filtered Transmission Electron Microscopy (EFTEM)**
  b. **Scanning Transmission Electron Microscopy (STEM)**
  c. **High Resolution Transmission Electron Microscopy (HR-TEM)**
- **Atomic Force Microscopy (AFM)**
  a. **Photoconductive Atomic Force Microscopy (pcAFM)**
  b. **Non-contact Scanning Kelvin Probe Microscopy (SKPM)**
  c. **Conducting Atomic Force Microscopy (c-AFM)**
- **Solid-State Nuclear Magnetic Resonance (NMR)**
- **Dynamic Secondary Ion Mass Spectrometry (DSIMS)**
- **Near-Edge X-ray Absorption Fine Structure (NEXAFS)**
- **Scanning Transmission X-ray Microscopy (STXM)**

Atomic Force Microscopy (AFM) has been used only in this work in order to get better profile value of surface roughness as mentioned above.

2.6.3 Open Circuit Voltage Evolution

To optimize BHJ OSC another key parameter is the open circuit voltage (V_{oc}), which is quite respectable in the production of OSCs because the determination of the OSC performance also depends on V_{oc} (Holmes, Brütting, & Adachi, 2012; Mihailetchi, Blom, Hummelen, & Rispens, 2003; Rauh, Wagenpfahl, Deibel, & Dyakonov, 2011). Thus, for understanding mechanisms of the V_{oc} generation, D:A interfaces and dissociation of exciton, controlling the semi-conductive polymer, donor and acceptor regarding energy states is critical (Brabec et al., 2011). For many common OSC devices, like P3HT or phthalocyanines with fullerenes to form D:A, the typical value of V_{oc} is around 0.5-0.6 V.

However, the V_{oc} value needs to be improved and greater than the typical value in order to get high efficiency (Fleetham, 2014). The maximum possible open circuit voltage is given in the device when the charge recombination is balanced with the charge generation due to the energetics of the D:A material system (Holmes et al., 2012). Moreover, the maximum achievable V_{oc} originates from the difference of energy between HOMO as the donor oxidation potential and LUMO as the acceptor reduction potential (Brabec et al., 2011).

It is well recognized at the junction in BHJ that charge separation occurs between the donor (absorber) and acceptor (electron transport) layer due to critical processes of exciton dissociation. Thus, the offset between the level of donor (absorber) material's HOMO and the acceptor (electron transporting) material's LUMO layer scales the V_{oc}. In this regard, the energy gap at the D:A heterojunction between the energy levels of HOMO and LUMO (ΔE_{DA}) is related to V_{oc} as suggested by numerous studies (Brabec, Christoph J et al., 2001; Brabec et al., 2011; Fleetham, 2014; Kooistra et al., 2007; Mutolo, Mayo, Rand, Forrest, & Thompson, 2006; Uhrich et al., 2008). In order to achieve higher V_{oc}, significant research efforts have been made in designing D and A materials with energy levels that increases ΔE_{DA} (Brabec, Christoph J et al., 2001; Uhrich et al., 2008). However, for some material system ΔE_{DA} can be two times greater than V_{oc}, which means the nature of the relationship between ΔE_{DA} and V_{oc} is still not resolved completely (Fleetham, 2014).

Forrest et al. demonstrated that the value of V_{oc} at organic solar cell is a function of ΔE_{DA} magnitude which depends on the materials employed (Rand, Burk, & Forrest, 2007). The latter implies that change in the morphological PCBM phase significantly effects the V_{oc} (Brabec et al., 2011). However, lower oxidation potential of the self-assembled polymer makes V_{oc} decrease in value as noted by some researchers (Camaioni, Ridolfi, Casalbore-Miceli, Possamai, & Maggini, 2002; Hiorns et al., 2006); change in the HOMO of polymer did not strongly effect the result found by other researchers (Brabec et al., 2011; Hoppe, Sariciftci, Egbe, Mühlbacher, & Koppe, 2005). Moreover, V_{oc} in each specific system of D:A material depends on various parameters such as the architecture of device (Xue, Rand, Uchida, & Forrest, 2005a, 2005b; Zheng & Xue, 2010), purity of materials (Salzman et al., 2005), incident light intensity (Xue, Uchida, Rand, & Forrest, 2004; Zheng & Xue, 2010), and temperature (Rand et al., 2007).

For the example of temperature effect, V_{oc} properties of solar cell using PBT was effected a little when annealed below glass transition T_{g1} (~ below 110 ℃), while it decreases and changes the performance above glass transition T_{g2} (~ 120-200 ℃) (Brabec et al., 2011; Hiorns et al., 2006). Other researchers studied device annealing effect for blend of P3HT and PCBM OSC, and they observed that V_{oc} decreased with annealing up to the T_{g2} vicinity (~ 170 ℃) and then again increased at temperatures between (170-200 ℃). However, the highest efficiency by annealing was achieved at 140 ℃ (Kim, Youngkyoo et al., 2005). For the case in this work, the V_{oc} of (ITO/PEDOT:PSS/PBTTT-C_{12}:PC_{71}BM/Al) OSC decreases after annealing at 50 ºC and 100 ºC and it gained back initial value after 150 ºC treatment, while the parameters are all improved at 150 ℃ compared to untreated annealing cells with record high efficiency under one sun (1.5 Air Mass (AM)) of stimulated solar illumination, then the efficiency decreased beyond 150 ℃ (Qadir et al., 2015).

2.6.4 Short Circuit Current Evolution

Short circuit current is the photo (light) generated current of OSC. This current is extracted when the load is zero (zero applied bias), where the positive and negative terminals are connected to each other (Tiwari & Dubey, 2010). The short circuit current (density) (I_{sc} and J_{sc}) heavily dependent on the charge separation efficiency, diffusion length, grain size, scaling with the area of the interface of D:A which would permit the separation process and charge carrier mobility's (Brabec et al., 2011; Machlin, 2005; Moliton & Nunzi, 2006). Moreover, I_{sc} and J_{sc} are affected by the number of absorbed photons. The affect originates from the linear relationship between incident intensity of light but as long as this is within the active layer no effects of saturation occur and if the absorption spectrum of the photoactive layer is extended to absorb wider visible spectrum, the I_{sc} can be maximized (Khan, 2011).

Less phase segregation is obtained from the blend structure that has intimate mixture (more uniform mixing) of D and A, resulting in network morphology have an importance effect on the I_{sc} of each component's morphology, which leads to increase the interaction degree between chains of conjugated polymers. In this manner I_{sc} increases because the polymeric semiconductor mobility improves (Brabec, Dyakonov, Parisi, & Sariciftci, 2013). On the other hand, the largest I_{sc} is linked with highest content of polymer in comparison varying compositions of polymer SCs (Beek, Wienk, & Janssen, 2006; Brabec et al., 2011; Chirvase, Parisi, Hummelen, & Dyakonov, 2004; de Bettignies, Leroy, Firon, & Sentein, 2005). In the case of this work, annealing makes surface morphology smoother, increasing the interpenetrating network between two domains (PBTTT-C_{12} and $PC_{71}BM$) which leads to form good contact and order structure hence contributing to the enhancement of I_{sc} (Qadir et al., 2015).

2.6.5 Fill Factor and Power Conversion Efficiency Evolution

In typical BHJ cells, the competition result between extraction of charge carriers and recombination is fill factor (FF), thus with increased mobility of charge carriers FF increases (Tress, 2014). Also, FF measures the current-voltage curve shape, and is therefore dependent on strength of space charge buildup, charge carrier recombination, series and shunt resistance. For example, a bad counter electrode leads to decrease FF because it has high inner resistance (Brabec et al., 2011; Karlsson, 2011). The slowest charge carriers limit photocurrent due to charge efficient confinement to different phases, allowing in each phase defective assembly to limit current (Brabec et al., 2011; Koster, Mihailetchi, & Blom, 2006). This parameter can be improved by annealing which is relative to the state of amorphous, as well as by morphology improvement.

For optimization of high M_w species, high temperature is required because their chains are recognized more slowly (Brabec et al., 2011; Hiorns et al., 2006). When PBT annealed below the glass transition, FF does not change while it increases above glass transition. For PHT samples, FF can be maximized below T_{g2} for samples that have low M_w (<10000) during 30 minutes of annealing, while the maxima for the species with high M_w occurs near vicinity of T_{g2}. These examples mentioned above do not measure transition temperatures but are only inferred from the literature on these samples (Brabec et al., 2011).

Fill factor decreases with several loss mechanisms (Khan, 2011; Tress, 2014):

- **High serial resistivity reducing the short circuit current while not changing the open circuit voltage, thus leading to flatten the IV curve in the fourth quadrant which reduces FF.**
- **Low parallel resistivity reduces open circuit voltage which decreases FF.**
- **Small shunt resistance obtains low FF because of leakage currents.**
- **Thick devices decrease FF due to limiting charge extraction. Then, a saturation of the FF of devices with high thickness at values larger than 25% due to effect of space charge induced by a strong imbalance in mobility's or by doping.**
- **For OPV devices, the value of FF is generally between 0.2-0.7 instead of unity due to losses caused by recombination and transport.**

A particular research goal is to reliably enhance (optimize) properties of device, maximizing power conversion efficiency. Controlled assembly and de-mixing of each phase is expected to enhance efficiency (Brabec et al., 2011). Increase in I_{sc} is most closely parallels with the efficiency evolution for samples annealed for 30 minutes. One of the reasons to enhance the efficiency of these polymer solar cells is improved contact to the electron collecting electrode and lowering the series resistance (Brabec et al., 2011; Hiorns et al., 2006; Ma et al., 2005). Finally, the performance peak for low M_w samples are below 100 ℃ then decrease while high M_w demonstrate some variability, however generally the increment occurs up to 150 ℃. Moreover, the performance degrades for all species of materials at higher temperatures. And, to clarify the relationship thermal analysis is required for all component materials BHJ OSCs (Brabec et al., 2011).

CHAPTER 3: MATERIALS AND METHODS

This chapter will give a brief overview of the materials used in fabricating bulk heterojunction (BHJ) solar cell and dye sensitized (DS) photo sensor devices. Here also shows the experimental setup and characterization techniques. Furthermore, this chapter contains basic information of prepared samples. Morphological information is gained by microscopy techniques.

3.1 Materials and Chemical

In this section a summary of properties of the employed materials in the preparation of the devices is presented. To begin the fabrication of BHJ solar cell and DS photo sensor devices, some chemicals and materials are needed to be on hand. All chemicals were reagent grade and used without further modification or purification unless otherwise noted. These include PEDOT:PSS layer, the solvents, organic materials, and glass substrates for depositing the organic films, electrodes and active layers onto them for BHJ solar cell. DS photo sensor includes organic dyes, TiO_2 as photo anode, electrolytes and (Pt or graphite) as counter electrode on glass substrate and Indium Tin Oxide (ITO) coated glass to realize the device fabrication. The analysis of these materials in their pure form is a basic need for an understanding of physical and chemical processes involving these materials. On these approaches, NiTsPc and MEH-PPV:PCPDTBT organic dyes as a sensitizer have been used in the fabrication dye sensitized photo sensors (Karwan et al., 2014) and (Karwan et al., 2015) respectively then assessed. In addition, poly[2,5-bis(3-dodecylthiophen-2-yl)thieno[3,2-*b*]thiophene] (PBTTT-C_{12}) and [6,6]-phenyl C_{71}-butyric acid methyl ester (mixture of isomers, $PC_{71}BM$) are widely used due to their structural, morphological, photophysical, optoelectronic, and thermal properties (Qadir et al., 2015).

3.1.1 Organic Dye and Polymer Materials

NiTsPc, PCPDTBT and MEH-PPV purchased from Sigma Aldrich and PBTTT-C_{12} from Luminescence Technology Corp. Taiwan were all the materials used as supplied.

Poly(3,4-ethylenedioxythiophene)-poly(styrenesulfonate) (PEDOT:PSS, CLEVIOS PH 1000) were purchased in soluble form from Sigma Aldrich, which is a water soluble hole transport chemical, and filtered prior to use through a 0.45 and 0.2 µm PTFE filter. The use of PEDOT:PSS between the ITO electrode in BHJ solar cells and active layers was seen to effectively enhance their PV performance. There are a number of reasons for this. First, it has sufficient optical transparency in the visible range. Second, it is effective in transporting holes and blocking negative carriers to the anode, and it improved the hole collection properties of the ITO bottom contact, smoothing out the ITO surface layer to enhance the hole injection as compared to the device without the anode buffer layer (ABL). Third, its relatively high work function (usually reported between 4.8 and 5.2 eV) allowed the formation of an ohmic contact with the most common donor polymers, and finally it is stable enough in ambient conditions (Po, Carbonera, Bernardi, & Camaioni, 2011).

PEDOT:PSS currently commercially available on multi-ton scale in several forms of water dispersion were purchased from H.C. Starck, which offer an extensive choice of properties, among which the most relevant is probably electrical conductivity. Furthermore, the PEDOT:PSS aqueous dispersion seems to contain all the necessary ingredients in the right combination for profitable use in polymer solar cells (Po et al., 2011).

The n-type acceptor semiconducting polymer $PC_{71}BM$ was purchased from Luminescence Technology Corp. Taiwan. The interaction between donor and accepter in solution or during the film drying process will be different when different solvents are used which could result in different active layer morphologies. In addition, poly(ethylene glycol) average M_n 400 ((C2H4O)nH2O) was purchased from Sigma Aldrich and used as received. PEG is one of the important additives in preparing the TiO_2 paste, which can form a great deal of interlaced net structures because of its long chain structure which favors better dispersity of TiO_2 paste (Wan, Lei, Zhang, Leng, & Liu, 2012). Processing solvents, chemical structures of the donor and acceptor materials, and surface properties are found critically important in determining the nanoscale phase separation and performance of polymer solar cells. Figure 3.1 represented the molecular structures of the polymers and organic materials used in the studies. Hereafter, their abbreviations are mentioned throughout the thesis.

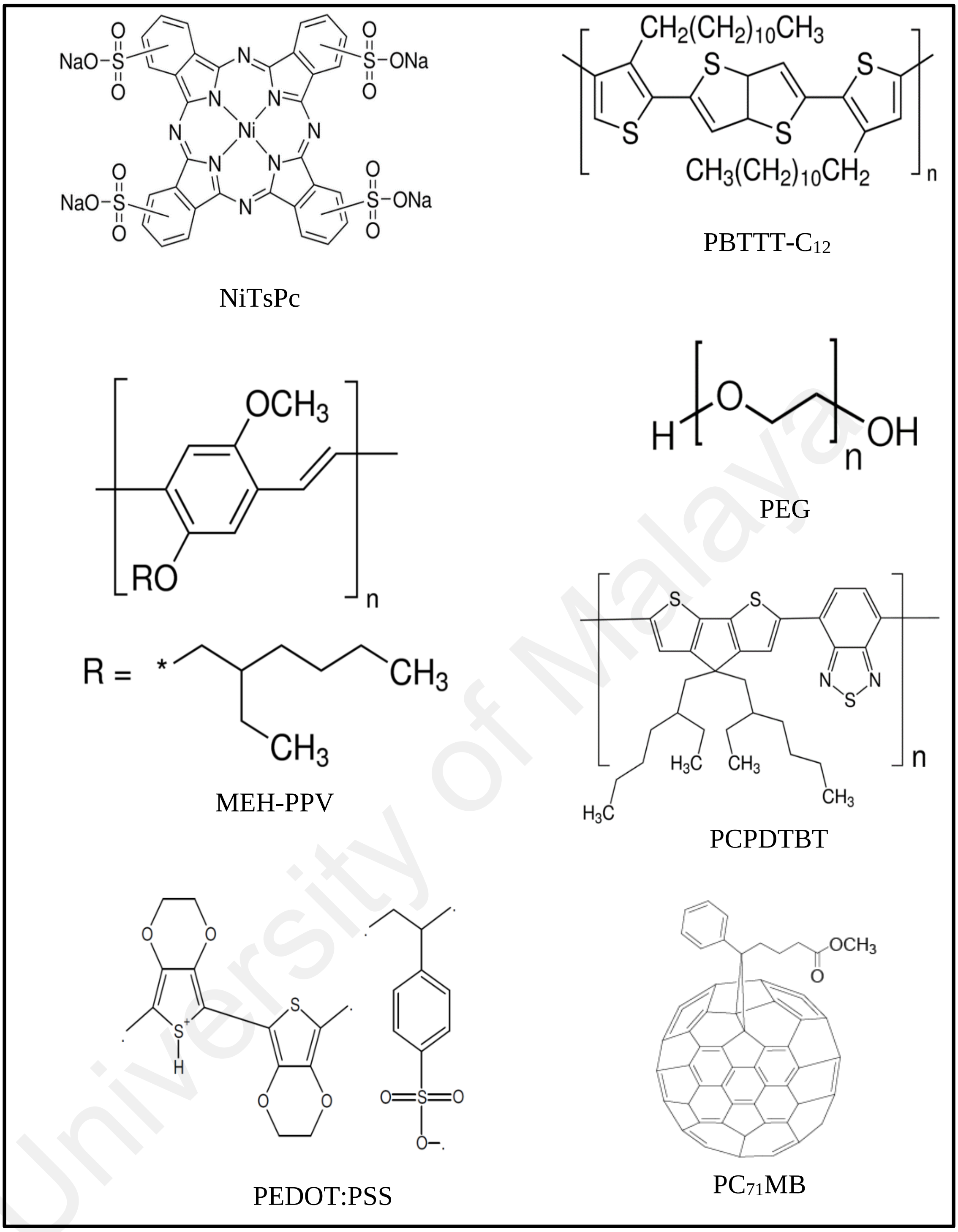

NiTsPc

PBTTT-C_{12}

MEH-PPV

PEG

PCPDTBT

PEDOT:PSS

$PC_{71}MB$

Figure 3.1: The molecular structure of polymers and dyes materials.

3.1.2 TiO_2 Anatase

Anatase is one of the three mineral forms of Titanium oxide, the other two being Brookite and Rutile. Commercially available Titanium (IV) oxide (Anatase nanopowder < 25 nm particle size), 99.7% trace metals basis (TiO_2) were supplied by Sigma Aldrich.

Figure 3.2 (a) depicted a molecular and crystal structure of the TiO_2 anatase material. The specifications of TiO_2 anatase can be found in Table 3.1. Analysis of crystallographic system and space group are shown in Figure 3.2b.

Table 3.1: Specifications of TiO_2 anatase nanoparticles (Aldrich, 2015).

Test	**Specifications**
Appearance (Color)	White
Appearance (Form)	Nanopowder
Particle size	<25 nm
X-Ray Diffraction	Conforms to Structure
Trace Metal Analysis	≤ 4000.0 ppm
Purity 99.7% Based on Trace Metals Analysis	Meets Requirements
Surface Area (m^2/g)	45-55
Melting Point	1825 ℃
Density	3.9 g/ml
Bulk Density	0.04-0.06 g/ml

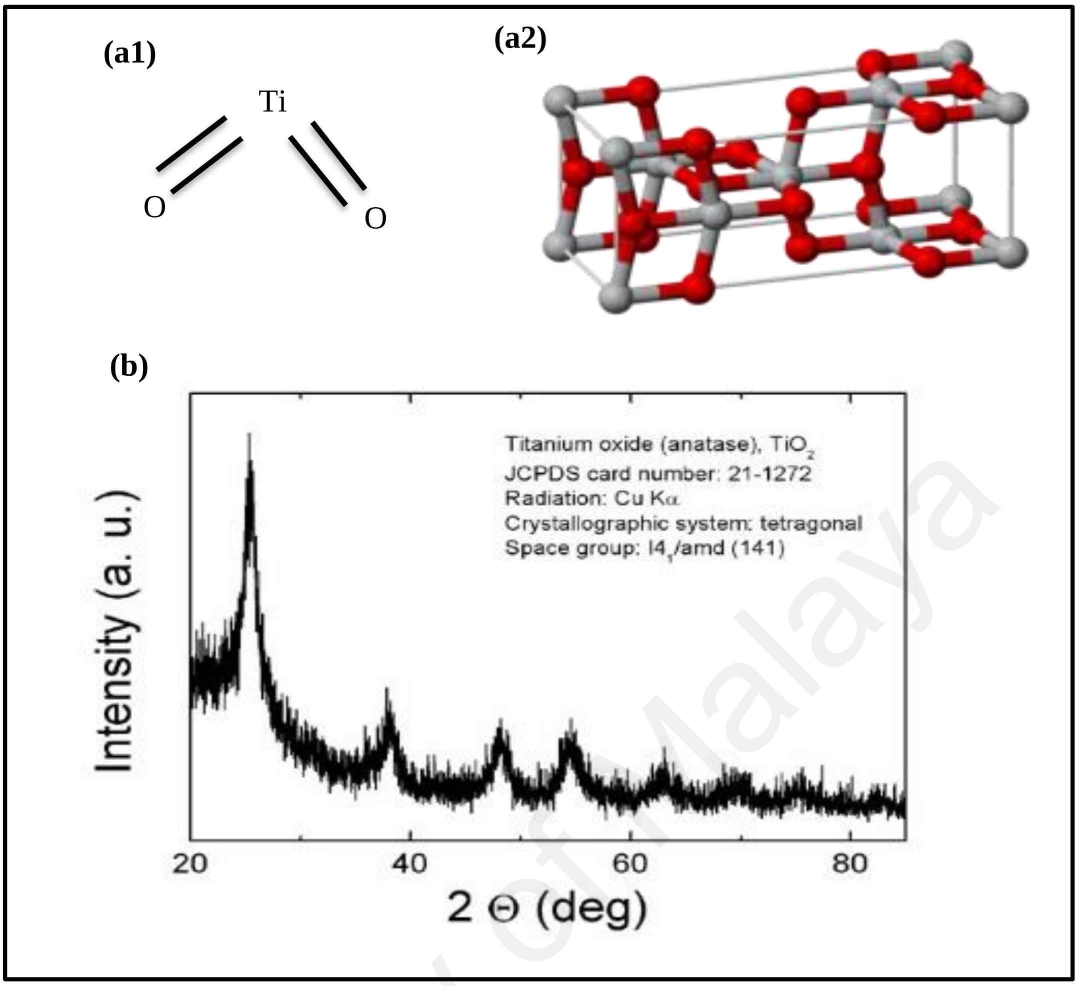

Figure 3.2: (a) Molecular and crystal structure of TiO_2 Anatase material, (b) XRD result of TiO_2 Anatase (Aldrich, 2015).

3.1.3 Solvents

When a solid (solute) is dissolved in a solvent, different events will occur depending on the properties of both the solvent and the solute. These differences and changes can largely be attributed to intermolecular forces both on a macroscopic and microscopic scale. The selection of the exact solvent is crucial to dissolve the dyes and chemicals. However, it is difficult to get a solvent capable of dissolving all the polymer and organic chemicals efficiently, while some of dyes and polymers are mostly known as poorly soluble materials (but comparably cheap materials). Among several pre-tried solvents, Absolute Ethanol 99.8% (C_2H_5OH), 1,2-dichlorobenzene 99% ($C_6H_4Cl_2$), and chloroform (for analysis) ($CHCl_3$), were selected to be used for dissolving the polymers and dyes, which are employed as received. Ortho-Dichlorobenzene is the most preferred solvent in preparing the bulk heterojunction solar cells and DS photo sensor due to the better solubility for $PC_{71}BM$ and PCPDTBT, respectively, as well as crystal packing structure (Baek et al., 2009). Recent studies confirmed that the optimum condition of donor/PCBM ratio can be about (1:4) (Hoppe et al., 2004; Iftimie et al., 2011), and higher ratio of PCBM compared to that of the donor (Bull, T. A., L. S. C. Pingree, S. A. Jenekhe, D. S. Ginger, & C. K. Luscombe, 2009) is favorable. However, purified fresh and PH neutral water is filtered through a nano membrane and is de-ionized to 16 MΩ.cm employing SYBRON/Barnstead (NANOpure II) as solvent for NiTsPc and cleaner for all the experiments done in this work. Table 3.2 shows the organic materials and dyes with their solvents and solutions concentration processed during the materials characterization and device fabrication procedures.

Recently, more and more attention has been paid to the fabrication of solar cells through aqueous approaches considering the green chemistry concept (Sweet, 2013). Typical laboratory solution processing uses organic solvents (chloroform, chlorobenzene, toluene, xylene, hexane, etc.) to dissolve the conjugated polymer and dye. Water is a more favorable solvent since exposure to organic solvents can result in toxicity to the nervous system, reproductive damage, liver and kidney damage, respiratory impairment, cancer, and dermatitis (U.S. Department of Labor, 2007). Water soluble polymers are also less susceptible to oxygen degradation which adversely affects the lifetime of PSC since water contains oxygen (Jørgensen, Norrman, & Krebs, 2008).

Water soluble polymers and dyes are advantageous because their solvent is cheap and environmentally friendly. Water soluble polymer thin film and sensitizer have also been used in the fabrication of DS photo sensors (Karwan et al., 2014), organic transistors (Cho et al., 2008), LEDs (Kim et al., 1998; Koo et al., 2007; Lee, Nam, & Woo, 2012), and fluorescent CdTe/polymer films (Zhang, H. et al., 2003).

Inside the electrolyte several ions are present in a solvent. The traditional redox couple mentioned iodide/triiodide or more recently a cobalt complex based system. The kinetics of these redox couples are quite well studied in an electrochemical manner (Feldt et al., 2013). In this research focus has been given on the iodide/triiodide system and the solvation of the ions in different organic solvents and water as presented in CHAPTER 4: and CHAPTER 5:). Solvation of these ions in different solvents will lead to different geometries and energy levels and is important for the energy matching in the dye sensitized photosensor.

Table 3.2: The organic materials, their respective solvents(s), and concentration of the solutions prepared for various studies.

Material	**Solvent**	**Solution concentration**
NiTsPc	de-ionized water	5 and 10 mg/ml
PBTTT-C_{12}	1,2-dichlorobenzene	5, 10, and 30 mg/ml
$PC_{71}BM$	1,2-dichlorobenzene	30 mg/ml
PCPDTBT	1,2-dichlorobenzene	10 mg/ml
MEH-PPV	Chloroform	10 mg/ml

3.1.4 Electrodes and Substrates

The majority of organic solar cells fabricated in laboratories around the world are made on glass substrates (99%) with ITO as transparent conductive electrode (95%), which incorporates substantial drawbacks (Jørgensen et al., 2013). Low abundance (0.05 ppm of continental earth crust), high demand from the display industry, and localized mining (50% from China) make indium a scarce and expensive element (Panayotova & Panayotov, 2013). For the optical and morphological characterizations purpose of film, quartz and glass were used as solid substrates, whereas for device fabrication, ITO coated glass substrates have been utilized. The importance of using quartz substrates is to help probe the photo-absorption behaviors of the films at higher photonic energy in the ultra-violet region. For the substrates transparent conductive glass (0.7 mm) coated Indium Tin Oxide (ITO) with thickness~150 nm and sheet resistance of ca 10 Ω/square are used. The substrates cut, patterned, and cleaned according to the desired sizes and shapes prior to their use in devices. Hereafter, the ITO size and active area are mentioned throughout the thesis.

In case of the DSPS fabrication, as DSSC the photoanode is a thin nanoporous layer of the annealed TiO_2 supported on ITO coated glass. Dye molecules which are sensitive to the visible light region in the solar spectrum are attached chemically onto the semiconductor electrode. The counter electrode consists of an ITO coated with a catalyst layer, typically platinum or graphite. Electrolyte typically containing the I^{-}/I_3^{-} redox couple is sandwiched in between these two electrodes. In the case of the organic solar cell fabrication, the anode is transparent ITO glass and cathode is an Al electrode. The ITO electrode is that side on which the devices (the organic solar cells) are exposed to light; therefore, it should provide a high possible transparency. ITO conductive electrodes usually show transparency of > 90%, which makes them strong candidates for application in the BHJ cells. The difference between the work function of Al (4.2 eV) and ITO (4.8

eV) provides a possible approach to design normal device structures by depositing the hole conductive materials onto the ITO side and electron conductive ones below the Al electrode.

3.1.5 Electrolytes

An electrolyte is a chemical system that provides an electrolytic contact between the DS solar cell electrodes. The photovoltaic performances of liquid electrolyte based dye sensitized photo sensor depend unequivocally on the choice of electrolyte solvent utilized. The electrolyte acts as a hole transporting material in dye sensitized photo sensor. It allows fast electron transfer from counter electrode to the oxidized dye molecules for efficient regeneration. The photo-excited electrons are then injected to the working electrode to complete the process (Hamann, Jensen, Martinson, Van Ryswyk, & Hupp, 2008; Reynal & Palomares, 2011). For electrolytes, two commercial electrolytes were purchased from Solaronix, Switzerland which are Iodolyte Z-100 (for long term performance with an intermediate concentration of 100 mM of triiodide) and Iodolyte HI-30 (for very high performance assessment of dye sensitized solar cells), which were used in the experiments as received.

3.2 Cleaning Substrates and Plasma Treatments

The substrate is a key component in solar cell synthesis, interfacing with the catalyst and interacting with the growth environment. The only substrate used in these studies is ITO glass. Commercially available ITO substrates were supplied from Sanyo, Japan with area sheet (370 × 470 cm^2) then cut by diamond glass cutter according to a desired structure. A pair of gloves, a goggle and a mask were employed to protect eyes and hands from glass shreds. After that, the substrates were cleaned according to a well-established protocol i.e. by ultrasonic agitation in Deacon Neutracon® foam solution for 15 min, followed by ultrasonic bath in Acetone (C_3H_6O), Iso Propyl Alcohol 99.7% (C_3H_8O) and DI water for two min for each step, respectively. Substrates were later dried and cleaned thoroughly by blown nitrogen gas.

Oxidation treatment of ITO surface substrate, such as oxygen plasma and UV-ozone, increase ITO effective work function by removing contamination of carbon and increasing oxygen concentration. Oxygen plasma treatment also produces an ITO surface with a more uniform electrical response (Brumbach et al., 2007). The work function of ITO treated with oxygen plasma increase 0.1-0.3 eV compared to bare ITO as Kahn et al. reported (Wu, Wu, Sturm, & Kahn, 1997).

Optoelectronic devices, including bulk heterojunction solar cells, dye sensitized solar cells, OLEDs, and organic photovoltaics fabricated with ITOs that have undergone plasma treatments have been reported to demonstrate enhanced performance (Djurišić, Kwong, Chui, & Chan, 2003; Ishii, Mori, Fujikawa, Tokito, & Taga, 2000; Kugler, Johansson, Dalsegg, Gelius, & Salaneck, 1997; Liu, Holman, & Kortshagen, 2008; MacDonald, Veneman, Placencia, & Armstrong, 2012; So, Choi, Cheng, Leung, & Kwong, 1999; Wang & Lin, 2009).

There are many benefits of plasma treatments for surface modification, such as changing surface properties without affecting the bulk material, modifying wettability to render a surface hydrophilic or hydrophobic with the appropriate process gas(es), improving surface coverage, spreading of coating and enhancing adhesion between two surfaces.

A Parallel Plate Etcher (POLARON PT7170) has been employed for plasma treatment. The ITO substrates were treated by O_2 plasma for ten min at a radio frequency (RF) power of 35 W. Chamber pressure was maintained up to 1×10^{-1} mbar during the treatment. Figure 3.3 illustrates a photograph of the ETCHER machine used in the experiments.

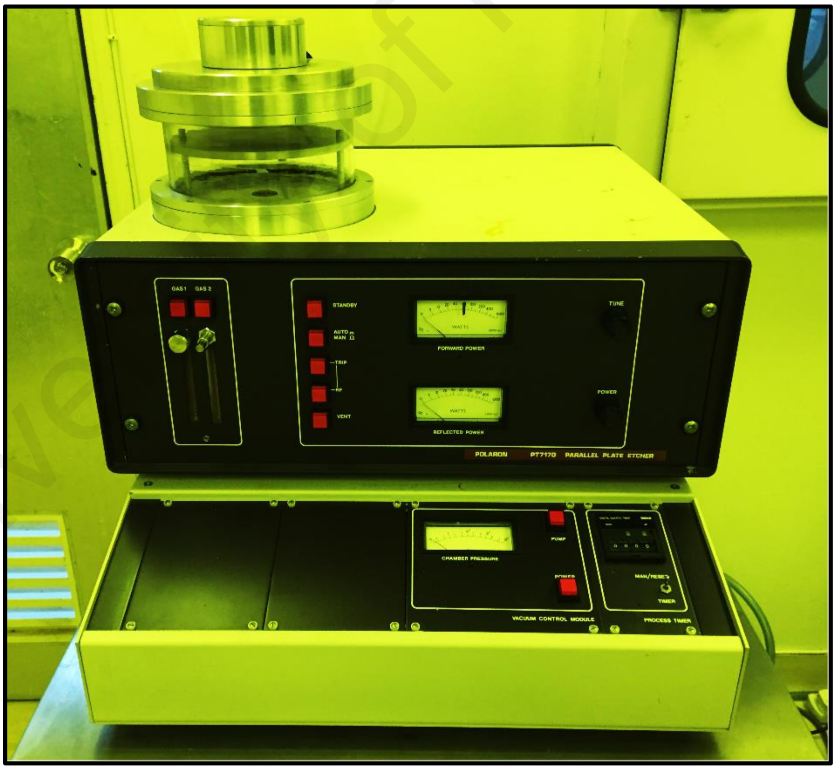

Figure 3.3: Photograph of the used ETCHER machine.

3.3 Preparation Methods

The deposition methods are explained in the following section. In particular, this chapter covers vacuum thermal evaporation, sputter coating, spin coating, and Doctor Blade technique with working electrode preparation which were employed to deposit thin films of the materials discussed in the previous chapter.

3.3.1 Vacuum Thermal Evaporation

The vacuum thermal evaporation deposition technique consists of heating until sublimation of the material to be deposited. When a high current is passed through a resistive element such as a light bulb, the filament gets white hot. Using a heavier filament and hooking a few pieces of metal wire (such as gold or aluminium) will result in the metal wire first melting and then flowing along the filament, like solder on a soldering iron (known as ‘wetting’) prior to evaporation. This is the crudest but probably most common form of resistive evaporation, known as filament evaporation.

Evaporation filaments typically draw 35-60 A at 6-20 V. Only small amounts of material can be evaporated in any individual evaporation and filaments are difficult to load, restricting its use in the lab.

The element need not be a helical filament though a thin sheet of tungsten or tantalum with a dimple or depression holds more material and is easier to hold. The material vapor finally condenses in the form of thin film on the substrate surface. Usually low pressure is used, about $10^{-6} - 10^{-5}$ mbar, to avoid reaction between the vapor and atmosphere. At low pressure, the mean free path of vapor atoms is greater than the vacuum chamber dimensions. Consequently, the evaporated metal travel in straight lines from the evaporation source towards the substrate.

In the BHJCs, vacuum thermal evaporation was used to deposit the top aluminium electrode onto different kinds of substrate. The method utilizes the volatility of materials upon heating. This requires materials which do not decompose during heating and evaporation. In this deposition technique, two different deposition techniques have been employed for the deposition of the thin films. An Edward AUTO 306 thermal evaporation system equipped with STM-100 / MF film thickness monitor and another one inside MIKROUNA super (1500/750) Glove Box (Figure 3.4 (a) and (b)) were used at the Clean Room, Low Dimensional Materials Research Centre, Department of Physics, Faculty of Science, University of Malaya.

The aluminium electrode was deposited on top of the organic thin active layer. The system consists of vacuum chamber, three TPRE-Z20-III EVAPORATION POWER, main power supply, a diffusion pump, two rotary pumps, a compound vacuum gauge, ionization gauge, thermal controller, two pirani gauges, main mechanical shutter, electrical shutter and rate/thickness monitor. The diffusion pump was cooled with flowing water for effective pumping. A base pressure of not less than 10^{-5} mbar must be achieved before any deposition was carried out. Figure 3.5 illustrated the schematic diagram of the Al thin film electrode deposited onto the active layer/buffer layer/ITO glass using a thermal evaporator.

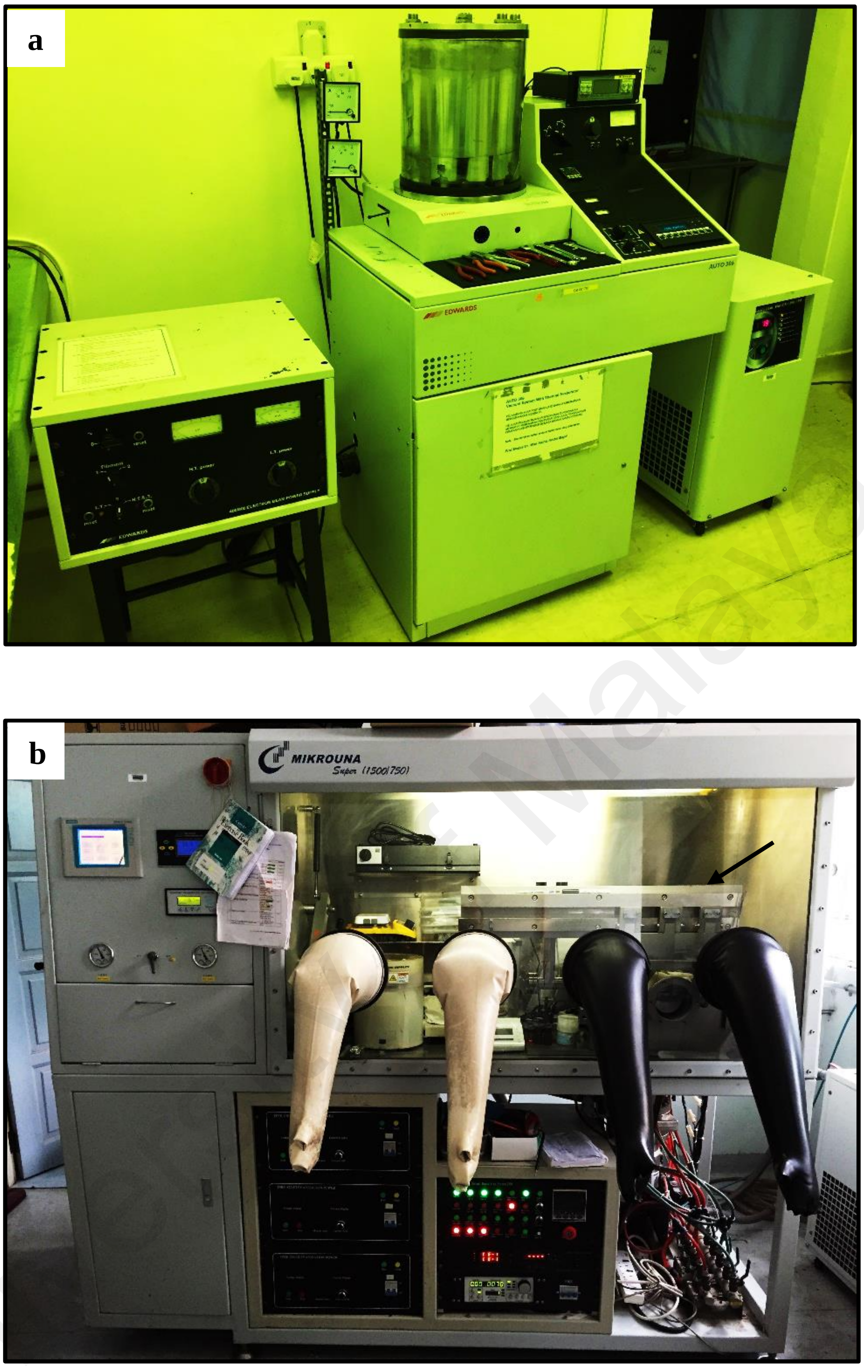

Figure 3.4: (a) Photograph of Thermal Evaporation System inside Low Dimensional Material Research Centre (LDMRC) Clean Room and (b) inside Glove Box.

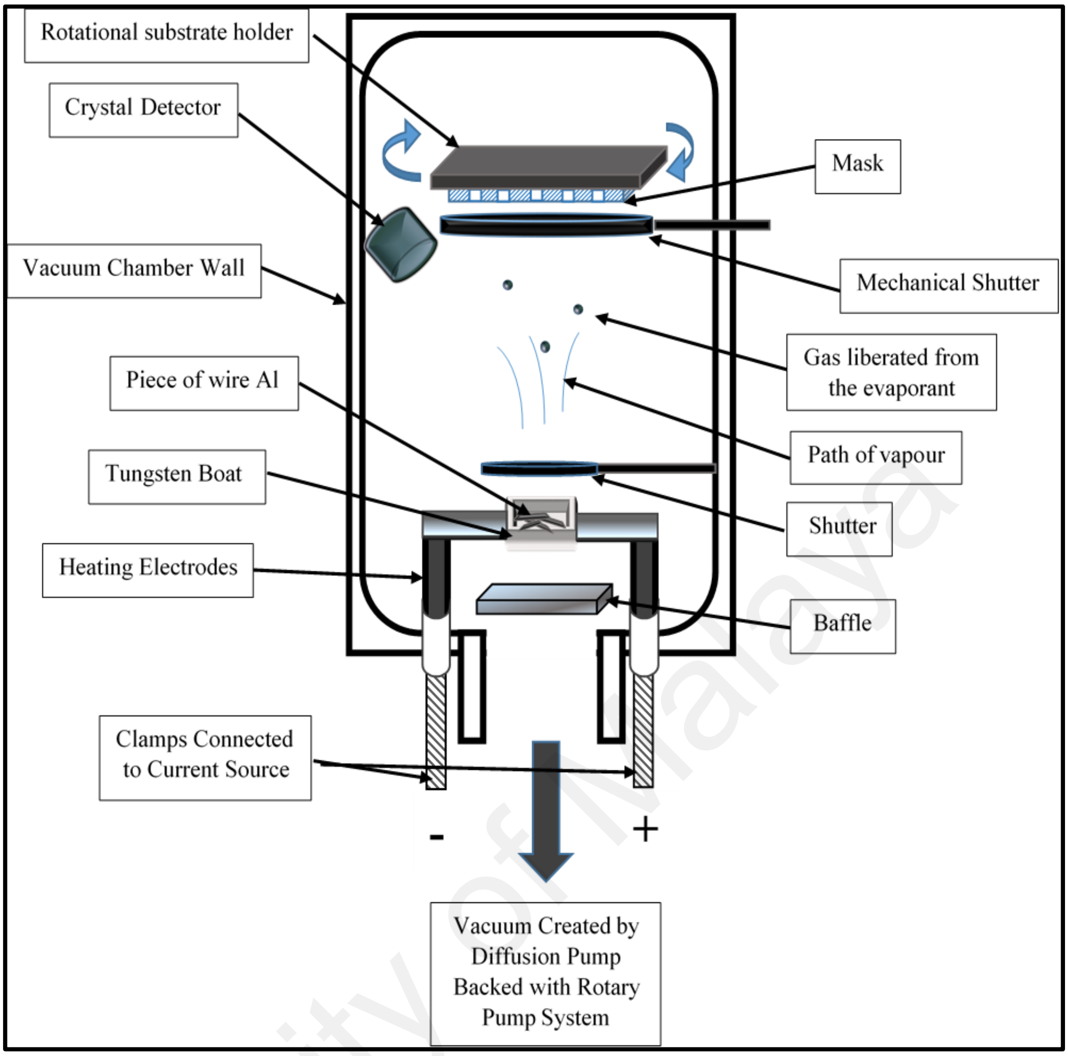

Figure 3.5: Schematic diagram of the thermal evaporation equipment inside Glove Box.

Initially, the substrates were kept at the top of the chamber upside down and put on the aluminium mask with the desired electrode pattern at room temperature (300 K) during the vapor application and throughout the whole deposition process. A series of $3-5$ pieces of approximately 0.8 cm of Al wire that are to be deposited are placed inside a tungsten boat sheet held by two electrodes capable of supplying sufficient heat to the materials upon passing the electrical current through this boat. After the pressure inside the chamber exceeded 10^{-5} mbar, a current was applied through the tungsten boat and increased slowly to about 35-40 A, which are enough to start sublimating the Al wires. The aluminium eventually melted and evaporated inside the chamber and after opening the main shutter, was finally deposited on the sample. The shutter was closed for a few minutes after the aluminium started to melt and evaporate to obtain a good quality deposition. First, the substrates slides were cleaned followed by the deposition of the buffer layer then active layer via spin casting process as described in section 3.2 (above) and 3.3.3 (below) respectively. The ITO glass substrates were selected because of their high optical transparency to just below 200 nm. All the measurements upon the deposited films were performed under ambient conditions and at room temperature. The construction of final device is shown in Figure 3.6.

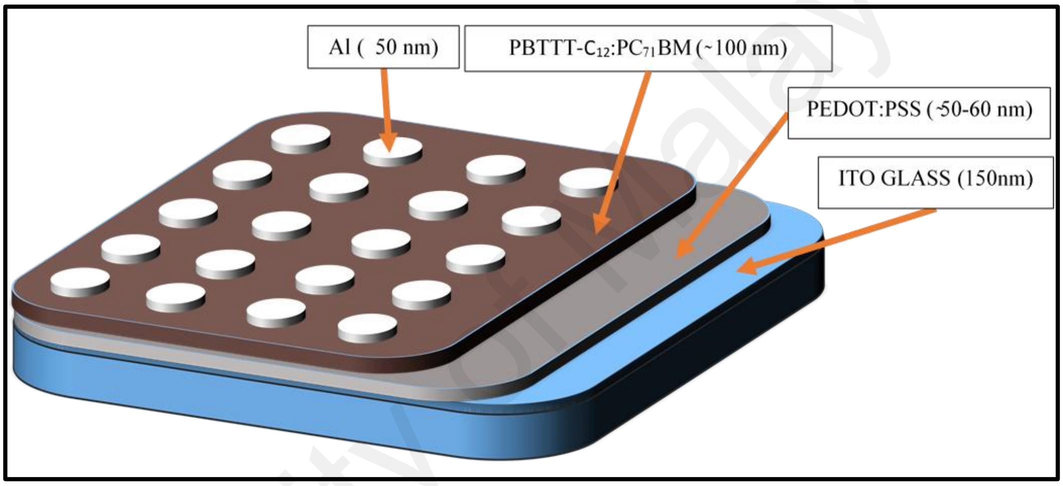

Figure 3.6: Schematic of a device BHJ solar cell with $\text{PBTTT-C}_{12}\text{:PC}_{71}\text{BM}$ blend.

3.3.2 Sputter Coating

Sputter coating is a well-established thin film deposition technique. It is used commercially for larger scale production since it can produce uniform films on large substrates several square meters in size. Physical sputtering is a process in which atoms are ejected from a source material due to impinging energetic particles.

Counter electrodes of the DS photo sensors are sputter coated (details in chapter 4) with platinum thin film by using JEOL JFC-1600 Auto Fine Coater. This system, consisting of the basic unit and a rotary pump unit, is designed to coat non-conductive specimens such as biological specimens primarily for use in a scanning electron microscope with high efficiency within a short time.

The specifications are mentioned in Table 3.3. Furthermore Figure 3.7 (a) and (b) show the coating rate for target Pt captured with specimen to target distance of 30 mm. and operating state respectively.

Table 3.3: Specifications of JEOL JFC-1600 Auto Fine Coater (JEOL, 2009).

Sputtering method	Magnetron type
Operating pressure	Around 10^{-1} Pa
Sputtering current	10, 20, 30, 40 mA, preset type
Target	57 mm in diameter, Pt (standard)
Specimen stage	64 mm in diameter
Vacuum chamber	120 mm-OD X 100 mm high
Vacuum monitor	Pirani vacuum gauge (also used for timer display)
Timer	Digital display 1 to 300 sec.
Gas control	Incorporated
Argon gas purging function	Incorporated (auto/manual selectable)
High voltage safety circuit	Incorporated
Pumping system	Metal exhaust pipe, direct drive oil-sealed rotary vacuum pump 30 L/min
Installation requirements	
Power requirements	100 VAC, 50/60 Hz, 300 VA
Dimensions and weight	
Basic unit	350 mm wide X 340 mm deep X 282 mm high, 12 kg
Rotary pump	280 mm wide X 120 mm deep X 215 mm high, 10 kg
Operating conditions	25 ℃ ± 5 ℃

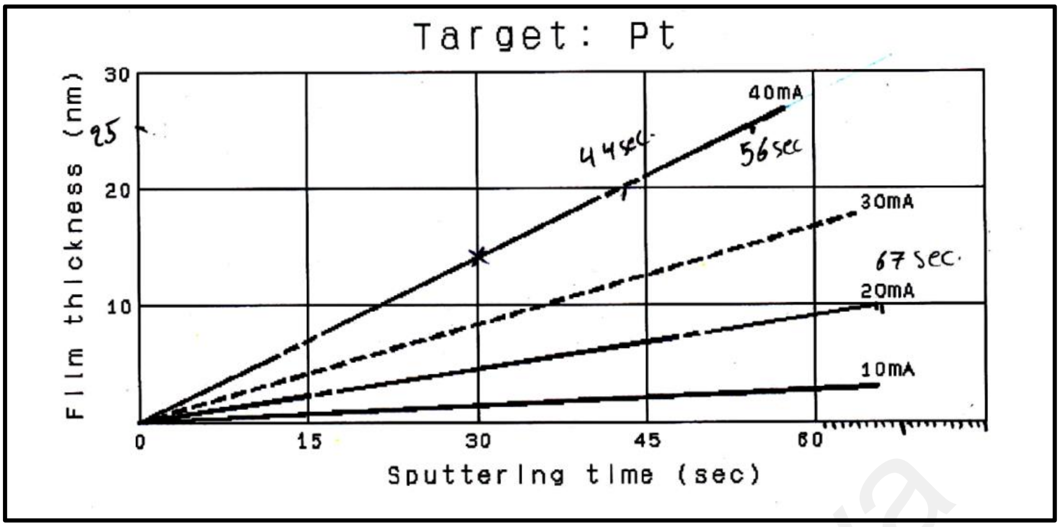

Figure 3.7 a: Reference sputter coating rate of Platinum thin film by JFC-1600 Auto Fine Coater.

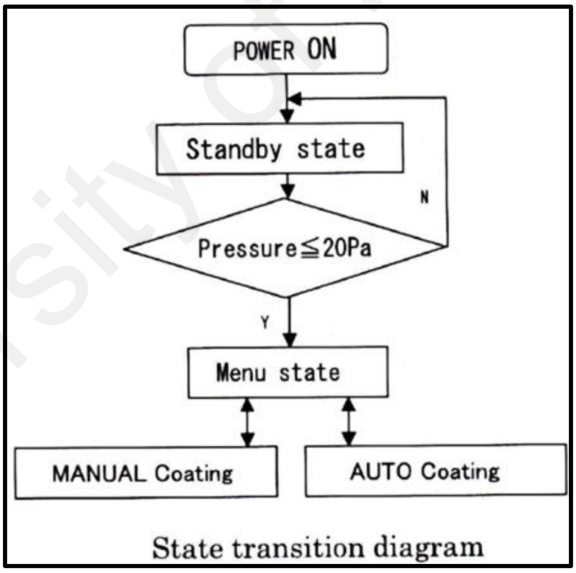

Figure 3.7 b: Flowchart of operating state of JFC-1600 Auto Fine Coater (JEOL, 2009).

3.3.3 Spin Coating

The spinner WS-650MZ-23NPP and WS-400B-6NPP/LITE manufactured by Laurell Technologies was employed at the Clean Room and inside Glove Box, Low Dimensional Material Research Centre (LDMRC), Department of Physics, University of Malaya, for spin coating deposition thin film. The spin coating machine and schematic of spin coating process is illustrated in Figure 3.8 (a) and (b). The spin coating depends on the centrifugal force that spreads the liquid precursor across and eventually off substrate, leaving a thin film of solution on the surface. Factors such as rotational speed, acceleration, and fume exhaust contribute to the properties of coated film. The thickness of the film depends upon a balance between the centrifugal force determined by the spin speed, viscosity of solution, substrate and adhesion. The coating processes were undertaken at room temperature. In this way, attempts have been made to realize reduction in cost and complexity of use.

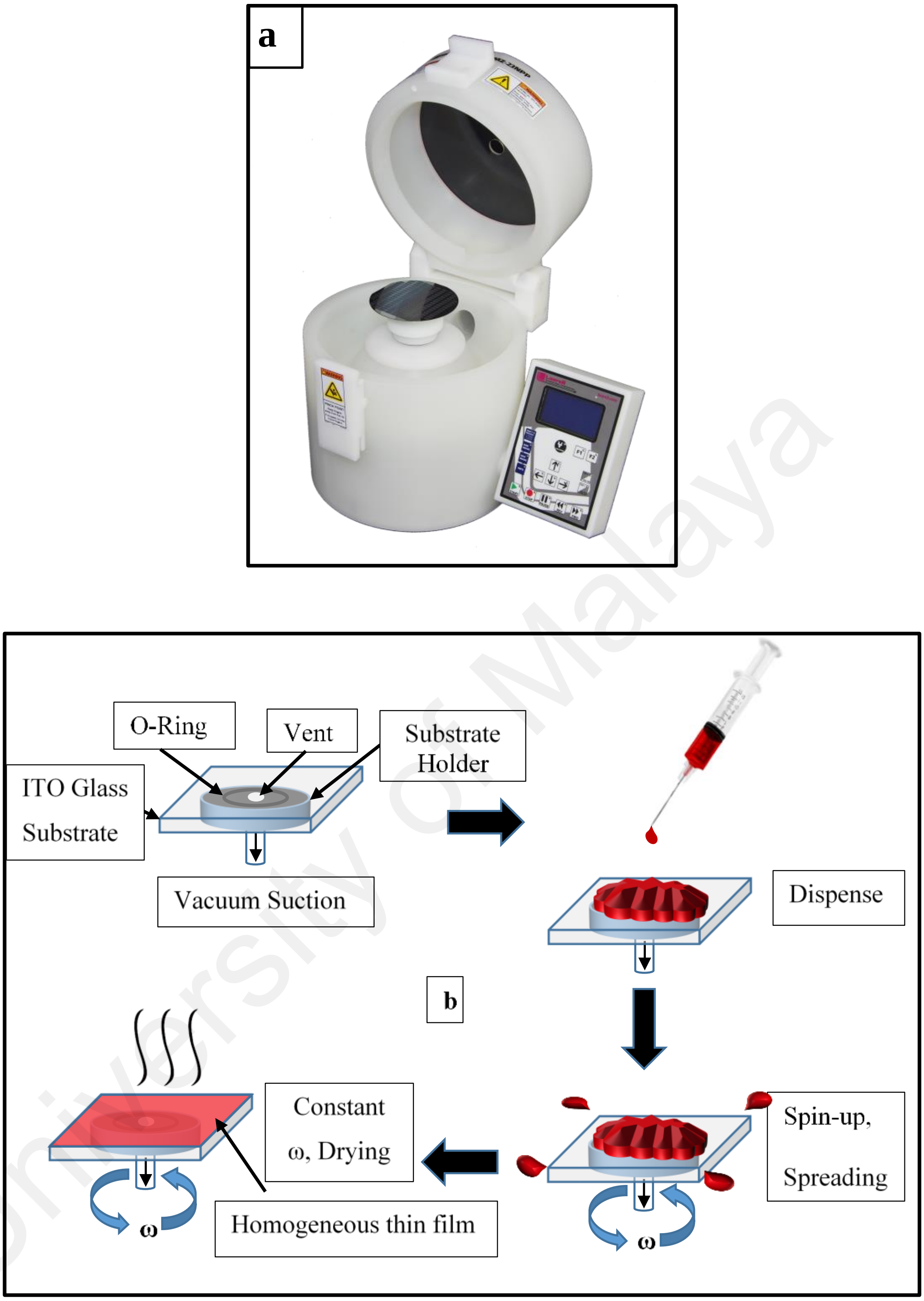

Figure 3.8: (a) The spin coating machine. (b) Schematic processes of the spin coating technique.

3.3.4 Doctor Blade Technique and Working Electrode Preparation

A common way of preparing thin TiO_2 films for dye sensitized photo sensor cells is Doctor Blading or blade coating, also known as knife coating on rigid substrates. The well-defined thickness is mainly controlled by the gap size from the blade to the surface. For the lab-scale processing the blade is often moved with a defined speed using a motorized stage, but a careful manual operation is possible as well. For large-scale R2R processes, the blade is fixed over the moving substrate. The ink is placed in front of the fixed blade whereby the substrate moves relative to the blade. Adjustable gap widths allow the deposition of wet layer thicknesses from low tens to hundreds of micrometers. The final wet layer thickness is roughly half of the gap width depending on the coating speed and flow behavior (Wengeler, Schmitt, Peters, Scharfer, & Schabel, 2013). Further coating parameters that influence the film formation are surface energy of the substrate, surface tension of the fluid, coating speed, viscosity, and surface temperatures. The dry layer thickness d can be calculated from the empirical relationship (Krebs, 2009)

$$d = \frac{1}{2} . g . \frac{c}{\rho}$$ **Equation 3-1**

where g is the gap width, c the concentration of the solids in the ink in g/cm^3, and ρ the density of the material in the final film in g/cm^3.

The TiO_2 electrode, where the sunlight is absorbed, is called the working electrode. Preparing working electrode films involved Doctor Blading a solution that contained the desired transition metal on a conducting glass slide surface with a layer of Indium Tin Oxide (ITO) and then sintering the film at a high temperature. For the preliminary oxides, ITO slides were cleaned as mentioned the detail in section 3.2) and their non-conductive sides were marked for use in future. A 0.5×0.5 cm^2 (1×1 cm^2 for larger test films) window was cut in a piece of special adhesive (Scotch Magic) tape with thickness 55-65 μm and put on the conductive side ITO glass near the end of one edge. Figure 3.9

represents the schematic of the typical blade coating deposition method. These defined the boundaries of the coating deposition area and created a height barrier (gap width) for the coating to be deposited. Layer of the tape produced was approximately 8-15 microns, and 2-5 microns with pressure thick film after annealing depending upon the viscosity of the dispersion. The paste was dispersed ultrasonically, as shaking the vial itself would cause air bubble formation preventing good deposition. 25-50 μL of nanocrystalline TiO_2 colloidal paste were dispensed on the window area, which is immediately wiped off (or evenly spread out) using a thin special blade in the downward direction. The wiping action evened out the TiO_2 paste in the deposition area set by the tape and removed the excess paste. This method produced very uniform and defect free coatings with high reproducibility. The tape was removed carefully and the paste was allowed to dry and relax for two min in a covered petri dish. The later was a critical step as it allows reducing surface irregularity and brings the air bubbles out. Paste preparation and details of annealing steps are described in section 4.3 and 5.2. Plastic and glass lab-ware were used as much as possible in every step of the fabrication; as iron contamination is found to have a negative effect on cell performance.

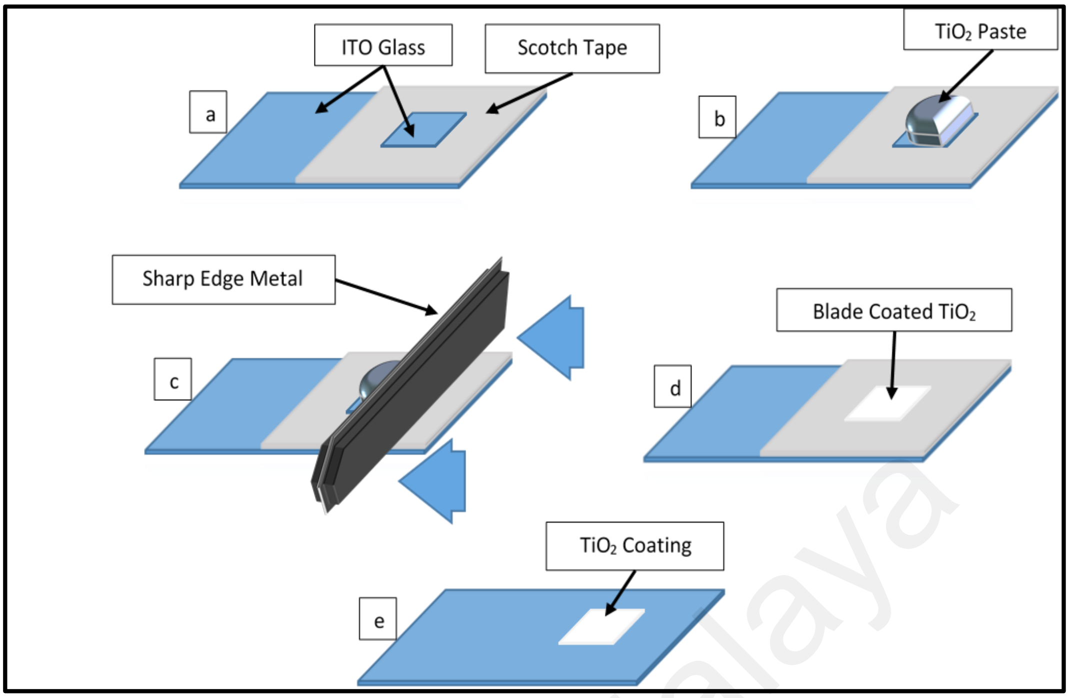

Figure 3.9: Schematic showing Doctor Blade Coating Technique.

3.4 Thickness Determination of Thin Films

The thickness of the layers and photoelectrode is an important parameter for organic solar cells and DS photo sensors, and strongly affects the device performance. The most common equipment that can be used to quantify film thickness is a surface profilometer, which requires a scratch in the thin film before measurement. Figure 3.10 shows a photograph of a surface profilometer instrument, KLA Tencor P.6, which was employed to determine the thickness of the layer films. Surface Profilometer maps surface topography by lightly dragging a sharp probe along the sample surface, thereby recording the surface roughness and height. The interaction of the tip with the surface determines whether it is contact or non-contact mode. A profilometer typically uses a mass cantilever system to keep the tip force constant during the scanning process. Profilometers utilize the same imaging fundamentals as a scanning probe microscopy, but with a much larger tip (2.5 microns in diameter) (Kalinin & Gruverman, 2010). The larger tip limits the vertical and horizontal resolution. The probe tip is usually made of diamond to reduce tip wear.

There are two basic types of surface profilometer technologies; contact and non-contact. Contact or stylus-based surface profilometers measure surface texture by dragging a sharp, pointed tool along the surface. Height variations of the tip are recorded and then used to form a texture profile. Roughness and waviness are also calculated from the surface profile data. Non-contact surface profilometers measure the texture by optically scanning a surface with a light or laser, as illustrated in Figure 3.11. With a proper selection of the stylus force both hard materials and soft materials can be measured, such as metal films, silicon nitrile, silicon oxide, silicon, organic and polymer materials on rigid substrates.

Spin coating is a simple and efficient method to get the homogeneous buffer layer and active layer of a BHJ solar cell. It is not necessary to measure the thickness for every fabricated device. In contrast, in Doctor Blading technique for DSPS, usually the surface profilometer has been employed, regarding, it gives usually non-uniform films compare to spin coating. Thus, several samples are needed to be measured in order to get the average thickness of the sample prepared via Doctor Blading.

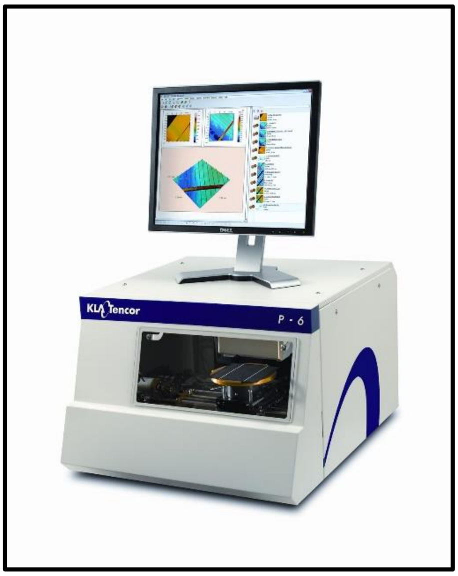

Figure 3.10: KLA Tencor P.6 surface profilometer equipment.

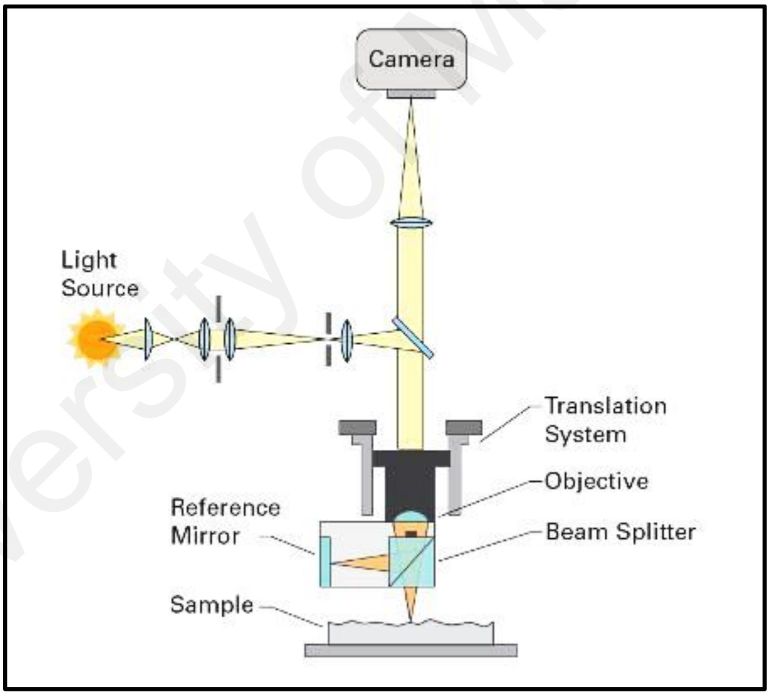

Figure 3.11: Standard schematic of an optical profilometer (AZoNetwork, 2015).

3.5 Characterization Technique

In this section, the instruments and experimental techniques that were employed to carry out the studies from material characterization to the device building and assessment are described in three main parts.

3.5.1 Electrical Characterization

3.5.1.1 Current-Voltage Characterization

The key performance parameters of the cell are obtained from current-voltage (IV) measurements. This is the most basic way to determine how much solar power is converted to electrical power by a solar cell. By recording the current flowing through a cell as a function of the voltage across its electrodes an IV curve is obtained then the efficiency (η) and the fill factor (FF) from Equation 3.2 and 3.3 are calculated. The J_{max} and V_{max} are determined from the P_{max}, which is the point where the largest rectangle can be fitted under the IV curve, as an example IV curve indicated in Figure 3.12. P_{in} is the power of the incident light.

For this curve the short circuit current (J_{sc}) can be extracted when $V = 0$ and the open circuit voltage (V_{oc}) when $J = 0$. On this curve, the maximum power point (MPP) can be found where d(IV)/d $V = 0$. The light to electricity conversion efficiency (η) of the cell at this point is given by (Gabrielsson, 2014):

$$\eta = \frac{P_{out}}{P_{in}} = \frac{V_{MP}J_{MP}}{P_{in}}$$ **Equation 3-2**

Typically the efficiency of a cell is described in terms of V_{oc} and J_{sc}, which requires the introduction of a dimensionless quantity called the fill factor (FF) (Gabrielsson, 2014):

$$FF = \frac{V_{MP}J_{MP}}{V_{oc}J_{sc}}$$ **Equation 3-3**

This allows the efficiency to be written as:

$$\eta = \frac{V_{oc}J_{sc}FF}{P_{in}}$$ **Equation 3-4**

A cell’s sunlight to electrical energy conversion efficiency is measured by illuminating it using a solar simulator tuned to the AM 1.5 G solar spectrum ($P_{in} = 100$ mW/cm^2).

It is also possible to collect IV curves without illuminating the device, in which case the resulting curve is referred to as a dark current curve.

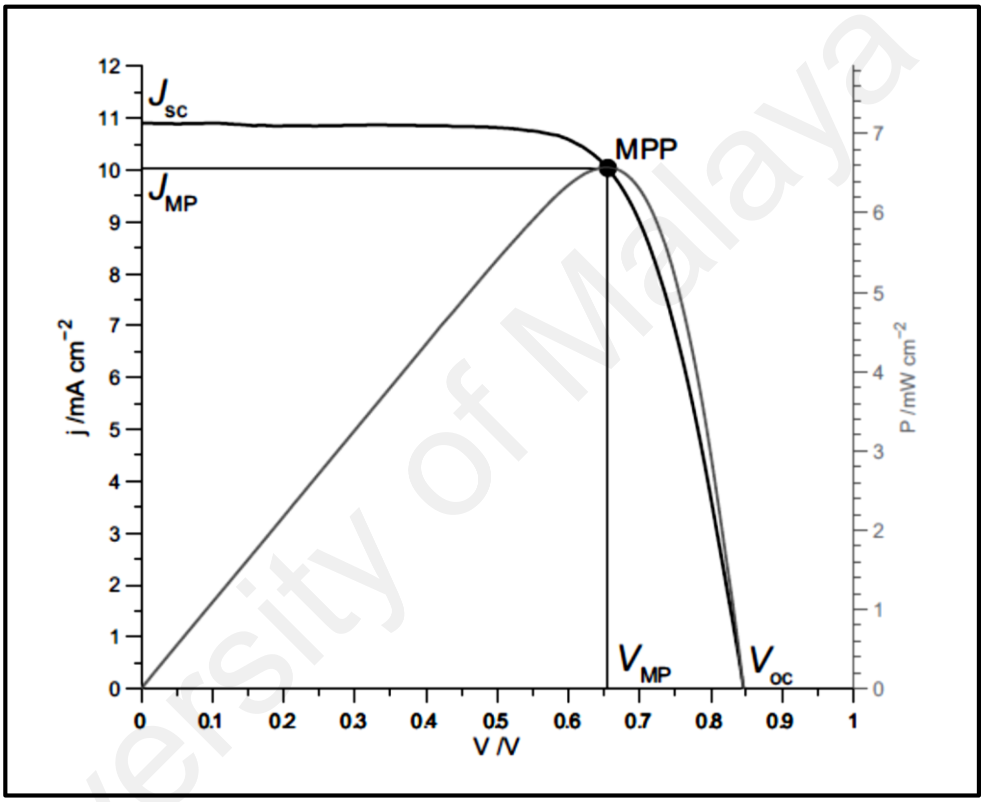

Figure 3.12: IV curve (black point) showing the MPP, J_{sc} and V_{oc} values. The grey curve represent the power-voltage curve (Gabrielsson, 2014).

After fabrication of devices, photovoltaic measurement was performed by recording the current versus voltage response of the devices under the standard light illumination . The major photovoltaic parameters can be extracted from the current-voltage measurements, while as the power-voltage (P-V) curve can also provide further significant estimation. In order to simulate the light intensity used for illuminating the devices under standard condition measurement, an Oriel solar simulator (model 67005) with an AM 1.5 filter was employed. This solar simulator photograph is shown in Figure 3.13. Solar simulators can imitate the spectral distribution of sunlight for a variety of environments by using high pressure xenon arc lamp sources to approximate the spectra emitted by the sun (see Figure 3.14). The spectral distribution from the xenon arc lamp is altered and refined using AM filters. The spectra emitted by the xenon source and the sun are both close to that of a 5800 K blackbody. Hence, by combination of the lamp and air mass filters the approximate standard light intensity condition of approximately 100 mW/cm^2 irradiance, AM 1.5 global reference spectrum at room temperature is being realized.

Figure 3.13: Photograph of the Oriel Solar Simulator.

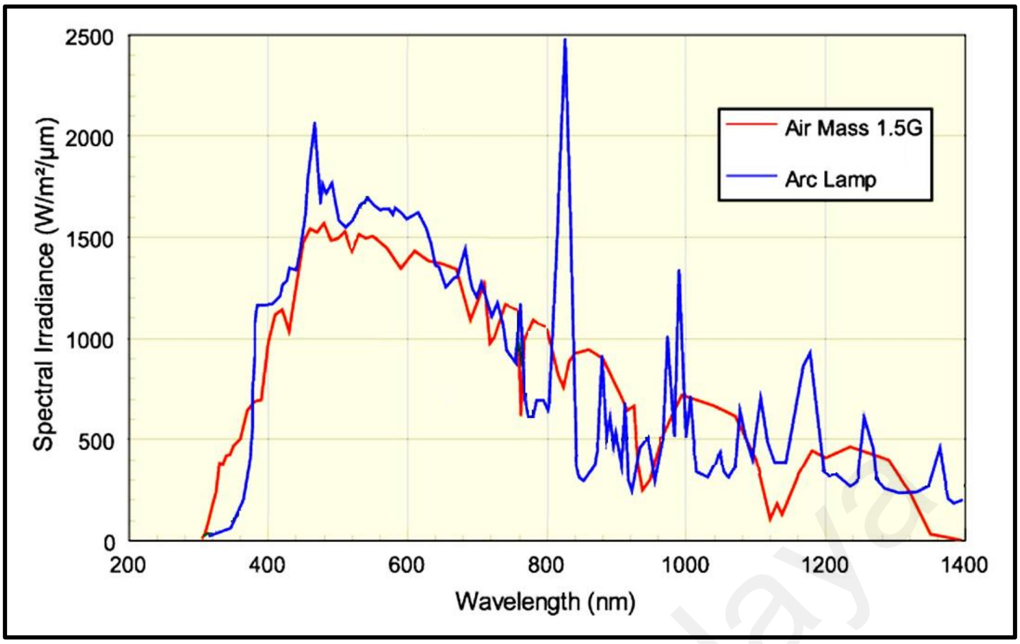

Figure 3.14: Comparison between the output spectrum of the xenon arc lamp and spectrum of the standard AM 1.5. As clear that the xenon light source was very close to that of sunlight which is a large portion of arc lamp spectra lie in the visible region (390-780 nm).

The IV characteristics were measured using a Keithley 236 Source Measure Unit (SMU) and KEYSIGHT B2902A (Precision Source/Measure Unit), which can source and measure both current and voltage. These SMU have four-quadrant source capability, and they can sink the cell current as a function of the applied voltage up to 100 mA (Keithley, 1990). Figure 3.15 (a) and (b) present the photograph of equipment and a schematic of a solar cell connected to its terminals for IV measurement, respectively. One side of the solar cell is connected to the force and sense terminals of SMU1, the other side is connected to the force and sense terminals of either SMU2 or the ground unit. With the four wire method, a voltage is sourced across the solar using one pair of test leads (between force HI and force LO), and the voltage drop across the cell is measured across a second set of leads (across Sense HI and Sense LO). The sense leads ensure that the voltage developed across the cell is the programmed output value and compensate for the lead resistance. Finally, to determine the current density (J) through the device, the measured current (I) values are divided by the device area (the total frontal area of the cell including the area covered by the grids and contacts) and as such, the J-V and P-V characteristic curves can be readily derived (Muhammad, 2011).

In case of response and recovery time measurement, the bias voltage is fixed on desired voltage according to the cell performance (details in 4.4 and 5.3), and the solar simulator opened and closed manually (in some cases) for a period of time.

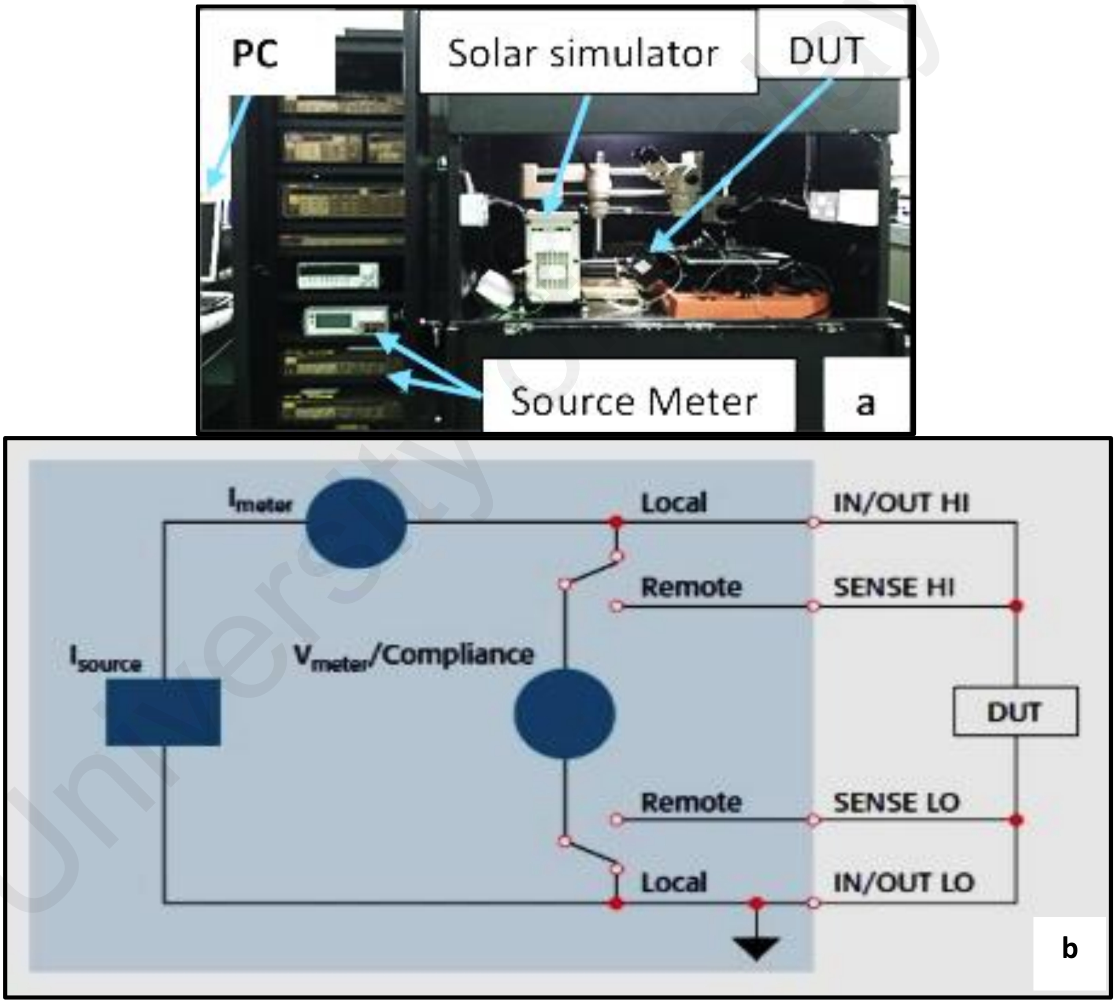

Figure 3.15: (a) Photograph of the Keithley 236 SMU Programmable IV Source equipment. (b) An SMU instrument configured as a constant current source and a voltmeter (analog-eetimes, 2015).

The rectangular steps of neutral density filters (NDL-25S-4) have been used to control the intensity of light with ten different optical density (*OD*) discrete steps which include 0.1, 0.2, 0.3, 0.4, 0.5, 0.8, 1.0, 2.0, 3.0 and 4.0. The sketch and dimension details are depicted in Figure 3.16. The rectangular step filter is composed of a UV fused silica glass substrate and a metallic Inconel coating (an alloy of nickel containing chromium and iron in order to resist aging and corrosion at high temperatures). However, it is recommended that neutral density filters be used below 100 ℃ temperatures in order to avoid oxidization. This filter is an ideal choice for applications from UV to near IR because the UV fused silica substrate employed in these filters exhibits high transmission and virtually no laser-induced fluorescence (as measured at 193 nm). The *OD* is specified at the design wavelength of 633 nm while wavelengths over the usable range will result in some variation in the *OD*. The drawback is that these ND filters are reflective and the Inconel coating absorbs some incident light which limits the use of these filters to low power applications (Thorlabs, 2016). The following equation defines the optical density:

$$OD = \log_{10}\left(\frac{1}{T}\right)$$ **Equation 3-5**

This means a greater reflection and lower transmission (*T*) of incident light corresponds to a higher optical density (*OD*).

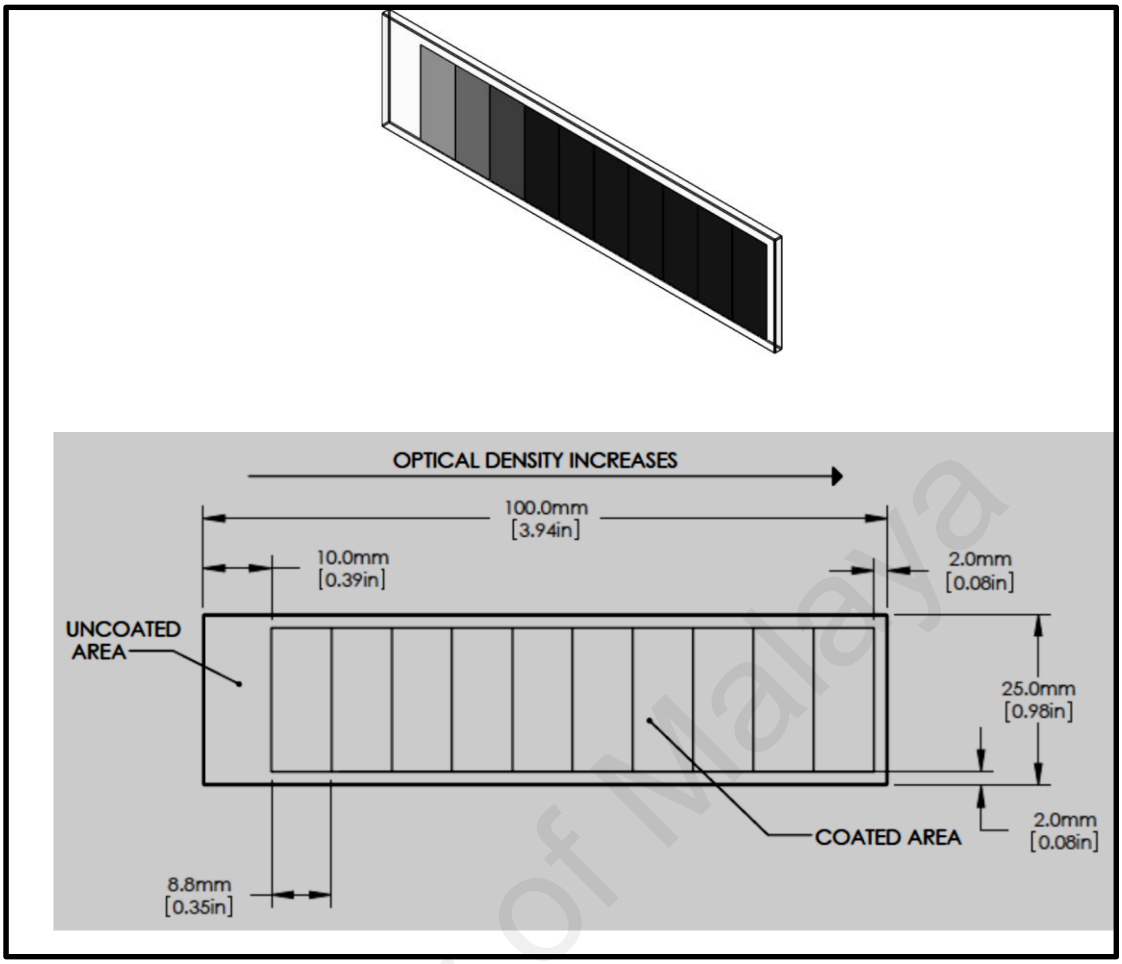

Figure 3.16: Architecture scheme of the rectangular step Neutral Density filters (NDL-25S-4) with dimension details (Thorlabs, 2016).

3.5.1.2 Incident Photon-to-Current Conversion Efficiency (IPCE)

The *IPCE* measurement reveals how efficient a device is at converting light of a specific wavelength into electrical current. *IPCE* is defined as:

$$IPCE = \frac{electrons\ out\ (\lambda)}{photons\ in\ (\lambda)} = \frac{hc}{e}\frac{J_{PH}(\lambda)}{\lambda P_{in}(\lambda)}$$ **Equation 3-6**

The data, usually presented in *IPCE* spectra, is measured by recording the device’s photocurrent as a monochromatic light source of a known intensity scans through a range of visible wavelengths. An example of an *IPCE* spectrum can be seen in Figure 3.17. Typically, the current is measured under short circuit conditions (i.e. no bias applied) using a relatively weak light source.

Several factors influence the *IPCE* value, which can be described as the product of the light harvesting efficiency (*LHE*), injection efficiency (φ_{inj}), regeneration efficiency (φ_{reg}) and charge collection efficiency (η_{cc}) (Gabrielsson, 2014):

$$IPCE = LHE.\varphi_{inj}.\varphi_{reg}.\eta_{cc}$$ **Equation 3-7**

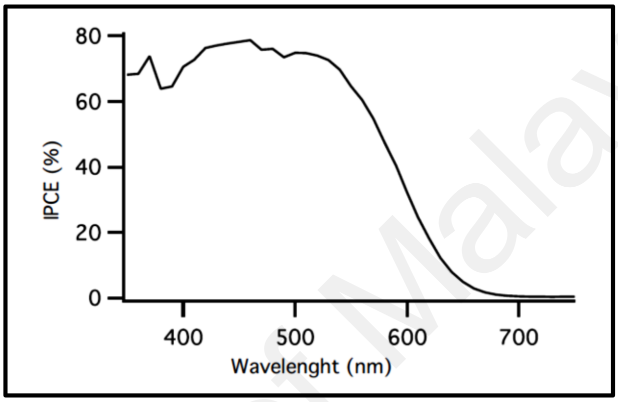

Figure 3.17: Characteristics of IPCE for a solar cell based on D35 and a cobalt electrolyte (Kaufmann Eriksson, 2014).

The principle of IPCE/EQE band gap structure in a semiconductor device introduces wavelength dependent absorptivity. A photon with energy larger than the band gap is typically absorbed by the material, while a photon with energy smaller than the band gap is not. The absorbed photon creates an electron-hole pair charge, which leads to creation of electricity. To determine a device's *QE*, one must know the power reaching the cell and its produced current at each wavelength. During a test, the computer records the currents produced by the test cell and by a calibrated photo detector. The ratio of cell current/cell (λ) to beam power is the cell responsivity, which is converted to units of quantum efficiency by using the following equation (ASTM, 1996):

$$QE = \frac{100\%.h.c.I_{cell}(\lambda)}{e.\lambda.I_{ref}.R(\lambda)}$$ **Equation 3-8**

where *h* is Planck's constant, *c* is the speed of light, *e* is the electron charge, I_{ref} (λ) is the current of the calibrated reference detector and *R(λ)* is the known responsivity value of the reference detector (in A/W).

To measure IPCE/EQE, different wavelengths were selected (350-800 nm) using the QEPVSI-b Quantum Efficiency Measurement System (NEWPORT) at School of Applied Physics, Faculty of Science and Technology, National University of Malaysia (UKM). The typical setup for IPCE/EQE measurement consists of a tunable light source, bias light source, detection system, and accessories for proper beam manipulation. The photograph of EQE system is shown in Figure 3.18. The main task of the system is to provide a nearly monochromatic light source with a typical band-pass of 1-10 nm, tunable over the whole wavelength range that the solar cell is active.

Two types of QE of a solar cell are often considered:

- **External QE (EQE) includes the effect of optical losses such as transmission through the cell and reflection of light away from the cell.**
- **Internal QE (IQE) refers to the efficiency under prohibiting of transmitted or reflected light by the cell. Only the absorbed portion of light can generate charge carriers that can generate current.**

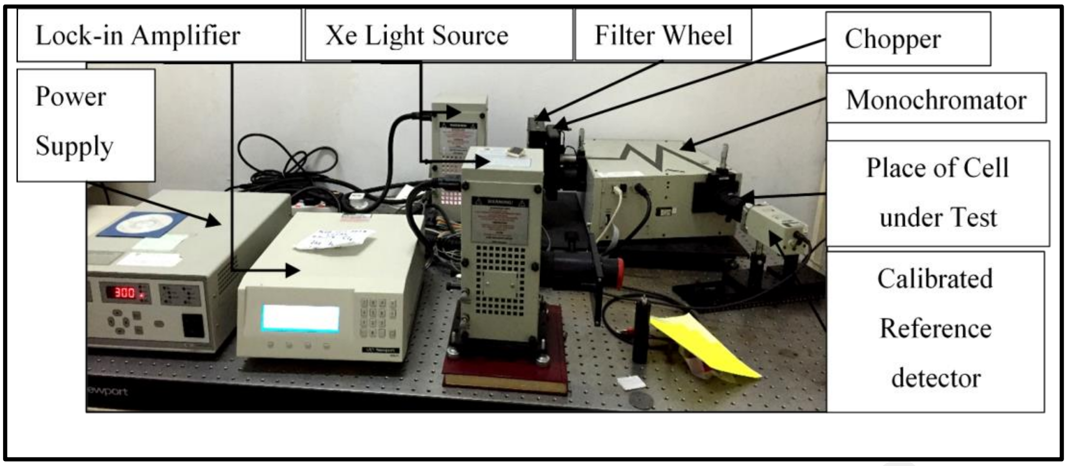

Figure 3.18: The QEPVSI-b Quantum Efficiency Measurement System.

3.5.2 Optical Characterization (Surface Spectroscopy)

3.5.2.1 Ultra-Violet-Visible-Near Infra-Red Spectrometer (UV-VIS-NIR)

Optical absorption is one of the important parameters of a solar cell. Organic materials can only absorb part of the solar spectrum. The near UV, visible and near IR part of the electromagnetic spectrum is between 0.1 µm and 2.5 µm. Absorption or reflection in this range directly affects the perceived color of a substance. The underlying effect is electronic transitions of valance electrons to higher energy states.

The materials used in this work show UV and Visible light absorption. Particle size 25 nm TiO_2 has a band gap of $E_{gap} = 3.14\,eV$ (Zielinska, Grzechulska, Grzmil, & Morawski, 2002) which corresponds to $\lambda = \frac{h.c}{E_{gap}} = 395\,nm$ which is in the UV region. The absorption can be explained by the nearly-free electron model (NFE) potential of a positive charged lattice (Pöttinger, 2014).

A Lambda 750 UV/VIS/NIR Spectrometer, whose photograph is shown in Figure 3.19, was employed to measure the optical functions of the materials. Based on the absorption spectrum data, other optical functions can be calculated such as absorption coefficient, extinction coefficient, optical energy gap, refractive index, dielectric parameters, etc., as well as finding the optical thickness of the material films through their transmittance spectra measurement.

Organic polymers and dyes are synthesized to absorb in the visible range. A model to describe the electronic states of molecules is the molecular orbital (MO) theory introduced by Friedrich, Hund and Mulliken. With this theory electron transitions of the highest occupied molecular orbital (HOMO) to the lowest unoccupied molecular orbital (LUMO) in simple molecules can be explained. The most common transitions in the near UV and Visible region are from bonding π and free non-bonding electrons into π^* or σ^* orbitals as depicted in Figure 3.19.

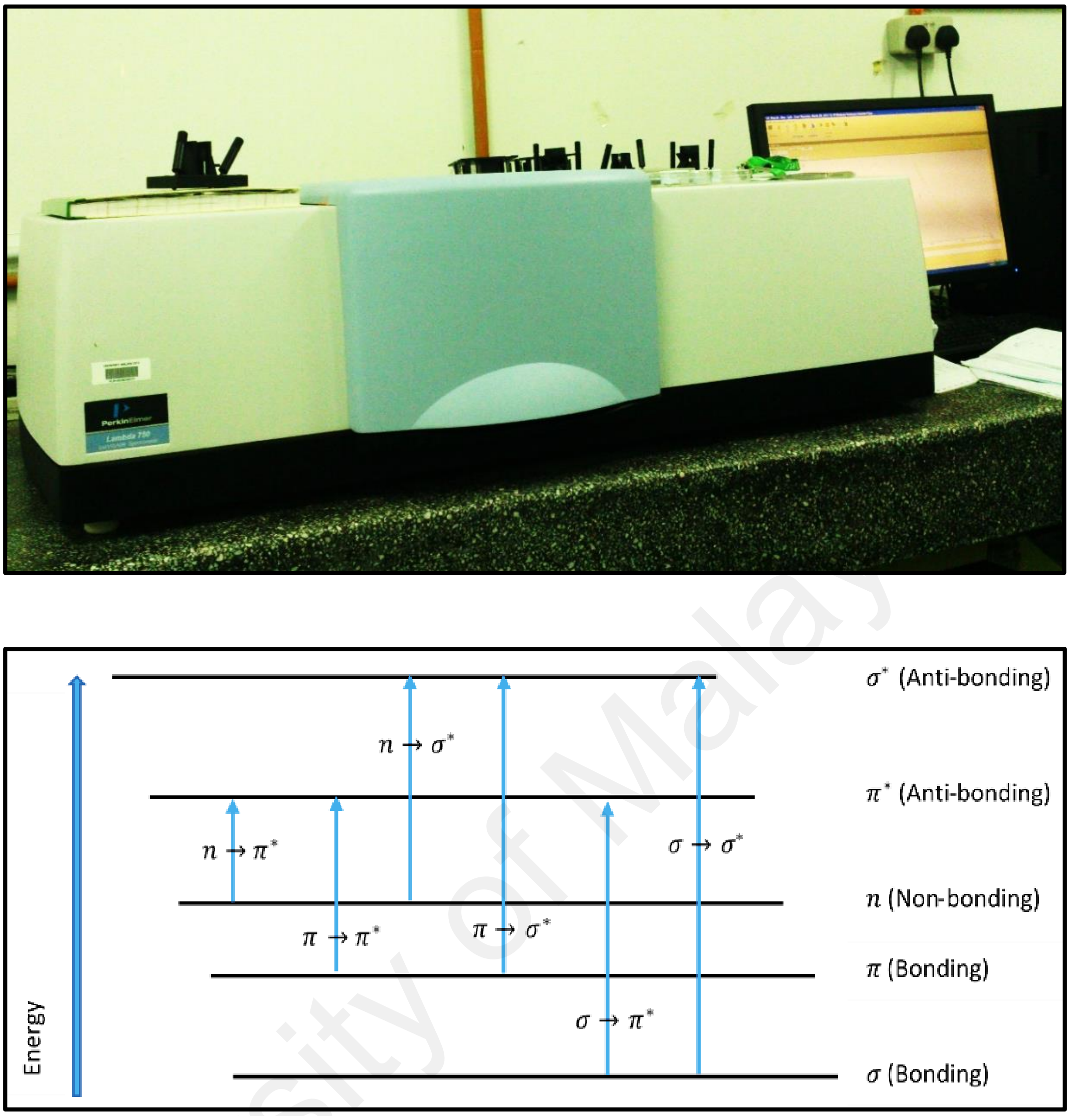

Figure 3.19: The photograph of Lambda 750 spectrometer and the energy diagram of electronic transitions in molecules. When the incoming photon energy matches the transition energy an electron can be excited and the excited state is empty.

A sample is irradiated with an intensity of UV-VIS-NIR light and the intensity I after the sample is compared to the intensity I_o of the same light before entering the medium. The ratio $\frac{I}{I_o}$ is the transmittance T of the medium, and the absorbance A can be defined using Johann H. Lambert and August Beer law:

$$A = -\log \frac{I}{I_o} = log\frac{1}{T} = \epsilon.c.d$$ **Equation 3-9**

where ϵ is the extinction coefficient (in L/(mol.cm)), *c* the concentration of absorbing species (in mol/L) and d the thickness (in cm) of the absorber.

In a solar cell photons are converted to electrons. It is therefore described that as many photons as possible are absorbed. UV-VIS-NIR spectroscopy is therefore a commonly used technique to evaluate polymers and dyes and their possibility to absorb photons at different wavelengths. By measuring the absorbance of sensitized TiO_2 films, it is possible to determine the light harvest efficiency (*LHE*) as shown in Equation 3-9, and the full formula of the *LHE* is in Equation 3-10.

$$LHE\ (\lambda) = 1 - 10^{-A(\lambda)}$$ **Equation 3-10**

$$LHE\ (\lambda) = 1 - T - R$$ **Equation 3-11**

where *T* is the transmitted light and *R* is the reflectance. In Equation 3-11*R* is assumed to be 0.

UV-VIS-NIR spectroscopy and Lambert-Beer law can be used to calculate dye coverage on the TiO_2 films. By absorbing the dye on the TiO_2 films, desorbing the dye in base solution (1,2-lorobenzene for example) and measuring absorbance of the solution, the concentration can be attained by Lambert-Beer law. If the molar extinction coefficient ϵ, of the dye in the base is known, the concentration can be calculated according to Equation 3-9. The surface coverage on the TiO_2 is given in mol/cm^2. By taking the concentration obtained, multiplying by the volume of the TiO_2, and dividing this by the surface area of the TiO_2, the surface coverage is calculated.

The three main components of UV-VIS-NIR spectrometer are a suitable light source, monochromator to select the light with the necessary wavelength, and a detector to record the intensity of the light transmitted. In the solution form, the sample is placed in a sample quartz tube called a cuvette. The intensity measured by the detector is converted into an electric signal and is displayed as a certain absorbance on the readout. Figure 3.20 illustrates the scheme diagram of the UV-VIS-NIR spectrometer operation principle (Pöttinger, 2014).

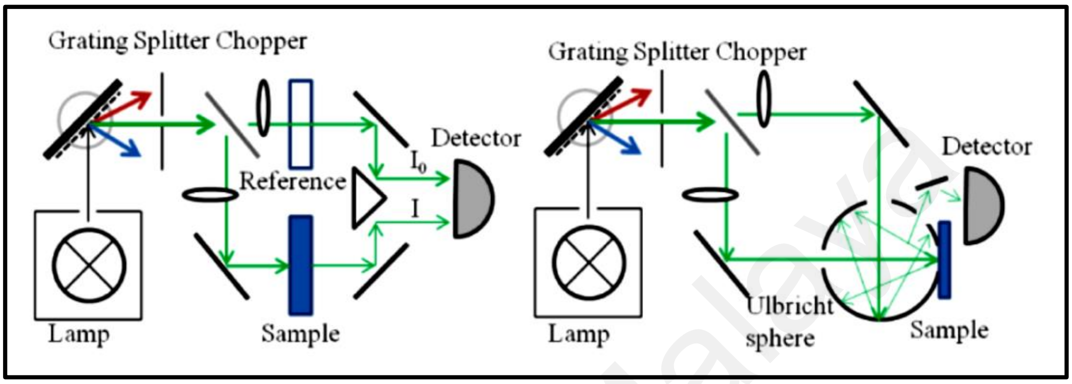

Figure 3.20: Operation principle of a two beam UV-VIS-NIR spectrometer in transmission and diffuse reflection geometry.

3.5.2.2 Photoluminescence Measurement

The PBTTT-C_{12} and PBTTT-C_{12}:$PC_{71}BM$ were dissolved in 1,2-Dichlorobenzene in the study of BHJCs. In addition, MEH-PPV in chloroform, PCPDTBT in 1,2-Dichlorobenzene, and MEH-PPV:PCPDTBT blend were prepared in the study of DS photo sensor. All solutions were spin coated on ITO glass substrate then kept for photoluminescence (PL) measurement. Steady state experiments were performed employing a RENISHAW *inVia* Raman Microscope. In Figure 3.21 is shown the photograph layout of a RENISHAW *inVia* Raman Microscope. Transient PL measurements, 10 ns exposure time pulses from a laser (IK Series He-Cd), with excitation laser 325 nm RPL near UV, low laser power 5% to prevent a heating effect on the thin films, 1200 lines/mm (633/780) grating, and 40x objective were used to excite the thin films in the spectrum wavelength range from 300-900 nm. Later, the wavelength was chosen based on the position of the highest absorption coefficient peak of the thin film.

All samples were illuminated from the top side (i.e. not through the glass substrate) in ambient pressure at room temperature.

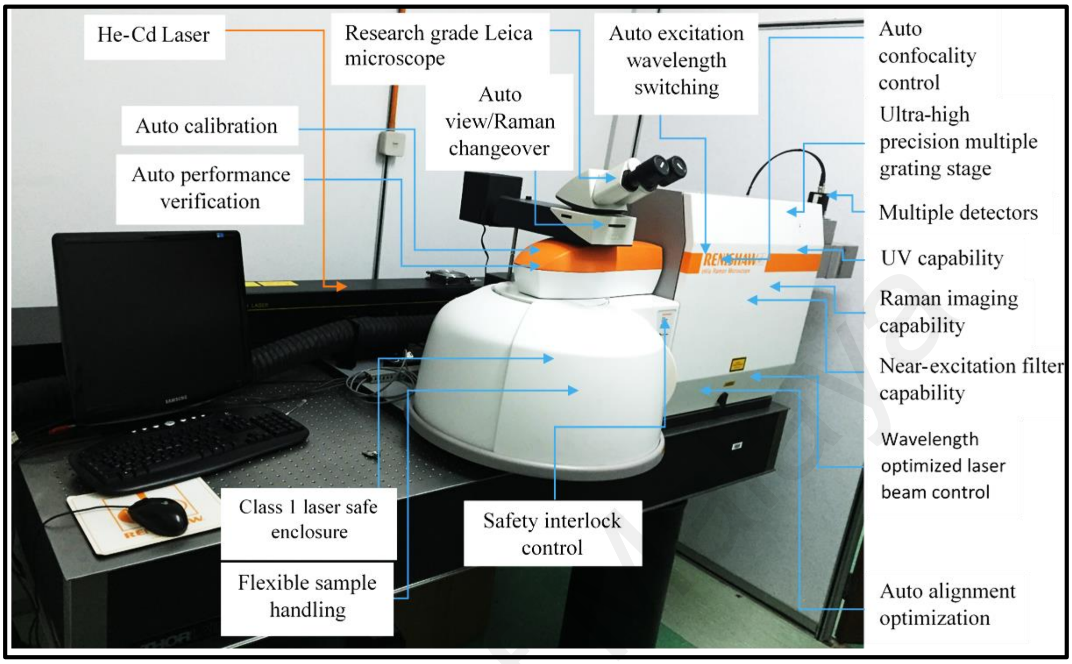

Figure 3.21: The layout of RENISHAW *inVia* Raman Microscope, with all the key components highlighted.

PL comprises both fluorescence and phosphorescence processes and the amount and type of PL depends on which material you are studying and which laser wavelength you are using. Unwanted fluorescence interference can normally be avoided by choosing an appropriate laser wavelength. PL results provide relatively direct information about recombination and relaxation processes, which are important phenomena in the photophysical consideration for both the organic BHJ and DS photo sensor materials. Luminescence is the conversion of radiation or other forms of energy to visible light. It occurs when the incident radiation excites electrons from the valence band (HOMO) through the energy gap and into the conduction band (LUMO). However, this process only can occur if the energy supplied to the electron is equal or larger than the energy gap. The excited electrons remain in the higher energy levels for a very short period of time, then they drop back to the valence band. Photons are emitted. If the wavelength of these photons is in the visible range, luminescence occurs. Energy diagram of the processes involved in the emission of light as fluorescence and phosphorescence are shown in Figure 3.22, while Figure 3.23 is illustrating the schematic of working principle behind the PL spectrometer.

Organic luminescence began in the late 1980s after pioneering work by Tang and van Slyke. Electrons and holes recombine in organic layers, leading to the emission of (visible) light. Issues here are charge transport (toward the emitting layer) and device stability. Emission can be due to band-to-band like transitions but also to optical transitions on rare-earth- (like Eu^{3+}) or transition metal ions (like Ir^{3+}) (Ronda & Srivastava, 2006).

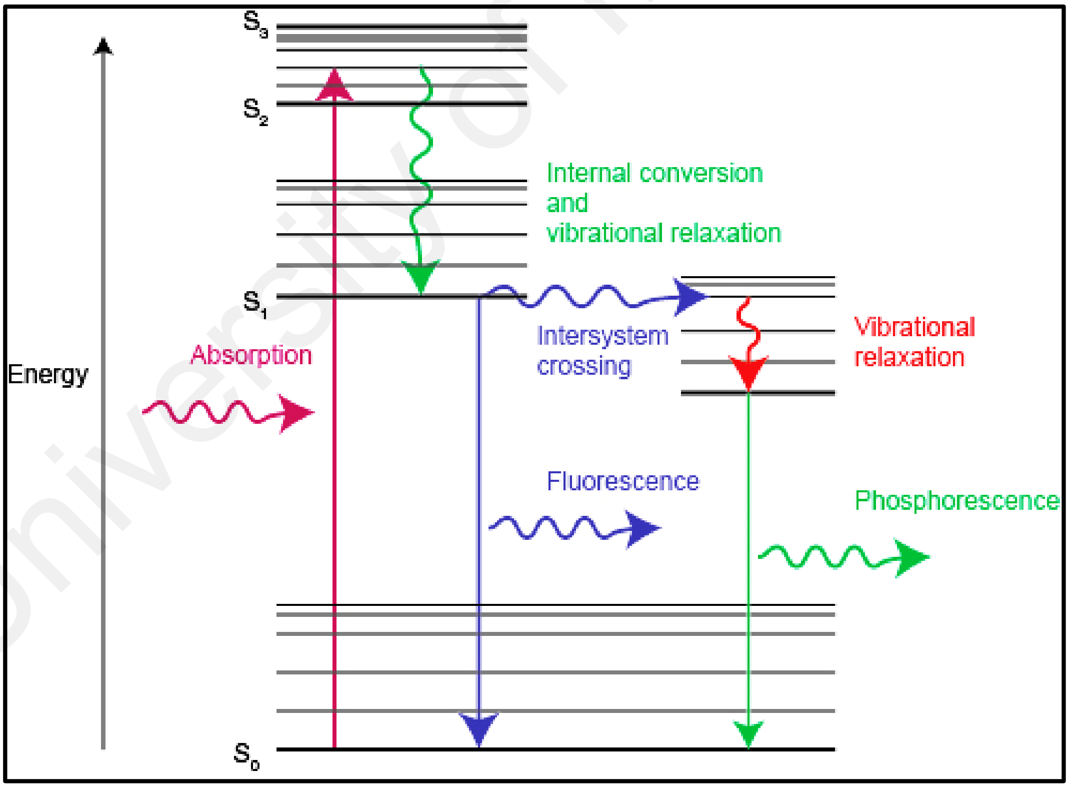

Figure 3.22: Energy diagram of absorption of light in organic materials (Renishaw, 2015).

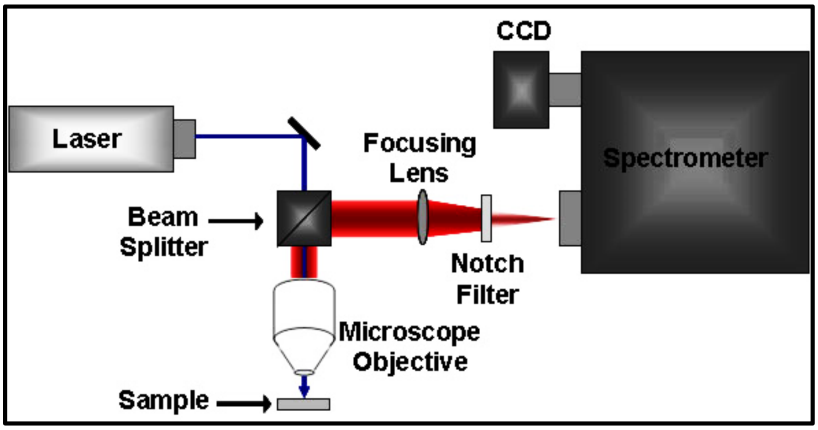

Figure 3.23: Schematic of working principle of the PL spectrometer.

3.5.3 Surface Topography

3.5.3.1 Atomic Force Microscopy (AFM)

The invention of Atomic Force Microscopy or scanning force microscopy was by Binnig et al. in 1986, and belongs to the group of scanning probe microscopes (Binnig, Quate, & Gerber, 1986). It is utilized to study the topography of the PBTTT-C_{12}:$PC_{71}BM$ thin films surfaces with sub-nm resolution. A fine microscopic tip is attached at the end to a cantilever which is made of either silicon or silicon nitride, in which the Van-der-Waals force between a scanning tip and the sample is utilized. In this work a Tapping mode of Veeco Dimension 3000 is used. The AFM is better than the scanning tunnelling microscope which was developed before, as it is able to measure insulating samples as well. The sample is typically mounted on a 3D piezoelectric scanner which is used to move the tip relative to the sample surface. The tip is forced to oscillate while scanning close to the surface. The frequency of the oscillation and the tip height over the surface are in a feedback loop. When the oscillating tip is approaching the surface utmost atoms interact due to induced dipole interaction. The amplitude of this oscillation is greater than 10 nm, typically 100 to 200 nm. A slight change in oscillating frequency is detected. The feedback system regulates the detected frequency back to the exciting frequency by regulating the distance from the surface, i.e. the bending of cantilever is detected by optical means using a laser beam and this laser beam is reflected from the backside of the cantilever. The tip follows the surface morphology and the motion is plotted. Basic working principle of AFM shown in Figure 3.24.

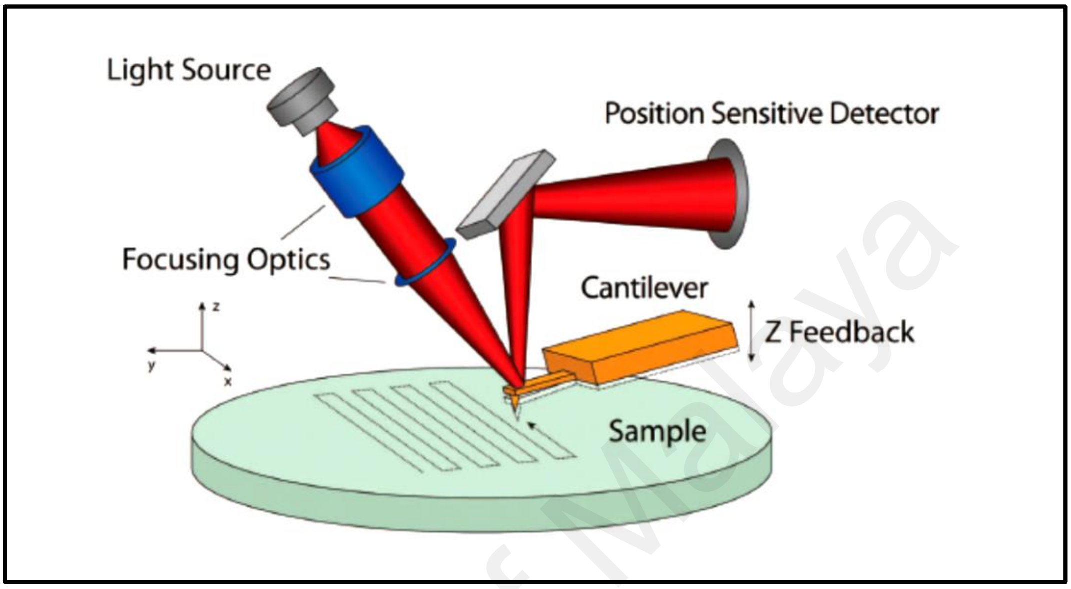

Figure 3.24: The working principle of the D3000 AFM (Pekkola, 2014).

AFM can be used in different modes according to the nature of the tip motion in order to study samples depending upon the type of sample and the required information. These techniques include contact mode, where the tip is remains constantly in contact with the surface of the sample and "dynamic modes" such as Tapping mode or non-contact mode.

In Tapping mode, and in ambient conditions, most samples develop a liquid meniscus layer. Keeping the probe tip close enough to the sample for short-range forces to obtain the required sensitivity, while preventing the tip from sticking to the surface presents a major problem for non-contact dynamic mode in ambient conditions. Dynamic contact mode (also called intermittent contact, AC mode or Tapping mode) was developed to bypass this problem (Zhong, Inniss, Kjoller, & Elings, 1993). Tapping mode, in which is both modes are combined, is gentle enough even for the visualization of supported lipid bilayers or adsorbed single polymer molecules (for instance, 0.4 nm thick chains of synthetic polyelectrolytes) under liquid medium. With proper scanning parameters, the conformation of single molecules can remain unchanged for hours (Roiter & Minko, 2005).

Depending on the imaging mode of the AFM, different interaction forces are employed to gain the topography of the sample. Hence, the repulsive forces in Figure 3.25 are detected. For smooth samples, the height of the cantilever is kept constant (constant height mode) and the repulsive force is measured directly, whereas for rough samples the force on the cantilever which is the bending of the cantilever is kept constant by adjusting the height of the sample (constant force mode). The bending of the cantilever is due to the interaction of the tip and the sample and can be described in good approximation by the Lennart-Jones potential.

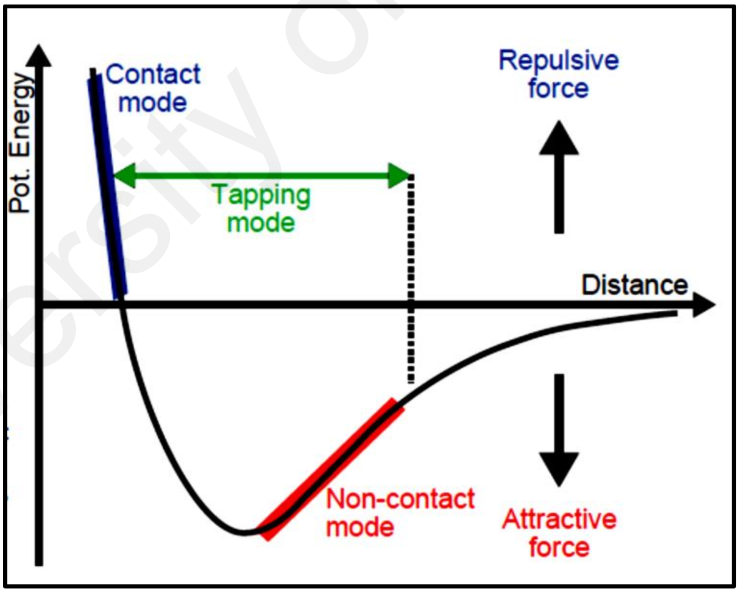

Figure 3.25: The different imaging mode of the AFM indicated in the Lennart-Jones potential.

3.5.3.2 Field Emission Scanning Electron Microscope (FESEM)

A field emission scanning electronic microscope provides surface morphology with a magnification of up to 10^6 by scanning the sample with a high energy focused beam of electrons instead of using light. The surface micrographs of the TiO_2 thin films obtained from FESEM are very important to visualize the surface morphology and structural distribution of the TiO_2 untreated and treated with NaOH thin films. More details are in CHAPTER 4: section 4.4. The photograph of this machine is shown in Figure 3.26 (Date taken 17th Feb 2015).

Figure 3.26: FESEM (JEOL JSM-7600F).

An electron gun emitted the electron beam which usually consists of a tungsten or lanthanum hexaboride (LaB_6) cathode which is focused and scanned over the sample by different electromagnetic lenses in the electron optical column. Therefore, the electro optical column has to be pumped to ultra-high vacuum conditions to minimize the interactions of the electrons with residual gas molecules in the column.

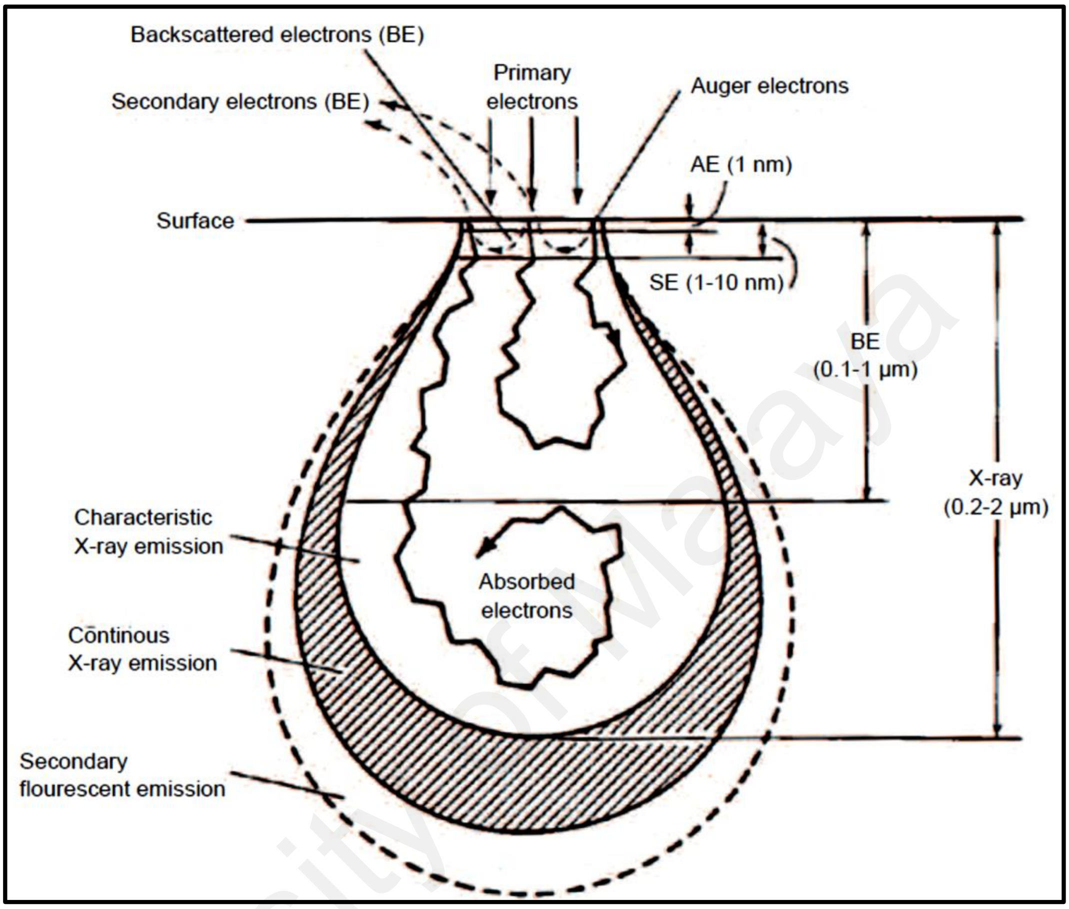

Figure 3.27: Areas of interaction of the electrons with the matter and the information depth of the detected radiation and electrons, respectively (Pekkola, 2014).

Inelastic scattering in the sample leads to ionization of the atoms. Because these so called secondary electrons (SE) have an energy of less than 50 eV, only electrons in a region less than 10 nm under the surface of the specimen are detected. A high topological contrast can be achieved by secondary electrons as the intensity of the SE varies strongly depending on the geometry of the specimen. For example, in a small particle and at an edge, more SE can leave the sample and be detected than on a flat structure, whereas, for example by tilting, certain regions of the sample can be shadowed by features which stand out. FESEM images taken in this work are mainly recorded by SE.

Another type of signal is backscattered electrons (BSE). These are primary electrons which are scattered elastically before leaving the sample. Depending on the losses due to the scattering processed within the specimen, their energy can reach the energy of the primary electrons. As the intensity of the BSE are strongly dependent on the atomic number of the specimen, an image can be created which mirrors the distribution of different elements in the sample.

In addition to SE and BSE, characteristic X-radiation can be used to characterize the sample. Similar to BSE, X-radiation originates from a larger volume than SE and is used to identify and map elements on the surface of a sample. Hereby, the incident electron beam ejects an electron from the sample atoms. Subsequently, characteristic X-ray radiation is emitted when an electron from an outer shell fills the vacancy of the ejected electron in one of the inner shells as shown in Figure 3.27 (above) (Pekkola, 2014).

Electron microscopes were developed due to the limitations of light microscopes which are limited by the physics of light in contrast to light microscopy (LM) which uses visible light as a source of illumination and optical (glass) lenses to magnify specimens in the range between approximately 10 to 1000 times their original size. The electron microscope takes advantage of the much shorter wavelength of the electron (i.e., λ = 0.005 nm at an accelerating voltage of 50 kV) when compared to the wavelengths of visible light (λ = 400-700 nm). Depending on the instrument used, specimens can be magnified roughly between 10 and 100000 times in SEM and to 300000 times in FESEM. Figure 3.28 is the schematic of the basic components of a SEM. Conventional electron microscopy as used today have now been adapted to operate under the guidance of computers which makes sample viewing, image storage and labelling, as well as micrograph analysis easier for the investigator (Stadtländer, 2007).

A field emission cathode in the electron gun of a scanning electron microscope provides narrower probing beams at low as well as high electron energy, resulting in both improved spatial resolution and minimized sample charging and damage. In summary, the major advantages of FESEM are (PhotoMetrics, 2014; physics.montana.edu, 2011):

- **Ultra-high resolution at low kV: 1.7 nm at 1 kV, and 4 nm at 0.1 kV. This is 3-6 times better than conventional SEM.**
- **Quantitative elemental analysis of the bulk material.**
- **Smaller-area contamination spots can be examined at electron accelerating voltages compatible with Energy Dispersive X-ray Spectroscopy.**
- **Fast elemental mapping and/or line scan of area of interest.**
- **Topographical, compositional and other information.**
- **Detection of small variations of trace element content.**
- **Reduced penetration of low kinetic energy electrons probes closer to the immediate material surface.**
- **Analysis and imaging of samples in their natural, hydrated state.**
- **Digital image capture, high quality, low voltage images are obtained with negligible electrical charging of samples. (Accelerating voltages range from 0.5 to 30 kV.)**
- **Oil-free vacuum.**
- **Need for placing conducting coatings on insulating materials is virtually eliminated.**
- **Large specimen capacity.**
- **Rapid (ten-minute turnaround) sample introduction.**

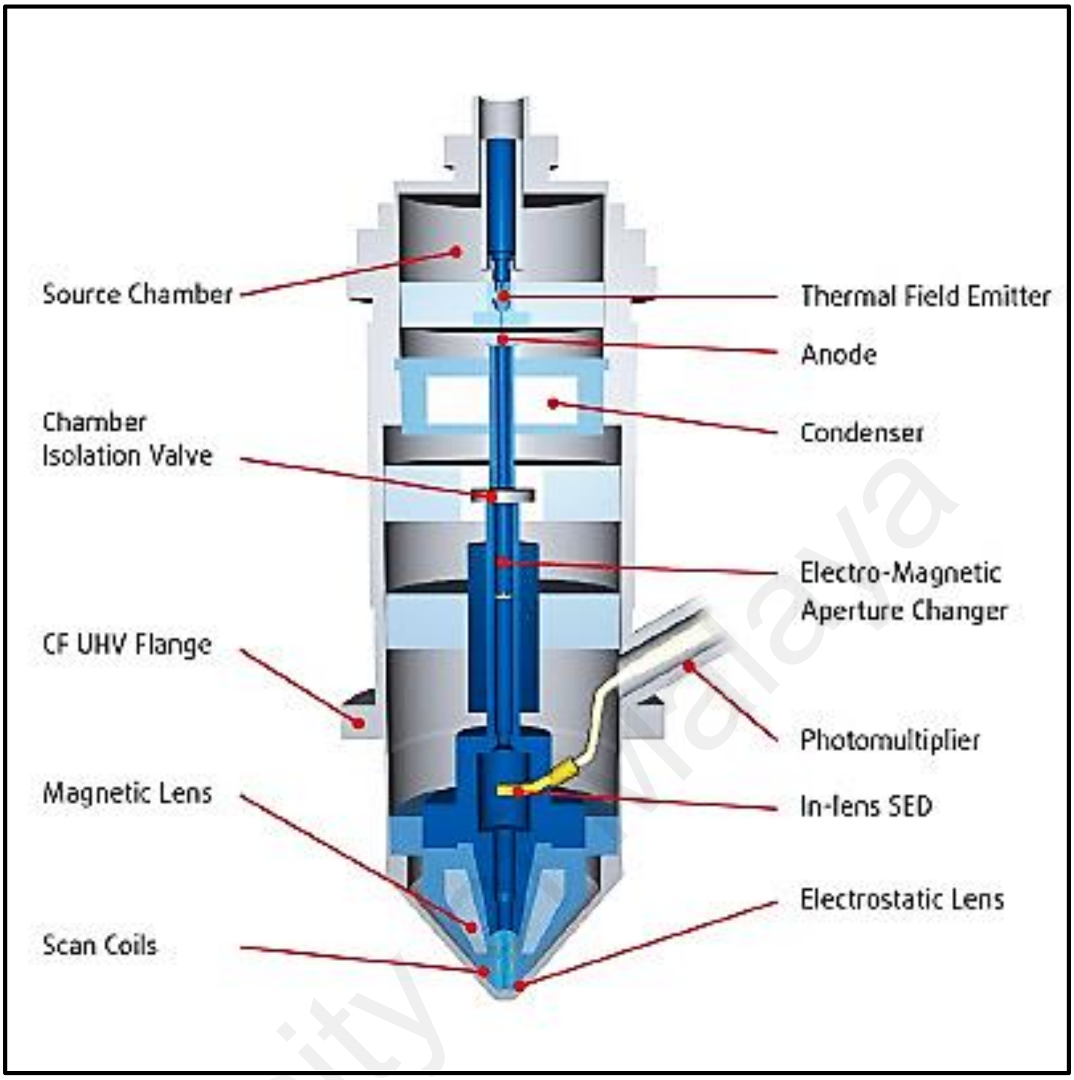

Figure 3.28: Schematic basic parts of a Scanning Electron Microscope.

CHAPTER 4: PERFORMANCE ENHANCEMENT OF NITSPC BASED PHOTO SENSOR USING TREATED TIO_2 NPs FILM

4.1 Chapter Overview

Present study, shows the possibility to make solution-based DS photo sensors by employing Nickel (II) phthalocyanine-tetrasulfonic acid tetrasodium salt (NiTsPc) aqueous solution. Surface morphological analysis has been performed by Field Emission Scanning Electron Microscope (FESEM) to study the effect of sodium hydroxide (NaOH) treatment on the performance of TiO_2 working electrode. NaOH treatment of TiO_2, is believed to increase the dye loading capacity which resultantly would help increase the sensing parameters of the device.

4.2 Introduction

Metallophthalocyanine (MPc) and related compounds have been extensively studied during past few decades because of their potential technological applicability in light harvesting applications (Dong, Zhu, Meng, Gong, & Hu, 2012; Rodriguez-Mendez, Gorbunova, & De Saja, 2002; Spadavecchia, Ciccarella, Siciliano, Capone, & Rella, 2004; Wu et al., 2013; Zhu, Petty, & Harris, 1990). The unique features of phthalocyanines such as photo sensitive semi-conductivity, fast enough photoresponse times, well-defined redox activity, and thermal stability (Crespilho et al., 2006; Rao & Rao, 2002) are by virtue of their macrocyclic molecular design and delocalized and two-dimensional π-electrons distribution. Yet another advantage is that the photophysical and chemical properties of MPc can be further tuned by regulating the molecular design, i.e., by judicious choice of central metal ion or by incorporating varied peripheral substituents by substituting the isoindole units of the MPc. For instance, J.R. Silva (Silva et al., 2011) reported that insoluble nickel phthalocyanine can be made water soluble by tuning sulfonation of the phthalocyanine ring molecular structure. Nickel (II) phthalocyanine-tetrasulfonic acid tetrasodium salt (NiTsPc) thus formed is a potential candidate for device applications in the area of electronics and optoelectronics (Fakir et al., 2012; Fernandes et al., 2010; Vieira et al., 2011; Wiziack et al., 2009). NiTsPc exhibits a p-type semi-conductivity which is proper to be adsorbed on the n-type metal oxide TiO_2 semiconductor and shows an ohmic and space-charged limited conduction at low and higher applied voltages, respectively, when suitable metal electrodes are employed (Anthopoulos & Shafai, 2002). Hole mobility of NiTsPc is reported as 10^{-5} m^2/Vs. As for the photophysical property, J.B. Brito previously reported that absorption spectrum of NiTsPc aqueous solution exhibits two absorption peaks in B and Q band, respectively (Brito et al., 2012). The intense peak in Q band (centered at 620 nm) is associated with dimers and a shoulder peak in same band within 650-660 nm which is attributed to NiTsPc monomers. The B band in the UV region (at around 340 nm) also dominates the absorption spectrum of NiTsPc. The choice of NiTsPc as sensitizer in this study is by virtue of its significant visible wavelength absorption, water solubility feature, and eco-friendly nature. Semiconductor TiO_2 (band gap, Eg ~ 3.2-4.2 eV, wavelength region that suits this energy is less 400 nm), has been used to facilitate light-induced redox processes because of its conductive electronic structure (Niehues et al., 2010).

4.3 Fabrication of Dye Sensitized Photo Sensor

For the fabrication of DS photo sensors, ITO substrates (dimension $= 2 \times 2$ cm^2, and thickness ~ 150 nm) with sheet resistance of 10 Ω/cm^2 were used. The ITO substrates were properly washed by previously explained cleaning procedure. To prepare the working TiO_2 electrodes (photo anode), TiO_2 powder was used with nanoparticle sizes of ~25 nm. Two different types of TiO_2 pastes were prepared by employing two different methods. The first (untreated) type was prepared by mixing the TiO_2 nanoparticles with poly(ethylene glycol) (PEG) in 10:1 by weight flowed by slow addition of ethanol to prevent the aggregation of the nanoparticles. However, in order to prepare the second (treated) TiO_2 paste, 0.375 g of TiO_2 nanopowder was first mixed with 10 M sodium hydroxide (NaOH) aqueous solution (30 ml) and stirred for 15 min. Then, the milky white solution was heated at 140 ℃ for 24 h. The resulting product was washed and centrifuged several times with de-ionized water. The product obtained thereafter, was treated with 0.1 M HCl and washed again. Finally, the low pH solution was calcined at 500 ℃ for 2 h under open air condition in Clean Room. The treated TiO_2 nanoparticles were then mixed with PEG in 10:1 (by weight) to prepare the paste, followed by the sonication for 2 h with slow addition of ethanol to prevent the aggregation of the particles. Both types of TiO_2 pastes were deposited on the ITO glass substrates, through a defined pattern mask with a square-shaped opening (dimension $= 1 \times 1$ cm^2), made with special adhesive (Scotch) tape. Thin films of TiO_2 pastes were then dried at 25 ℃, followed by sintering for 30 min at 450 ℃ (temperature rise and fall rate $=$ 2 ℃/min) to get TiO_2 compact films.

The semiconductor dye, NiTsPc was dissolved in de-ionized water with concentration of 10 mg/ml. The dye solution was drop casted on both types of compact TiO_2 films. The amount of dye load in each photoanode was $\sim 8.17 \times 10^{-7}$ mol/cm^2 which is in the standard range of 10^{-5} to 10^{-8}, whereas the optimum thickness of TiO_2 film was ~15 µm. Films were later heated at 80 ℃ for 20 min (temperature rise and fall rate = 4 ℃/min). As for the counter electrodes, platinum thin films (~10 nm thick) were sputter coated on ITO glass substrates. Subsequently, both the TiO_2+dye (photo anode) and Pt-coated electrodes (photo cathode) were assembled in such away that the commercially available electrolyte (Iodolyte Z100, redox couple: iodide/triiodide) was sandwiched in between. The sealing was achieved utilizing thermoplastic film (100 µm thick). The purpose of the electrolyte is to act as a pure relay substances for the transport of charges, because of their redox potential (Gratzel & Liska, 1992). The molecular structure of NiTsPc and device design is depicted in Figure 4.1.

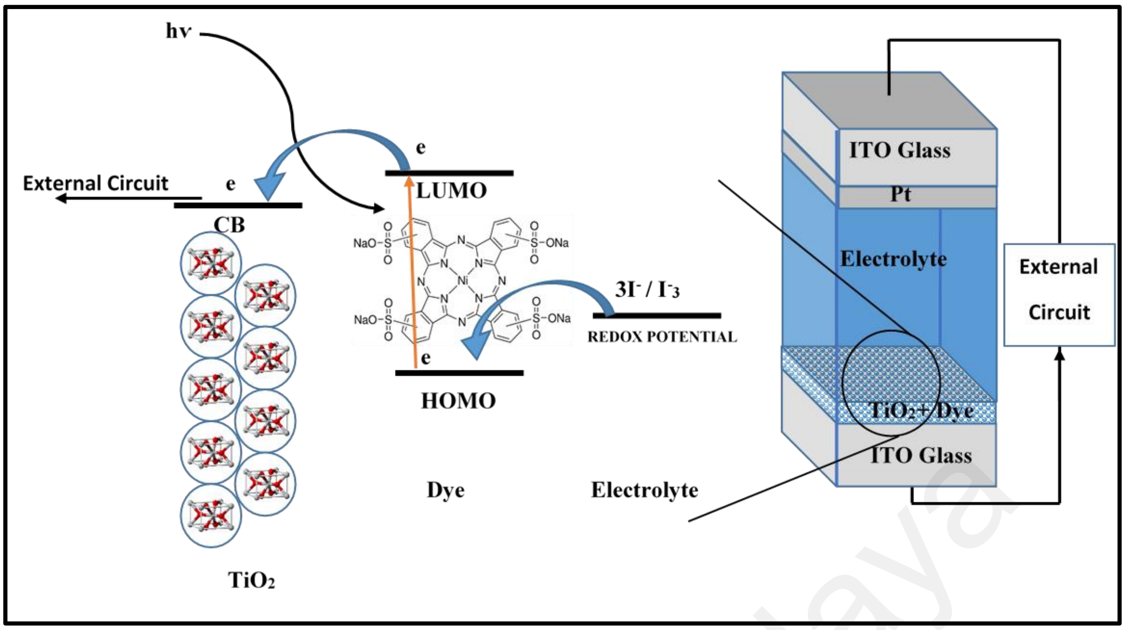

Figure 4.1: Molecular structure of NiTsPc, device design and working mechanism of the photo sensors.

4.4 Results and Discussion

The FESEM micrographs of the TiO_2 films prepared by both methods are presented in Figure 4.2. FESEM micrograph of the TiO_2 film obtained from untreated is shown in Figure 4.2 (a), whereas Figure 4.2 (b) represents the FESEM image of the film obtained by the TiO_2 nanoparticles treated with NaOH. It can be observed that both the films exhibit crack-free morphology. However, it can be perceived that in micrograph Figure 4.2 (a), the TiO_2 nanoparticles formed agglomerates. Further, the thin film in sample Figure 4.2 (a) also possesses high voids, since the PEG binder has decomposed after the sintering process in the paste. However, in micrograph Figure 4.2 (b), TiO_2 nanoparticles after treatment with NaOH are well separated and look quite arranged. This arrangement, therefor, allows the NiTsPc dye to penetrate homogeneously to inter pore region leading to the homogeneous distribution of the dye.

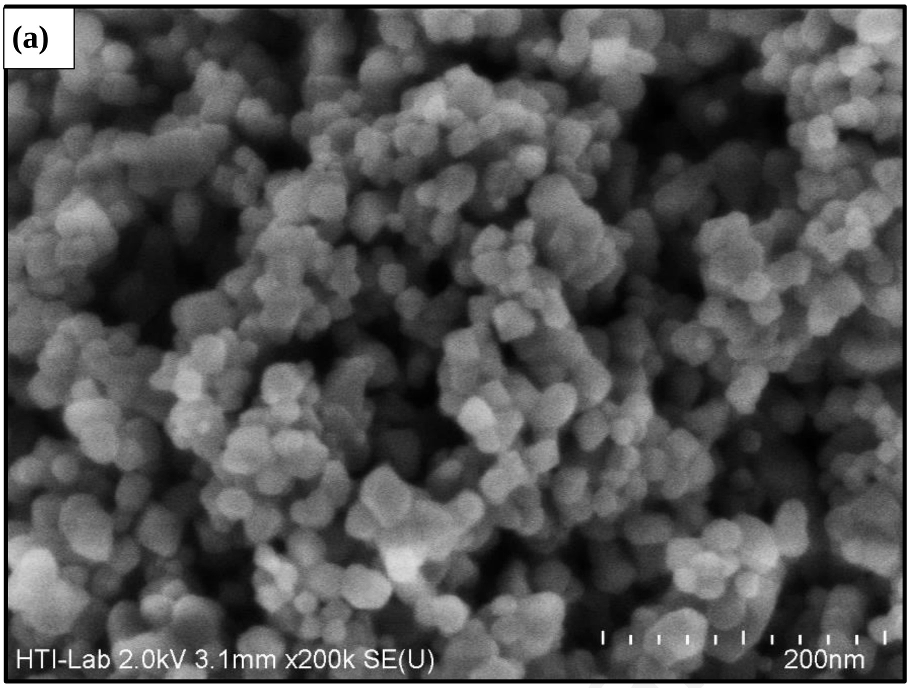

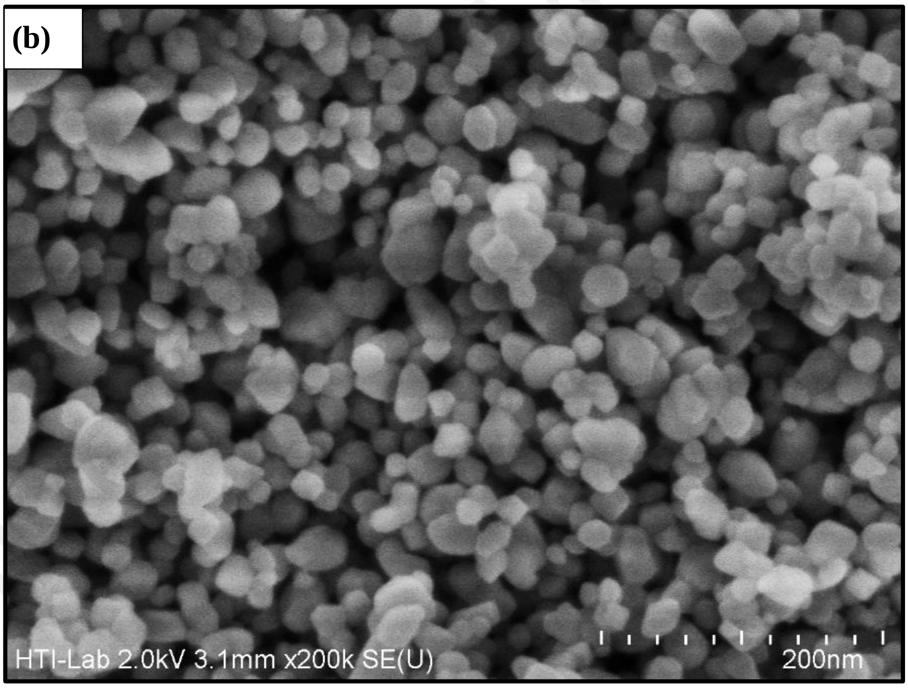

Figure 4.2: FESEM micrographs: (a) untreated TiO_2 film and (b) TiO_2 film obtained after treating with NaOH.

The current/voltage versus illumination relationship for the samples is given in Figure 4.3. Figure 4.3 (a) shows the voltage and current as a function of different illumination levels ranging from 0 to 150 mW/cm^2 with delay time of 10^{-6} sec for the ITO/dye covered untreated TiO_2/electrolyte/Pt/ITO. The standard deviation (error values) of the measurements were found around $\pm$ 0.029 for the voltage and $\pm 8.22 \times 10^{-7}$ for the current. It is observed that the photocurrent exponentially enhanced as the intensity increase. The voltages were almost constant over the whole investigated intensity range. The current-voltage dependence of the intensity of light in ITO/dye covered treated TiO_2/Electrolyte/Pt/ITO is depicted in Figure 4.3 (b). The standard deviation (error values) of the measurements were found around $\pm$ 0.027 for the voltage and $\pm 1.89 \times 10^{-7}$ for the current. It is evident that the current is linearly proportional to illumination intensity, indicating no limit of mass (charge) transport. It is observed that the increment in the short circuit current is higher using the treated TiO_2 with the increased light intensity, indicating that the number of electrons through treated TiO_2 diffused higher than through untreated TiO_2 and decreases the rate of undesired electron recombination at the TiO_2-electrolyte interface. By the following equation, the photocurrent dependence of illumination light can be evidenced (Ahmad, Abdullah, et al., 2013):

$$I_{Ph} = Const. F^{\propto}$$

Equation 4-1

where I_{Ph} is the photocurrent, F is the optical power, and α is an empirical value that can be obtained from the slope of I_{Ph} is a function of F (illumination of light). The photosensing phenomenon is believed to involve, first, the light absorption which is carried out by the chromophore, i.e., NiTsPc. This leads to exciton generation in the dye component, subsequently these excitons are separated at the dye/TiO_2 interface. Once the dye NiTsPc has been exposed to sunlight, the molecules are excited and the electrons are drifted to the edge of conduction band of the porous TiO_2 thin film. These electrons are collected by the external load for completing the cycle before it goes to the electrolyte of the cathode surface. The electrolyte as a redox couple system regenerates the NiTsPc dye molecule by collecting the electrons through the Pt counter electrode. The difference between the redox potential of the electrolyte and the Fermi level of electron in the solid (metal oxide semiconductor TiO_2) corresponds to generate the photovoltaic in DS photo sensors. Photocurrent is due to the charge carriers, which are generated as a result of the excited charge at the NiTsPc dye, covalently attached to the surface of TiO_2 mesoporous oxide layer. As a result, at a certain voltage, when the light intensity increases the current is increased. The fabrication of the DS photosensors was done in ambient condition, and electrical characterization of the photosensors was performed after the aging process. The devices exhibit poor photovoltaic parameters, which are not suitable for the solar cell applications. However, they are quite adequate for the photosensing application.

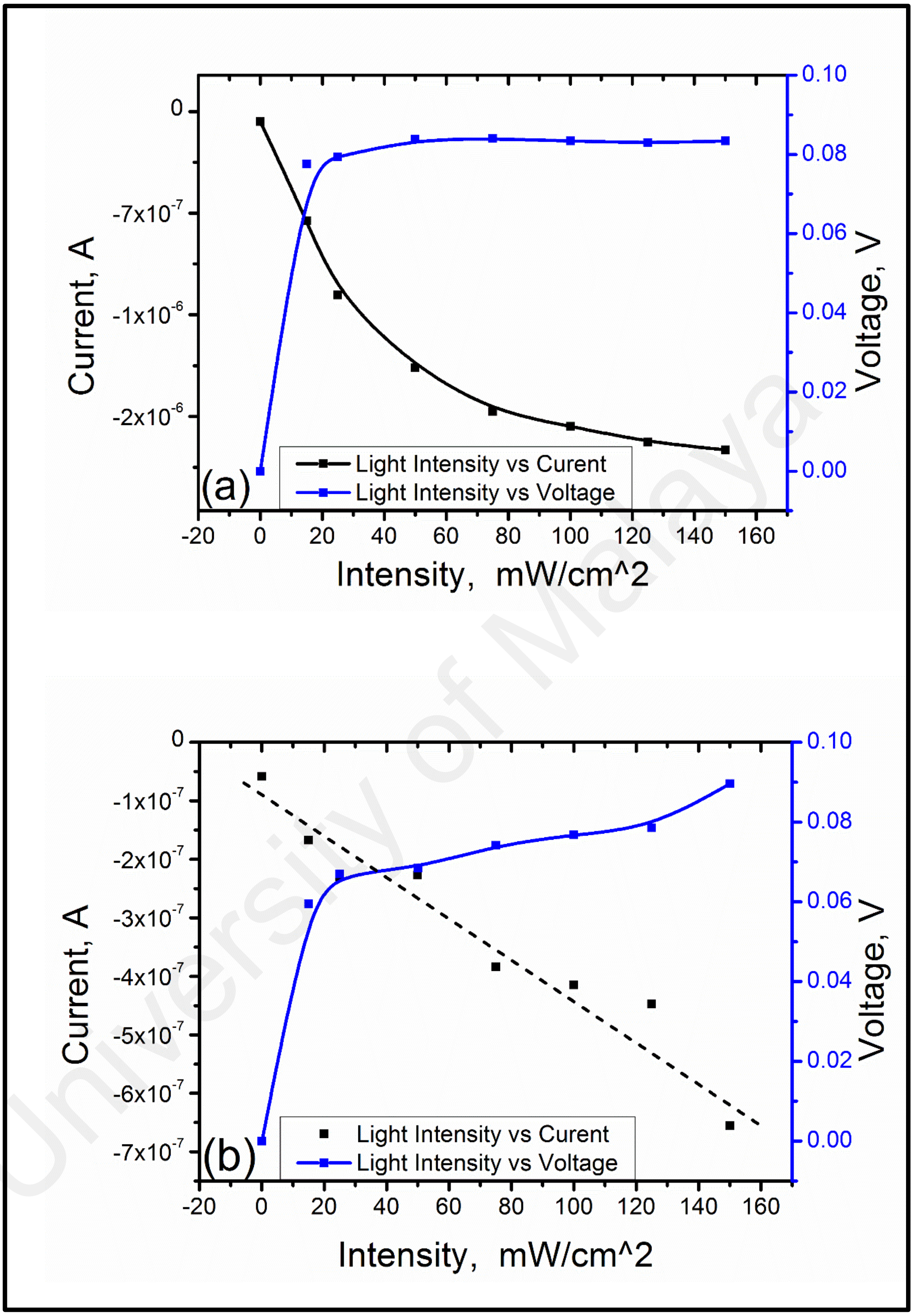

Figure 4.3: The characteristic behavior of current vs. illumination intensity and voltage vs. illumination intensity of the photo sensors. (a) Photo sensors fabricated using untreated TiO_2. (b) Photo sensors fabricated using treated TiO_2.

Using the data acquired by studying photovoltage and photocurrent at various incident light intensities, dependence of logarithmic photocurrent and voltage on logarithmic light intensity of the photo sensors was also studied. These experimental results are depicted in Figure 4.4. The photocurrent is linearly proportional to the illumination intensity with slopes of 1.35 and 3.37 in photo sensors Figure 4.4 (a) and (b), respectively. Moreover, the photovoltage has also been found proportional to logarithmic illumination in both photo sensors Figure 4.4 (a) and (b). The standard deviation (error values) of the measurements were found around ± 0.029 and ± 0.027 for the voltage of (a), (b) and $\pm 8.22 \times 10^{-7}$ and $\pm 1.89 \times 10^{-7}$ for the (a), (b) current, respectively. The irregular distribution of data points and saturation of current (Figure 4.4 (a)) may due to mass (charge) transport limitations (Hara et al., 2000). In addition, the data points distribute and diverge more in the Figure 4.4 (a) than the Figure 4.4 (b) which mean that the treated TiO_2 has less limitation to charge transport and enhance charge transport compared to untreated TiO_2. Despite this, variation of photo voltage was observed in the photo sensor Figure 4.4 (b) at 100 mW/cm^2 suggesting that with increasing illumination, temperature of the cell will increase. By the following equation, photocurrent and photo voltage relationship are evidenced (Hara et al., 2000):

$$V_{oc} = \frac{nKT}{Q} ln\left(\frac{I_{sc}/A}{I_o} + 1\right) \qquad \textbf{Equation 4-2}$$

where, Q, T, K, and n are the electric charge, the absolute temperature, the Boltzmann constant, and the quality diode factor, respectively, A is the active area of photo anode and I_o is the saturation current. According to the Figure 4.4, the photo voltages show the logarithmic dependence on illumination, therefore, the photo voltage relationship in Equation 4-2 can be used for the NiTsPc photo sensors.

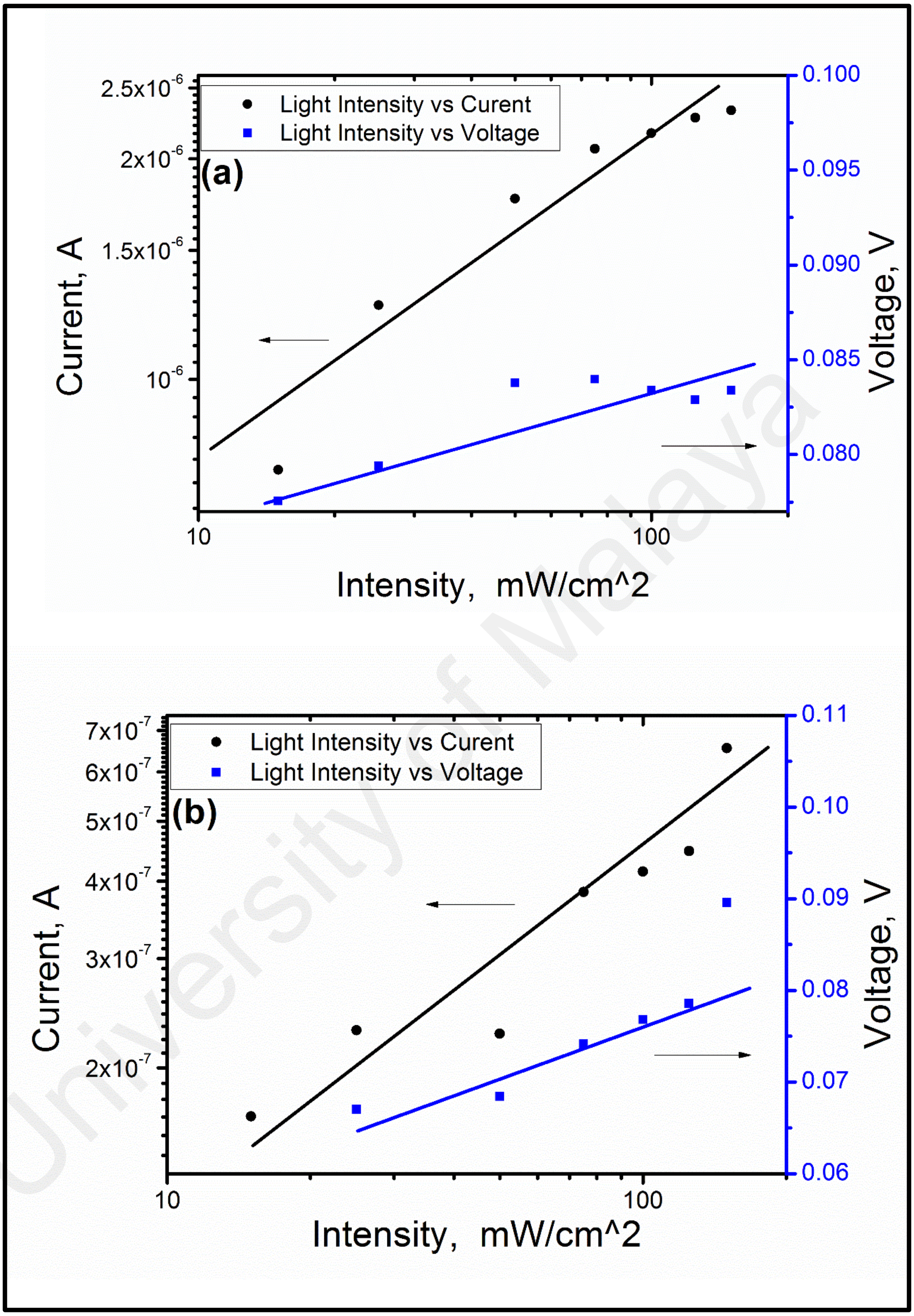

Figure 4.4: The characteristic behavior of dependences logarithmic current and voltage on logarithmic light intensity of the photo sensors for (a) photo sensors fabricated using untreated TiO_2, (b) photo sensors fabricated using treated TiO_2.

Photo-conductivity, photo-sensitivity, and response/recovery time of both types of the photo sensors have been compared. The photoresponse characteristics of the sensors have been studied as a function of periodic stepped light input. Figure 4.5, depicts the repeated cycles of photocurrent variation of the photo sensors (input bias = 0.2 V) under the on and off modulation of the incident light (the pulse width was ~5 sec). In general, if the electrolyte has no mass transport issue, the photocurrent should rapidly reach a high value and remain constant for a defined period, and thereafter reach a low value when the light is periodically turning on and off, respectively. From the measurements, the response (t_r) and recovery times (t_c) for sensor Figure 4.5 (a) were estimated to be (t_r = 300 ms, t_c = 800 ms). In contrast, in case of sensor Figure 4.5 (b) the photocurrent indicates comparatively fast response and recovery time (t_r = 200 ms, t_c = 300 ms). Relatively improved results for sensor Figure 4.5 (b) may be attributed to enhanced electron transport observed in NaOH-treated TiO_2 thin film. It is worth noting, that in case of the sensor Figure 4.5 (b), the photocurrent value also exhibits a relatively more stable plateau, once the light was switched on and off for a certain duration. Overall, both sensors showed rapid changes in states of photocurrent as a function of stepped light input. Photo-conductivity sensitivity of the photo sensors can be determined by the following relation:

$$S = \frac{I_{ph-current}\,T}{PAV} \qquad \textbf{Equation 4-3}$$

where $I_{Ph-Current}$ is the current under initial state, T is the thickness of the cell (from ITO to Pt electrode), P is the power of light, A is the cell's active area, and V is the bias voltage. The value of the photo-conductivity sensitivity of the photo sensors is determined to be 6.65×10^{-5} and 1.87×10^{-4} Sm/W, respectively. The responsivities of the sensors were found to be 3.3×10^{-5} A/W and 3.7×10^{-5} A/W, respectively.

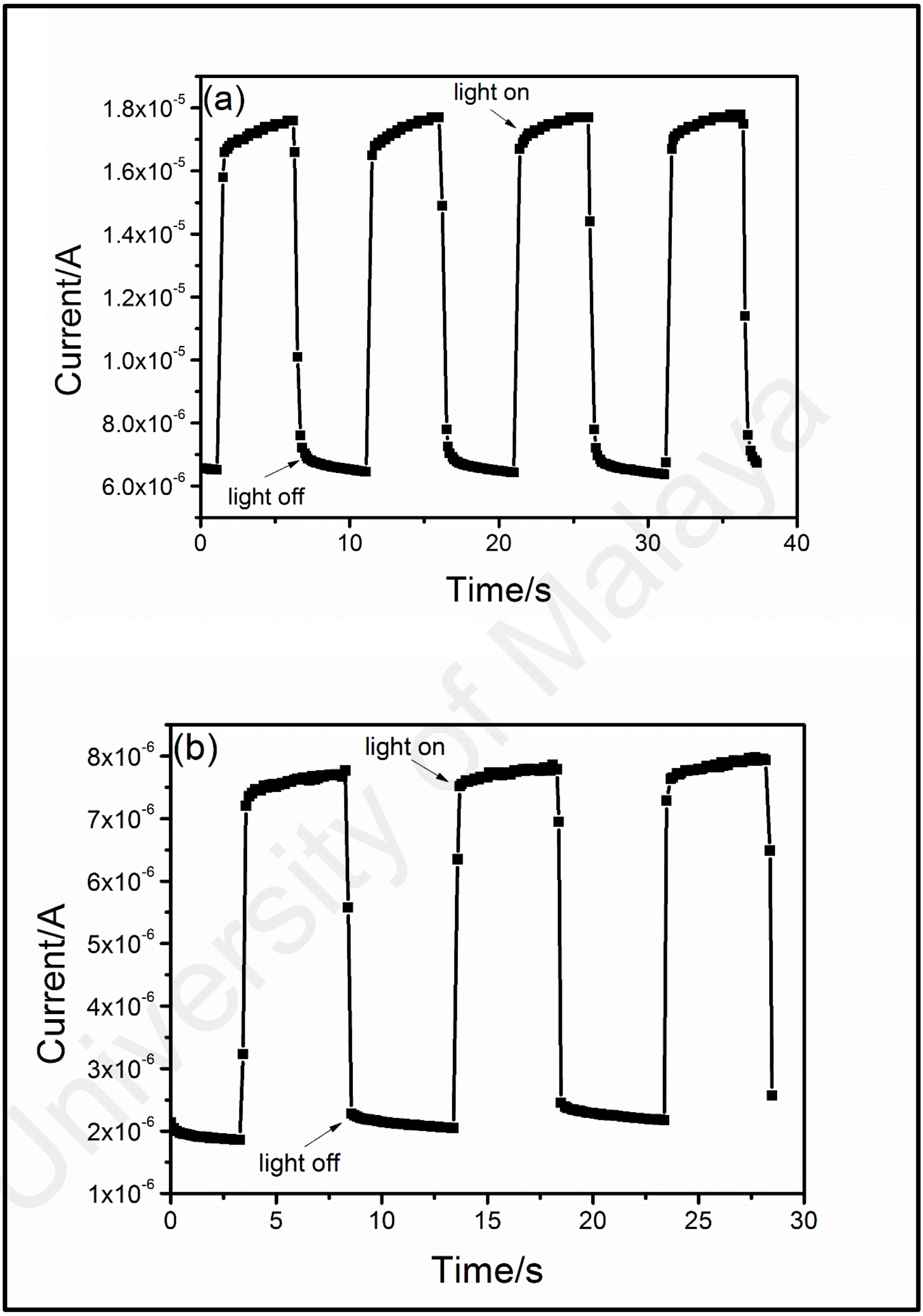

Figure 4.5: Dynamic photocurrent vs. time of the DS photo sensors at +0.2 V with periodic on/off 150 mW/cm^2 illumination light.

4.5 Conclusion

In conclusion, the fabrication of the DS photosensors was done in ambient condition, and electrical characterization of the photosensors was performed after the aging process. Nanoparticles TiO_2 with NaOH have been treated to enhance the photo anode (TiO_2 + NiTsPc as sensitizer). The thickness of photo anode is around 15 μm which has been determined by means of KLA Tencor P.6 surface profilometer equipment. In addition, structural and morphologically treated and untreated TiO_2 have been presented, the micrograph obtained using field emission scanning electron microscopy (FESEM). TiO_2 nanoparticles after treatment with NaOH are well separated and look quite arranged which leads to penetration into the inter pore region and the homogeneous distribution of the dye.

The relationship between current/voltage with the different illumination levels ranging from 0 to 150 mW/cm^2 for both dye covered untreated TiO_2 and dye covered treated TiO_2 photo sensors have been presented and discussed. The voltages were almost constant over the entire investigated intensity range and the current is linearly proportional to illumination intensity using the treated TiO_2. The device exhibits poor photovoltaic parameters which are not suitable for solar cell applications. However, they are quite adequate for photosensing applications. Dependence of logarithmic photocurrent and voltage on logarithmic light intensity of the photo sensors were also studied. The photocurrent is linearly proportional to the illumination intensity with slopes of 1.35 and 3.37 in photo sensors fabricated using untreated and treated TiO_2 respectively. Moreover, the photovoltage has also been found proportional to logarithmic illumination in both photo sensors. Despite this, variation of photo voltage was observed in the photo sensor (treated TiO_2) at 100 mW/cm^2 suggesting that with increasing illumination, temperature of the cell will increase.

Finally, photo-conductivity, photo-sensitivity, and response/recovery time of both types of the photo sensors have been compared. The photoresponse characteristics of the sensors have been studied as a function of periodic stepped light input with 0.2 V input bias. The response (t_r) and recovery times (t_c) for sensors have also been measured for both cases to be (t_r = 300 ms, t_c = 800 ms) and (t_r = 200 ms, t_c = 300 ms) respectively. The relatively improved results for sensor is attributed to enhanced electron transport observed in NaOH-treated TiO_2 thin film. Moreover, the photocurrent value in the second sensor also exhibits a relatively more stable plateau once the light was switched on and off for a certain duration (5 sec). Overall, both sensors have shown rapid changes in photocurrent states as a function of stepped light input. The value of the photo-conductivity sensitivity of the photo sensors has been determined in both sensors to be 6.65×10^{-5} (for untreated) and 1.87×10^{-4} Sm/W (treated), respectively and the responsivities of the photo sensors were found to be 3.3×10^{-5} A/W and 3.7×10^{-5} A/W, respectively.

CHAPTER 5: BINARY BLEND BASED DYE SENSITIZED PHOTO SENSOR USING PCPDTBT AND MEH-PPV COMPOSITE AS A LIGHT SENSITIZER

5.1 Introduction

The photo sensing properties of dye sensitized photo sensor fabricated with binary (PCPDTBT:MEH-PPV) interpenetrating sensitizer blended structures have been investigated. The visible wavelength absorption capability of individual and binary blend films has been demonstrated via NIR-UV-VIS spectroscopy. The different volumetric ratio of blends has been optimized by the photoluminescence study. To investigate the wavelength dependent sensitivity of the individual and blend films of sensors, EQE spectra of the photo sensor devices have been studied and presented in this chapter. Because the high value of EQE in the specific range of UV-Visible spectrum indicating that the absorption of dye sensitizer is the primary source of harvesting light and exciton generation. The photocurrent relationship with stimulated illumination intensity of the individual polymers and binary blend based dye sensitized photo sensor (DSPS) have been studied. The key photo sensing parameters such as photo-conductivity sensitivity, responsivity and response time of all photo sensors have also been discussed.

In this study, the binary blend of poly[2-methoxy-5-(2-ethylhexyloxy)-1,4-phenylenevinylene] (MEH-PPV) and poly[2,6-(4,4-bis-(2-ethylhexyl)-4H-cyclopenta [2,1-b;3,4-b’]dithiophene)-alt-4,7(2,1,3-benzothiadiazole)] (PCPDTBT) were used as a sensitizer for the reported DSPS. These polymers are known as electron donor polymers (Liang et al., 2014). Because only a suitable donor dye or donor–acceptor π-conjugated (D-π-A) dye adsorbed on the n-type metal oxide semiconductor (such as TiO_2, SnO_2, Cs_2CO_3, Nb_2O_5 ZnO, In_2O_3 or mixtures thereof) in order to harvest light and generate charge carriers at the interface of metal oxide. Whereas, an acceptor dye is proper to adsorb on p-type metal oxide like NiO_x, V_2O_5, MoO_3, or mixtures thereof. MEH-PPV and PCPDTBT have been investigated individually in numerous of works (Agostinelli et al., 2008; Ahmad, Suhail, et al., 2013; Chu et al., 2011; Liu, X. et al., 2012; Mühlbacher et al., 2006; Peet et al., 2007; Zafar et al., 2015; Zafar et al., 2014). The absorption of MEH-PPV occurs too far from the interface in range 400 to 550 nm to contribute to the photocurrent. However, the absorption of PCPDTBT lies in the range of 550-850 nm which occurs by the convolution of several electronic transitions. PCPDTBT was the first push-pull low bandgap organic dye copolymer which has the carboxylic acid anchoring group designed to transfer electron density towards TiO_2 semiconductor. The combination of these both materials would significantly broaden the absorption spectrum. In continuation of efforts to make inexpensive, reliable, environmentally friendly photo detectors for the entire visible solar spectrum, in the present work, it is aimed to demonstrate an organic visible photo sensor in order to enhance the photo-sensitivity range and facilitate light-induced redox processes.

5.2 Fabrication Method of Dye Sensitized Photo Sensor (DSPS)

To prepare photoanode layer, 360 mg TiO_2 nanoparticles (size ~25nm) were added in 120 mg of poly(ethylene glycol) (PEG) and 240 µl acetic acid followed by the 600 µl ethanol addition. The white mixture was sonicated in an ultrasonic bath for 15 min at 35 ℃ without shaking, resulting in a dispersed-viscous TiO_2 paste, as shaking the vial itself would cause air bubble formation preventing good deposition. The sonication time is very important because it causes further break down of large TiO_2 nanoparticle agglomerates thus increase the homogeneity of the viscous TiO_2 paste. The viscous paste was coated on the cleaned ITO coated glass substrates using Doctor Blade method. The commercially available ITO substrates were first washed through previously explained cleaning procedure. The substrates were dried by nitrogen blow. The dimension and the sheet resistance of the ITO substrates were 1×2 cm^2 and 10 Ω/cm^2, respectively. The thickness and area of the TiO_2 film were~9 µm and 0.25 cm^2, respectively. The samples were kept in the open air for a while followed by the gradual heating from 25-380 ℃ on a hot plate for 15 min to burn off the poly(ethylene glycol) (PEG) and to evaporate the solvents (Nedelcu et al., 2010). Later on the sintering of the samples was done for 30 min at 450 ℃ (temperature rise and fall rate were 2 ℃/min) in order to get TiO_2 compact films. The counter electrode consisted of an ITO coated with a graphite layer. As an I^-/I_3^- redox couple-based ionic liquid electrolyte, Iodolyte HI-30 was used.

To prepare dye sensitized photo sensor (DSPS), 10 mg/ml concentrated solutions of MEH-PPV and PCPDTBT, were prepared in chloroform and dichlorobenzene, respectively. The dye sensitized electrodes were prepared by dipping the TiO_2 deposited ITO substrates in the different volumetric ratio blends of MEH-PPV and PCPDTBT. The DSPS devices were prepared using the dye covered TiO_2 electrodes (photo anodes) assembled with the graphite counter electrodes, filled with the redox couple electrolyte (HI-30). The controlled sample for the PCPDTBT and MEH-PPV were also fabricated, separately. Figure 5.1 shows an energy level diagram of the DSPS device. As obvious, the LUMO energy level of the organic blend sensitizer (PCPDTBT:MEH-PPV) is lie above the conduction band of metal oxide semiconductor (TiO_2), which means the LUMO energetic level of blend sensitizer is much negative than the conduction band edge of TiO_2 (-4.26 eV). However, the HOMO energy level of blend dye sensitizer is lower than potential of the redox couple (HI-30) i.e. the HOMO (ground state) level of blend dye sensitizer is more positive than the redox couple potential of the electrolyte which are the key factors to achieve efficient charge injection. Figure 5.2 describes the schematic diagram and working mechanism of the DSPS. The photo-excitation of the organic dyes leads to the injection of an electron into the TiO_2 conduction band. The electron passes through the conductive oxide layer and the external load. The liquid electrolyte (iodide/triiodide) in an organic solvent as a redox system regenerate the oxidized organic dyes which penetrate into the porous structure by collecting electron through the graphite counter electrode i.e. I^-reduces the positively charged organic dye whereby I_3^- ions are formed which diffuse to the cathode (graphite). I_3^- reduced to I^- and hence the cycle is completed (Hug, Bader, Mair, & Glatzel, 2014).

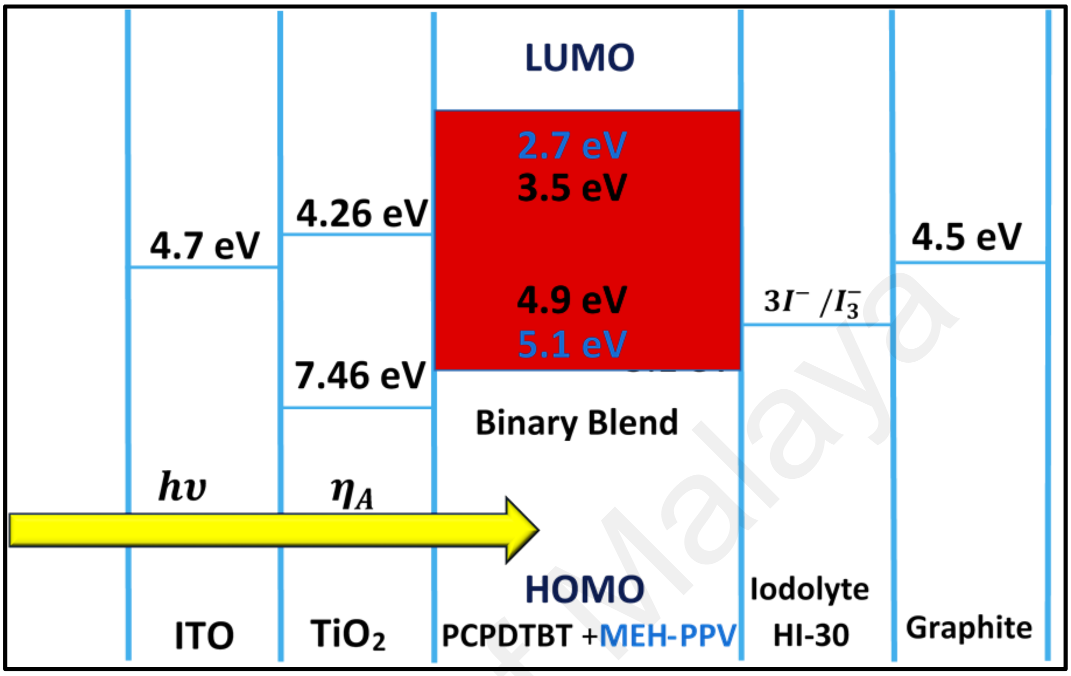

Figure 5.1: A schematic approximate energy level diagram of modelled DSPS with a I^-/I_3^-redox electrolyte (Iodolyte). Which is illustrated the LUMO (or electron affinity (EA)) and the HOMO (or ionization potential (IP)) of PCPDTBT and MEH-PPV binary blend polymer donors as well as the electrodes work function used in this device. A band gap of an organic polymer is the difference between the energy of its LUMO and HOMO.

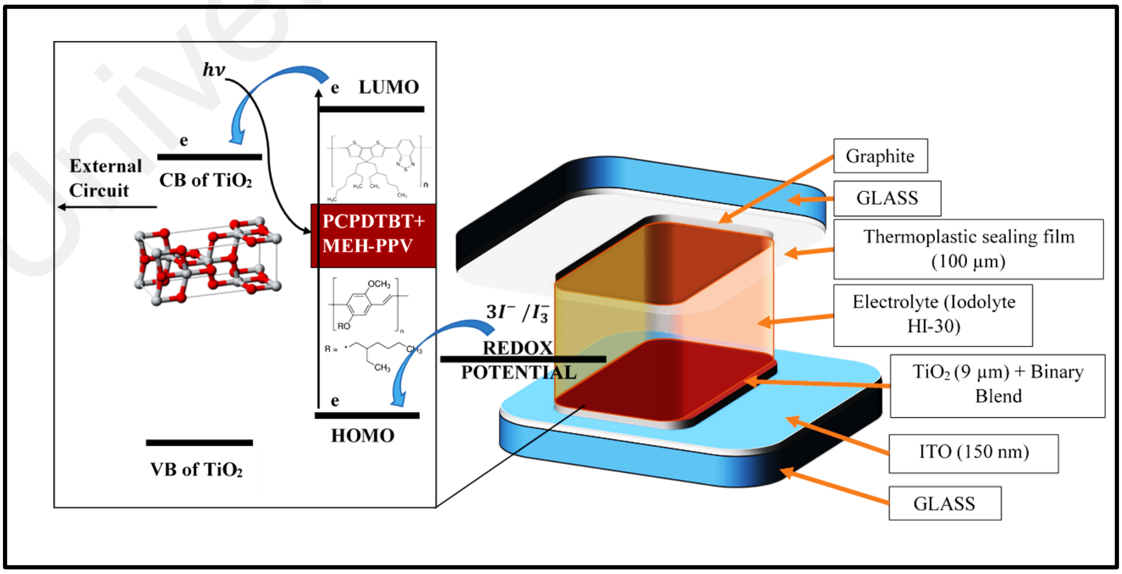

Figure 5.2: Design and schematic working mechanism of the DSPS.

5.3 Result and Discussion:

Figure 5.3, shows the optical absorption spectra of the three different volume ratios of PCPDTBT:MEH-PPV (1:0.4, 1:0.6, and 1:0.8) blend. Figure 5.4, depict the optical absorption spectra of PCPDTBT and MEH-PPV independent films. The combination of these two organic polymers would have a significant influence on the optical properties of the DSPS because of efficient photon captures by the blend in the visible part of the solar spectrum. The absorption spectrum of PCPDTBT exhibits the absorption in the visible region of the solar spectrum from 500 nm onward whereas MEH-PPV absorbs in the range of 400-550 nm. The absorption spectrum of PCPDTBT exhibits two maxima, the first is located at 415 and the second at 730 nm, whereas the MEH-PPV exhibits a peak at 515 nm. Therefore, the binary blend covers most part of the visible light spectrum. The broader absorption spectrum of the binary blend film is expected to be favorable for broad range visible spectrum sensitivity of the sensor. It is observed that the ratios 1:0.4, 1:0.6 and 1:0.8 of PCPDTBT:MEH-PPV blend are the optimum ratios in term of flat absorption profile as compare to other ratios (It is noteworthy that, several different ratios of PCPDTBT:MEH-PPV blend have been investigated (1:1, 1:1.2, and 1:1.4); only the best three with more uniform and even absorption height have been shown in Figure 5.3). However, it is found that there are two dips in the absorption spectrum of the blend films which are located around 450 and 575 nm, respectively. Thus, the inlay of MEH-PPV into the PCPDTBT would significantly broaden the absorption spectrum of the PCPDTBT:MEH-PPV binary bulk heterojunction dye sensitizer.

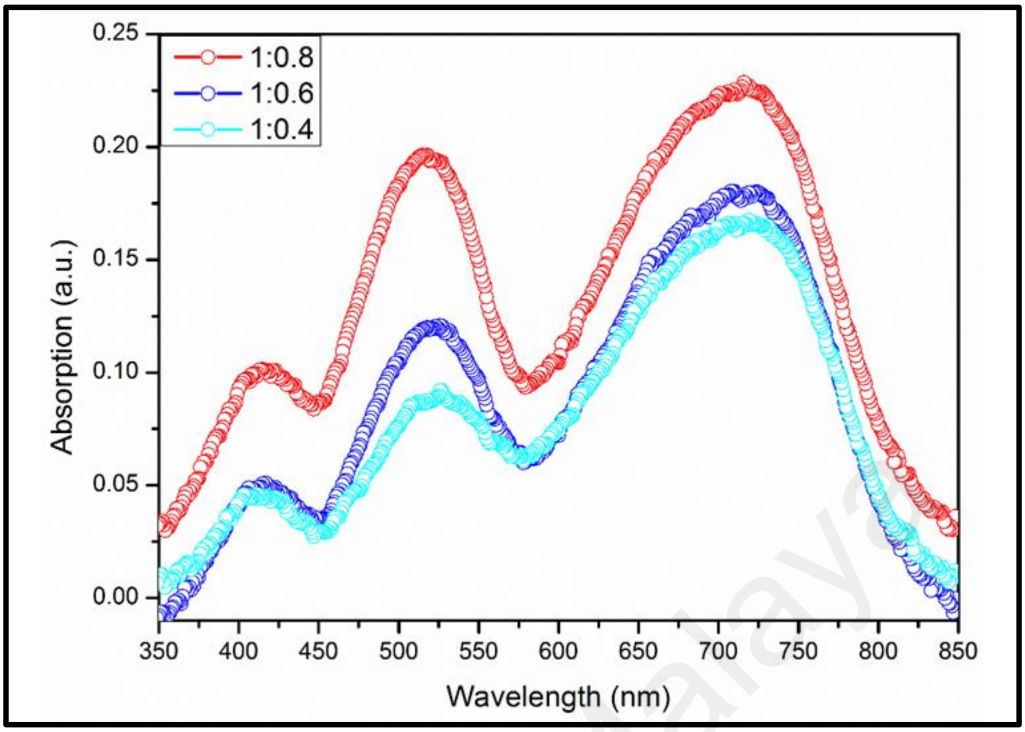

Figure 5.3: Ultra-violet/visible/infra-red (UV-VIS-IR) optical spectra of PCPDTBT: MEH-PPV blend films at different volumetric ratio. Which are the optimum ratios in term of flat absorption profile with more uniform and even absorption height as compare to other ratios.

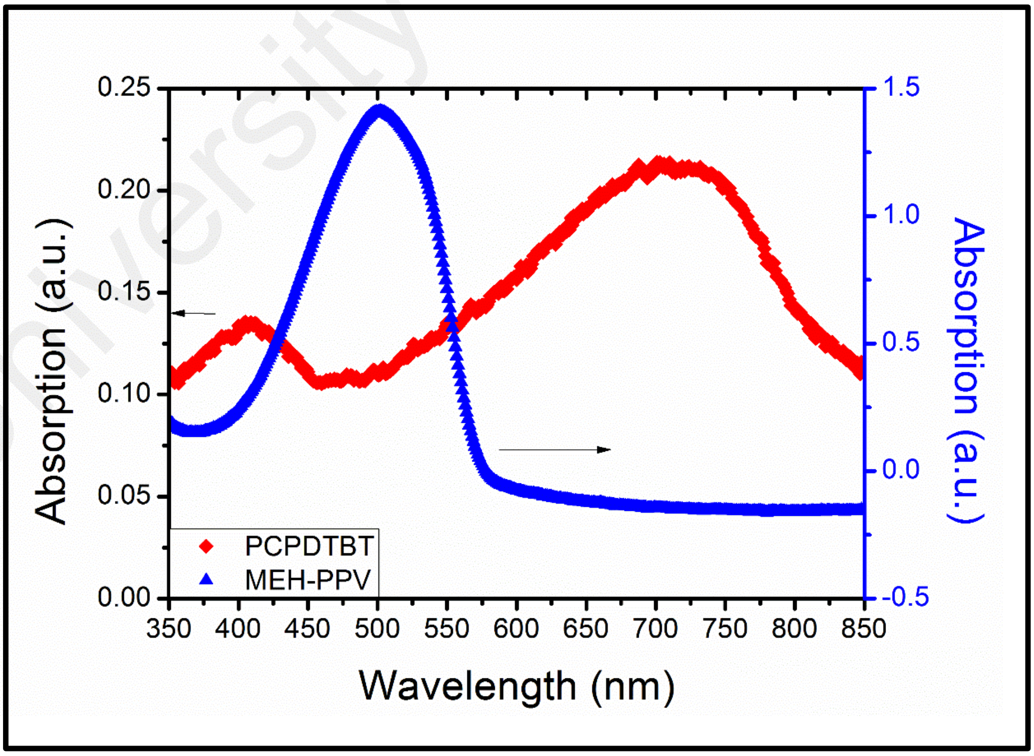

Figure 5.4: The UV-VIS-NIR spectra of organic polymer MEH-PPV and PCPDTBT independent thin films.

Figure 5.5 shows the photoluminescence (PL) spectra of PCPDTBT:MEH-PPV blend films at different volumetric ratios (1:0.4, 1:0.6 and 1:0.8). At 1:0.6 volumetric ratio of the PCPDTBT:MEH-PPV blend, the PL intensity is significantly quenched, indicating a clue of more efficient charge transfer in the PCPDTBT:MEH-PPV blend at that certain ratio. Figure 5.6 shows that the PCPDTBT exhibit a shoulder at 590 nm and a peak 720 nm, whereas the MEH-PPV gives a PL peak at 610 nm. In the case of PCPDTBT:MEH-PPV blend, a wide PL band is observed in the range of 500-620nm which is contributed to by the shoulder of PCPDTBT and the peak of MEH-PPV. It is also observed that the quenching of the PL spectrum changes with the change in the ratio of MEH-PPV, while the peak position does not change. The decrease of PL intensity indicates the better exciton disassociation between PCPDTBT and MEH-PPV complex. For more accurate elaboration of the PL quenching, the absorption intensity of the blend film should be taken into account. The higher PL emission of PCPDTBT:MEH-PPV for the case blend ratio (1:0.8) might also be contributed by the higher absorption of the blend film (Yang, Leung, & Wang, 2013; Yang et al., 2015). However, in the case of the remaining two ratios (1:0.6 and 1:0.4) the PL intensity is not proportional to the absorption intensity. This confirms that the quenching effect is more significant in the case of 1:0.6. Here it is important to mention that the film thicknesses were kept constant (~100±2 nm) for the all samples for PL and UV/Vis studies. There is a strong relationship between the photocurrent and PL intensity (Chae, Kim, Kim, & Kang, 2010). The absorption of incident photon flux in sensitizer of DSPS would generate coulombically bound electron-hole pairs (excitons). These photo-generated excitons may either move back to the ground state or dissociate at TiO_2/sensitizer dyes, or at the interface of bulk heterojunction of the two polymers, creating a photocurrent in the external circuit.

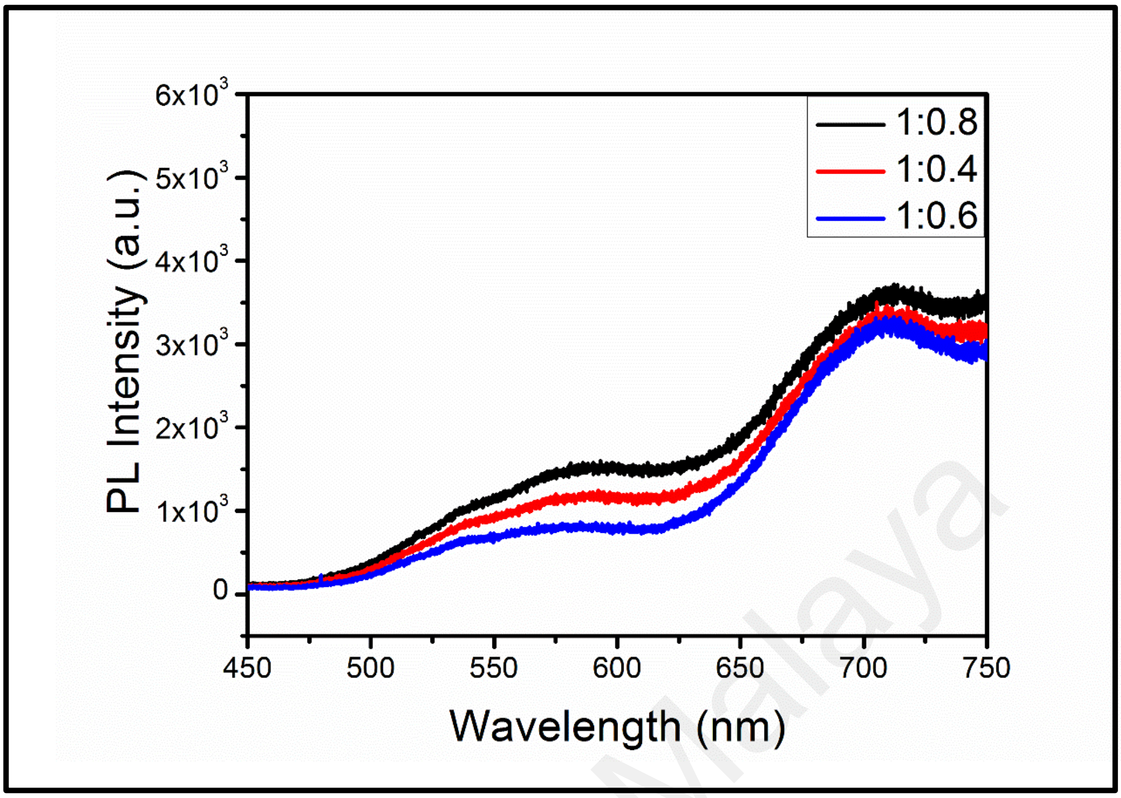

Figure 5.5: PL spectra of PCPDTBT:MEH-PPV blends at different volumetric ratio.

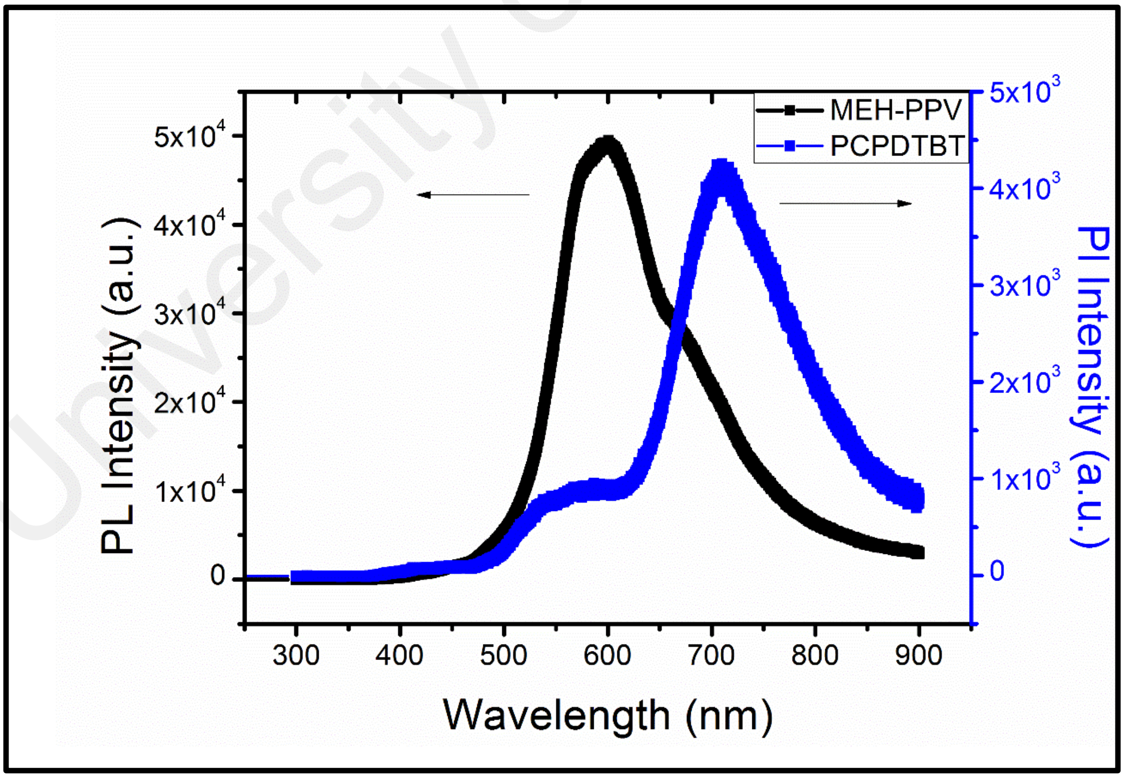

Figure 5.6: The PL spectra of MEH-PPV and PCPDTBT independently.

Figure 5.7, shows the photocurrent relationship of the binary blend based dye sensitized photo sensor (DSPS) and stimulated illumination intensity. The standard deviation (error values) of the measurements were found around $\pm 2.21 \times 10^{-6}$, $\pm 2.43 \times 10^{-6}$ and $\pm 2.03 \times 10^{-6}$ for the blend ratios of 1:0.4, 1:0.6 and 1:0.8 respectively. The graphs showed almost a linear relationship between photo generated current and illumination intensity. The increase in light intensity leads more molecules of the sensitizer to be excited and results in the increased photocurrent due to increase in the generation rate of mobile charge carriers, consequently generating more I^{-} species in the DSPS. It can be observed that the photocurrent in PCPDTBT:MEH-PPV (1:0.6) is relatively higher as compared to the other ratios, which indicates that the optimum ratio of the PCPDTBT:MEH-PPV blend can give rise to the pronounced magnitude of photocurrent. The recombination of the charge carriers might be lower and optimum phase separation might be attained in PCPDTBT:MEH-PPV (1:0.6) volumetric ratio which may lead to higher photocurrent. Phase separation at other PCPDTBT:MEH-PPV ratios might contribute to the reduced interfacial area between PCPDTBT and MEH-PPV, thus resulting in lower photocurrent. Figure 5.8 depicts the photo-generated current vs luminance intensity relationship for the PCPDTBT and MEH-PPV independently. The standard deviation (error values) of the measurements were found around $\pm 3.40 \times 10^{-6}$ and $\pm 6.55 \times 10^{-7}$ for MEH-PPV and PCPDTBT respectively. It is observed that the photocurrent magnitude of both organic polymers PCPDTBT and MEH-PPV are individually less than the blend. This might be due to a broader absorption range of the PCPDTBT:MEH-PPV organic blend and more uniform phase distribution of the molecules of the both polymers in the specific volumetric ratio of the organic bulk heterojunction blend.

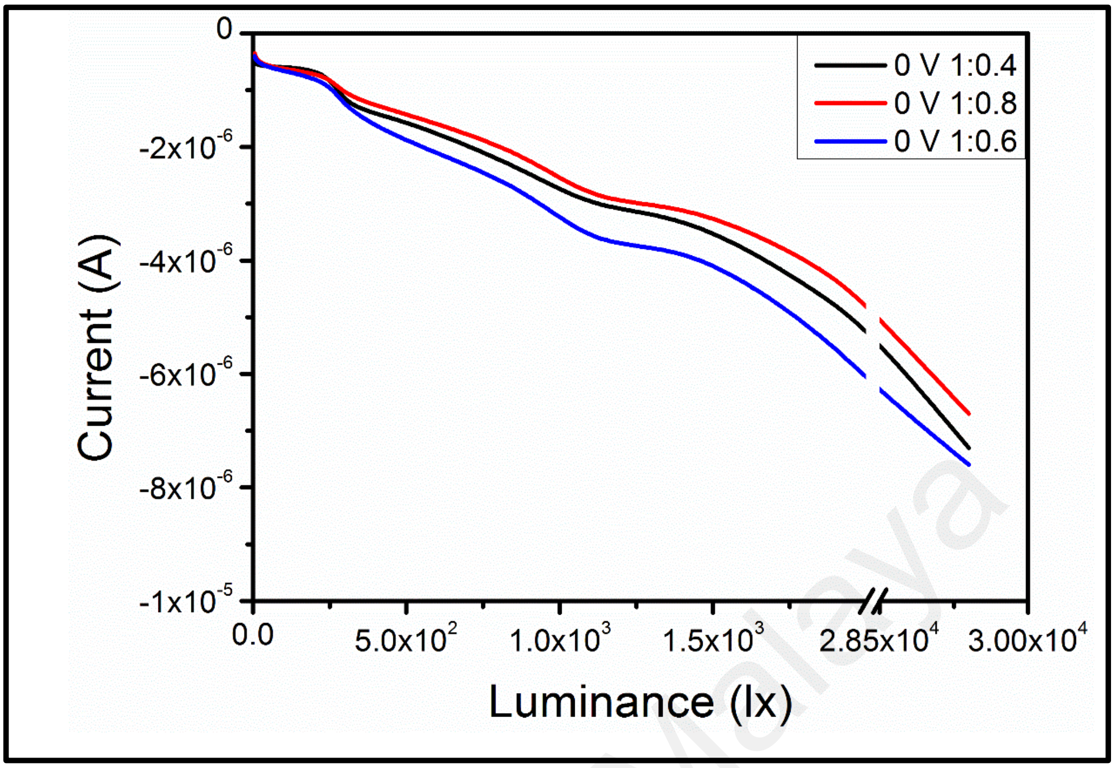

Figure 5.7: Illuminance vs. I_{sc} measurements for PCPDTBT:MEH-PPV DSPS with different ratios at (0) bias voltage at room temperature.

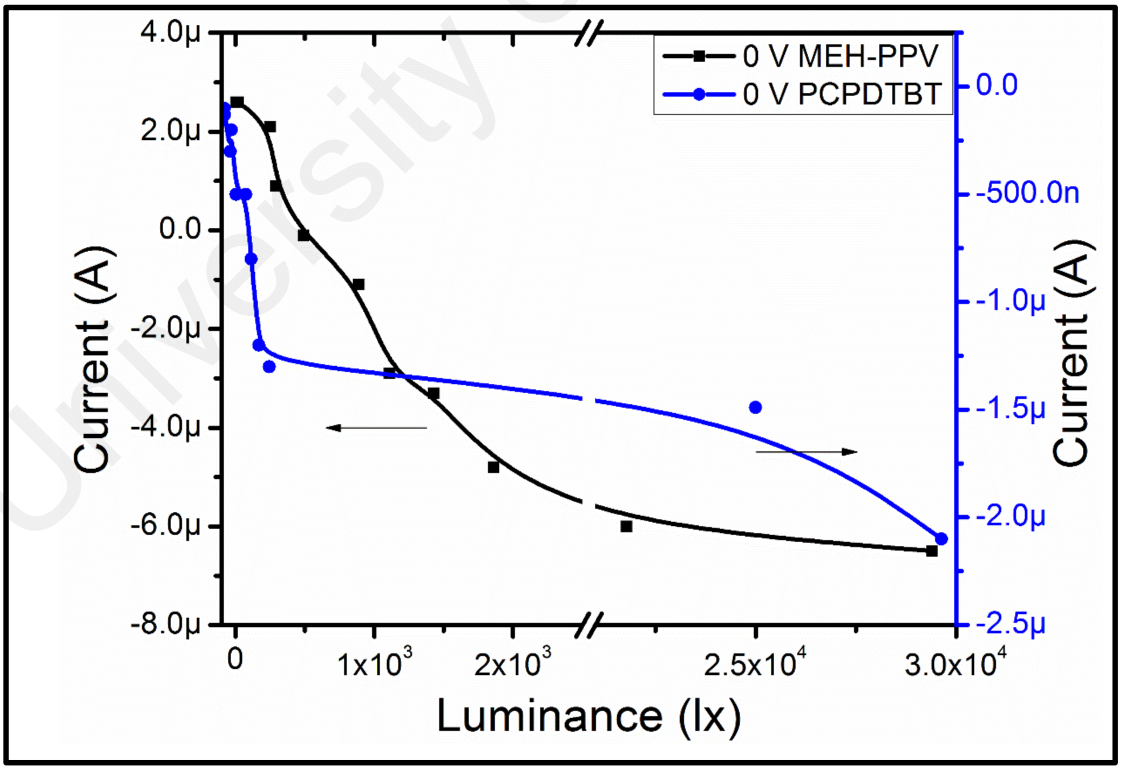

Figure 5.8: Illuminance vs. I_{sc} measurements of PCPDTBT and MEH-PPV independently at (0) bias voltage at room temperature.

The response/recovery time and temporal photo-sensitivity are important parameters in order to evaluate the behavior of the photo sensor for practical application. Response and recovery times (t_r and t_c) are generally defined as the time required for the photocurrent to increase the final settled value or vice versa (Li et al., 2011). Experimentally, response mean from on to off light while recovery is vice versa. The photo response characteristics of the fabricated DSPSs demonstrate a sharp change in its magnitude of photocurrent as a function of periodic pulsed stimulated solar light as shown in Figure 5.9. In order to record the response time, 100 mW/cm^2 illumination was employed by an Oriel solar simulator (model 67005). The pulse width was ~5 sec. The average response time (t_r) for the independent PCPDTBT and MEH-PPV DSPS are given in Figure 5.9 (a), and (b) and were found to be (t_r = 937 ms and 685 ms), respectively. The average response times for the PCPDTBT:MEH-PPV volumetric ratios of 1:0.4, 1:0.6 and 1:0.8 in Figure 5.9 (c), (d) and (e) are (488, $\sim$382, and 686) ms respectively. The time-resolved response time is regular, steady and repeatable as shown by three consecutive cycles of abrupt switching between dark and luminance states. Typically the response times for bulk heterojunction based photo sensors are in the range of (10^{-8} to 10^{-3}) s (Soci et al., 2010) which is comparable with inorganic photo sensors. It is worth noting, that the binary blend based photo sensor exhibits good photoconductive performance in terms of sensitivity, response time as compared to the individual organic polymer based devices. However, it can be further reduced by using a ternary blend system. It is obvious from (Figure 5.7 and Figure 5.8) above, the higher intensity of the incident illumination gives noticeable upsurge in the photocurrent. Indeed, there are a couple of bottlenecks which limits the response of the photo sensor: a) limited absorption; b) restricted generation and splitting of excitons and c) incompetent transport of charges towards the collection electrodes. The bulk heterojunction blend technique supports the improvement in light absorption and exciton dissociation only. However, the movement of splitted exciton towards electrodes is external field assisted.

The reproducibility and repeatability of the response time measurements were investigated for all devices and the devices are found to be very stable and reproducible. Furthermore, the photo-conductivity sensitivity, responsivity and response time of the DSPS have also been investigated. Comparison of the key sensing parameters of the DSPSs such as photo-conductivity sensitivity, responsivity, response time is given in Table 5.1. The photo-conductivity sensitivity and the responsivity of the DSPSs have been described in detail in the previous research (Karwan et al., 2014), see CHAPTER 4:4.4. Figure 5.10 depicted the external quantum efficiency (EQE) versus wavelength measured EQE spectrum for MEH-PPV and PCPDTBT films individually and their blend films. Other organic dyes usually convert photons up to 600 nm with high quantum efficiency whereas with using PCPDTBT organic dye copolymer the photo sensor harvests light up to 800 nm which cause to generate extra excitons at red spectrum and increase the sensitivity even in low energy light. The EQE spectra are in good agreement with the absorption spectra of the individual and blend films.

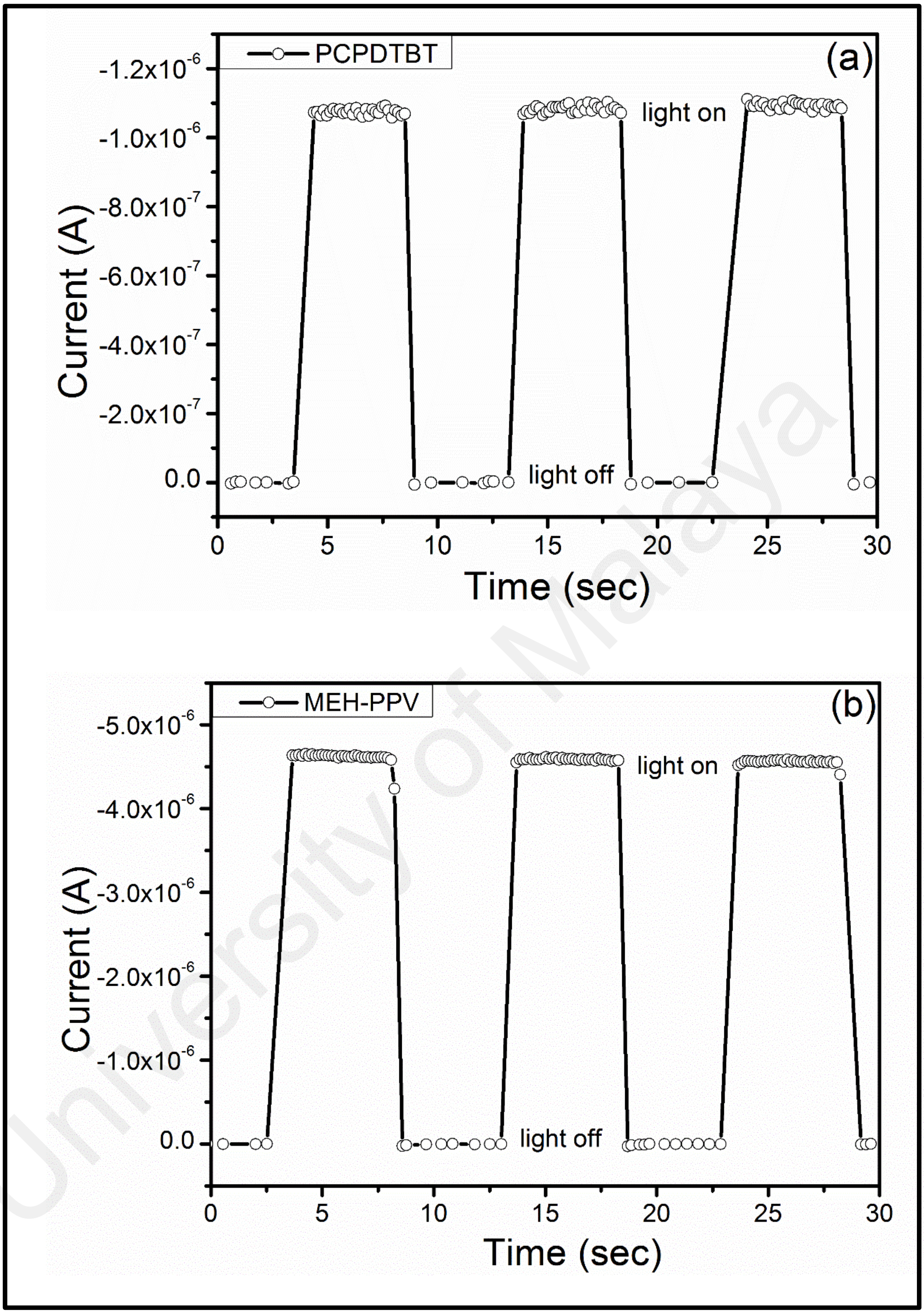

Figure 5.9: The response time of the DSPS devices: PCPDTBT (a), MEH-PPV (b), PCPDTBT:MEH-PPV (1:0.4) (c), PCPDTBT:MEH-PPV (1:0.6) (d) and PCPDTBT:MEH-PPV (1:0.8) (e), under pulsed optical illumination intensity 100 mW/cm^2 at 0V biasing voltage and delay time 0.01 sec.

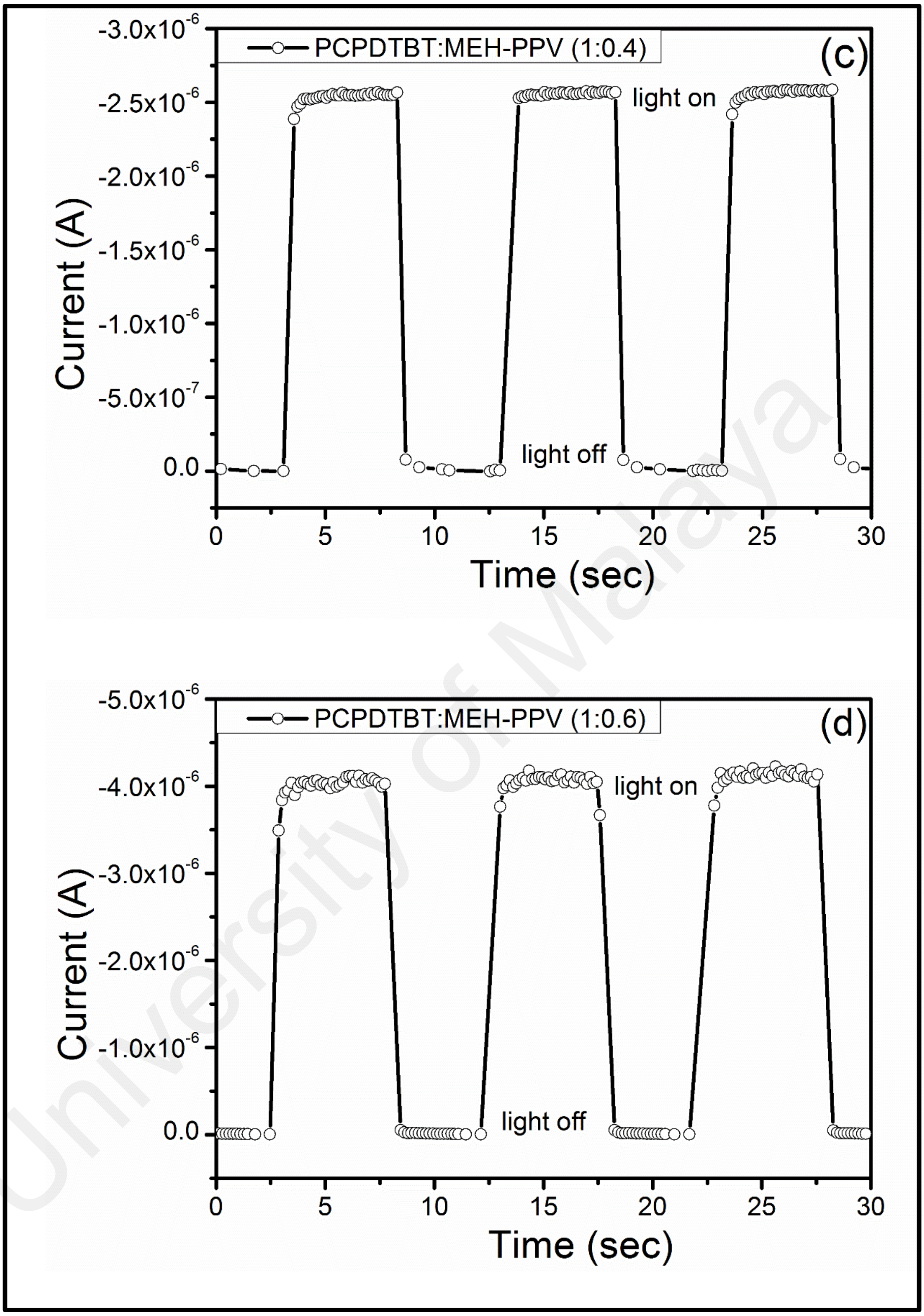

Figure 5.9: (CONTINUED) The response time of the DSPS devices: PCPDTBT (a), MEH-PPV (b), PCPDTBT:MEH-PPV (1:0.4) (c), PCPDTBT:MEH-PPV (1:0.6) (d) and PCPDTBT:MEH-PPV (1:0.8) (e), under pulsed optical illumination intensity 100 mW/cm^2 at 0V biasing voltage and delay time 0.01 sec.

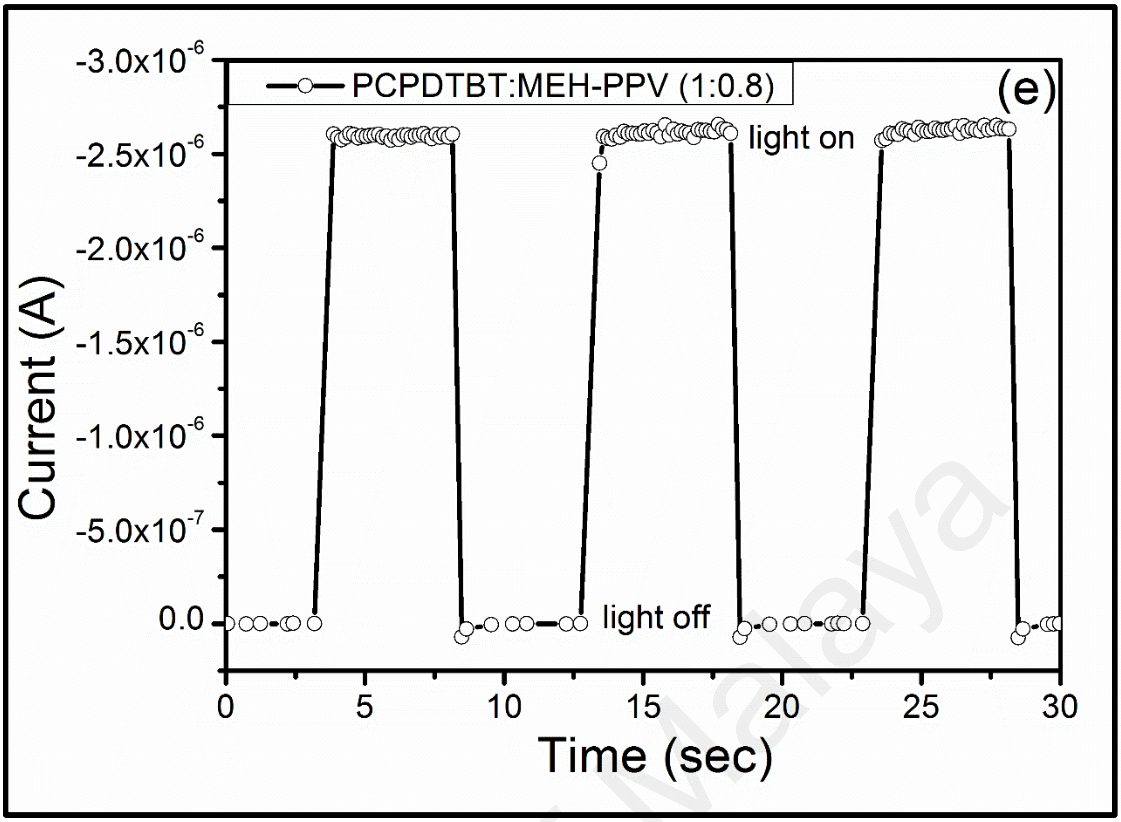

Figure 5.9: (CONTINUED) The response time of the DSPS devices: PCPDTBT (a), MEH-PPV (b), PCPDTBT:MEH-PPV (1:0.4) (c), PCPDTBT:MEH-PPV (1:0.6) (d) and PCPDTBT:MEH-PPV (1:0.8) (e), under pulsed optical illumination intensity 100 mW/cm2 at 0V biasing voltage and delay time 0.01 sec.

Table 5.1: Comparison of the key sensing parameters of the DSPS.

Sensing Parameters	PCPDTBT	MEH-PPV	PCPDTBT:MEH-PPV 1:0.4	PCPDTBT:MEH-PPV 1:0.6	PCPDTBT:MEH-PPV 1:0.8
Photo-conductivity sensitivity (Sm/W)	8.77×10^{-6}	3.67×10^{-5}	2.02×10^{-5}	3.29×10^{-5}	2.07×10^{-5}
Responsivity (A/W)	1.12×10^{-5}	4.7×10^{-5}	2.59×10^{-5}	4.22×10^{-5}	2.65×10^{-5}
Response time (t_r) (ms)	~937	~685	488	~382	686

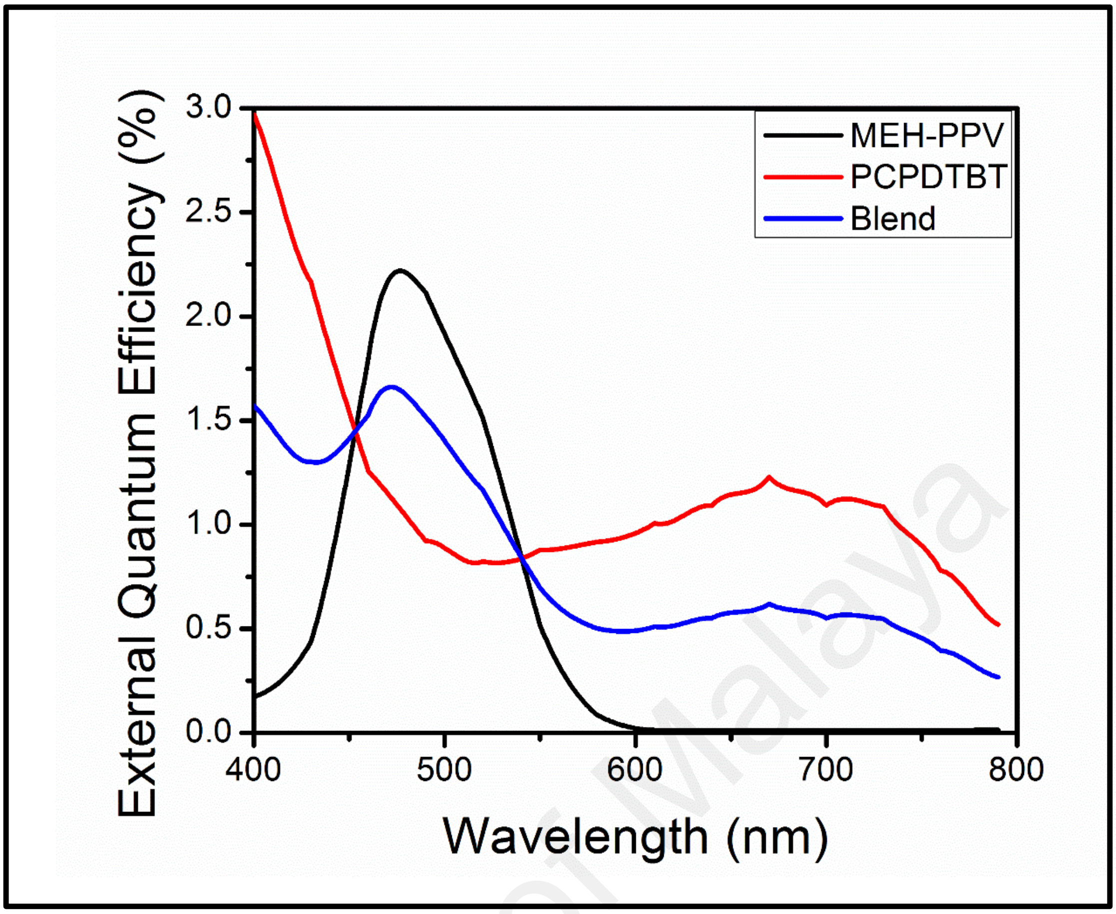

Figure 5.10: External quantum efficiency (EQE) spectrum of the PCPDTBT and MEH-PPV and blend films based DSPS.

5.4 Conclusion

In conclusion, a solution processable binary blend (PCPDTBT:MEH-PPV) based DSPS has been successfully fabricated with improved sensing performance. Under the illumination range of 0-30000 lx and zero-bias condition, the optical sensing properties of the DSPSs have been investigated. The thickness and area of the TiO_2 film, recorded as almost 9 µm and 0.25 cm^2, respectively, have been obtained by means of blade technique. Two steps of the annealing have been employed. The first step was from 25-380 ℃ on a hot plate for 15 min to burn off the PEG and to evaporate the solvents, and in the second, the sintering of the samples was done for 30 min at 450 ℃ (temperature rise and fall rate were 2 ℃/min) in order to get TiO_2 compact films. The DSPS devices have been prepared using the dye covered TiO_2 (MEH-PPV or PCPDTBT or in the different volumetric ratios blend of them with 10 mg/ml concentration) electrodes (photo anode) assembled with the graphite counter electrodes (photo cathode), filled with the liquid redox electrolyte (Iodolyte HI-30). In addition, the energy level diagram, the schematic diagram and working mechanism of the DSPS device have been shown.

The optical absorption spectra of the three different volume ratios of PCPDTBT:MEH-PPV (1:0.4, 1:0.6, and 1:0.8) blend (which are the optimum ratios in term of flat absorption profile as compare to other ratios) and independent films of PCPDTBT and MEH-PPV have been obtained using via NIR-UV-VIS spectroscopy. The absorption spectrum of PCPDTBT in the visible region of the solar spectrum have been demonstrated from 500 nm onward with two maxima, located at 415 and 730 nm, whereas MEH-PPV absorbs in the range of 400-550 nm with a peak at 515 nm. However, two dips in the absorption spectrum of the blend films have been found which are located around 450 and 575 nm, respectively. A significant influence on the optical properties of the DSPS by the combination of these two polymers have been investigated because of the efficient photon captured by the blend in the visible part of the solar spectrum which led to cover most part of the visible light spectrum. The broader absorption spectrum of the binary blend film has been investigated to be favorable for broad range visible spectrum sensitivity of the sensor.

Moreover, the photoluminescence (PL) spectra of PCPDTBT:MEH-PPV blend films at different volumetric ratios (1:0.4, 1:0.6 and 1:0.8) and the individual dye polymers has been performed employing a RENISHAW *inVia* Raman Microscope. A shoulder at 590 nm and a peak 720 nm in the PCPDTBT have been observed, whereas the MEH-PPV gives a PL peak at 610 nm. The shoulder of PCPDTBT and the peak of MEH-PPV contributed to the wide PL band which has been observed in the range of 500-620 nm in

PL blend spectrum. A significant quenching at 1:0.6 volumetric ratio of the blend has been investigated, which indicated a more efficient charge transfer in the PCPDTBT:MEH-PPV blend at that certain ratio. Furthermore, the changing of the quenching of the PL blend spectrum with the change in the ratio of MEH-PPV has been observed, while the peak position did not change. It has been observed that the PL intensity is not proportional to the absorption intensity in the case of the two ratios (1:0.6 and 1:0.4), which confirms that the quenching effect is more significant in the case of 1:0.6. For all samples of PL and UV/Vis studied, the film thicknesses have been kept constant around 100±2 nm.

The photocurrent relationship with the stimulated illumination intensity of the binary blend and the independent polymer based dye sensitized photo sensor (DSPS) have been studied. It has been observed that the photocurrent magnitude of both organic polymers PCPDTBT and MEH-PPV are individually less than the blend. This might be due to a broader absorption range of the PCPDTBT:MEH-PPV blend and more uniform phase distribution of the molecules of both polymers in the specific volumetric ratio of the bulk heterojunction blend. However, the photocurrent graphs for the blend shown almost a linear relationship with the illumination intensity. The increasing photocurrent with the increase in light intensity has been investigated because increase in light intensity leads to more molecules of the sensitizer to be excited and results in an increase in the generation rate of mobile charge carriers, consequently generating more I^- species in the DSPS. In addition, a relatively higher photocurrent in PCPDTBT:MEH-PPV (1:0.6) as compared to the other ratios has been observed, which indicates that the optimum ratio of the PCPDTBT:MEH-PPV blend can give rise to the pronounced magnitude of photocurrent.

Furthermore, the photo response characteristics of the fabricated DSPSs has demonstrated a sharp change in its magnitude of photocurrent as a function of periodic pulsed (~5 sec) stimulated solar light with 100 mW/cm^2 illumination. The average response time (t_r) for the independent PCPDTBT and MEH-PPV DSPS has been determined to be (t_r = 937 ms and 685 ms), respectively, while the average response time for the PCPDTBT:MEH-PPV volumetric ratios of 1:0.4, 1:0.6 and 1:0.8 was (488, ~382, and 686) ms respectively . The time-resolved response time has been observed regular, steady and repeatable as shown by three consecutive cycles of abrupt switching between dark and illumination states which was comparable with inorganic photo sensors. The binary blend based photo sensor has shown good photoconductive performance in terms of sensitivity, response time as compared to the individual organic polymer based devices.

Finally, the reproducibility and repeatability of the response time measurements were also investigated for all devices and the devices are found to be very stable and reproducible. In addition, the photo-conductivity sensitivity and the responsivity of the DSPS have also been investigated as shown in the Table 5.1. Then the external quantum efficiency (EQE) has been measured for MEH-PPV and PCPDTBT films individually and their blend films are in good agreement with the absorption spectra of the individual and blend films.

CHAPTER 6: THERMAL ANNEALING EFFECT ON THE OPTICAL, ELECTRICAL AND MORPHOLOGICAL PROPERTIES OF THE PBTTT-C_{12}:$PC_{71}BM$ BLEND FILMS

6.1 Chapter Overview

This work has been performed to explore the temperature dependent PV properties of PBTTT-C_{12} donor material. The optical and morphological properties of organic semiconductor blend (PBTTT-C_{12}:$PC_{71}BM$) have been investigated. Later the solar cell has been fabricated for the optimized photoactive layer. The effect of the film morphology on the device performance in terms of short circuit current and efficiency has been demonstrated and discussed in this chapter, under the effect of thermal annealing.

6.2 Introduction

Controlled surface morphology and thermal and solvent treatments are important techniques in the optimization of major PV parameters such as open circuit voltage, short circuit current, and fill factor. Thermal annealing is one of the simplest ways to improve the active layer morphology and can significantly improve the properties and structure of materials (Wang et al., 2005). However, in order to obtain the high mobilities and enhanced exciton dissociation in organic solar cells, polymer morphology and chain alignment are still the major issues, which need to be addressed. Kim et al. (Kim et al., 2007) also reported the annealing effect on the morphology of the P3HT:PCBM film and electronic properties. Their investigation exhibits that the annealing step not only leads to more efficient charge transport and charge collection at the electrodes but can also contribute a slight increment in the absorption intensity. In the P3HT:PCBM blend, the most effective strategy toward constructing the nanoscale donor-acceptor percolated networks with well-optimized morphology is the application of annealing treatment at high temperature. However, in contrast, devices based on the new generation donor materials such as PCDTBT are better performed without the post thermal annealing step.

For instance, Zhao et al. (Zhao et al., 2013) reported that the topography of the PCDTBT:$PC_{71}BM$ blend films become more rough with increased root mean square (rms) roughness for the annealing temperature is above 60 ℃ and the more efficient PCDTBT:$PC_{71}BM$ solar cell can be realized without any thermal annealing treatment.

In this study, the effect of thermal annealing on the fabrication of BHJ cells by using a blend of poly[2,5-bis(3-dodecylthiophen-2-yl)thieno[3,2-*b*]thiophene] (PBTTT-C_{12}) and [6,6]-phenyl C_{71} butyric acid methyl ester ($PC_{71}BM$) were used as an active layer. The PBTTT-C_{12} can be dissolved in many different solvents such as chloroform and dichlorobenzene, and showed high degree of crystallization, which is important for high mobility in the desired direction of charge transport. According to the investigation of Parmer et al. (Parmer et al., 2008a) the hole mobility in pBTTT:PCBM cells measured by space charge limited current model was found to be 3.8×10^{-4} cm^2 V^{-1} s^{-1}. They reported a maximum efficiency of 2.3% for a 1:4 blend ratio with a short circuit current density of 9.37 mA/cm^2, an open circuit voltage of 0.525 V, and a fill factor of 0.48. No work has been reported on thermal annealing of PBTTT-C_{12}.

6.3 Fabrication of Bulk Heterojunction Cells

In order to fabricate the samples, first, Indium Tin Oxide (ITO) coated glass substrates were cleaned through previously defined cleaning procedure. 30 mg/ml solutions of PBTTT-C_{12} and $PC_{71}BM$ were prepared in dichlorobenzene and mixed with 1:4 (PBTTT-C_{12}:$PC_{71}BM$). For the device fabrication, the blend was spin coated on the poly(3,4-ethylenedioxythiophene) poly (styrenesulfonate) (PEDOT:PSS) coated ITO glass substrates (ITO/PEDOT:PSS, 50 nm PEDOT:PSS was coated on ITO substrate) at the rotational speed of 1000 rpm for 60 s, resulting in a thickness of ~100 nm. Then the samples were annealed at different temperatures ranging from 0-150±5 ℃, and finally, the top Al electrodes were thermally deposited on the blend films under a pressure of

1.8×10^{-4} Pa to complete the fabrication process. Sixteen devices were studied for each case. Each device was in round shape with a diameter of 2 mm. All the fabrication was performed in the Glove Box, under the nitrogen ambient condition.

6.4 Results and Discussion

Figure 6.1 shows the UV/Vis/NIR absorption spectra of the PBTTT-C_{12} thin film and PBTTT-C_{12}:$PC_{71}BM$ blend samples as a function of annealing temperature at 50 ℃, 100 ℃ and 150 ℃. The annealing was performed for 30 min in the nitrogen ambient condition. It is observed that PBTTT-C_{12}:$PC_{71}BM$ blend shows absorption in the wavelength range from ~300 nm to ~650 nm. The light absorption spectrum of PBTTT-C_{12}:$PC_{71}BM$ thin film samples in Figure 6.1 exhibit a high energy peak at 480 nm and a relatively low energy peak at 378 nm. Peak at 480 nm may took place from the ground state from a_{1u} (π) HOMO to e_g (π^*) LUMO of the PBTTT-C_{12} (Davidson, 1982). In the near UV regime of the spectrum, the peak may arise from π molecular orbital (HOMO) to π^* (LUMO) transition in the $PC_{71}BM$. It is observed from the spectra of the annealed and non-annealed samples that there is no shift in the spectra after thermal annealing. Only a small enhancement in the absorption is observed at longer wavelengths. The increase in the absorption can be recognized as a better molecular organization in the annealed samples. The results shown in Figure 6.1 indicate that in order to achieve maximum light absorption within the photoactive layer, the PBTTT-C_{12}:$PC_{71}BM$ blend films should be annealed at ~150 ℃. It is obvious that when the annealing temperature increases the intensity of the PL peak is decreased as depicted in Figure 6.2. This indicates that the increase in annealing temperature improves the charge transfer between the PBTTT-C_{12}:$PC_{71}BM$ and hence it would contribute to the enhancement of the short circuit current of the PV devices based on this blend system. From the PL results it is expected that the samples annealed at 150 ℃ should show better photocurrent. To confirm this, further investigation of the morphological and electrical characteristics has been given below.

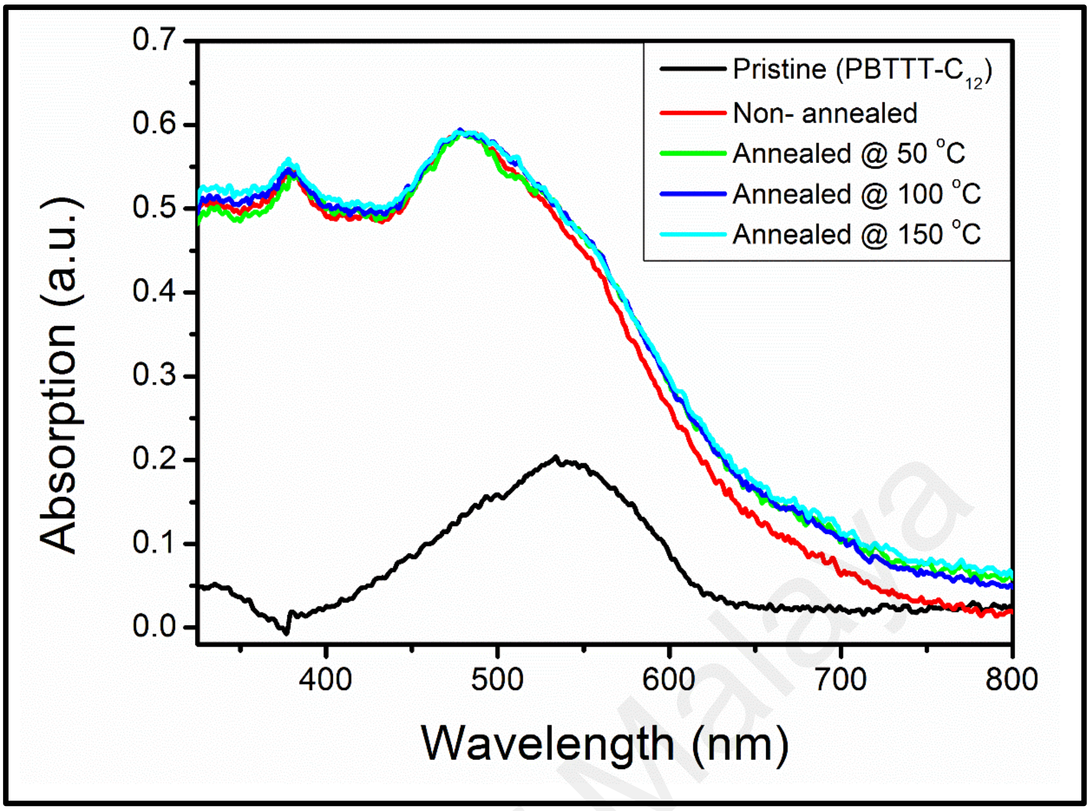

Figure 6.1: Absorption spectra of the PBTTT-C_{12} and PBTTT-C_{12}:$PC_{71}BM$ blend as a function of annealing temperature in the visible light spectrum regions.

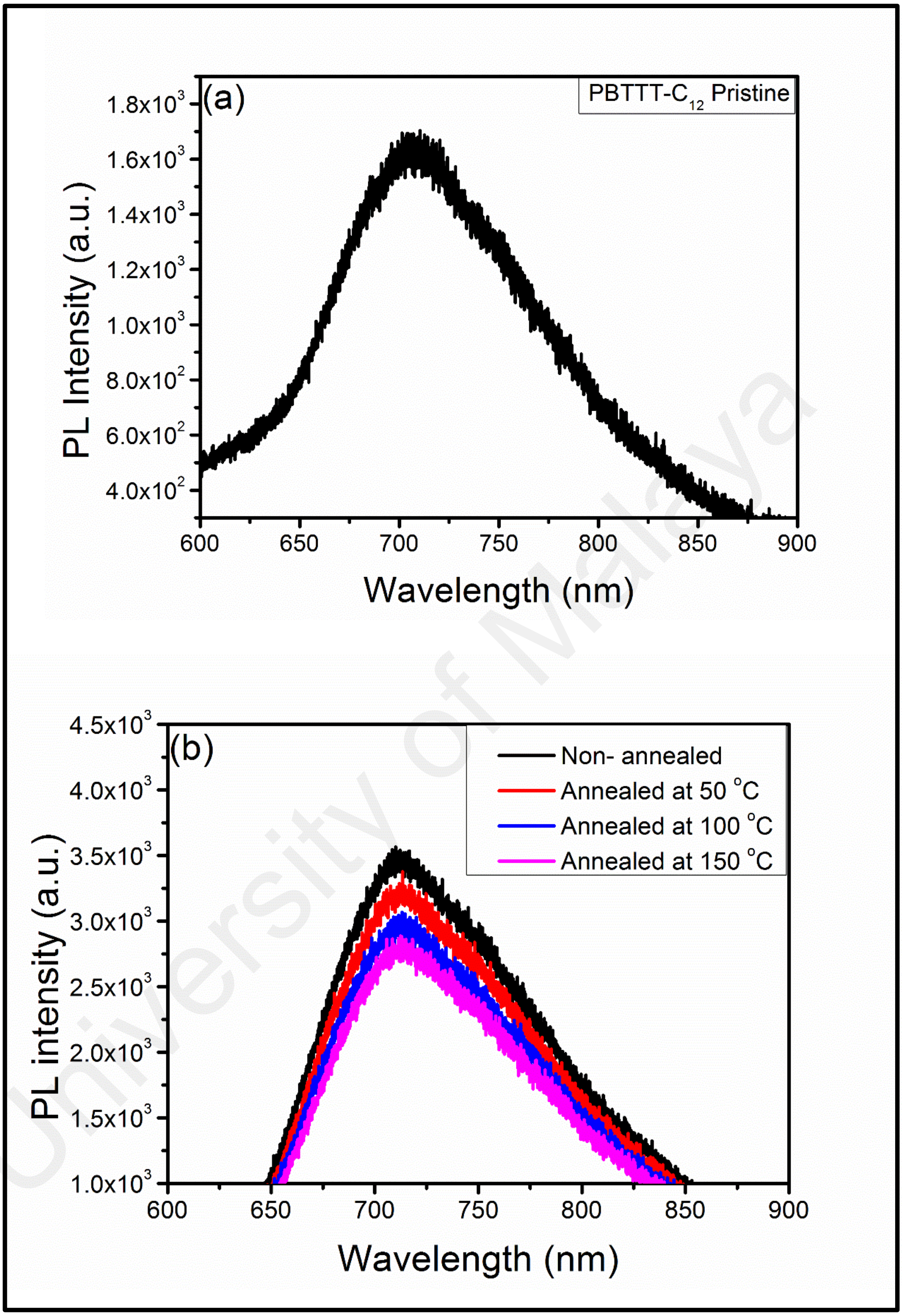

Figure 6.2: (a) Shows the PL spectrum of the PBTTT-C_{12} pristine thin film on glass. (b) PL spectra of the blend films a function of annealing temperature.

The AFM results of the non-annealed and annealed samples have been investigated to obtain a better insight into the topographical changes as a result of the thermal annealing treatment. The AFM images of the PBTTT-C_{12}:$PC_{71}BM$ blend thin films are shown in Figure 6.3. It is observed that the non-annealed and thermally annealed samples exhibit different surface morphologies and with an increase in the annealing temperature the change in the surface morphology is observed. The morphology of the non-annealed film exhibits rather a rough and non-uniform surface. The top surface of the samples become smoother and more uniform under the increase of the thermal annealing temperature (see Figure 6.3 (a)-(d)). The image in Figure 6.3 (d) suggests that the samples have less roughness with a much smoother surface and reduced sharp peaks as compared to the other samples. The rms roughness of the non-annealed film is ~4.3 nm. The thermally annealed samples at 50 ℃, 100 ℃ and 150 ℃ showed 2.8 nm, 2.1 nm and 1.6 nm rms roughnesses, respectively. In order to check these results some of the samples were thermally treated at 70 and 130 ^{o}C. The samples that have undergone thermal treatment at 70 and 130 ℃ showed more rough and non-uniform surfaces as compared to the film annealed at 150 ^{o}C. The best topographical characteristic is achieved at 150 ℃ with reduced surface unevenness 2/3 times as compared to the non-annealed samples. These results are in agreement with those obtained from electrical characteristics of the solar cell as shown in Figure 6.3. The smooth topography of the samples advocates the creation of the interpenetrating molecular network of the blend in the films, and hence, it enhances the well-ordered structure formation in the samples. The correlation between the PV parameters and annealing temperature shows that the smooth film results in higher short circuit current which may also be due to the formation of good contacts in addition to the enhanced ordered structure formation.

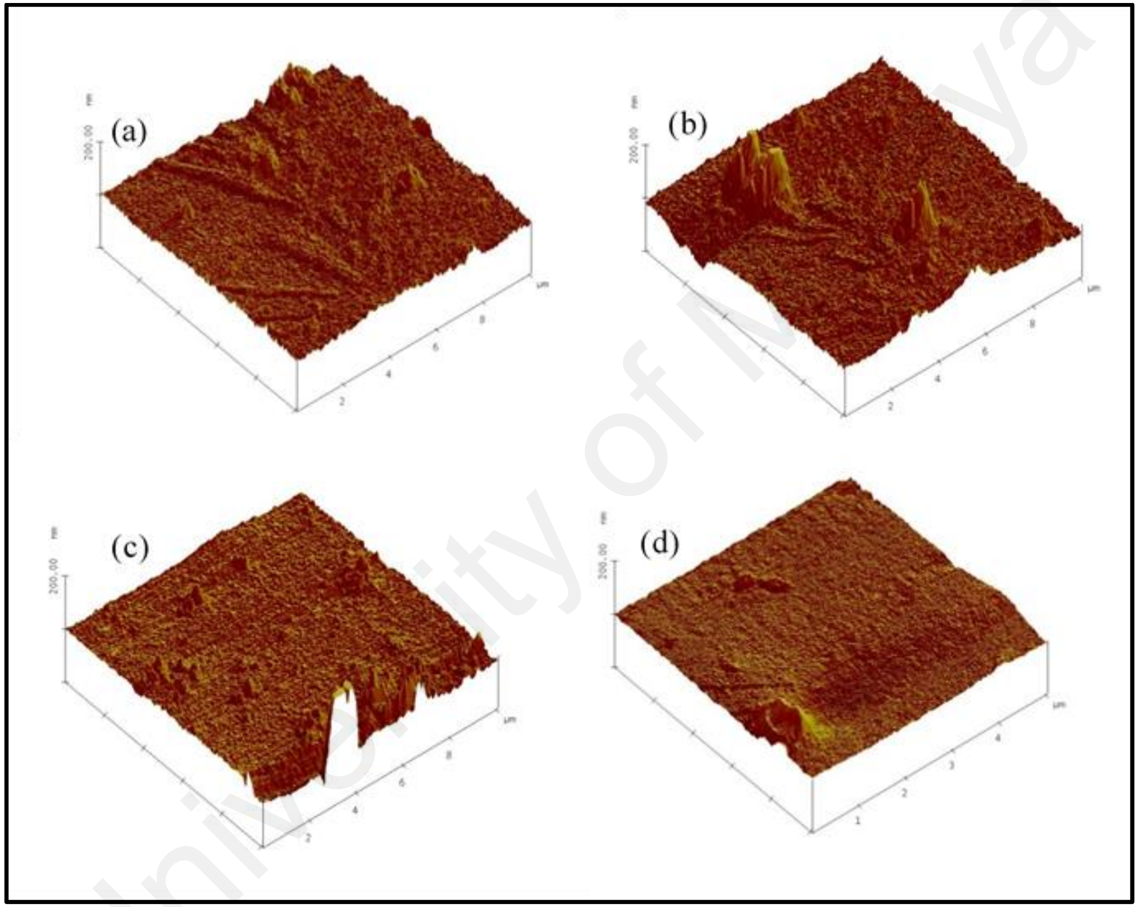

Figure 6.3: AFM images of the PBTTT-C_{12}:$PC_{71}BM$ (1:4) thin films on ITO coated glass substrates, (a) non-annealed, (b) annealed at 50 ℃, (c) annealed at 100 ℃, and (d) annealed at 150 ℃.

The current-voltage (J-V) characteristics of the ITO/PEDOT:PSS/PBTTT-C_{12}:$PC_{71}BM$/Al PV devices are shown in Figure 6.4. The standard deviation (error values) of the measurements were found around $\pm\ 0.0108, \pm\ 0.0139, \pm\ 0.0107$ and $\pm\ 0.0108$ for (0, 50, 90 and 150) ℃ respectively. The J_{sc} of the non-annealed cell is 10 ± 0.1 mAcm^{-2}. After annealing at 150 ℃, it attains a maximum of 13 ± 0.1 mAcm^{-2}. The fill factor increases from 0.33 to 0.34. Consequently, the efficiency is enhanced from 1.85% to 2.48%. The PV parameters of the solar cell have been improved after thermal treatment except V_{oc}. After annealing at 50 ℃ and 100 ℃ the V_{oc} of the cells decreases and it returned to its initial value at 150 ℃ treatment. The overall PV conversion efficiency of the OPV cells has increased about 1.35 times as compared to the non-annealed samples. However, the reason for the decreased value of V_{oc} is unknown and still under investigation. This may happen due to the restructuring of donor chains with respect to the PEDOT:PSS film below 150 ºC (Kim, Y et al., 2005). However, the samples annealed at 150 ºC exhibit the improved parameters even without the decrease of V_{oc} as compared to the non-annealed samples. A decrease in the efficiencies of the samples at thermal treatment higher than 150 ℃ has also been observed. This may be due to the aggregation formation of the $PC_{71}BM$ molecules above 150 ℃ that cause the decrease of the interfacial area between donor and acceptor molecules (Ma et al., 2005), which results in the reduction in the dissociation excitons. The comparison between this work and the previous report (Parmer et al., 2008b) is shown in Table 6.1, as clear this work surpassed in terms of bandwidth, photo current, open circuit voltage, and photo conversion efficiency.

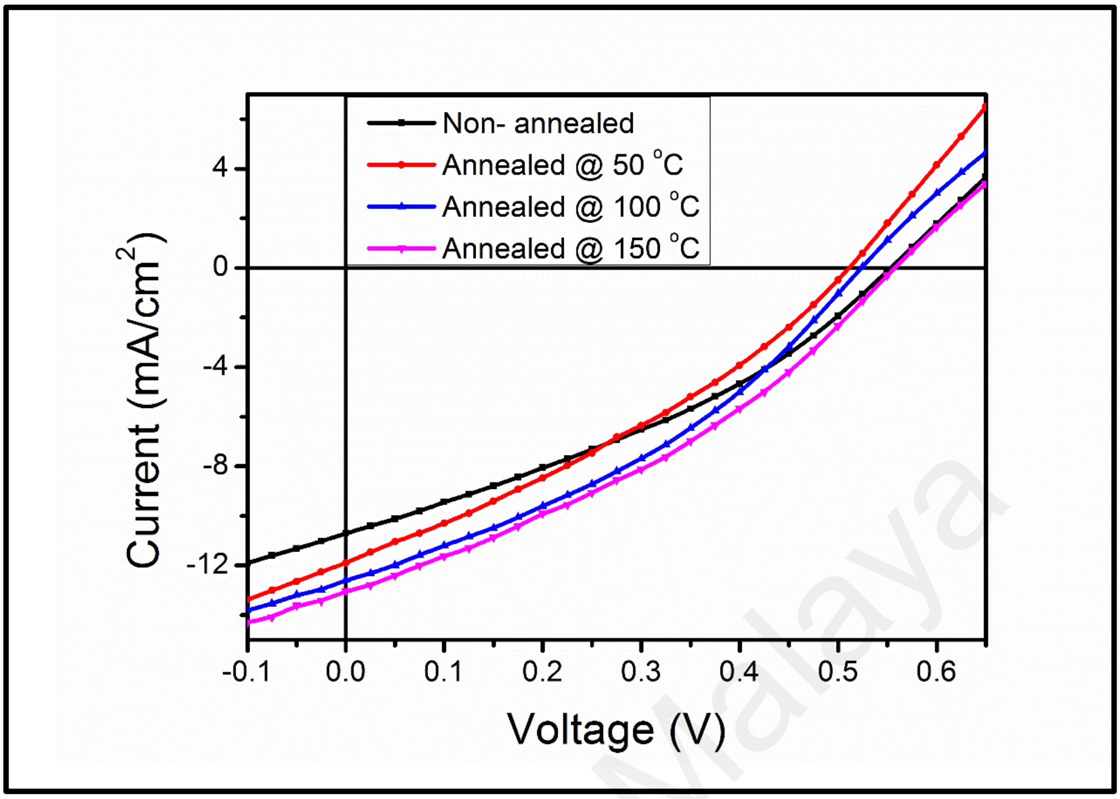

Figure 6.4: J-V characteristics of ITO/PEDOT:PSS/PBTTT-C$_{12}$:PC$_{71}$BM/Al BHJ solar cells annealed at different temperatures.

Table 6.1 Comparison result between the present work and a previous work

Reference	Spin Coat (RPM)	Active Layer Thickness (nm)	Bandwidth (nm)	J_{sc} (mA/cm^2)	V_{oc} (V)	FF	PCE (%)
Present Work (non-annealed)	**1000**	**100**	**325-800**	**10**	**0.55**	**0.33**	**1.85**
Present Work (150 ℃)	**1000**	**100**	**325-800**	**13**	**0.55**	**0.34**	**2.48**
Literature (60 ℃)	**700**	**115**	**300-700**	**9.37**	**0.525**	**0.48**	**2.34**

6.5 Conclusion

In conclusion, the effect of thermal annealing on the fabrication of BHJ cells is presented. The morphological and PV properties of blend of poly[2,5-bis(3-dodecylthiophen-2-yl)thieno[3,2-*b*]thiophene]:[6,6]-phenyl C_{71} butyric acid methyl ester (PBTTT-C_{12}:PC_{71}BM) thin film samples have been considerably influenced by the thermal treatment. The effect of the film morphology on the device performance in terms of short circuit current and efficiency has also been demonstrated under the effect of thermal annealing.

The UV/Vis/NIR absorption spectra of the PBTTT-C_{12} thin film and PBTTT-C_{12}:PC_{71}BM blend samples as a function of annealing temperature at 50 ℃, 100 ℃ and 150 ℃ as well as non-annealed have been shown. It has been observed that PBTTT-C_{12}:PC_{71}BM blend shows absorption in the wavelength ranging from ~300 nm to ~650 nm. A high energy peak at 480 nm and a relatively low energy peak at 378 nm have been investigated in the light absorption spectrum of PBTTT-C_{12}:PC_{71}BM thin film samples. Peak at 480 nm has been considered to take place from the ground state from a_{1u} (π) HOMO to e_g (π^*) LUMO of the PBTTT-C_{12}. However, in the near UV regime of the spectrum, the peak may arise from π molecular orbital (HOMO) to π^* (LUMO) transition in the PC_{71}BM. It has been observed that there is no shift in the spectra after thermal annealing, only a small enhancement in the absorption has been observed at longer wavelengths which can be recognized as a better molecular organization in the annealed samples. A maximum light absorption within the photoactive layer has been achieved in the annealed PBTTT-C_{12}:PC_{71}BM blend films at ~150 ℃.

It has also been observed that when the annealing temperature increases the intensity of the PL peak is decreased because of improved charge transfer between the PBTTT-C_{12}:PC_{71}BM, thus contributing to the enhancement of the short circuit current of the PV devices based on this blend system. From the PL results it has been investigated that the lowest peak was annealed at 150 ℃ which was later confirmed to be the best photocurrent through the morphological and electrical characteristics.

The surface morphology of the non-annealed and annealed blend films has been investigated by means of Atomic Force Microscopy (AFM) to obtain a better insight into the topographical changes as a result of the thermal annealing treatment. It has observed that with an increase in the annealing temperature, change occurs in the surface morphology in which the morphology of the non-annealed film exhibited a rather rough and non-uniform surface; the top surface of the samples then become smoother and more uniform under increased thermal annealing temperature. It has investigated that the samples annealed at 150 ℃ have less roughness with a much smoother surface and reduced sharp peaks as compared to the other samples. Further, the rms roughness of the non-annealed film was ~4.3 nm while the thermally annealed samples at 50 ℃, 100 ℃ and 150 ℃ obtained roughness of 2.8 nm, 2.1 nm and 1.6 nm rms, respectively. As a result, the best topographical characteristic has been achieved at 150 ℃ with reduced surface unevenness 2/3 times as compared to the non-annealed samples. The result promoted the creation of the interpenetrating molecular network of the blend in the films, thereby enhancing the well-ordered structure formation in the samples. Moreover, the smooth film results have shown higher short circuit current which may also be due to the formation of good contacts in addition to the enhanced ordered structure formation.

Finally, the current-voltage (J-V) characteristics of the ITO/PEDOT:PSS/PBTTT-C_{12}:$PC_{71}BM$/Al BHJ solar cells have been performed and shown. The J_{sc} determined for the non-annealed cell was 10 ± 0.1 $mAcm^{-2}$ and after annealing at 150 ℃, it achieved a maximum of 13 ± 0.1 $mAcm^{-2}$. Moreover, the fill factor and the efficiency have been enhanced, increasing from 0.33 to 0.34 and from 1.85% to 2.48% respectively. It is worth noting that the PV parameters of the solar cell have been improved after thermal treatment except for V_{oc}, as after annealing at 50 ℃ and 100 ℃ the V_{oc} of the cells decreased then returning to its initial value at 150 ℃ treatment. The decreased value of V_{oc} may be due to the restructuring of donor chains with respect to the PEDOT:PSS film below 150 ºC. However, it has been investigated that the samples annealed at 150 ºC exhibit the improved parameters even without the decrease of V_{oc} as compared to the non-annealed samples. However, overall PV conversion efficiency of the OPV cells has been increased about 1.35 times as compared to the non-annealed samples. Finally, at thermal treatment higher than 150 ℃ a decrease in the efficiencies of the samples has also been observed. This may be due to the aggregation formation of the $PC_{71}BM$ molecules above 150 ℃ that caused the decrease of the interfacial area between donor and acceptor molecules, which resulted in the reduction in the dissociation excitons.

CHAPTER 7: SUMMARIES AND FUTURE DIRECTIONS

The research work presented in this thesis falls into three sections. Summary of each section is given below. The summary section is followed by the future direction outlook, which is recommended as follow-up to the present study.

7.1 Summary

1. **In this presented study the advantages of electrical and optical properties of selected organic semiconductor materials has been demonstrated and the employing these organic semiconductors in application aspects has been explained in detail. Thus, a solution processable in the form of Thin Film Bulk Heterojunction Organic Solar Cell and binary blend based Dye Sensitized Photo Sensor have been successfully fabricated**
2. **Dye sensitized sensors were fabricated using an environmentally friendly aqueous solution of organic compound, NiTsPc, as photo sensitizer. The electrical parameters, current, and voltage across the devices were found dependent upon illumination levels. The magnitude of current and voltage were observed to be increasing linearly as a function of the progressively increasing illumination level of impinging light. The photo-conductivity sensitivities of the untreated and NaOH-treated photo sensors were determined to be $\mathbf{6.65 \times 10^{-5}}$ and $\mathbf{1.87 \times 10^{-4}}$ Sm/W, respectively. Further, the sensors have been observed to exhibit quick reversible changes in electrical parameters as a function of light switching. Response (t_r) and recovery times (t_c) for both sensors were estimated to be (t_r = 300 ms, t_c = 800 ms) and (t_r = 200 ms, t_c = 300 ms), respectively, whereby the photocurrent also showed more stable plateau values for the treated sensor when the light was periodically switched on and off. It is concluded that proposed**

sensor based on organic compound NiTsPc has potential to be applied for photovoltaic sensors.

3. **A solution processable binary blend (PCPDTBT:MEH-PPV) based DSPS has been successfully fabricated with improved sensing performance. The optical sensing properties of the DSPSs have been investigated in the illumination range of 0-30000 lx, under zero-bias condition. It is observed that the increment of photocurrent is illumination level dependent and the improvement in sensing parameters have been observed. The photo-conductivity sensitivities of the DSPS is $\mathbf{2.02 \times 10^{-5}}$ Sm/W. The average response time of the DSPS is ~382 ms. It can be concluded that the binary blend based DSPS could be an attractive route to fabricate a potential photodetector in the visible range of the solar spectrum.**
4. **The morphological and PV properties of PBTTT-C_{12}:PC_{71}BM thin film samples have been considerably influenced by the thermal treatment. With a rise in temperature, the PL intensity peak of active layer has significantly decreased and $\boldsymbol{J_{sc}}$ of the ITO/PEDOT:PSS/PBTTT-C_{12}:PC_{71}BM/Al annealed at 150 ℃ has been increased thus the efficiency of the cell has increased 1.35 times compare to the pristine cell and surpassed the previous reports. It is found that the annealing procedure significantly reduces the surface unevenness. However, a temperature beyond 150 ℃ has upset the film development due to the aggregation formation of the acceptor molecules above 150 ℃ that cause the decrease of the interfacial area between donor and acceptor molecules thus reduce the exciton dissociation. It can be concluded that by thermal annealing treatment on the spin coated PBTTT-C_{12}:PC_{71}BM thin films, the features of surface morphology of the films can be improved.**

7.2 Future Outlook

The performance of the organic photo sensors is mainly limited by low absorption profile of sensing material, low charge carrier mobility and the short exciton diffusion length. It is believed that progress on these aforementioned fronts is necessary to drive sensitivities of the OP sensors higher, ultimately leading to economical, efficient and environmentally benign light sensors.

In the fabricated photo sensor, it was demonstrated that the common polymer materials were used however in the future it possible to examine many existing organic semiconductor materials with the introduction of (nano particles (NPs), nano tubes (NTs), or nano-roads (NRs), either in single solution or binary or ternary blends) to increase the sensing parameters of the DSPS.

One of the important components of the DSPS and DSSCs is counter electrode (CE), which is usually platinum (Pt) or carbon (C) used due to its high catalytic activity and good electrical conductivity. However, platinum is expensive and scarce. Thus, in order to develop DSPS towards commercial applications, conducting polymer as a CE material has recently drawn great attention to DSSC. Among many conducting polymers, PEDOT:PSS was successfully added to the counter electrode of DSSCs due to its high electrical conductivity, low cost material, good film-forming ability and excellent electro-catalytic as shown in Figure 7.1.

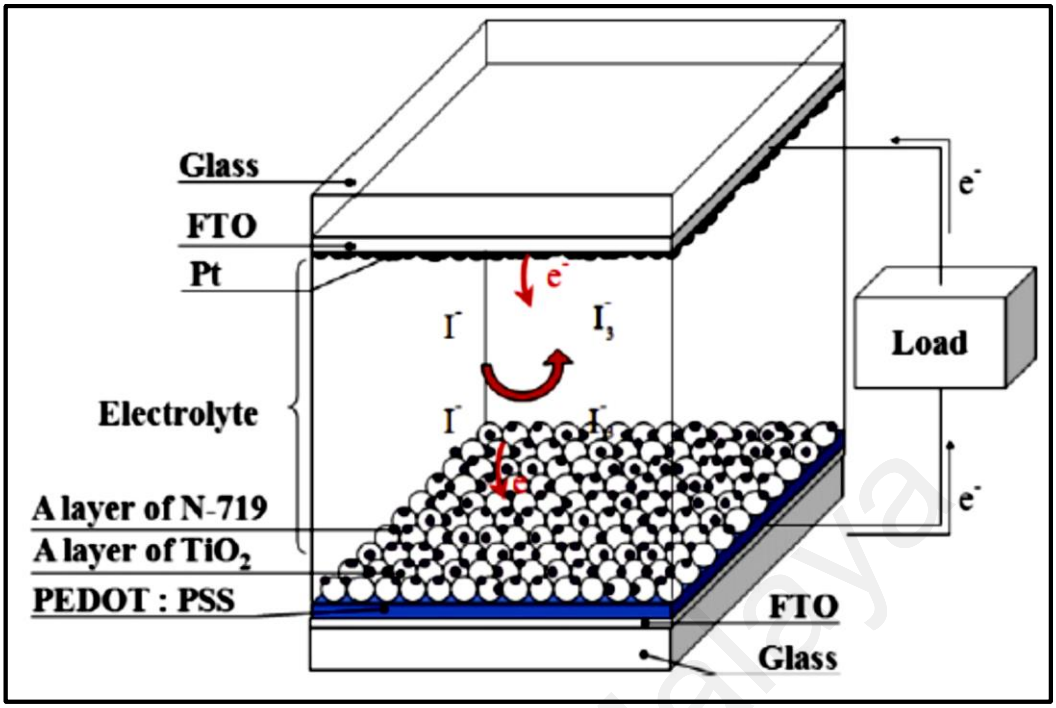

Figure 7.1: A PEDOT:PSS film as a CE in schematic of the DSSC (Chou, Chou, Kuo, & Wang, 2013).

In this thesis, PBTTT-C_{12}:$PC_{71}BM$ were used as active layer materials and have achieved performance surpassing the best previous cell devices with same material in the literature. However, the organic photovoltaic materials in recent years have been reported showing greater than 10% of the PCE values. This make these and even more efficient materials such as (PBDTT-FTTE and Solarmer's PffBT4T-2OD with 10.3% and 10.8% of PCE, respectively) become commercially available. Thus, to make realistic modules with the proposed new geometry, it would be important to continue to adapt and fine tune the appropriate interfacial materials.

In this work, PEDOT:PSS as the main interlayer has been used for the solution processed BHJ cell. However, interlayer with larger work function than PEDOT:PSS values is required to extract and collect positive carriers from the active layer for high efficiency devices. In order to develop high efficiency devices, organic dopant molecules and/or physisorbed (physically adsorbed) polymers will be necessary which lead to surface dipoles which may increase the work function. On the other hand, for the electron collecting side, the PEI or PEIE which have low work function values and are air stable conductors in the wide range are a compelling solution. Finally, in OPV devices, towards optimizing collection of the electron, the use of n-type dopants should not be ignored and would constitute a direction for future work.

REFERENCES

Addington, D Michelle, & Daniel L Schodek. (2005). *Smart materials and new technologies: for the architecture and design professions*: Routledge.

Agostinelli, T, M Caironi, D Natali, M Sampietro, G Dassa, Ev Canesi, C Bertarelli, G Zerbi, J Cabanillas-Gonzalez, & S De Silvestri. (2008). A planar organic near infrared light detector based on bulk heterojunction of a heteroquaterphenoquinone and poly [2-methoxy-5-(2′-ethyl-hexyloxy)-1, 4-phenylene vinylene]. *Journal of Applied Physics, 104*(11), 114508-114508-114505.

Ahmad, S., T. Bessho, F. Kessler, E. Baranoff, J. Frey, C. Y. Yi, M. Graetzel, & M. K. Nazeeruddin. (2012). A new generation of platinum and iodine free efficient dye-sensitized solar cells. *Physical Chemistry Chemical Physics, 14*(30), 10631-10639. doi:10.1039/c2cp41611e

Ahmad, Zubair, Shahino Mah Abdullah, & Khaulah Sulaiman. (2012). Temperature-sensitive chemical cell based on Nickel (II) phthalocyanine-tetrasulfonic acid tetrasodium salt. *Sensors and Actuators A: Physical, 179*(0), 146-150. doi:http://dx.doi.org/10.1016/j.sna.2012.03.037

Ahmad, Zubair, Shahino Mah Abdullah, & Khaulah Sulaiman. (2013). Bulk heterojunction photodiode: To detect the whole visible spectrum. *Measurement, 46*(7), 2073-2076. doi:http://dx.doi.org/10.1016/j.measurement.2013.02.006

Ahmad, Zubair, M. H. Sayyad, M. Yaseen, K. C. Aw, M. M-Tahir, & M. Ali. (2011). Potential of 5,10,15,20-Tetrakis(3',5'-di-tertbutylphenyl)porphyrinatocopper(II) for a multifunctional sensor. *Sens. Actuat. B, 155*, 81-85. doi:DOI: 10.1016/j.snb.2010.11.029

Ahmad, Zubair, Mahdi Hasan Suhail, Issam Ibrahim Muhammad, Wissam Khayer Al-Rawi, Khaulah Sulaiman, Qayyum Zafar, Ahmad Sazali Hamzah, & Zurina Shaameri. (2013). MEH-PPV/Alq3-based bulk heterojunction photodetector. *Chinese Physics B, 22*(10), 100701.

Al-Ibrahim, Maher, H-Klaus Roth, Uladzimir Zhokhavets, Gerhard Gobsch, & Steffi Sensfuss. (2005). Flexible large area polymer solar cells based on poly (3-hexylthiophene)/fullerene. *Solar Energy Materials and Solar Cells, 85*(1), 13-20.

Aldrich, Sigma. (2015, May 5 2015). TiO2 Anatase, XRD. Retrieved from http://www.sigmaaldrich.com/catalog/product/aldrich/637254?lang=en&region=MY

Ameri, Tayebeh, Ning Li, & Christoph J. Brabec. (2013). Highly efficient organic tandem solar cells: a follow up review. *Energy & Environmental Science, 6*(8), 2390-2413. doi:10.1039/c3ee40388b

Analog-Eetimes. (2015, Jan 5 2015). An SMU instrument configured as a constant current source and a voltmeter. Retrieved from http://tm-eetimes.com/images/01-edit-photo-uploads/2014/2014-03-march/keithley-biosensors/fig2.jpg

Anthopoulos, T. D., & T. S. Shafai. (2002). Effects of temperature on electronic properties of nickel phthalocyanine thin sandwich film structures. *Journal of Vacuum Science & Technology A, 20*(2), 295-298. doi:doi:http://dx.doi.org/10.1116/1.1432963

Anthopoulos, Td, & Ts Shafai. (2003). Electrical properties of α-nickel phthalocyanine/aluminium interfaces: effects of oxygen doping and thermal annealing. *Journal of Physics and Chemistry of Solids, 64*(7), 1217-1223.

Astm. (1996, Feb 7 2015). PA: American Society for Testing and Materials. Retrieved from http://www.renewableenergyworld.com/rea/news/article/2010/07/instrumentation_for_quantum_efficiency_measurement_of_solar_cells

Azonetwork. (2015, Feb 4 2015). optical interferometer. Retrieved from http://www.azooptics.com/Article.aspx?ArticleID=339

www.azonetwork.comwww.azonetwork.com

Baek, Woon-Hyuk, Hyun Yang, Tae-Sik Yoon, C. J. Kang, Hyun Ho Lee, & Yong-Sang Kim. (2009). Effect of P3HT:PCBM concentration in solvent on performances of organic solar cells. *Solar Energy Materials and Solar Cells, 93*(8), 1263-1267. doi:http://dx.doi.org/10.1016/j.solmat.2009.01.019

Barbe, Christophe J, Francine Arendse, Pascal Comte, Marie Jirousek, Frank Lenzmann, Valery Shklover, & Michael Grätzel. (1997). Nanocrystalline titanium oxide electrodes for photovoltaic applications. *Journal of the American Ceramic Society, 80*(12), 3157-3171.

Beek, Waldo Je, Martijn M Wienk, & René Aj Janssen. (2006). Hybrid solar cells from regioregular polythiophene and ZnO nanoparticles. *Advanced Functional Materials, 16*(8), 1112-1116.

Berson, Solenn, Rémi De Bettignies, Séverine Bailly, & Stéphane Guillerez. (2007). Poly (3-hexylthiophene) fibers for photovoltaic applications. *Advanced Functional Materials, 17*(8), 1377.

Binnig, G., C. F. Quate, & Ch Gerber. (1986). Atomic Force Microscope. *Physical Review Letters, 56*(9), 930-933.

Bisquert, J, & A Zaban. (2003). The trap-limited diffusivity of electrons in nanoporous semiconductor networks permeated with a conductive phase. *Applied Physics A, 77*(3-4), 507-514.

Bisquert, Juan, & Vyacheslav S Vikhrenko. (2004). Interpretation of the time constants measured by kinetic techniques in nanostructured semiconductor electrodes and dye-sensitized solar cells. *The Journal of Physical Chemistry B, 108*(7), 2313-2322.

Boschloo, Gerrit, & Anders Hagfeldt. (2009). Characteristics of the iodide/triiodide redox mediator in dye-sensitized solar cells. *Accounts of Chemical Research, 42*(11), 1819-1826.

Boschloo, Gk, A Goossens, & J Schoonman. (1997). Photoelectrochemical study of thin anatase TiO2 films prepared by metallorganic chemical vapor deposition. *Journal of the Electrochemical Society, 144*(4), 1311-1317.

Brabec, C.J. (2004). Organic photovoltaics: technology and market. *Solar Energy Materials and Solar Cells, 83*(2), 273-292.

Brabec, C.J., N.S. Sariciftci, & J.C. Hummelen. (2001). Plastic solar cells. *Advanced Functional Materials, 11*(1), 15-26.

Brabec, Christoph J, Antonio Cravino, Dieter Meissner, N Serdar Sariciftci, Thomas Fromherz, Minze T Rispens, Luis Sanchez, & Jan C Hummelen. (2001). Origin of the open circuit voltage of plastic solar cells. *Advanced Functional Materials, 11*(5), 374-380.

Brabec, Christoph J, Srinivas Gowrisanker, Jonathan Jm Halls, Darin Laird, Shijun Jia, & Shawn P Williams. (2010). Polymer–fullerene bulk-heterojunction solar cells. *Advanced Materials, 22*(34), 3839-3856.

Brabec, Christoph J. (2004). Organic photovoltaics: technology and market. *Solar Energy Materials and Solar Cells, 83*(2–3), 273-292. doi:http://dx.doi.org/10.1016/j.solmat.2004.02.030

Brabec, Christoph Joseph, Vladimir Dyakonov, Jürgen Parisi, & Niyazi Serdar Sariciftci. (2013). *Organic photovoltaics: concepts and realization* (Vol. 60): Springer Science & Business Media.

Brabec, Christoph, Ullrich Scherf, & Vladimir Dyakonov. (2011). *Organic photovoltaics: materials, device physics, and manufacturing technologies*: John Wiley & Sons.

Braun, A., & J. Tcherniac. (1907). Über die Produkte der Einwirkung von Acetanhydrid auf Phthalamid. *Berichte der deutschen chemischen Gesellschaft, 40*(2), 2709-2714. doi:10.1002/cber.190704002202

Brito, Jackeline B, Douglas Jc Gomes, Vanessa D Justina, Aline Mf Lima, Clarissa A Olivati, Josmary R Silva, & Nara C De Souza. (2012). Nanostructured films from phthalocyanine and carbon nanotubes: surface morphology and electrical characterization. *Journal of Colloid and Interface Science, 367*(1), 467-471.

Brumbach, Michael , P Alex Veneman, F Saneeha Marrikar, Thomas Schulmeyer, Adam Simmonds, Wei Xia, Paul Lee, & Neal R Armstrong. (2007). Surface composition and electrical and electrochemical properties of freshly deposited and acid-etched indium tin oxide electrodes. *Langmuir, 23*(22), 11089-11099.

Bull, Tricia A, Liam Sc Pingree, Samson A Jenekhe, David S Ginger, & Christine K Luscombe. (2009). The role of mesoscopic PCBM crystallites in solvent vapor annealed copolymer solar cells. *Acs Nano, 3*(3), 627-636.

Bull, Tricia A., Liam S. C. Pingree, Samson A. Jenekhe, David S. Ginger, & Christine K. Luscombe. (2009). The Role of Mesoscopic PCBM Crystallites in Solvent Vapor Annealed Copolymer Solar Cells. *Acs Nano, 3*(3), 627-636. doi:10.1021/nn800878c

Burschka Julian, Pellet Norman, Moon Soo-Jin, Humphry-Baker Robin, Gao Peng, Nazeeruddin Mohammad K., Gratzel, Michael. (2013). Sequential deposition as a route to high-performance perovskite-sensitized solar cells. *Nature, 499*(7458), 316-319.

Camaioni, Nadia, Giovanni Ridolfi, Giuseppe Casalbore-Miceli, Giorgia Possamai, & Michele Maggini. (2002). The Effect of a Mild Thermal Treatment on the Performance of Poly (3-alkylthiophene)/Fullerene Solar Cells. *Advanced Materials, 14*(23), 1735-1738.

Cardinaletti, Ilaria, Jurgen Kesters, Sabine Bertho, Bert Conings, Fortunato Piersimoni, Jan D’haen, Laurence Lutsen, Milos Nesladek, Bruno Van Mele, & Guy Van Assche. (2014). Toward bulk heterojunction polymer solar cells with thermally stable active layer morphology. *Journal of Photonics for Energy, 4*(1), 040997-040997.

Chabinyc, Michael L, Michael F Toney, R Joseph Kline, Iain Mcculloch, & Martin Heeney. (2007). X-ray scattering study of thin films of poly (2, 5-bis (3-alkylthiophen-2-yl) thieno [3, 2-b] thiophene). *Journal of the American Chemical Society, 129*(11), 3226-3237.

Chae, J., D. Y. Kim, S. Kim, & M. Kang. (2010). Photovoltaic efficiency on dye-sensitized solar cells (DSSC) assembled using Ga-incorporated TiO2 materials. *Journal of Industrial and Engineering Chemistry, 16*(6), 906-911. doi:10.1016/j.jiec.2010.09.012

Chang, Dong Wook, Hyo Joong Lee, Jong H. Kim, Soo Young Park, Su-Moon Park, Liming Dai, & Jong-Beom Baek. (2011). Novel Quinoxaline-Based Organic Sensitizers for Dye-Sensitized Solar Cells. *Organic Letters, 13*(15), 3880-3883. doi:10.1021/ol2012378

Chen, Dong-Yi Chen, Chao-Ling Chen, Che-Wei Hsu, Hui-Chu Hsu, Kuan-Lin Wu, Shih-Hung Liu, Pi-Tai Chou, & Yun Chi. (2011). Donor-acceptor dyes with fluorine substituted phenylene spacer for dye-sensitized solar cells. *Journal of Materials Chemistry, 21*(6), 1937-1945. doi:10.1039/C0JM02433C

Chen, Guo, Hisahiro Sasabe, Zhongqiang Wang, Xiao-Feng Wang, Ziruo Hong, Yang Yang, & Junji Kido. (2012). Co-evaporated bulk heterojunction solar cells with> 6.0% efficiency. *Advanced Materials, 24*(20), 2768-2773.

Chen, Hsiang-Yu, Jianhui Hou, Shaoqing Zhang, Yongye Liang, Guanwen Yang, Yang Yang, Luping Yu, Yue Wu, & Gang Li. (2009a). Polymer solar cells with enhanced open-circuit voltage and efficiency. *Nature Photonics, 3*(11), 649-653.

Chen, Hsiang-Yu, Jianhui Hou, Shaoqing Zhang, Yongye Liang, Guanwen Yang, Yang Yang, Luping Yu, Yue Wu, & Gang Li. (2009b). Polymer solar cells with enhanced open-circuit voltage and efficiency. *Nat Photon, 3*(11), 649-653.

Chen, Ruikui, Xichuan Yang, Haining Tian, Xiuna Wang, Anders Hagfeldt, & Licheng Sun. (2007). Effect of Tetrahydroquinoline Dyes Structure on the Performance of Organic Dye-Sensitized Solar Cells. *Chemistry of Materials, 19*(16), 4007-4015. doi:10.1021/cm070617g

Chirvase, Dana, Jürgen Parisi, Jan C Hummelen, & Vladimir Dyakonov. (2004). Influence of nanomorphology on the photovoltaic action of polymer–fullerene composites. *Nanotechnology, 15*(9), 1317.

Cho, Jeong Ho, Jiyoul Lee, Yu Xia, Bongsoo Kim, Yiyong He, Michael J. Renn, Timothy P. Lodge, & C. Daniel Frisbie. (2008). Printable ion-gel gate dielectrics for low-voltage polymer thin-film transistors on plastic. *Nat Mater, 7*(11), 900-906. doi:http://www.nature.com/nmat/journal/v7/n11/suppinfo/nmat2291_S1.html

Choi, Y. J., K. M. Kang, & H. H. Park. (2013). Post-Annealing Effects on the Surface Roughness of Undoped and Al-Doped ZnO Thin Films Deposited by Atomic Layer Deposition. In J. Wu, X. Lu, H. Xu, & N. Nakagoshi (Eds.), *Resources and Sustainable Development, Pts 1-4* (Vol. 734-737, pp. 2492-2495). Stafa-Zurich: Trans Tech Publications Ltd.

Chou, Chuen-Shii, Chuen-Shyong Chou, Yi-Ting Kuo, & Chun-Po Wang. (2013). Preparation of a working electrode with a conducting PEDOT: PSS film and its applications in a dye-sensitized solar cell. *Advanced Powder Technology, 24*(1), 336-343.

Chu, F. H., L. Ye, J. Q. Zhang, B. S. Yang, M. Zhao, D. Z. Huang, & S. H. Zhen. (2011). Study of TNT sensor based on fluorescence quenching of conjugated polymer MEH-PPV. In Q. Luo & D. Zeng (Eds.), *Information Technology for Manufacturing Systems Ii, Pts 1-3* (Vol. 58-60, pp. 2688-2692). Stafa-Zurich: Trans Tech Publications Ltd.

Chua, Lay-Lay, Jana Zaumseil, Jui-Fen Chang, Eric C. W. Ou, Peter K. H. Ho, Henning Sirringhaus, & Richard H. Friend. (2005). General observation of n-type field-effect behaviour in organic semiconductors. *Nature, 434*(7030), 194-199. doi:http://www.nature.com/nature/journal/v434/n7030/suppinfo/nature03376_S1.html

Clifford, John N, Emilio Palomares, Md K Nazeeruddin, M Grätzel, Jenny Nelson, X Li, Nicholas J Long, & James R Durrant. (2004). Molecular control of recombination dynamics in dye-sensitized nanocrystalline TiO2 films: Free energy vs distance dependence. *Journal of the American Chemical Society, 126*(16), 5225-5233.

Coakley, K.M., & M.D. Mcgehee. (2004). Conjugated polymer photovoltaic cells. *Chemistry of Materials, 16*(23), 4533-4542.

Cong, Jiayan, Xichuan Yang, Jing Liu, Jinxia Zhao, Yan Hao, Yu Wang, & Licheng Sun. (2012). Nitro group as a new anchoring group for organic dyes in dye-sensitized solar cells. *Chemical Communications, 48*(53), 6663-6665. doi:10.1039/C2CC31516E

Crespilho, Frank N, Valtencir Zucolotto, Jr Siqueira, Antônio Jf Carvalho, Cn Francisco, & On Oliveira. (2006). Using electrochemical data to obtain energy diagrams for layer-by-layer films from metallic phthalocyanines. *Int. J. Electrochem. Sci, 1*, 151-159.

Daeneke, Torben, Tae-Hyuk Kwon, Andrew B. Holmes, Noel W. Duffy, Udo Bach, & Leone Spiccia. (2011). High-efficiency dye-sensitized solar cells with ferrocene-based electrolytes. *Nat Chem*, *3*(3), 211-215. doi:http://www.nature.com/nchem/journal/v3/n3/abs/nchem.966.html#supplementary-information

Dang, Minh Trung, Lionel Hirsch, Guillaume Wantz, & James D Wuest. (2013). Controlling the morphology and performance of bulk heterojunctions in solar cells. Lessons learned from the benchmark poly (3-hexylthiophene):[6, 6]-phenyl-C61-butyric acid methyl ester system. *Chemical reviews, 113*(5), 3734-3765.

Davidson, A. T. (1982). The effect of the metal atom on the absorption spectra of phthalocyanine films. *The Journal of chemical physics, 77*(1), 168-172. doi:doi:http://dx.doi.org/10.1063/1.443636

De Bettignies, Rémi, Jocelyne Leroy, Muriel Firon, & Carole Sentein. (2005). *Study of P3HT: PCBM bulk heterojunction solar cells: influence of components ratio and of the nature of electrodes on performances and lifetime.* Paper presented at the Optics & Photonics 2005.

Dennler, G, C Lungenschmied, H Neugebauer, Ns Sariciftci, M Latreche, G Czeremuszkin, & Mr Wertheimer. (2006). A new encapsulation solution for flexible organic solar cells. *Thin Solid Films, 511*, 349-353.

Dittmer, Janke J, Elisabeth A Marseglia, & Richard H Friend. (2000). Electron trapping in dye/polymer blend photovoltaic cells. *Advanced Materials, 12*(17), 1270-1274.

Djurišić, Ab, Cy Kwong, Pc Chui, & Wk Chan. (2003). Indium–tin–oxide surface treatments: Influence on the performance of CuPc/C60 solar cells. *Journal of Applied Physics, 93*(9), 5472-5479.

Dong, Huanli, Hongfei Zhu, Qing Meng, Xiong Gong, & Wenping Hu. (2012). Organic photoresponse materials and devices. *Chem. Soc. Rev., 41*(5), 1754-1808.

Dualeh, Amalie. (2014). *Analysis of Key Electronic, Optical and Structural Parameters in Mesoscopic Solid-State Solar Cells.* (Doctor of Philosophy), LAUSANNE, Suisse.

Ellis, Hanna. (2014). *Characterization of dye-sensitized solar cells.* (Philosophy in Physical Chemistry), Uppsala University.

Erb, Tobias, Uladzimir Zhokhavets, Gerhard Gobsch, Sofiya Raleva, Bernd Stühn, Pavel Schilinsky, Christoph Waldauf, & Christoph J Brabec. (2005). Correlation between structural and optical properties of composite polymer/fullerene films for organic solar cells. *Advanced Functional Materials, 15*(7), 1193-1196.

Fakir, Muhamad Saipul, Zubair Ahmad, & Khaulah Sulaiman. (2012). Modification of Optical Band Gap and Surface Morphology of NiTsPc Thin Films. *Chinese Physics Letters, 29*(12), 126802.

Feldt, S. M., P. W. Lohse, F. Kessler, M. K. Nazeeruddin, M. Gratzel, G. Boschloo, & A. Hagfeldt. (2013). Regeneration and recombination kinetics in cobalt polypyridine based dye-sensitized solar cells, explained using Marcus theory. *Physical Chemistry Chemical Physics, 15*(19), 7087-7097. doi:10.1039/c3cp50997d

Feldt, S. M., G. Wang, G. Boschloo, & A. Hagfeldt. (2011). Effects of Driving Forces for Recombination and Regeneration on the Photovoltaic Performance of Dye-Sensitized Solar Cells using Cobalt Polypyridine Redox Couples. *Journal of Physical Chemistry C, 115*(43), 21500-21507. doi:10.1021/jp2061392

Feldt, Sandra M, Elizabeth A Gibson, Erik Gabrielsson, Licheng Sun, Gerrit Boschloo, & Anders Hagfeldt. (2010). Design of organic dyes and cobalt polypyridine redox mediators for high-efficiency dye-sensitized solar cells. *Journal of the American Chemical Society, 132*(46), 16714-16724.

Fernandes, Edson Gr, Nirton Cs Vieira, Alvaro Aa De Queiroz, Francisco Eg Guimaraes, & Valtencir Zucolotto. (2010). Immobilization of poly (propylene imine) dendrimer/nickel phtalocyanine as nanostructured multilayer films to be used as gate membranes for SEGFET pH sensors. *The Journal of Physical Chemistry C, 114*(14), 6478-6483.

Fleetham, Tyler Blain. (2014). *Organic Optoelectronic Devices Employing Small Molecules.* (PhD), Arizona State University.

Fujishima, Akira, & Kenichi Honda. (1972). Electrochemical Photolysis of Water at a Semiconductor Electrode. *Nature, 238*(5358), 37-38.

Gabrielsson, Erik. (2014). Molecular Engineering of D-π-A Dyes for Dye-Sensitized Solar Cells. *Thesis,* 66

Gaudiana, Russell, & Christoph Brabec. (2008). Organic materials: Fantastic plastic. *Nat Photon, 2*(5), 287-289.

Gerischer, H, Me Michel-Beyerle, F Rebentrost, & H Tributsch. (1968). Sensitization of charge injection into semiconductors with large band gap. *Electrochimica Acta, 13*(6), 1509-1515.

Giribabu, L., K. Sudhakar, & V. Velkannan. (2012). Phthalocyanines: potential alternative sensitizers to Ru(II) polypyridyl complexes for dye-sensitized solar cells. *Current Science, 102*(7), 991-1000.

Gong, J. W., J. Liang, & K. Sumathy. (2012). Review on dye-sensitized solar cells (DSSCs): Fundamental concepts and novel materials. *Renewable & Sustainable Energy Reviews, 16*(8), 5848-5860. doi:10.1016/j.rser.2012.04.044

Gong, Xiong, Ming-Hong Tong, Sung Heum Park, Michelle Liu, Alex Jen, & Alan J Heeger. (2010). Semiconducting polymer photodetectors with electron and hole blocking layers: High detectivity in the near-infrared. *Sensors, 10*(7), 6488-6496.

Gratzel, M. (2003). Dye-sensitized solar cells. *Journal of Photochemistry and Photobiology C-Photochemistry Reviews, 4*(2), 145-153. doi:10.1016/s1389-5567(03)00026-1

Gratzel, Michael, & Paul Liska. (1992). Photo-electrochemical cell and process of making same: Google Patents.

Green, M. A. . (2002). Third generation photovoltaics: solar cells for 2020 and beyond. *Physica E-Low-Dimensional Systems & Nanostructures, 14*, 65 doi:doi:10.1016/S1386-9477(02)00361-2

Green, Martin A., Keith Emery, Yoshihiro Hishikawa, Wilhelm Warta, & Ewan D. Dunlop. (2014). Solar cell efficiency tables (version 43). *Progress in Photovoltaics: Research and Applications, 22*(1), 1-9. doi:10.1002/pip.2452

Green, Martin A., Keith Emery, Yoshihiro Hishikawa, Wilhelm Warta, & Ewan D. Dunlop. (2015). Solar cell efficiency tables (Version 45). *Progress in Photovoltaics: Research and Applications, 23*(1), 1-9. doi:10.1002/pip.2573

Hagfeldt, A., G. Boschloo, L. C. Sun, L. Kloo, & H. Pettersson. (2010). Dye-Sensitized Solar Cells. *Chemical reviews, 110*(11), 6595-6663. doi:10.1021/cr900356p

Halls, Jjm, Ca Walsh, Nc Greenham, Ea Marseglia, Rh Friend, Sc Moratti, & Ab Holmes. (1995). Efficient photodiodes from interpenetrating polymer networks.

Hamann, Thomas W, Rebecca A Jensen, Alex Bf Martinson, Hal Van Ryswyk, & Joseph T Hupp. (2008). Advancing beyond current generation dye-sensitized solar cells. *Energy & Environmental Science, 1*(1), 66-78.

Han, Yu, Jennifer M Pringle, & Yi-Bing Cheng. (2014). Photovoltaic characteristics and stability of flexible dye-sensitized solar cells on ITO/PEN substrates. *Rsc Advances, 4*(3), 1393-1400.

Handa, Samantha, Helga Wietasch, Mukundan Thelakkat, James R. Durrant, & Saif A. Haque. (2007). Reducing charge recombination losses in solid state dye sensitized solar cells: the use of donor-acceptor sensitizer dyes. *Chemical Communications*(17), 1725-1727. doi:10.1039/B618700E

Hao, Yan, Xichuan Yang, Jiayan Cong, Haining Tian, Anders Hagfeldt, & Licheng Sun. (2009). Efficient near infrared D-[small pi]-A sensitizers with lateral anchoring group for dye-sensitized solar cells. *Chemical Communications*(27), 4031-4033. doi:10.1039/B908396K

Hara, Kohjiro, Takaro Horiguchi, Tohru Kinoshita, Kazuhiro Sayama, Hideki Sugihara, & Hironori Arakawa. (2000). Highly efficient photon-to-electron conversion with mercurochrome-sensitized nanoporous oxide semiconductor solar cells. *Solar Energy Materials and Solar Cells, 64*(2), 115-134. doi:http://dx.doi.org/10.1016/S0927-0248(00)00065-9

Harlow, Lisa Jean. (2014). *Photoelectrochemical characteristics of dye-sensitized solar cells incorporating innovative and inexpensive materials.* (Doctor of Philosophy), Michigan State University.

Hasobe, Taku, Shunichi Fukuzumi, Prashant V Kamat, & Hideyuki Murata. (2008). Fullerene-based supramolecular nanoclusters with poly [2-methoxy-5-(2'-ethylhexyloxy)-p-phenylenevinylene] for light energy conversion. *Japanese Journal of Applied Physics, 47*(2S), 1223.

Hau, Steven K, Kevin M O'malley, You-Jung Cheng, Hin-Lap Yip, Hong Ma, & Alex K-Y Jen. (2010). Optimization of active layer and anode electrode for high-performance inverted bulk-heterojunction solar cells. *Selected Topics in Quantum Electronics, IEEE Journal of, 16*(6), 1665-1675.

He, Ming, Feng Qiu, & Zhiqun Lin. (2011). Conjugated rod–coil and rod–rod block copolymers for photovoltaic applications. *Journal of Materials Chemistry, 21*(43), 17039-17048.

Heeger, Alan J. (2001). Nobel Lecture: Semiconducting and metallic polymers: The fourth generation of polymeric materials. *Reviews of Modern Physics, 73*(3), 681.

Hegde, Raghavendra, Nathan Henry, Ben Whittle, Huidong Zang, Bin Hu, Jihua Chen, Kai Xiao, & Mark Dadmun. (2012). The impact of controlled solvent exposure on the morphology, structure and function of bulk heterojunction solar cells. *Solar Energy Materials and Solar Cells, 107*, 112-124.

Henson, Zachary B, Klaus Müllen, & Guillermo C Bazan. (2012). Design strategies for organic semiconductors beyond the molecular formula. *Nature chemistry, 4*(9), 699-704.

Hiorns, Roger C, Remi De Bettignies, Jocelyne Leroy, Severine Bailly, Muriel Firon, Carole Sentein, Abdel Khoukh, Hugues Preud'homme, & Christine Dagron-Lartigau. (2006). High Molecular Weights, Polydispersities, and Annealing Temperatures in the Optimization of Bulk-Heterojunction Photovoltaic Cells Based on Poly (3-hexylthiophene) or Poly (3-butylthiophene). *Advanced Functional Materials, 16*(17), 2263-2273.

Holmes, Russell J, Wolfgang Brütting, & Chihaya Adachi. (2012). *Physics of Organic Semiconductors*: John Wiley & Sons.

Hoppe, H, Ns Sariciftci, Dam Egbe, D Mühlbacher, & M Koppe. (2005). Plastic Solar Cells Based on Novel PPE-PPV-Copolymers. *Mol. Cryst. Liq. Cryst., 426*(1), 255-263.

Hoppe, H., M. Niggemann, C. Winder, J. Kraut, R. Hiesgen, A. Hinsch, D. Meissner, & N. S Sariciftci. (2004). Nanoscale Morphology of Conjugated Polymer/Fullerene-Based Bulk- Heterojunction Solar Cells. *Advanced Functional Materials, 14*(10), 1005-1011. doi:10.1002/adfm.200305026

Huang, Y., E. J. Kramer, A. J. Heeger, & G. C. Bazan. (2014). Bulk Heterojunction Solar Cells: Morphology and Performance Relationships. *Chemical reviews, 114*(14), 7006-7043. doi:10.1021/cr400353v

Huang, Ye, Xia Guo, Feng Liu, Lijun Huo, Yuning Chen, Thomas P Russell, Charles C Han, Yongfang Li, & Jianhui Hou. (2012). Improving the Ordering and Photovoltaic Properties by Extending π–Conjugated Area of Electron-Donating Units in Polymers with D-A Structure. *Advanced Materials, 24*(25), 3383-3389.

Huang, Ye, Lijun Huo, Shaoqing Zhang, Xia Guo, Charles C Han, Yongfang Li, & Jianhui Hou. (2011). Sulfonyl: a new application of electron-withdrawing substituent in highly efficient photovoltaic polymer. *Chemical Communications, 47*(31), 8904-8906.

Huang, Ye, Mingqian Zhang, Long Ye, Xia Guo, Charles C. Han, Yongfang Li, & Jianhui Hou. (2012). Molecular energy level modulation by changing the position of electron-donating side groups. *Journal of Materials Chemistry, 22*(12), 5700-5705. doi:10.1039/C2JM16474D

Hug, H., M. Bader, P. Mair, & T. Glatzel. (2014). Biophotovoltaics: Natural pigments in dye-sensitized solar cells. *Applied Energy, 115*, 216-225. doi:10.1016/j.apenergy.2013.10.055

Iftimie, S., A. Radu, M. Radu, C. Besleaga, I. Pana, S. Craciun, M. Girtan, L. Ion, & S. Antohe. (2011). Influence Of Pedot:Pss Layer On The Performances Of "Bulk-Heterojunction" Photovoltaic Cells Based On Meh-Ppv:Pcbm(1:4) Polymeric Blends. *Digest Journal of Nanomaterials and Biostructures*, *6*(4), 1631-1638.

Imahori, Hiroshi, Yusuke Matsubara, Hiroaki Iijima, Tomokazu Umeyama, Yoshihiro Matano, Seigo Ito, Marja Niemi, Nikolai V Tkachenko, & Helge Lemmetyinen. (2010). Effects of meso-diarylamino group of porphyrins as sensitizers in dye-sensitized solar cells on optical, electrochemical, and photovoltaic properties. *The Journal of Physical Chemistry C, 114*(23), 10656-10665.

Imahori, Hiroshi, Tomokazu Umeyama, & Seigo Ito. (2009). Large π-aromatic molecules as potential sensitizers for highly efficient dye-sensitized solar cells. *Accounts of Chemical Research, 42*(11), 1809-1818.

Ishii, M, T Mori, H Fujikawa, S Tokito, & Y Taga. (2000). Improvement of organic electroluminescent device performance by in situ plasma treatment of indium–tin-oxide surface. *Journal of Luminescence, 87*, 1165-1167.

Jeol. (2009, Jan 22 2015). Instructions JFC-1600 Auto Fine Coater. Retrieved from https://www.datum.jeol.co.jp/en/related_items/jfc-1600.html

Jeon, Nam Joong, Jun Hong Noh, Woon Seok Yang, Young Chan Kim, Seungchan Ryu, Jangwon Seo, & Sang Il Seok. (2015). Compositional engineering of perovskite materials for high-performance solar cells. *Nature*, *517*(7535), 476-480.

Jørgensen, Mikkel, Jon E. Carlé, Roar R. Søndergaard, Marie Lauritzen, Nikolaj A. Dagnæs-Hansen, Sedi L. Byskov, Thomas R. Andersen, Thue T. Larsen-Olsen, Arvid P. L. Böttiger, Birgitta Andreasen, Lei Fu, Lijian Zuo, Yao Liu, Eva Bundgaard, Xiaowei Zhan, Hongzheng Chen, & Frederik C. Krebs. (2013). The state of organic solar cells—A meta analysis. *Solar Energy Materials and Solar Cells, 119*(0), 84-93. doi:http://dx.doi.org/10.1016/j.solmat.2013.05.034

Jørgensen, Mikkel, Kion Norrman, & Frederik C Krebs. (2008). Stability/degradation of polymer solar cells. *Solar Energy Materials and Solar Cells, 92*(7), 686-714.

Jung, Soyoun, Taeksoo Ji, & Vijay K Varadan. (2007). Temperature sensor using thermal transport properties in the subthreshold regime of an organic thin film transistor. *Applied Physics Letters, 90*(6), 062105.

Kalinin, Sergei V, & Alexei Gruverman. (2010). *Scanning probe microscopy of functional materials: nanoscale imaging and spectroscopy*: Springer Science & Business Media.

Kalyanasundaram, Kuppuswamy. (2010). *Dye-sensitized solar cells*: EPFL press.

Kang, M. S., J. H. Kim, Y. J. Kim, J. Won, N. G. Park, & Y. S. Kang. (2005). Dye-sensitized solar cells based on composite solid polymer electrolytes. *Chemical Communications*(7), 889-891. doi:10.1039/b412129p

Karimov, Kh S, M Saleem, Zm Karieva, A Mateen, M Tariq Saeed Chani, & Q Zafar. (2012). Humidity sensing properties of Cu2O-PEPC nanocomposite films. *Journal of Semiconductors, 33*(7), 073001.

Karlsson, Karl Martin. (2011). Design, synthesis and properties of organic sensitizers for dye sensitized solar cells.

Karwan, Wasman, Zubair Ahmad, Khaulah Sulaiman, Chi Chin Yap, & Farid Touati. (2015). Binary blend based dye sensitized photo sensor using PCPDTBT and MEH-PPV composite as a light sensitizer. *Synthetic Metals, 210, Part B,* 392-397. doi:http://dx.doi.org/10.1016/j.synthmet.2015.11.005

Karwan, Wasman Qadir, Zubair Ahmad, & Khaulah Sulaiman. (2014). Performance enhancement of NiTsPc based photo sensor using treated TiO2 NPs film. *Journal of Nanoparticle Research, 16*(11), 1-8. doi:10.1007/s11051-014-2705-7

Katusic, Stipan, Peter Albers, Rainer Kern, Frank-Martin Petrat, Ronald Sastrawan, Sarmimala Hore, Andreas Hinsch, & Andreas Gutsch. (2006). Production and characterization of ITO-Pt semiconductor powder containing nanoscale noble metal particles catalytically active in dye-sensitized solar cells. *Solar Energy Materials and Solar Cells, 90*(13), 1983-1999.

Kaufmann Eriksson, Susanna. (2014). *Interfaces in Dye-Sensitized Solar Cells Studied with Photoelectron Spectroscopy at Elevated Pressures.* (Doctor of Philosophy), Uppsala University.

Keithley. (1990). Quick Reference Guide to Source Measure Units, SMU: Keithley Instruments Inc.

Kelzenberg, Michael D, Shannon W Boettcher, Jan A Petykiewicz, Daniel B Turner-Evans, Morgan C Putnam, Emily L Warren, Joshua M Spurgeon, Ryan M Briggs, Nathan S Lewis, & Harry A Atwater. (2010). Enhanced absorption and carrier collection in Si wire arrays for photovoltaic applications. *Nature Materials, 9*(3), 239-244.

Khan, Mohd Taukeer. (2011). *Study Of Charge Transport Mechanism In Organic And Organic/Inorganic Hybrid Systems With Application To Organic Solar Cells.* (Doctor Of Philosophy), University Of Delhi.

Khatiwada, Devendra, Swaminathan Venkatesan, Qiliang Chen, Jihua Chen, Nirmal Adhikari, Ashish Dubey, Abu Farzan Mitul, Lal Mohammed, & Qiquan Qiao. (2015). Improved performance by morphology control via fullerenes in PBDT-TBT-alkoBT based organic solar cells. *Journal of Materials Chemistry A, 3*(29), 15307-15313. doi:10.1039/C5TA02709H

Kim, Heejoo, Won-Wook So, & Sang-Jin Moon. (2007). The importance of post-annealing process in the device performance of poly (3-hexylthiophene): methanofullerene polymer solar cell. *Solar Energy Materials and Solar Cells, 91*(7), 581-587.

Kim, J., K. G. Chittibabu, M. J. Cazeca, H. C. Wang, W. Kim, J. Kumar, & S. K. Tripathy. (1998). Fabrication of polymer led through layer-by-layer complexation of water-soluble conjugated polymer - Europium (III) multilayer. *Abstracts of Papers of the American Chemical Society, 216,* U87-U88.

Kim, Jin Young, Sun Hee Kim, Hyun-Ho Lee, Kwanghee Lee, Wl Ma, Xiong Gong, & Alan J Heeger. (2006). New architecture for high-efficiency polymer photovoltaic cells using solution-based titanium oxide as an optical spacer.

Kim, Y, Sa Choulis, J Nelson, Ddc Bradley, S Cook, & Jr Durrant. (2005). Composition and annealing effects in polythiophene/fullerene solar cells. *Journal of Materials Science, 40*(6), 1371-1376.

Kim, Yoojin. (2014). *Charge generation and recombination in solid-state dye-sensitized solar cells.* (Doctor of Science), Johannes Gutenberg University.

Kim, Youngkyoo, Stelios A Choulis, Jenny Nelson, Donal Dc Bradley, Steffan Cook, & James R Durrant. (2005). Composition and annealing effects in polythiophene/fullerene solar cells. *Journal of Materials Science, 40*(6), 1371-1376.

Kline, R Joseph, Dean M Delongchamp, Daniel A Fischer, Eric K Lin, Lee J Richter, Michael L Chabinyc, Michael F Toney, Martin Heeney, & Iain Mcculloch. (2007). Critical role of side-chain attachment density on the order and device performance of polythiophenes. *Macromolecules, 40*(22), 7960-7965.

Köhler, Anna, & Heinz Bässler. (2015). *Electronic Processes in Organic Semiconductors: An Introduction*: John Wiley & Sons.

Koo, B. W., S. Y. Lee, J. S. Hahn, J. Y. Kim, W. K. Bon, Y. L. Sang, S. H. Jung, & Y. K. Joo. (2007). US2007259476-A1; KR2007107887-A; US7994071-B2; KR1249097-B1. Samsung Electronics Co., Ltd.

Kooistra, Floris B, Joop Knol, Fredrik Kastenberg, Lacramioara M Popescu, Wiljan Jh Verhees, Jan M Kroon, & Jan C Hummelen. (2007). Increasing the open circuit voltage of bulk-heterojunction solar cells by raising the LUMO level of the acceptor. *Organic Letters, 9*(4), 551-554.

Koster, Sean E Shaheen, & Jan C Hummelen. (2012). Pathways to a new efficiency regime for organic solar cells. *Advanced Energy Materials, 2*(10), 1246-1253.

Koster, Lja, Vd Mihailetchi, & Pwm Blom. (2006). Bimolecular recombination in polymer/fullerene bulk heterojunction solar cells. *Applied Physics Letters, 88*(5), 052104.

Krebs, Frederik C. (2008). *Polymer photovoltaics: a practical approach* (Vol. 175): SPIE press Bellingham, WA.

Krebs, Frederik C. (2009). Fabrication and processing of polymer solar cells: A review of printing and coating techniques. *Solar Energy Materials and Solar Cells, 93*(4), 394-412. doi:http://dx.doi.org/10.1016/j.solmat.2008.10.004

Krüger, Jessica, Robert Plass, Le Cevey, Marco Piccirelli, Michael Grätzel, & Udo Bach. (2001). High efficiency solid-state photovoltaic device due to inhibition of interface charge recombination. *Applied Physics Letters, 79*(13), 2085-2087.

Ku, Shu-Yuan, & Shih-Yuan Lu. (2011). Inexpensive room temperature ionic liquids for low volatility electrolytes of dye-sensitized solar cells. *Int. J. Electrochem. Sci, 6*(11), 5219-5227.

Kugler, Th, Å Johansson, I Dalsegg, U Gelius, & Wr Salaneck. (1997). Electronic and chemical structure of conjugated polymer surfaces and interfaces: applications in polymer-based light-emitting devices. *Synthetic Metals, 91*(1), 143-146.

Kumar, B Rajesh, & T Subba Rao. (2012). AFM Studies on surface morphology, topography and texture of nanostructured zinc aluminum oxide thin films. *Digest Journal of Nanomaterials and Biostructures, 7*(4), 1881-1889.

Kumar, Challuri Vijay, Lydia Cabau, Aurelien Viterisi, Subhayan Biswas, Ganesh D. Sharma, & Emilio Palomares. (2015). Solvent Annealing Control of Bulk Heterojunction Organic Solar Cells with 6.6% Efficiency Based on a Benzodithiophene Donor Core and Dicyano Acceptor Units. *The Journal of Physical Chemistry C, 119*(36), 20871-20879. doi:10.1021/acs.jpcc.5b07130

Lee, Nam, & Woo. (2012). KR2013126785-A; KR1354468-B1. Google Patents.

Li, Denghua, Han Yan, Chao Li, Yanlian Yang, Zhixiang Wei, & Chen Wang. (2014). Nanoscale structural and electronic evolution for increased efficiency in polymer solar cells monitored by electric scanning probe microscopy. *Chinese Science Bulletin, 59*(4), 360-368.

Li, Gang, Vishal Shrotriya, Jinsong Huang, Yan Yao, Tom Moriarty, Keith Emery, & Yang Yang. (2005). High-efficiency solution processable polymer photovoltaic cells by self-organization of polymer blends. *Nature Materials, 4*(11), 864-868.

Li, Gang, Vishal Shrotriya, Yan Yao, & Yang Yang. (2005). Investigation of annealing effects and film thickness dependence of polymer solar cells based on poly (3-hexylthiophene). *Journal of Applied Physics, 98*(4), 043704.

Li, Gang, Yan Yao, Hoichang Yang, Vishal Shrotriya, Guanwen Yang, & Yang Yang. (2007). " Solvent annealing" effect in polymer solar cells based on poly (3-hexylthiophene) and methanofullerenes. *Advanced Functional Materials, 17*(10), 1636.

Li, Gang, Rui Zhu, & Yang Yang. (2012). Polymer solar cells. *Nature Photonics, 6*(3), 153-161.

Li, Liang, Erwin Auer, Meiyong Liao, Xiaosheng Fang, Tianyou Zhai, Ujjal K. Gautam, Alois Lugstein, Yasuo Koide, Yoshio Bando, & Dmitri Golberg. (2011). Deep-ultraviolet solar-blind photoconductivity of individual gallium oxide nanobelts. *Nanoscale, 3*(3), 1120-1126. doi:10.1039/C0NR00702A

Li, Shao-Lu, Ke-Jian Jiang, Ke-Feng Shao, & Lian-Ming Yang. (2006). Novel organic dyes for efficient dye-sensitized solar cells. *Chemical Communications*(26), 2792-2794. doi:10.1039/B603706B

Liang, Chunjun, Yongsheng Wang, Dan Li, Xingchen Ji, Fujun Zhang, & Zhiqun He. (2014). Modeling and simulation of bulk heterojunction polymer solar cells. *Solar Energy Materials and Solar Cells, 127*, 67-86.

Liang, Yongye, Yue Wu, Danqin Feng, Szu-Ting Tsai, Hae-Jung Son, Gang Li, & Luping Yu. (2008). Development of new semiconducting polymers for high performance solar cells. *Journal of the American Chemical Society, 131*(1), 56-57.

Liang, Yongye, Zheng Xu, Jiangbin Xia, Szu-Ting Tsai, Yue Wu, Gang Li, Claire Ray, & Luping Yu. (2010). For the bright future—bulk heterojunction polymer solar cells with power conversion efficiency of 7.4%. *Advanced Materials, 22*(20), E135-E138.

Liao, C. Z., & F. Yan. (2013). Organic Semiconductors in Organic Thin-Film Transistor-Based Chemical and Biological Sensors. *Polymer Reviews, 53*(3), 352-406. doi:10.1080/15583724.2013.808665

Lin, Lurng-Shehng Lee, & Ching-Chiun Wang. (2010). Silicon based photodetector: Google Patents.

Lin, Ching, Feng-Yu Tsai, Min-Hsueh Lee, Chia-Hua Lee, Ta-Chang Tien, Lih-Ping Wang, & Song-Yeu Tsai. (2009). Enhanced performance of dye-sensitized solar cells by an Al 2 O 3 charge-recombination barrier formed by low-temperature atomic layer deposition. *Journal of Materials Chemistry, 19*(19), 2999-3003.

Listorti, Andrea, Brian O’regan, & James R Durrant. (2011). Electron transfer dynamics in dye-sensitized solar cells. *Chemistry of Materials, 23*(15), 3381-3399.

Liu, Chin-Yi, Zachary C Holman, & Uwe R Kortshagen. (2008). Hybrid solar cells from P3HT and silicon nanocrystals. *Nano Letters, 9*(1), 449-452.

Liu, Feng, Yu Gu, Jae Woong Jung, Won Ho Jo, & Thomas P Russell. (2012). On the morphology of polymer-based photovoltaics. *Journal of Polymer Science Part B: Polymer Physics, 50*(15), 1018-1044.

Liu, Jianli, Runsheng Zeng, Chunmei Zhou, & Jianping Zou. (2011). Copper (II) and 1, 1′-Trimethylene-2, 2′-biimidazole-promoted Arylation of Acetylacetone with Aryl Iodides. *Chinese Journal of Chemistry, 29*(2), 309-313.

Liu, Weili, Ruigang Liu, Wen Wang, Weiwei Li, Wenyong Liu, Kai Zheng, Lin Ma, Ye Tian, Zhishan Bo, & Yong Huang. (2009). Tailoring nanowire network morphology and charge carrier mobility of poly (3-hexylthiophene)/C60 films. *The Journal of Physical Chemistry C, 113*(26), 11385-11389.

Liu, Xilan, Hangxing Wang, Tingbin Yang, Wei Zhang, I. Fan Hsieh, Stephen Z. D. Cheng, & Xiong Gong. (2012). Solution-processed near-infrared polymer photodetectors with an inverted device structure. *Organic Electronics, 13*(12), 2929-2934. doi:http://dx.doi.org/10.1016/j.orgel.2012.08.017

Lu, Gh, Lg Li, & Xn Yang. (2007). Achieving Perpendicular Alignment of Rigid Polythiophene Backbones to the Substrate by Using Solvent-Vapor Treatment. *Advanced Materials, 19*(21), 3594-3598.

Luque, Antonio, & Steven Hegedus. (2011). *Handbook of photovoltaic science and engineering*: John Wiley & Sons.

Ma, Wanli, Cuiying Yang, Xiong Gong, Kwanghee Lee, & Alan J Heeger. (2005). Thermally stable, efficient polymer solar cells with nanoscale control of the interpenetrating network morphology. *Advanced Functional Materials, 15*(10), 1617-1622.

Macdonald, Gordon A, P Alexander Veneman, Diogenes Placencia, & Neal R Armstrong. (2012). Electrical property heterogeneity at transparent conductive oxide/organic semiconductor interfaces: mapping contact ohmicity using conducting-tip atomic force microscopy. *Acs Nano, 6*(11), 9623-9636.

Machlin, E.S. (2005). *Materials Science in Microelectronics: The effects of structure on properties in thin films*: Elsevier.

Madhavan, Nandita. (2002). Small-molecule organic semiconductors. *Illinois University*.

Maiellaro, G., E. Ragonese, R. Gwoziecki, S. Jacobs, N. Marjanovic, M. Chrapa, J. Schleuniger, & G. Palmisano. (2014). Ambient Light Organic Sensor in a Printed Complementary Organic TFT Technology on Flexible Plastic Foil. *Ieee Transactions on Circuits and Systems I-Regular Papers, 61*(4), 1036-1043. doi:10.1109/tcsi.2013.2286031

Marchioro, Arianna. (2014). *Interfacial Charge Transfer Dynamics in Solid-State Hybrid Organic-Inorganic Solar Cells.* École Polytechnique Fédérale De Lausanne.

Mathew, S., A. Yella, P. Gao, R. Humphry-Baker, B. F. E. Curchod, N. Ashari-Astani, I. Tavernelli, U. Rothlisberger, M. K. Nazeeruddin, & M. Gratzel. (2014). Dye-sensitized solar cells with 13% efficiency achieved through the molecular engineering of porphyrin sensitizers. *Nature chemistry, 6*(3), 242-247. doi:10.1038/nchem.1861

Mawhinney, Douglas B, Viktor Naumenko, Anya Kuznetsova, John T Yates, J Liu, & Re Smalley. (2000). Surface defect site density on single walled carbon nanotubes by titration. *Chemical Physics Letters, 324*(1), 213-216.

Mayer, Ac, Michael F Toney, Shawn R Scully, Jonathan Rivnay, Christoph J Brabec, Marcus Scharber, Marcus Koppe, Martin Heeney, Iain Mcculloch, & Michael D Mcgehee. (2009). Bimolecular crystals of fullerenes in conjugated polymers and the implications of molecular mixing for solar cells. *Advanced Functional Materials, 19*(8), 1173.

Mcculloch, Iain, Martin Heeney, Clare Bailey, Kristijonas Genevicius, Iain Macdonald, Maxim Shkunov, David Sparrowe, Steve Tierney, Robert Wagner, & Weimin Zhang. (2006). Liquid-crystalline semiconducting polymers with high charge-carrier mobility. *Nature Materials, 5*(4), 328-333.

Mckeown, Neil Bruce. (1998). *Phthalocyanine materials: synthesis, structure, and function*: Cambridge University Press.

Meng, Q. B., K. Takahashi, X. T. Zhang, I. Sutanto, T. N. Rao, O. Sato, A. Fujishima, H. Watanabe, T. Nakamori, & M. Uragami. (2003). Fabrication of an efficient solid-state dye-sensitized solar cell. *Langmuir, 19*(9), 3572-3574. doi:10.1021/la026832n

Mihailetchi, Valentin D, Hx Xie, Bert De Boer, L Jan A Koster, & Paul Wm Blom. (2006). Charge transport and photocurrent generation in poly (3-hexylthiophene): methanofullerene bulk-heterojunction solar cells. *Advanced Functional Materials, 16*(5), 699-708.

Mihailetchi, Vd, Pwm Blom, Jc Hummelen, & Mt Rispens. (2003). Cathode dependence of the open-circuit voltage of polymer: fullerene bulk heterojunction solar cells. *Journal of Applied Physics, 94*(10), 6849-6854.

Mishra, Amaresh, & Peter Bäuerle. (2012). Small molecule organic semiconductors on the move: promises for future solar energy technology. *Angewandte Chemie International Edition, 51*(9), 2020-2067.

Moliton, André, & Jean-Michel Nunzi. (2006). How to model the behaviour of organic photovoltaic cells. *Polymer International, 55*(6), 583-600.

Morana, M., M. Wegscheider, A. Bonanni, N. Kopidakis, S. Shaheen, M. Scharber, Z. Zhu, D. Waller, R. Gaudiana, & C. Brabec. (2008). Bipolar charge transport in PCPDTBT-PCBM bulk-heterojunctions for photovoltaic applications. *Advanced Functional Materials, 18*(12), 1757-1766. doi:10.1002/adfm.200701428

Morooka, Masahiro, Yusuke Suzuki, & Reiko Yoneya. (2008). Dye-sensitized photoelectric conversion device and method of manufacturing the same: Google Patents.

Moser, J. (1887). Monatshefte fur Chemie. *Chemical Monthly, 8*, 373.

Muhammad, Fahmi Fariq. (2011). *Tris (8-Hydroxyquinolinate) Metals For Solution Processed Organic Solar Cells.* (PhD Degree), University of Malaya.

Mühlbacher, D., M. Scharber, M. Morana, Z. Zhu, D. Waller, R. Gaudiana, & C. Brabec. (2006). High Photovoltaic Performance of a Low-Bandgap Polymer. *Advanced Materials, 18*(21), 2884-2889. doi:10.1002/adma.200600160

Murphy, Tom. (2015). Solarprint: Harvesting and Recycling light. Retrieved from http://technologyvoice.com/2011/01/24/solarprint-harvesting-and-recycling-light

Mutolo, Kristin L, Elizabeth I Mayo, Barry P Rand, Stephen R Forrest, & Mark E Thompson. (2006). Enhanced open-circuit voltage in subphthalocyanine/C60 organic photovoltaic cells. *Journal of the American Chemical Society, 128*(25), 8108-8109.

National Renewable Energy Laboratory, Nrel. (2015, Jan 5 2016). Solar Cell Efficiency Record Chart. Retrieved from http://www.nrel.gov/ncpv/images/efficiency_chart.jpg

Nedelcu, M., S. Guldin, M. C. Orilall, J. Lee, S. Huttner, E. J. W. Crossland, S. C. Warren, C. Ducati, P. R. Laity, D. Eder, U. Wiesner, U. Steiner, & H. J. Snaith. (2010). Monolithic route to efficient dye-sensitized solar cells employing diblock copolymers for mesoporous TiO2. *Journal of Materials Chemistry, 20*(7), 1261-1268. doi:10.1039/b920077k

Nelson, Jenny. (1999). Continuous-time random-walk model of electron transport in nanocrystalline TiO 2 electrodes. *Physical Review B, 59*(23), 15374.

Nelson, Jenny. (2011). Polymer: fullerene bulk heterojunction solar cells. *Materials today, 14*(10), 462-470.

Ngamsinlapasathian, S., T. Sreethawong, Y. Suzuki, & S. Yoshikawa. (2006). Doubled layered ITO/SnO2 conducting glass for substrate of dye-sensitized solar cells. *Solar Energy Materials and Solar Cells, 90*(14), 2129-2140. doi:10.1016/j.solmat.2005.12.005

Nie, Wanyi, Hsinhan Tsai, Reza Asadpour, Jean-Christophe Blancon, Amanda J Neukirch, Gautam Gupta, Jared J Crochet, Manish Chhowalla, Sergei Tretiak, & Muhammad A Alam. (2015). High-efficiency solution-processed perovskite solar cells with millimeter-scale grains. *Science, 347*(6221), 522-525.

Niehues, Eduardo, Ieda S Scarminio, & Keiko Takashima. (2010). Optimization of photocatalytic decolorization of the azo dye direct orange 34 by statistical experimental design. *Journal of the Chilean Chemical Society, 55*(3), 320-324.

Nusbaumer, H., S. M. Zakeeruddin, J. E. Moser, & M. Gratzel. (2003). An alternative efficient redox couple for the dye-sensitized solar cell system. *Chemistry-a European Journal, 9*(16), 3756-3763. doi:10.1002/chem.200204577

O'regan, B., & M. Gratzel. (1991). A low-cost, high-efficiency solar cell based on dye-sensitized colloidal Ti02 films. *Nature, 353*(6346), 737-740.

O'regan, Brian, Jacques Moser, Marc Anderson, & Michael Graetzel. (1990). Vectorial electron injection into transparent semiconductor membranes and electric field effects on the dynamics of light-induced charge separation. *Journal of Physical Chemistry, 94*(24), 8720-8726.

Ooyama, Yousuke, Naoya Yamaguchi, Ichiro Imae, Kenji Komaguchi, Joji Ohshita, & Yutaka Harima. (2013). Dye-sensitized solar cells based on D-[small pi]-A fluorescent dyes with two pyridyl groups as an electron-withdrawing-injecting anchoring group. *Chemical Communications, 49*(25), 2548-2550. doi:10.1039/C3CC40498F

Oregan, B., & M. Gratzel. (1991). A Low-Cost, High-Efficiency Solar-Cell Based On Dye-Sensitized Colloidal Tio2 Films. *Nature, 353*(6346), 737-740. doi:10.1038/353737a0

Padinger, Franz, Roman S Rittberger, & Niyazi S Sariciftci. (2003). Effects of postproduction treatment on plastic solar cells. *Advanced Functional Materials, 13*(1), 85-88.

Palma, Giuseppina. (2014). *Nanostructured dye-sensitized solar cells.* (PhD degree), Università Degli Studi Di Trieste. Retrieved from http://hdl.handle.net/10077/9972

Panayotova, Marinela, & Vladko Panayotov. (2013). Indium–one of crucial metals for the sustainable society development. *ANNUAL OF THE UNIVERSITY OF MINING AND GEOLOGY, 56*, 159–164.

Papageorgiou, N. (2004). Counter-electrode function in nanocrystalline photoelectrochemical cell configurations. *Coordination Chemistry Reviews, 248*(13), 1421-1446.

Papageorgiou, N, Wf Maier, & M Grätzel. (1997). An iodine/triiodide reduction electrocatalyst for aqueous and organic media. *Journal of the Electrochemical Society, 144*(3), 876-884.

Park, Nam-Gyu, & Kyungkon Kim. (2008). Transparent solar cells based on dye-sensitized nanocrystalline semiconductors. *physica status solidi (a), 205*(8), 1895-1904.

Parmer, Jack E, Alex C Mayer, Brian E Hardin, Shawn R Scully, Michael D Mcgehee, Martin Heeney, & Iain Mcculloch. (2008a). Organic bulk heterojunction solar cells using poly (2, 5-bis (3-tetradecyllthiophen-2-yl) thieno [3, 2,-< equation> b</equation>] thiophene). *Applied Physics Letters, 92*(11), 113309-113309-113303.

Parmer, Jack E, Alex C Mayer, Brian E Hardin, Shawn R Scully, Michael D Mcgehee, Martin Heeney, & Iain Mcculloch. (2008b). Organic bulk heterojunction solar cells using poly (2, 5-bis (3-tetradecyllthiophen-2-yl) thieno [3, 2,-b] thiophene). *Applied Physics Letters, 92*(11), 113309.

Peet, J., J. Y. Kim, N. E. Coates, W. L. Ma, D. Moses, A. J. Heeger, & G. C. Bazan. (2007). Efficiency enhancement in low-bandgap polymer solar cells by processing with alkane dithiols. *Nat Mater, 6*(7), 497-500. doi:http://www.nature.com/nmat/journal/v6/n7/suppinfo/nmat1928_S1.html

Peet, Jeffery, C Soci, Rc Coffin, Tq Nguyen, A Mikhailovsky, Daniel Moses, & Guillermo C Bazan. (2006). Method for increasing the photoconductive response in conjugated polymer/fullerene composites. *Applied Physics Letters, 89*(25), 252105.

Pekkola, René. (2014). *Electronic Structure of Solid-State Dye-Sensitized Solar Cells: Synchrotron Induced Photoelectron Spectroscopy on Nanocrystalline TiO2, Newly Developed Dyes and Spiro-MeOTAD.* (Doctor-Engineering), Technische Universitat Damstadt. Retrieved from http://tuprints.ulb.tu-darmstadt.de/3984/

Pelet, Serge, Jacques-E Moser, & Michael Grätzel. (2000). Cooperative effect of adsorbed cations and iodide on the interception of back electron transfer in the dye sensitization of nanocrystalline TiO2. *The Journal of Physical Chemistry B, 104*(8), 1791-1795.

Pellejà I Puxeu, Laia. (2014). *Exploring novel dye concepts in dye sensitized solar cells.* (PhD), Universitat Rovira I Virgili. Retrieved from http://hdl.handle.net/10803/284156

Perepichka, Igor F, & Dmitrii F Perepichka. (2009). *Handbook of thiophene-based materials: applications in organic electronics and photonics*: Wiley Online Library.

Peumans, Peter, Aharon Yakimov, & Stephen R. Forrest. (2003). Small molecular weight organic thin-film photodetectors and solar cells. *Journal of Applied Physics, 93*(7), 3693-3723. doi:doi:http://dx.doi.org/10.1063/1.1534621

Photometrics. (2014, Feb 15 2015). Field Emission Scanning Electron Microscopy (FESEM). Retrieved from http://www.photometrics.net/fesem.html

Physics.Montana.Edu. (2011, Feb 15 2015). FESEM. Retrieved from http://www.physics.montana.edu/ical/instrumentation/fesem.asp

Po, Riccardo, Chiara Carbonera, Andrea Bernardi, & Nadia Camaioni. (2011). The role of buffer layers in polymer solar cells. *Energy & Environmental Science, 4*(2), 285-310. doi:10.1039/C0EE00273A

Pöttinger, Leo. (2014). *Spectroscopic characterization of dye sensitized TiO_2 with CO_2 co-adsorption and visible light excitation.* (Doctor of Natural Sciences Dissertation), University of Geneva, , Germany, Heidelberg. Retrieved from http://www.ub.uni-heidelberg.de/archiv/16122

Qadir, Karwan Wasman, Zubair Ahmad, & Khaulah Sulaiman. (2015). Thermal Annealing Effect on the Optical, Electrical and Morphological Properties of the PBTTT-C12:PC71BM Blend Films. *Journal of Solar Energy Engineering, 137*(3), 034503-034503. doi:10.1115/1.4029230

Qiao, Qiquan. (2015). *Organic Solar Cells: Materials, Devices, Interfaces, and Modeling* (Vol. 38): CRC Press.

Qiu, Bin, Zhenyu Lin, Jian Wang, Zhihuang Chen, Jinhua Chen, & Guonan Chen. (2009). An electrochemiluminescent biosensor for glucose based on the electrochemiluminescence of luminol on the nafion/glucose oxidase/poly(nickel(II)tetrasulfophthalocyanine)/multi-walled carbon nanotubes modified electrode. *Talanta, 78*(1), 76-80. doi:http://dx.doi.org/10.1016/j.talanta.2008.10.067

Rand, & H Richter. (2014). Organic Solar Cells: fundamentals, devices, and upscaling. *Pan Stanford: Florida*.

Rand, Barry P, Diana P Burk, & Stephen R Forrest. (2007). Offset energies at organic semiconductor heterojunctions and their influence on the open-circuit voltage of thin-film solar cells. *Physical Review B, 75*(11), 115327.

Rao, S Venugopal, & D Narayana Rao. (2002). Excited state dynamics in phthalocyanines studied using degenerate four wave mixing with incoherent light. *Journal of Porphyrins and Phthalocyanines, 6*(03), 233-237.

Rauch, Tobias, Michaela Böberl, Sandro F Tedde, Jens Fürst, Maksym V Kovalenko, Günter Hesser, Uli Lemmer, Wolfgang Heiss, & Oliver Hayden. (2009). Near-infrared imaging with quantum-dot-sensitized organic photodiodes. *Nature Photonics, 3*(6), 332-336.

Rauh, Daniel, Alexander Wagenpfahl, Carsten Deibel, & Vladimir Dyakonov. (2011). Relation of open circuit voltage to charge carrier density in organic bulk heterojunction solar cells. *arXiv preprint arXiv:1110.0588*.

Ren, Xiaoming, Quanyou Feng, Gang Zhou, Chun-Hui Huang, & Zhong-Sheng Wang. (2010). Effect of cations in coadsorbate on charge recombination and conduction band edge movement in dye-sensitized solar cells. *The Journal of Physical Chemistry C, 114*(15), 7190-7195.

Renishaw. (2015, Mar 10 2015). Photoluminescence explained. Retrieved from http://www.renishaw.com/media/img/en/291217c1d36948608830dede97d3d1c1.jpg

Reynal, Anna, & Emilio Palomares. (2011). Ruthenium polypyridyl sensitisers in dye solar cells based on mesoporous TiO2. *European Journal of Inorganic Chemistry, 2011*(29), 4509-4526.

Robertson, Neil. (2006). Optimizing Dyes for Dye-Sensitized Solar Cells. *Angewandte Chemie International Edition, 45*(15), 2338-2345.

Rodriguez-Mendez, Ml, Y Gorbunova, & Ja De Saja. (2002). Spectroscopic properties of Langmuir-Blodgett films of lanthanide bis (phthalocyanine) s exposed to volatile organic compounds. Sensing applications. *Langmuir, 18*(24), 9560-9565.

Roiter, Yuri, & Sergiy Minko. (2005). AFM Single Molecule Experiments at the Solid−Liquid Interface: In Situ Conformation of Adsorbed Flexible

Polyelectrolyte Chains. *Journal of the American Chemical Society, 127*(45), 15688-15689. doi:10.1021/ja0558239

Ronda, Cees, & Alok Srivastava. (2006). Luminescence science and display materials. *Interface-Electrochemical Society, 15*(1), 55-58.

Rouse, Margaret. (2005, Dec 15 2015). photosensor. Retrieved from http://whatis.techtarget.com/definition/photosensor

Saito, Y., T. Azechi, T. Kitamura, Y. Hasegawa, Y. Wada, & S. Yanagida. (2004). Photo-sensitizing ruthenium complexes for solid state dye solar cells in combination with conducting polymers as hole conductors. *Coordination Chemistry Reviews, 248*(13-14), 1469-1478. doi:10.1016/j.ccr.2004.03.025

Saleem, Muhammad, Muhammad H Sayyad, Khasan S Karimov, Muhammad Yaseen, & Mukhtar Ali. (2009). Cu (II) 5, 10, 15, 20-tetrakis (4′-isopropylphenyl) porphyrin based surface-type resistive–capacitive multifunctional sensor. *Sensors and Actuators B: Chemical, 137*(2), 442-446.

Salzman, Rhonda F, Jiangeng Xue, Barry P Rand, Alex Alexander, Mark E Thompson, & Stephen R Forrest. (2005). The effects of copper phthalocyanine purity on organic solar cell performance. *Organic Electronics, 6*(5), 242-246.

Sayyad, Mh, M Shah, Ks Karimov, Z Ahmad, M Saleem, & M Maroof Tahir. (2008). Fabrication and study of NiPc thin film based surface type photocapacitors. *J. Optoelectron. Adv. Mater, 10*, 2805-2810.

Scharber, Markus C, David Muhlbacher, Markus Koppe, Patrick Denk, Christoph Waldauf, Alan J Heeger, & Christoph J Brabec. (2006). Design rules for donors in bulk-heterojunction solar cells-towards 10% energy-conversion efficiency. *ADVANCED MATERIALS-DEERFIELD BEACH THEN WEINHEIM-, 18*(6), 789.

Schoch, Kf, & Ta Temofonte. (1988). IR response of phthalocyanine thin films to nitrogen dioxide. *Thin Solid Films, 165*(1), 83-89.

Schwoerer, Markus, & Hans Christoph Wolf. (2008). *Organic molecular solids*: John Wiley & Sons.

Seah, M. P. (2014). Measurement of the roughness of nano-scale surfaces, both unannealed and with limited anneal, by atomic force microscopy. *Measurement Science & Technology, 25*(10), 12. doi:10.1088/0957-0233/25/10/105001

Semendy, Fred, Greg Meissner, & Priyalal Wijewarnasuriya. (2011). *Electrical and Optical Response Properties of MEH-PPV Semiconductor Polymer Schottky Diodes*. Retrieved from

Shah, Mutabar. (2010). *Fabrication and Investigation of Nickel Phthalocyanine Based Electronic and Optoelectronic Devices.* (Doctor of Philosophy), Ghulam Ishaq Khan Institute of Engineering Sciences and Technology, Pakistan.

Shaheen, S.E., C.J. Brabec, N.S. Sariciftci, F. Padinger, T. Fromherz, & J.C. Hummelen. (2001). 2.5% efficient organic plastic solar cells. *Applied Physics Letters, 78*(6), 841-843.

Shahroozi, Ali. (2015). *Synthesis of novel porous nanostructures via template-directed methods and applications in photovoltaics.* (Doctor of Philosophy), University of Sussex.

Silva, Josmary R, Jackeline B Brito, Sonia T Tanimoto, & Nara C De Souza. (2011). Morphological structure characterization of PAH/NiTsPc multilayer nanostructured films. *Materials Sciences and Applications, 2*(11), 1661.

Skorka, Orit, & Dileepan Joseph. (2011). Design and fabrication of vertically-integrated CMOS image sensors. *Sensors, 11*(5), 4512-4538.

Skotheim, Terje A, & John Reynolds. (2007). *Handbook of Conducting Polymers, 2 Volume Set*: CRC press.

Snaith, Henry J, & Michael Grätzel. (2007). Electron and Hole Transport through Mesoporous TiO2 Infiltrated with Spiro-MeOTAD. *Advanced Materials, 19*(21), 3643-3647.

Snow, Arthur W. (2003). Phthalocyanine Aggregation 109. *The Porphyrin Handbook: Phthalocyanines: Properties and Materials, 17*, 129.

So, Sk, Wk Choi, Ch Cheng, Lm Leung, & Cf Kwong. (1999). Surface preparation and characterization of indium tin oxide substrates for organic electroluminescent devices. *Applied Physics A: Materials Science & Processing, 68*(4), 447-450.

Soci, Cesare, In-Wook Hwang, Daniel Moses, Zhengguo Zhu, David Waller, Russel Gaudiana, Christoph J Brabec, & Alan J Heeger. (2007). Photoconductivity of a low-bandgap conjugated polymer. *Advanced Functional Materials, 17*(4), 632.

Soci, Cesare, Arthur Zhang, Xin-Yu Bao, Hongkwon Kim, Yuhwa Lo, & Deli Wang. (2010). Nanowire photodetectors. *Journal of Nanoscience and Nanotechnology, 10*(3), 1430-1449.

Södergren, Sven, Anders Hagfeldt, Jörgen Olsson, & Sten-Eric Lindquist. (1994). Theoretical models for the action spectrum and the current-voltage characteristics of microporous semiconductor films in photoelectrochemical cells. *The Journal of Physical Chemistry, 98*(21), 5552-5556.

Solbrand, Anita, Henrik Lindström, Håkan Rensmo, Anders Hagfeldt, Sten-Eric Lindquist, & Sven Södergren. (1997). Electron transport in the nanostructured TiO2-electrolyte system studied with time-resolved photocurrents. *The Journal of Physical Chemistry B, 101*(14), 2514-2518.

Spadavecchia, J, G Ciccarella, P Siciliano, S Capone, & R Rella. (2004). Spin-coated thin films of metal porphyrin–phthalocyanine blend for an optochemical sensor of alcohol vapours. *Sensors and Actuators B: Chemical, 100*(1), 88-93.

Spanggaard, Holger, & Frederik C Krebs. (2004). A brief history of the development of organic and polymeric photovoltaics. *Solar Energy Materials and Solar Cells, 83*(2), 125-146.

Stadtländer, Ctkh. (2007). Scanning electron microscopy and transmission electron microscopy of mollicutes: challenges and opportunities. *Modern research and educational topics in microscopy, 1*, 122-131.

Sun, Yanming, Gregory C Welch, Wei Lin Leong, Christopher J Takacs, Guillermo C Bazan, & Alan J Heeger. (2012). Solution-processed small-molecule solar cells with 6.7% efficiency. *Nature Materials, 11*(1), 44-48.

Sweet, Marshall L. (2013). *Water soluble polymer solar cells based on electrospray deposition.* (PhD), Virginia Commonwealth University.

Takada, Shunji, Masayuki Hayashi, Tetsuro Mitsui, Yoshiki Maehara, & Mikio Ihama. (2007). *CMOS Color Image Sensor Overlaid with Organic Photoelectric Conversion Layers: Depression of Dark Current.* Paper presented at the Proc. 2007 International Image Sensor Workshop, Ogunquit Maine, USA June.

Thorlabs. (2016, Jan 10 2016). Rectangular Step Variable Metallic Neutral Density Filters. Retrieved from https://www.thorlabs.com/newgrouppage9.cfm?objectgroup_id=1624&pn=NDL-25S-4

Tian, H. N., E. Gabrielsson, P. W. Lohse, N. Vlachopoulos, L. Kloo, A. Hagfeldt, & L. C. Sun. (2012). Development of an organic redox couple and organic dyes for aqueous dye-sensitized solar cells. *Energy & Environmental Science, 5*(12), 9752-9755. doi:10.1039/c2ee23263d

Tiwari, Gopal Nath, & Swapnil Dubey. (2010). *Fundamentals of photovoltaic modules and their applications*: Royal Society of Chemistry.

Tress, Wolfgang. (2014). *Organic Solar Cells: Theory, Experiment, and Device Simulation* (Vol. 208): Springer.

Tsai, Dung-Sheng, Chin-An Lin, Wei-Cheng Lien, Hung-Chih Chang, Yuh-Lin Wang, & Jr-Hau He. (2011). Ultra-High-Responsivity Broadband Detection of Si Metal–Semiconductor–Metal Schottky Photodetectors Improved by ZnO Nanorod Arrays. *Acs Nano, 5*(10), 7748-7753.

U.S. Department of Labor, Solvents - Safety and Health Topics-Osha (2007). Solvents.

Uhrich, Christian, David Wynands, Selina Olthof, Moritz K Riede, Karl Leo, Stefan Sonntag, Bert Maennig, & Martin Pfeiffer. (2008). Origin of open circuit voltage in planar and bulk heterojunction organic thin-film photovoltaics depending on doped transport layers. *Journal of Applied Physics, 104*(4), 3107.

Valouch, Sebastian, Klaus Huska, Jurana Hetterich, Jurana Hetterich, Alexander Colsmann, Carola Moosmann, Katja Dopf, Matthias Wissert, Siegfried Kettlitz, & Nico Christ. (2007). Nanostructured organic photodiodes.

Vieira, Nirton, Alessandra Figueiredo, Alvaro Aa De Queiroz, Valtencir Zucolotto, & Francisco Eg Guimarães. (2011). Self-assembled films of dendrimers and metallophthalocyanines as FET-based glucose biosensors. *Sensors, 11*(10), 9442-9449.

Wan, J., Y. Lei, Y. R. Zhang, Y. Leng, & J. Liu. (2012). Study on TiO2 photoelectrode to improve the overall performance of dye-sensitized solar cells. *Electrochimica Acta, 59*, 75-80. doi:10.1016/j.electacta.2011.10.040

Wang, Fu-You Li, & Chun-Hui Huang. (2000). Highly efficient sensitization of nanocrystalline TiO films with styryl benzothiazolium propylsulfonate. *Chemical Communications*(20), 2063-2064. doi:10.1039/B006427K

Wang, Wl Li, B Chu, Ll Chen, G Zhang, Zs Su, Yr Chen, Df Yang, Jz Zhu, & Sh Wu. (2010). Visible-blind ultraviolet photo-detector using tris-(8-hydroxyquinoline) rare earth as acceptors and the effects of the bulk and interfacial exciplex emissions on the photo-responsivity. *Organic Electronics, 11*(7), 1301-1306.

Wang, Ergang, Lintao Hou, Zhongqiang Wang, Stefan Hellström, Fengling Zhang, Olle Inganäs, & Mats R Andersson. (2010). An Easily Synthesized Blue Polymer for High-Performance Polymer Solar Cells. *Advanced Materials, 22*(46), 5240-5244.

Wang, Jian, & Sungjoo Lee. (2011). Ge-photodetectors for Si-based optoelectronic integration. *Sensors, 11*(1), 696-718.

Wang, Jin, & Zhiqun Lin. (2009). Dye-Sensitized TiO2 Nanotube Solar Cells with Markedly Enhanced Performance via Rational Surface Engineering. *Chemistry of Materials, 22*(2), 579-584. doi:10.1021/cm903164k

Wang, L., Y. Pu, W. Fang, J. Dai, C. Zheng, C. Mo, C. Xiong, & F. Jiang. (2005). Effect of high-temperature annealing on the structural and optical properties of ZnO films. *Thin Solid Films, 491*(1-2), 323-327.

Wang, P., S. M. Zakeeruddin, P. Comte, R. Charvet, R. Humphry-Baker, & M. Gratzel. (2003). Enhance the performance of dye-sensitized solar cells by Co-grafting amphiphilic sensitizer and hexadecylmalonic acid on TiO2 nanocrystals. *Journal of Physical Chemistry B, 107*(51), 14336-14341. doi:10.1021/jp0365965

Wang, P., S. M. Zakeeruddin, J. E. Moser, R. Humphry-Baker, & M. Gratzel. (2004). A solvent-free, SeCN-/(SeCN)(3)(-) based ionic liquid electrolyte for high-efficiency dye-sensitized nanocrystalline solar cells. *Journal of the American Chemical Society, 126*(23), 7164-7165. doi:10.1021/ja048472r

Wang, Peng, Qing Dai, Shaik M Zakeeruddin, Maria Forsyth, Douglas R Macfarlane, & Michael Grätzel. (2004). Ambient temperature plastic crystal electrolyte for efficient, all-solid-state dye-sensitized solar cell. *Journal of the American Chemical Society, 126*(42), 13590-13591.

Wang, Peng, Shaik M Zakeeruddin, Jacques E Moser, Mohammad K Nazeeruddin, Takashi Sekiguchi, & Michael Grätzel. (2003). A stable quasi-solid-state dye-sensitized solar cell with an amphiphilic ruthenium sensitizer and polymer gel electrolyte. *Nature Materials, 2*(6), 402-407.

Wannier, Gregory H. (1937). The structure of electronic excitation levels in insulating crystals. *Physical Review, 52*(3), 191.

Webster, J.G., & H. Eren. (2014). *Measurement, Instrumentation, and Sensors Handbook, Second Edition: Electromagnetic, Optical, Radiation, Chemical, and Biomedical Measurement*: CRC Press.

Wei, G. D., R. R. Lunt, K. Sun, S. Y. Wang, M. E. Thompson, & Stephen R. Forrest. (2010). Efficient, Ordered Bulk Heterojunction Nanocrystalline Solar Cells by Annealing of Ultrathin Squaraine Thin Films. *Nano Letters, 10*(9), 3555-3559. doi:10.1021/nl1018194

Wengeler, Lukas, Marcel Schmitt, Katharina Peters, Philip Scharfer, & Wilhelm Schabel. (2013). Comparison of large scale coating techniques for organic and hybrid films in polymer based solar cells. *Chemical Engineering and Processing: Process Intensification, 68,* 38-44.

Wenger, Bernard, Christophe Bauer, Mohammad K. Nazeeruddin, Pascal Comte, Shaik M. Zakeeruddin, Michael Grätzel, & Jacques- E. Moser. (2006). *Electron donor-acceptor distance dependence of the dynamics of light-induced interfacial charge transfer in the dye-sensitization of nanocrystalline oxide semiconductors*.

Wienk, Martijn M, Jan M Kroon, Wiljan Jh Verhees, Joop Knol, Jan C Hummelen, Paul A Van Hal, & René Aj Janssen. (2003). Efficient methano [70] fullerene/MDMO-PPV bulk heterojunction photovoltaic cells. *Angewandte Chemie, 115*(29), 3493-3497.

Wiggins, Bryan Cortez. (2013). *Structural and electronic properties of porphyrins and phthalocyanines self assembled on conductive surfaces.* (Doctor Of Philosophy), Washington State University.

Wiziack, Nkl, A Catini, M Santonico, A D'amico, R Paolesse, Lg Paterno, Fj Fonseca, & C Di Natale. (2009). A sensor array based on mass and capacitance transducers for the detection of adulterated gasolines. *Sensors and Actuators B: Chemical, 140*(2), 508-513.

Wu, Cc, Ci Wu, Jc Sturm, & A Kahn. (1997). Surface modification of indium tin oxide by plasma treatment: An effective method to improve the efficiency, brightness, and reliability of organic light emitting devices. *Applied Physics Letters, 70*(11), 1348-1350.

Wu, X. F., G. Q. Shi, F. E. Chen, S. H. Han, & J. B. Peng. (2004). High-quality poly 2-methoxy-5-(2 '-ethylhexyloxy)-p-phenylenevinylene synthesized by a solid-liquid two-phase reaction: Characterizations and electroluminescence properties. *Journal of Polymer Science Part a-Polymer Chemistry, 42*(12), 3049-3054. doi:10.1002/pola.20171

Wu, Yiming, Xiujuan Zhang, Huanhuan Pan, Wei Deng, Xiaohong Zhang, Xiwei Zhang, & Jiansheng Jie. (2013). In-situ device integration of large-area patterned organic nanowire arrays for high-performance optical sensors. *Scientific Reports, 3*.

Wudl, F. & Srdanov, G. (1993). Conducting polymer formed of poly(2-methoxy-5-(2'-ethylhexyloxy)-p-phenylene vinylene). *US patent, 5*(189), 136.

Xie, Jingjing. (2013). *Characterisation of low noise InGaAs/AlAsSb avalanche photodiodes.* University of Sheffield.

Xu, Mingfei, Difei Zhou, Ning Cai, Jingyuan Liu, Renzhi Li, & Peng Wang. (2011). Electrical and photophysical analyses on the impacts of arylamine electron donors in cyclopentadithiophene dye-sensitized solar cells. *Energy & Environmental Science, 4*(11), 4735-4742. doi:10.1039/C1EE02432A

Xue, Jiangeng, Barry P Rand, Soichi Uchida, & Stephen R Forrest. (2005a). A hybrid planar–mixed molecular heterojunction photovoltaic cell. *Advanced Materials, 17*(1), 66-71.

Xue, Jiangeng, Barry P Rand, Soichi Uchida, & Stephen R Forrest. (2005b). Mixed donor-acceptor molecular heterojunctions for photovoltaic applications. II. Device performance. *Journal of Applied Physics, 98*(12), 124903.

Xue, Jiangeng, Soichi Uchida, Barry P Rand, & Stephen R Forrest. (2004). 4.2% efficient organic photovoltaic cells with low series resistances. *Applied Physics Letters, 84*, 3013.

Yam, Vivian Ww. (2010). *WOLEDs and Organic Photovoltaics: Recent Advances and Applications*: Springer Science & Business Media.

Yang, Cy, & Aj Heeger. (1996). Morphology of composites of semiconducting polymers mixed with C 60. *Synthetic Metals, 83*(2), 85-88.

Yang, Hong Fang, Ya Shan Zhang, Bin Qiu, & Zhen Yu Lin. (2012). The electrochemiluminescent behavior of nickel phthalocyanine (NiTSPc)/H 2 O 2 system on a heated ITO electrode. *Chinese Chemical Letters, 23*(6), 711-714.

Yang, Lei. (2014). *Hole Transport Materials for Solid-State Mesoscopic Solar Cells.* (Doctor of Philosophy), Uppsala, Sweden.

Yang, Lijun, Wallace Woon-Fong Leung, & Jingchuan Wang. (2013). Improvement in light harvesting in a dye sensitized solar cell based on cascade charge transfer. *Nanoscale, 5*(16), 7493-7498.

Yang, Xiaoniu, Joachim Loos, Sjoerd C Veenstra, Wiljan Jh Verhees, Martijn M Wienk, Jan M Kroon, Matthias Aj Michels, & René Aj Janssen. (2005). Nanoscale morphology of high-performance polymer solar cells. *Nano Letters, 5*(4), 579-583.

Yang, Yang, Wei Chen, Letian Dou, Wei-Hsuan Chang, Hsin-Sheng Duan, Brion Bob, Gang Li, & Yang Yang. (2015). High-performance multiple-donor bulk heterojunction solar cells. *Nat Photon, 9*(3), 190-198. doi:10.1038/nphoton.2015.9

http://www.nature.com/nphoton/journal/v9/n3/abs/nphoton.2015.9.html#supplementary-information

Yao, Qiao-Hong, Lu Shan, Fu-You Li, Dong-Dong Yin, & Chun-Hui Huang. (2003). An expanded conjugation photosensitizer with two different adsorbing groups for solar cells. *New Journal of Chemistry, 27*(8), 1277-1283. doi:10.1039/B302552G

Yeh, N., & P. Yeh. (2013). Organic solar cells: Their developments and potentials. *Renewable & Sustainable Energy Reviews, 21*, 421-431. doi:10.1016/j.rser.2012.12.046

Yella, Aswani, Hsuan-Wei Lee, Hoi Nok Tsao, Chenyi Yi, Aravind Kumar Chandiran, Md Khaja Nazeeruddin, Eric Wei-Guang Diau, Chen-Yu Yeh, Shaik M Zakeeruddin, & Michael Grätzel. (2011). Porphyrin-sensitized solar cells with cobalt (II/III)–based redox electrolyte exceed 12 percent efficiency. *Science, 334*(6056), 629-634.

You, Jingbi, Letian Dou, Ken Yoshimura, Takehito Kato, Kenichiro Ohya, Tom Moriarty, Keith Emery, Chun-Chao Chen, Jing Gao, & Gang Li. (2013). A polymer tandem solar cell with 10.6% power conversion efficiency. *Nature Communications, 4*, 1446.

Yu, G., K. Pakbaz, C. Zwang, & A. J. Heeger. (1994). Photosensitivity Of MEH-PPV Sandwich Devices And Its Implication To Polymer Electronic-Structure. *Molecular Crystals and Liquid Crystals Science and Technology Section a-Molecular Crystals and Liquid Crystals, 256*, 543-548. doi:10.1080/10587259408039289

Yu, Gang, Jun Gao, Jan C Hummelen, Fred Wudl, & Alan J Heeger. (1995). Polymer photovoltaic cells: enhanced efficiencies via a network of internal donor-acceptor heterojunctions. *Science-AAAS-Weekly Paper Edition, 270*(5243), 1789-1790.

Yu, Lihong. (2014). *Electron transfer study for selected dye sensitized solar cell and polymer solar cell by time-resolved spectroscopy.* The University of Hong Kong (Pokfulam, Hong Kong). Retrieved from http

Yuan, Wen. (2013). *Design and development of efficient solid-state dye-sensitized solar cells.* (Doctor of Philosophy), Michigan State University.

Zafar, Qayyum. (2015). *Fabrication, Characterization and Performance Optimization of Photodetectors Based On Solution Processed Organic Bulk-Heterojunction Blend.* (Doctor of Philosophy), University of Malaya.

Zafar, Qayyum, Zubair Ahmad, & Khaulah Sulaiman. (2015). PFO-DBT: MEH-PPV: PC71BM Ternary Blend Assisted Platform as a Photodetector. *Sensors, 15*(1), 965-978.

Zafar, Qayyum, Zubair Ahmad, Khaulah Sulaiman, Ahmad Sazali Hamzah, & Zurianti Abd Rahman. (2014). A MEHPPV/VOPcPhO composite based diode as a photodetector. *Sensors and Actuators A: Physical, 206*, 138-143.

Zhang, Chih-Piao Chuu, Jing-Kai Huang, Chang-Hsiao Chen, Meng-Lin Tsai, Yung-Huang Chang, Chi-Te Liang, Yu-Ze Chen, Yu-Lun Chueh, & Jr-Hau He. (2014). Ultrahigh-Gain Photodetectors Based on Atomically Thin Graphene-MoS2 Heterostructures. *Scientific Reports, 4*.

Zhang, F. L., M. Johansson, M. R. Andersson, J. C. Hummelen, & O. Inganas. (2003). Polymer solar cells based on MEH-PPV and PCBM. *Synthetic Metals, 137*(1-3), 1401-1402. doi:10.1016/s0379-6779(02)01059-7

Zhang, Guan, Gonu Kim, & Wonyong Choi. (2014). Visible light driven photocatalysis mediated via ligand-to-metal charge transfer (LMCT): an alternative approach to solar activation of titania. *Energy & Environmental Science, 7*(3), 954-966.

Zhang, Guang, Wenlian Li, Bei Chu, Zisheng Su, Dongfang Yang, Fei Yan, Yiren Chen, Dongyu Zhang, Liangliang Han, & Junbo Wang. (2009). Highly efficient photovoltaic diode based organic ultraviolet photodetector and the strong electroluminescence resulting from pure exciplex emission. *Organic Electronics, 10*(2), 352-356.

Zhang, Guang, Wenlian Li, Bei Chu, Fei Yan, Jianzhuo Zhu, & Yiren Chen. (2010). Very high open-circuit voltage ultraviolet photovoltaic diode with its application in optical encoder field. *Applied Physics Letters, 96*(7), 073301-073301-073303.

Zhang, H., Z. Cui, Y. Wang, K. Zhang, X. Ji, C. Lü, B. Yang, & M. Gao. (2003). From Water-Soluble CdTe Nanocrystals to Fluorescent Nanocrystal–Polymer Transparent Composites Using Polymerizable Surfactants. *Advanced Materials, 15*(10), 777-780. doi:10.1002/adma.200304521

Zhang, Min, Jingyuan Liu, Yinghui Wang, Difei Zhou, & Peng Wang. (2011). Redox couple related influences of π-conjugation extension in organic dye-sensitized mesoscopic solar cells. *Chemical Science, 2*(7), 1401-1406.

Zhang, Yong, Jingyu Zou, Hin-Lap Yip, Kung-Shih Chen, David F Zeigler, Ying Sun, & Alex K-Y Jen. (2011). Indacenodithiophene and quinoxaline-based conjugated polymers for highly efficient polymer solar cells. *Chemistry of Materials, 23*(9), 2289-2291.

Zhao, Ling, Suling Zhao, Zheng Xu, Wei Gong, Qianqian Yang, Xing Fan, & Xurong Xu. (2013). Influence of morphology of PCDTBT: PC71BM on the performance of solar cells. *Applied Physics A*, 1-8.

Zhao, Yue, Guoxiong Yuan, Philippe Roche, & Mario Leclerc. (1995). A calorimetric study of the phase transitions in poly (3-hexylthiophene). *Polymer, 36*(11), 2211-2214.

Zheng, Ying, & Jiangeng Xue. (2010). Organic photovoltaic cells based on molecular donor-acceptor heterojunctions. *Polymer Reviews, 50*(4), 420-453.

Zhong, Chengmei, Shengjian Liu, Fei Huang, Hongbin Wu, & Yong Cao. (2011). Highly efficient electron injection from indium tin oxide/cross-linkable amino-functionalized polyfluorene interface in inverted organic light emitting devices. *Chemistry of Materials, 23*(21), 4870-4876.

Zhong, Q., D. Inniss, K. Kjoller, & V. B. Elings. (1993). Fractured polymer/silica fiber surface studied by tapping mode atomic force microscopy. *Surface Science Letters, 290*(1–2), L688-L692. doi:http://dx.doi.org/10.1016/0167-2584(93)90906-Y

Zhu, Dg, Mc Petty, & M Harris. (1990). An optical sensor for nitrogen dioxide based on a copper phthalocyanine Langmuir—Blodgett film. *Sensors and Actuators B: Chemical, 2*(4), 265-269.

Zielinska, Beata, Joanna Grzechulska, Barbara Grzmil, & Antoni W Morawski. (2002). Photocatalytic degradation of reactive Black 5-A comparison between TiO2-Tytanpol A11 and TiO2-Degussa P25 photocatalysts. *Applied Catalysis B-Environmental, 35*(1), L1.

Zribi, A., & J. Fortin. (2009). *Functional Thin Films and Nanostructures for Sensors: Synthesis, Physics and Applications*: Springer.

Zubair, Ahmad. (2011). *Fabrication and Study of Metal-Organic Semiconductor-Metal Structures for Applications in Electronics.* (PhD), Ghulam Ishaq Khan Institute of Engineering Sciences & Technology, Swabi.

LIST OF PUBLICATIONS AND PAPERS PRESENTED

A. The following publications resulted from the work of this thesis

1- **Karwan Wasman Qadir, Ahmad, Z., & Sulaiman, K. (2014). Performance enhancement of NiTsPc based photo sensor using treated TiO_2 NPs film. Journal of Nanoparticle Research, 16(11), 1-8. doi:10.1007/s11051-014-2705-7.**

2- **Karwan Wasman Qadir, Ahmad, Z., & Sulaiman, K. (2015). Thermal Annealing Effect on the Optical, Electrical and Morphological Properties of the PBTTT-C_{12}:PC_{71}BM Blend Films. Journal of Solar Energy Engineering, 137(3), 034503-034503. doi:10.1115/1.4029230.**

3- **Karwan Wasman Qadir, Ahmad, Z., Sulaiman, K., Yap, C. C., & Touati, F. (2015). Binary blend based dye sensitized photo sensor using PCPDTBT and MEH-PPV composite as a light sensitizer. *Synthetic Metals, 210, Part B,* 392-397. doi:http://dx.doi.org/10.1016/j.synthmet.2015.11.005**

B- Conference Contributions and Paper Presented

1- **The 3rd ISESCO International Workshop and Conference On Nanotechnology 2012 (IWCN2012), December 5-7 2012, Universiti Kebangsaan Malaysia, Selangor, Malaysia (Participant) http://www.ukm.my/iwcn2012/.**

2- **The 4th International Conference on Functional Materials & Devices 2013 (ICFMD2013), April 8-11 2013, Rainbow Paradise Hotel, Penang, Malaysia PO43 (Investigation of new hydrazone dyes for dye-sensitized solar cells), http://umconference.um.edu.my/ICFMD2013.**

3- 5th Molecular Materials Meeting (M3), on August 3rd – 5th, 2015, Resorts World Convention Centre, Sentosa, Singapore, Paper no. O-MS-0057 http://www.imre.a-star.edu.sg/m3conference

C- Seminars

1- Collaboration seminar, "Performance enhancement of NiTsPc based photo sensor using treated TiO_2 NPs film", King Faisal Convention Center, King AbdulAziz University, Jeddah, Saudi Arabia, December 4th, 2014.

2- Postgraduate seminar, "Performance enhancement of NiTsPc based photo sensor using treated TiO_2 NPs film", Auditorium Fizik, Block C, Department of Physics, Faculty of Science, University of Malaya, Malaysia, January 8th, 2015.

3- Postgraduate candidature defense, "study of organic semiconductor based photovoltaic devices: light sensors and solar cells", Auditorium Fizik, Block C, Department of Physics, Faculty of Science, University of Malaya, Malaysia, May 21st, 2015.

4- Viva-voce (Presentation for PhD evaluation), "study of organic semiconductor based photovoltaic devices: light sensors and solar cells", Meeting Room, Dean Office, Faculty of Science, University of Malaya, Malaysia, Tuesday, May 31st, 2016, 11:30 am.

D- Training

1- Workshop on "Dye-sensitized Solar Cells: Theory and Laboratory Practical", Centre for Ionics, Department of Physics, Faculty of Science, University of Malaya, Malaysia, August 20th - 21st, 2013.

2- Workshop on "Conducting a Literature Search & Writing Review Paper", Centre for Research Services, Institute of Research Management & Monitoring, University of Malaya, Malaysia, November 4th & 5th, 2015.

3- Workshop on "How to Publish in High Quality ISI-Indexed Journal", Faculty of Computer Science and Information Technology, University of Malaya, Malaysia, November 17th & 18th, 2015.

4- Workshop on "Impedance Spectroscopy: Theory, Applications and Laboratory Instruction" Centre for Ionics, Department of Physics, Faculty of Science, University of Malaya, Malaysia, April 12th-14th, 2016.

5- As an organizing committee member for "Workshop on Nano-Materials for Energy and Environment", Department of Physics, Faculty of Science, University of Malaya, Malaysia, April 21st, 2016.

E- Participation

1- "PhD GOT IT PROGRAMME", Institute of Graduate Students, University of Malaya, Malaysia, May 28th & 29th, 2014.

2- University of Malaya Three Minute Thesis Competition 2016, Faculty level, (UM3MT 2016), March 23rd, 2016.